Large-scale Spatially Extended Atmospheric Pressure Plasma

By

Zhi Cao

A Doctoral Thesis

Submitted in partial fulfilment of the requirements for the award of

Doctor of Philosophy of Loughborough University

July 2010

Abstract

This thesis presents experimental studies of low-temperature atmospheric pressure plasma sources with generic ability to effectively treat large-scale three-dimensional (3D) objects. The reported large-scale plasma sources are developed through parallelisation of single plasma jets. This strategy outshines the other reported strategies for treatment of uneven surfaces by being able to produce spatially extended plasma directly onto the surface of heavily three-dimensional objects. Comparable studies of the design of elemental plasma jets bring out a hybrid electrode configuration, the capillary-ring jet, as the best elemental jet to be used in the parallelisation. It is found that the introduction of a ballast resistor to the individual jet circuit or built-in capacitance is important to assure the jet-to-jet synchronism, stability and uniformity. Electrical and optical analyses of one-dimensional (1D) array of atmospheric pressure plasma jets demonstrate robust temporal and spatial jet-to-jet uniformity both for flat and sloped surfaces. Hexagonally-arranged two-dimensional (2D) arrays of atmospheric pressure plasma jets show good level of insusceptibility to variations of the downstream samples in their physical dimensions as well as structural and material properties. The reaction chemistry impact area of a 2D 37-jet array is estimated to be 18.6 cm^2. These confirm the plasma jet arrays as a viable option as large-scale atmospheric plasma sources, well suited for many processing applications including plasma medicine. The spatially separated dual-frequency excitation further benefits the plasma jet in that separate control of different important plasma parameters is possible. Enhanced plasma properties achieved by the dual-frequency offer greater potential to the jet arrays.

Key words: gas discharge, atmospheric pressure glow discharge, plasma source development, plasma jet, plasma jet arrays, dual-frequency

Acknowledgements

First of all, I would like to express my deep gratitude to my supervisor, Professor Michael G Kong, for his tireless guidance throughout my PhD study. His broad and profound expertise, unceasing willingness to explore scientific frontiers, and great personality have deeply impressed me and led me to become a young researcher in the intriguing research field of cold atmospheric plasmas. His encouragements and care go beyond the supervision of my study, from which I will benefit for my life.

I am grateful to the British government for an ORSAS award and Department of Electronic and Electrical Engineering in Loughborough University for a full PhD studentship.

I would also like to express my sincere appreciation to a number of people who have helped me during my PhD study. Especially, my thanks go to Dr Felipe Iza, Dr James Walsh, Miss Qiuyue Nie, Mr Danny Bayliss, Dr Jianjun Shi and Dr Xutao Deng for their warm-hearted support. I am also thankful for Dr Jan Benedikt, Mr Dirk Ellerweg and Prof. Achim von Keudell of Ruhr-Universität Bochum for their kindly support when I carried out experiments in Bochum.

Last but not least, I would like to express my deepest love to my family and my fiancée Miss Yali Zhu. The journey of my PhD study could not be so colourful without their endless support and love.

Publications

Journal Publications:

1. J. L. Walsh, **Z. Cao** and M. G. Kong, Atmospheric Dielectric-Barrier Discharges Scalable From 1 mm to 1 m, *IEEE Trans. Plasma Sci.*, **36**, 1314-1315 (2008)
2. **Z. Cao**, J. L. Walsh, and M. G. Kong, Atmospheric Plasma Jet Array in Parallel Electric and Gas Flow Fields for Three-dimensional Surface Treatment, *Appl. Phys. Lett.,* **94**, 021501 (2009)
3. Q. Nie, **Z. Cao**, C. S. Ren, D. Z. Wang and M. G. Kong, A Two-dimensional Cold Atmospheric Plasma Jet Array for Uniform Treatment of Large-area Surfaces for Plasma Medicine, *New Journal of Physics*, **11**, 115015 (2009)
4. **Z. Cao**, Q. Nie and M. G. Kong, A Cold Atmospheric Plasma Jet Controlled with Spatially Separated Dual Frequency Excitations, *J. Phys. D: Appl. Phy*s. **42**, 222003 (2009)
5. **Z. Cao**, Q. Nie, D. L. Bayliss, J. L. Walsh, C. S. Ren, D. Z. Wang and M. G. Kong, Spatially Extended Atmospheric Plasma Arrays, *Plasma Sources Sci. Technol*., **19**, 025003 (2010)

Conference Publications:

1. **Z. Cao**, J. L. Walsh, J. J. Shi and M. G. Kong, A parametric study of a cold atmospheric plasma jet, *34th IEEE International Conference on Plasma Science,* New Mexico, US, June 2007.
2. **Z. Cao**, J. L. Walsh and M. G. Kong, Electrical and optical characterization of a wide plasma brush in atmospheric helium flow, *35th IEEE International Conference on Plasma Science*, Karlsruhe, Germany, June 2008.
3. **Z. Cao,** J. L. Walsh and M. G. Kong, Large-scale cold atmospheric plasma systems, *Technological Plasma Workshop 2008*, Milton Keynes, UK, December 2008

4. **Z. Cao**, Q. Nie and M. G. Kong, Cold atmospheric plasma jet arrays: fundamental characterization and treatment of 3D surgical instruments, *Fundamentals and Applications of Microplasmas 2009*, San Diego, US, March 2009.

5. **Z. Cao**, J. L. Walsh and M. G. Kong, Large-scale cold atmospheric plasma systems, *Fundamentals and Applications of Microplasmas 2009*, San Diego, US, March 2009.

6. Q. Nie, **Z. Cao**, M. G. Kong, D. Z. Wang and C. S. Ren, A comparison study of atmospheric plasma jets, *Fundamentals and Applications of Microplasmas 2009*, San Diego, US, March 2009.

7. D. W. Liu, J. L. Walsh, **Z. Cao**, F. Iza and M. G. Kong, Cold atmospheric microplasmas, *Frontiers in Low Temperature Plasma Diagnostics VIII*, Blansko, Czech Republic, April 2009.

8. J. L. Walsh, **Z. Cao** and M. G. Kong, Large area atmospheric pressure plasma sources and their applications, *Plasmas Surfaces and Thin Films, IOP*, London, UK, June 2009.

9. **Z. Cao**, Q. Nie, D. L. Bayliss, J. L. Walsh, D. Z. Wang, C. S. Ren and M. G. Kong, Cold atmospheric plasma jets arranged in a honeycomb array, *19th International Symposium on Plasma Chemistry*, Bochum, Germany, July 2009.

10. Q. Nie, **Z. Cao**, D. L. Bayliss, D. Z. Wang, C. S. Ren and M. G. Kong, Effects of electrode configurations in atmospheric plasma jets, *19th International Symposium on Plasma Chemistry*, Bochum, Germany, July 2009.

11. D. L. Bayliss, J. L. Walsh, **Z. Cao**, F. Iza, G. Shama and M. G. Kong, Degradation and removal of proteinaceous matter using cold atmospheric plasmas, *19th International Symposium on Plasma Chemistry*, Bochum, Germany, July 2009.

12. D. L. Bayliss, G. Shama, **Z. Cao**, Q. Nie, J. L. Walsh, F. Iza and M. G. Kong, Cold atmospheric plasma sterilization: from bacteria to biomolecules, *62nd Annual Gaseous Electronics Conference*, New York, USA, Oct 2009.

Content

Chapter 1
Introduction

1.1 Historical review of gas plasma

Plasma, the so-called the fourth state of matter, is essentially a group of electrons, ions, neutral particles and UV photons. Though it contains charged particles, it maintains approximately electrical neutrality as a whole.

Most matters in the universe are in the state of plasma, such as astrophysical medium, stars and ionosphere. However, the plasma presented in our daily life is often realised by means of ionisation, either naturally or artificially produced. Lightning and the polar aurora are examples of naturally occurring plasmas. They are ionised due to either strong electrical field induced by accumulated charges or collision with solar wind particles. Indeed, electrical discharge is the most straightforward way to realise ionisation and thus produce plasma. In most cases, it happens in a gas medium, so the generation of plasmas is often related to gas discharge.

The early research of gas discharges can be regarded as the genesis of modern electronic and electrical engineering, and the progress of its research has been contributing to the development of modern science greatly. The earliest human acquaintance with gas discharge can certainly be traced back to the observation of lightning. However, it was not until the 18^{th} century that scientific experiments were conducted to study gas discharges. The pioneer scientists at that time were E G von Kleist who invented the *Leyden jar*, a primitive capacitor, in 1745 and Benjamin Franklin who introduced the

concept of *positive* and *negative polarity* as well as *single fluid theory* in 1750's[1.1]. Franklin also explained the lightning phenomenon experimentally.

The 19th century witnessed a rapid progress in the gas discharge research. Russian scientist V. V. Petrov and English scientist Sir Humphry Davy reported and studied arc discharge in the early years of the 19th century[1.2]. Sir Humphry Davy's laboratory assistant, Michael Faraday, carried on experiments in direct current (DC) electrical discharge tubes at pressure of 1 Torr and voltage up to 1 kV. This classical work first discovered glow discharge in 1830's. Michael Faraday also named some basic terms in electrical science such as '*electrode*', '*anode*', '*cathode*' and '*ion*'[1.1].

Gas discharge research in the late 19th and early 20th century was very active and it led to the origin of atomic physics. Sir Joseph John Thomson carried out experiments and obtained quantitative result of the charge-to-mass ratio (i.e. *e/m*) in 1897[1.2]. This confirmed the existence of the electron which later was officially proposed by Dutchman Hendrik Antoon Lorentz to use the term '*electron*' in 1906[1.1]. Sir William Crookes introduced the term '*ionisation*' in 1898[1.1]. Beginning in 1900, John Sealy Edward Townsend, a student of J. J. Thomson conducted various experiments and studied the electrical conduction of gases[1.2], which later developed into the *Townsend Theory* that describes how electron multiplication results in gas breakdown. He also directly measured the value of the electrical charge of an electron.

The concepts of '*plasma*' and '*sheath*' were introduced by Irving Langmuir in 1928 and 1925 respectively[1.1]. He also made great contributions to gas discharge physics and invented the *Langmuir probe*, an important plasma diagnostics device for determining electron temperature, electron density and electric potential of a plasma generated at reduced gas pressures.

Gas discharge research in the 20th century was vibrant. On one hand, the research on DC discharges continued. On the other hand, the research was directed into gas discharges excited at ever-increasing frequencies. For

instance, radio frequency (RF) excited plasmas were first observed in 1891 and the understanding of the mechanism of discharge initiation was reported in 1920's[1.2]. The radar technology developed during the Second World War stimulated the use of microwave frequency for gas discharges, and in 1970's the laser technology were also used for gas breakdown[1.1,1.2].

Plasma science had been developing in line with the development of gas discharges since the introduction of the term '*plasma*', but it has its own impetus. The ongoing interest in energy sources from controlled fusion has led to a key and significant research activity since 1950's and this massive scientific program spurred plasma research in universities and national laboratories worldwide[1.1]. The attempt to create and confine high temperature plasma magnetically also benefited industrial plasma applications. From 1970's, the microelectronics industry has undergone a rapid development and it was the cornerstone for the so-called information revolution. Plasma technology is now extensively used in microelectronics fabrication, such as deposition and etching. It is so indispensable that for manufacturing a modern integrated circuit, plasma-related work takes up one third of the whole fabrication process[1.3]. Other plasma application areas include lighting, metallurgy, aerospace, automotive and biomedicine, just to name a few.

A noticeable new trend of plasma research is driven by the advent of atmospheric pressure plasma, especially atmospheric pressure glow discharge (APGD), back to some thirty years ago[1.4]. Since then, APGD has been an attractive topic in the plasma research community. Glow discharge, which was discovered at reduced gas pressures in 1830's, once again became the focus of attention because its atmospheric pressure version removes the need for the vacuum system and as a result opens the door to a vast range of new applications. This thesis is largely motivated by the considerable application potentials of and the related technical requirements for APGD.

There are two important concepts associated with gas plasma, namely

degree of ionisation and *temperature*. The degree of ionisation is used to characterise the ionisation level in a plasma and it is defined as[1.2]

$$Ionisation\ degree = n_e/(n_e + n_n) \tag{1.1}$$

where n_e and n_n are the densities of electrons and neutral atoms. By this definition, a plasma can be regarded as *fully ionised* if its ionisation degree approaches unity, *partially ionised* if its ionisation degree is significantly less than unity, and *weakly ionised* if its ionisation degree is between 10^{-6} and 10^{-1}[1.5]. According to the ideal gas law,

$$p = nkT \tag{1.2}$$

where p, n and T are the pressure, density and temperature of the gas respectively, and k is Boltzmann's constant. For a gas at one atmosphere and 300 K, its density is approximately 2.447×10^{19} molecules (or atoms) per cubic centimetre. Given $n_e = 10^9 \sim 10^{12}$ cm^{-3} for a typical APGD[1.6,1.7], APGDs are weakly ionised plasmas.

Temperature in the context of gas plasma is a reflection of the thermal kinetic energy of particles and is often measured in Kelvin (K). Electron temperature (T_e) is used to reflect the electron kinetic energy, and depends on the electron energy distribution function. As the electron energy distribution function is difficult to measure, particularly at atmospheric pressure, a common approximation is to use its population-averaged, or the mean electron energy. For a Maxwellian energy distribution function the relationship between this mean energy and the electron temperature is given by $<\varepsilon>=3/2kT_e$. Although the mean electron energy is a function of space and time, it is sometimes described as a constant of a range (e.g. 1 ~ 5 eV) to indicate the broad scope of chemical reactions the plasma can initiate. In general, for *non-equilibrium plasma* or *non-thermal plasma*, the electron temperature is much larger than the neutral particle temperature (T_n), while for *equilibrium plasma* or *thermal plasma*, $T_e \approx T_n$. APGDs are non-thermal

plasmas. Figure 1-1 shows typical densities and electron temperatures of plasmas, both naturally occurring and laboratory-generated[1.3,1.8]. They include non-thermal plasmas and thermal plasmas.

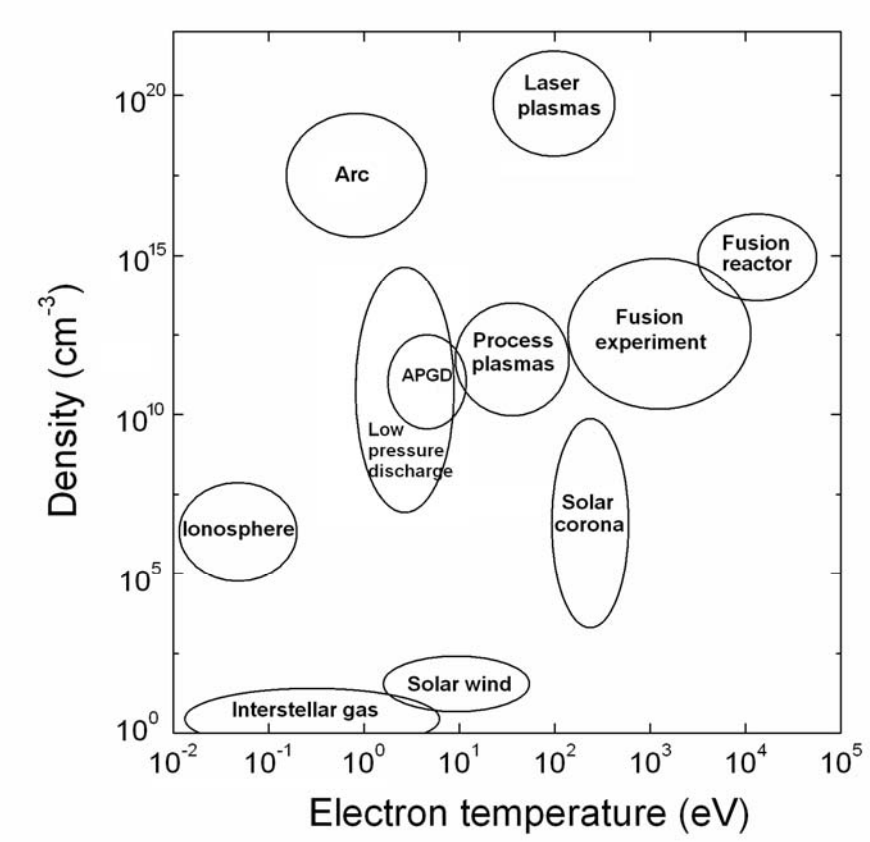

Fig 1-1: Typical densities and electron temperatures of natural and laboratorial plasmas[1.3,1.8].

Rotational temperature and *vibrational temperature* describe the population of rotational and vibrational states in molecular species respectively. As the population of rotational state is controlled by collisions with heavy particles, rotational temperature may be used to approximate gas temperature. Vibrational transitions, on the other hand, are primarily dominated by electron collisions, so vibrational temperature is sometimes related to electron temperature[1.9].

1.2 Low-pressure gas discharges

1.2.1 Regimes

A classical experiment was done in a DC electrical discharge tube at low pressure and it may be used to illustrate different gas discharges. Figure 1-2 shows the current-voltage characteristic (CVC) of this DC low-pressure discharge, sustained between two circular electrodes[1.1]. Basically the discharges can be divided into three broad regimes, namely *dark discharge*, *glow discharge* and *arc discharge*, which are labelled in red in the graph.

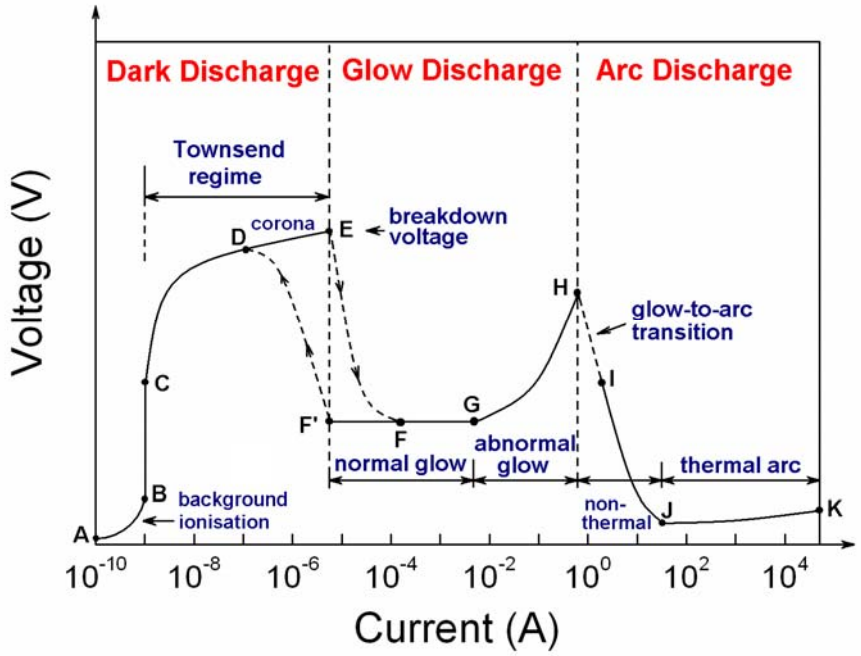

Fig 1-2: Current-voltage characteristic of a DC low-pressure electrical discharge[1.1].

In the dark discharge, the region between point *A* and *B* in figure 1-2 is called the *background ionisation regime* where ionisation caused by the cosmic rays or other radiation provides a current flow. With an increasing voltage, the current increases in this regime as more charged particles are able to flow into the electrodes. The background ionisation regime is followed by the *saturation regime* which is located between point *B* and *C*. As all the

charged particles caused by the background ionisation have reached electrodes and the applied voltage is not high enough to create new ionisation in this regime, its current stops to increase with voltage. *Townsend regime* occupies the curve between point *C* and *E*, in which *Townsend theory* applies. Townsend theory features an avalanche, multiplication of electrons and positive ions. This avalanche happens because the electric field is strong enough to energise electrons above the ionisation energy of the gas atoms or molecules before they reach the anode. As a result of the avalanche, the current increases exponentially with the voltage. Just as its name implies, the dark discharge is weak and normally no visible light can be observed except the region between point *D* and *E*, which is called the *corona discharge*. In this regime, the local electric field on the surface of the cathode exceeds the breakdown strength of the working gas due to sharp edges or tiny protuberances of the electrode. Light can be seen near these locally enhanced regions.

The point *E* represents the end of the dark discharge. After that, the discharge develops into the *glow discharge* and immediately transfers to the point *F*, which is located in the *normal glow discharge* region. Now the current is significantly higher and the discharge is clearly visible. In the normal glow discharge region from point *F* to *G*, the current undergoes an increase of several orders of magnitude while the voltage remains approximately constant. This is because the discharge coverage on the electrode surface is not 100% but keeps increasing till the current reaches the point *G*, at which the entire electrode surfaces are occupied by the plasma. From point *G* to *H*, the discharge is in the *abnormal glow discharge* region, which features a positive slope of the current-voltage curve. If the discharge starts from the glow discharge regime and moves to the left in the CVC curve, then a hysteresis is likely to happen. Instead of going from point *F* to *E*, the discharge remains in the normal glow discharge region till the point *F'*. This

is a condition with much lower plasma density than in the point *F*, and only after the discharge reaches *F'* then it transits back to the Townsend regime.

At point *H*, the current density is so high that it heats the cathode and triggers a glow-to-arc transition as indicated by the dotted line between point *H* and *I*. This transition is instantaneous, after which the discharge is in the arc discharge regime. The arc discharge can be divided into *non-thermal arc* and *thermal arc* depending on whether electrons and ions are in thermal equilibrium state. They also feature different current-voltage characteristics. For the non-thermal arc region between point *I* and *J*, the current increases as the voltage decreases. For the thermal arc region from point *J* to *K* on the other hand, the voltage undergoes a slow increase with increasing current.

1.2.2 Applications

Early activities in the history of gas discharge research focused mainly on low-pressure discharges and they have resulted in extensive understanding. This has been critical in underpinning the industrial applications of low-pressure plasmas. The majority of current plasma industrial applications are carried out at reduced gas pressures between 1 mTorr to a few Torr. This is partly because at low-pressure it is easy to obtain a large-volume plasma with good stability. Large-volume plasma can in turn facilitate a high product yield, a key factor for large-scale industrial applications.

Most low-pressure plasma applications utilise glow discharges. Microelectronics industry is one such example. Etching, deposition (specifically plasma enhanced chemical vapour deposition, PECVD), stripping and cleaning, all these necessary working procedures of semiconductor processing rely on the participation of glow discharge plasma[1.3]. Similarly, these plasma-assisted procedures are also critical for the fast-developing panel display industry[1.10].

Other major application areas of low-pressure glow discharges include surface modification[1.11], manufacture of novel materials[1.12], lighting[1.13] and sterilisation[1.14]. These have benefited a broad range of industries.

1.3 Atmospheric pressure glow discharge

The different discharge regimes found in the aforementioned classical DC electrical discharge can all be found at atmospheric pressure. Different from the corona discharge, which occurs in a non-uniform electric field with plasma only produced in a relatively small region near the electrode area of high potential gradient, and the arc discharge, which is often formed in a narrow conductive channel with a high temperature and a high current density, APGD features a uniform and normally stable discharge with reasonably high plasma density.

Since most current industrial plasma applications are based on low-pressure glow discharges, it is both desirable and timely to explore APGD given its practical advantages. Specifically for low-pressure plasma processing, a sealed chamber and its affiliated pumps are necessary. This inevitably increases the costs of investment and maintenance, and also limits the processing speed because of the need to work in a batch fashion. Although APGDs have a relatively short history, and their research and applications lag behind that of low-pressure plasmas, the chamber-free APGDs are found to be able to broaden the scope of plasma industrial applications and even substitute low-pressure plasmas for some of their current applications.

It should be noted that atmospheric plasmas operate in a very different parametric range to their low-pressure counterparts. At atmospheric pressure, the collision frequency is in the terahertz range and the electron mean-free path is at most a few micrometres[1.15]. This is very different from the low-pressure plasma, and also a much higher voltage is needed to break down

the gas at atmospheric pressure. Once broken down, the gas discharge is relatively susceptible to transition from a stable glow discharge plasma to an unstable streamer or arc, compared to the low-pressure case. In other words, the glow-to-arc transition occurs much easier at atmospheric pressure than at low pressures. The resulting localised plasma, such as streamer and arc, is normally with high gas temperature which tends to damage the objects being treated. APGDs, on the other hand, can be produced with a gas temperature close to room temperature. This thesis focuses on APGD.

1.3.1 Generation of APGD

The generation of an atmospheric pressure glow discharge normally requires a much higher voltage than in the case of low-pressure, and the glow-to-arc transition is a major challenge for maintaining APGD. Noble gases are often used as the gas medium for generating APGDs because they have much smaller Townsend ionisation coefficients than molecular gases when the ratios of the applied electric field to the breakdown electric field are the same. As a result, if the overvoltage and the gap distance are not too large, the electron multiplication in a noble gas is usually kept under the critical value, over which glow-to-arc transition happens. Helium and argon gases are the most common gases used for producing AGPDs and a trace of molecular gas may be mixed into noble gas to enhance plasma chemistry.

In terms of the means by which electrical power is coupled to produce AGPD, both inductively coupling and capacitively coupling are feasible. Inductively coupled plasmas tend to have a high plasma density with relatively high gas temperature, which limits their use to cases where high temperature is tolerated. Capacitively coupled plasmas, on the other hand, can produce low-temperature plasmas at frequencies from a few Hz to a few hundred MHz. The following discussion focuses on capacitively coupled

APGDs.

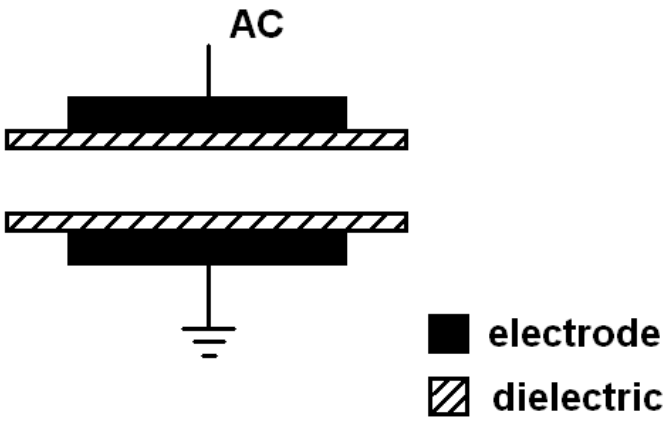

Fig 1-3: A schematic of a dielectric barrier discharge.

There are several approaches to mitigate glow-to-arc transition. Dielectric barrier discharge (DBD) is an effective and common approach and it has been demonstrated both experimentally and theoretically[1.16]. DBD can be generated using various electrode configurations for which at least one electrode is covered by dielectric material or a dielectric is placed between the electrodes. The dielectric can restrict an uncontrolled increase of the discharge current and limit the current density within the glow discharge regime. In general, alternative current (AC) sinusoidal waveform is used to generate DBDs. A schematic of a DBD is shown in figure 1-3. Electron avalanches develop from the dielectric surface at the instantaneous cathode and the number of electrons doubles with each generation of ionizing collisions. These electrons drift towards the instantaneous anode until they are blocked by the dielectric and then distribute on the surface of the dielectric. At the cathode side, the avalanche-generated ions are also blocked. These blocked electrons and ions form an electric field which is in the opposite direction to that of the original electric field in the discharge gap. As a result, the voltage drop on the discharge gap starts to reduce and the discharge dies away. When the voltage polarity changes in the next half cycle, the above

process happens again. This leads to repetitive generation and extinction of a uniform APGD in the discharge gap.

A similar approach to the above is to employ resistive electrodes[1.17,1.18]. The resistive electrodes are essentially ballast resistors and they provide a negative feedback to the applied voltage and keep the voltage drop on the gas gap to a moderate extent.

A dramatically different strategy to the control of glow-to-arc transition is to use either radio frequency excitation[1.19-1.22] or pulse power[1.23,1.24]. In these situations, APGDs can be achieved even without the use of dielectric barrier. For a RF discharge, the transition time of an electron travelling from one electrode to the other can be longer than the half cycle of the applied voltage so both electrons and ions can be trapped between the electrodes in the oscillating electric field[1.25]. This prevents the discharge from arcing and makes it possible to generate an APGD. As for a pulsed discharge, the periodic short voltage pulses make the discharge as a sequence of transient breakdown. The pulse widths of the voltage pulses are either comparable or shorter than the timescale of the glow-to-arc transition. This allows the glow-to-arc transition to be effectively mitigated[1.26].

1.3.2 Applications of APGDs

Since the late 1980's[1.4], with the development of various APGD plasma sources, APGDs have been used for widespread applications. It is found that APGD is able to be used in some of the application areas of low-pressure plasmas. These include deposition[1.27-1.29], etching[1.30], surface modification[1.31,1.32] and material synthesis[1.33]. In addition, APGD has opened doors to new areas of applications, such as plasma aerodynamics[1.34,1.35], photonics[1.36-1.43], microfluidic[1.44], modification of electromagnetic propagation[1.45,1.46], remediation of volatile organic compounds[1.47], synthesis

of nanoparticles[1.48] and plasma medicine[1.49].

Perhaps the most remarkable application area of APGDs is biomedical applications. Since those earliest results published in late 1990's[1.50-1.52], this field has undergone an exponential growth and led to the birth of *plasma medicine*, an emerging interdisciplinary research subject sitting at the frontier of plasma science. It involves different subjects such as plasma science, medicine, biology, microbiology, physics, chemistry and engineering. Broadly speaking, plasma medicine investigates the use of non-thermal plasma in medicine. In the following paragraphs, attention is paid to plasma medicine, as the goal of this thesis is to develop large-scale plasma sources for biomedical applications.

Plasma medicine has a relatively short history[1.49,1.53,1.54], with its first report on bacteria inactivation by APGD in 1996[1.50]. Since then the depth and breadth of the field have been expanding much further. Now the attention goes beyond the bactericidal effects to more broad topics such as hospital hygiene issues, wound healing and skin disinfection. The initial results achieved by the pioneer researchers showed great promise, and plasma medicine could be a hot research area in the centuries-old plasma science and can bring profound benefits to humanity in the 21st century.

The generation of plasma is a complex process, and all the participants such as UV radiation, reactive species, charged particles, heat, current and electric field, can interact with the target to be treated. This interaction is target-specific, i.e. some factor is effective while others may be not. In some cases, synergistic effects exist. As for the treatment targets, they are in various forms from bacteria, cell to living tissue and skin. Based on their cellular structure, they are grouped into prokaryotic cells and eukaryotic cells in the following discussion[1.49].

The interaction between plasma and prokaryotic cells can be roughly divided into three areas, namely sterilisation of inanimate objects, disinfection

of biological surfaces, and modification of cellular functions[1.49]. Sterilisation of inanimate objects has been the major component of plasma medicine research so far. It is found that APGD can be effective against both gram-positive[1.53] and gram-negative bacteria[1.55], spores[1.52], viruses[1.56], fungi[1.57,1.58] and biomolecules[1.59,1.60]. It could also inactivate biofilm[1.61], an extracellular polysaccharide matrix in which bacteria are embedded. The results targeting two stubborn biological contaminants, namely prion and Methicillin-resistant *Staphylococcus aureus* (MRSA), are worth particular attention. Prion is a misfolded protein causing for transmissible spongiform encephalopathy. While all current commercial decontamination methods are ineffective against prion, it has been found that low-temperature plasmas can remove protein substantially and this suggests its capability to inactivate prion [1.59,1.60,1.62]. MRSA is a bacterium and it is a major source of the so-called hospital acquired infections. The proved bactericidal effect of APGD on MRSA in laboratory could open the door for an effective approach to stop hospital acquired infections[1.63].

Disinfection of biological living tissues is more complex than sterilisation of inanimate objects. This is because biological tissues have more complicated structures and an overdose of plasma-generated substances is harmful to healthy living tissues. Balance has to be made between effectiveness and toxicity. The progress in this direction is directly linked to other applications such as food decontamination[1.64], disinfection of open wound[1.54] and skin disease treatment[1.58]. For modification of cellular functions, research on genetic effects of APGD was reported recently[1.65].

The interaction between plasma and eukaryotic cells has a broad range of applications including disinfection of living tissues[1.66], blood coagulation[1.54], induction of apoptosis in malignant tissues[1.67], localised modulation of cell adhesion[1.67] and proliferation[1.68], and tissue modification in electrosurgery[1.49]. All these provide a hope that in the future APGD can be

extensively used during a clinical procedure as well as aftertreatment. Similar to how low-pressure plasmas had benefited the growth of microelectronics industry, atmospheric plasma technologies could have a profound impact on medicine and healthcare.

Generally speaking, oxidation is the major reason for the bactericidal effect induced by a typical helium/oxygen plasma generated at frequencies below very high frequency band of 30 ~ 300 MHz and the most important bactericidal species of APGD is believed to include oxygen atoms[1.49,1.69]. Ozone may also be an important participant but it depends on its yield in the plasma[1.49]. OH radicals and UV photons are believed to play minor roles as their yields are normally small[1.70]. This suggests that for sterilisation and disinfection applications by a helium/oxygen plasma, plasma source designs should seek a maximum production of oxygen atoms. Plasma-generated reactive oxygen and nitrogen species are also believed to be the factors causing coagulation, necrosis and apoptosis, while charged particles and electric field are responsible for cell membrane permeabilisation[1.49].

1.3.3 Plasma source design for biomedical applications

The objects to be treated by plasma in biomedical applications are broad. They include the inanimate objects such as surgical instruments and catheters, as well as biological objects such as human skin, tissue, tooth and wound. In most cases, these objects are uneven, and some of them have heavily three-dimensional structures. Moreover, these objects quite likely have a surface with a few centimetres at least in one dimension. Consequently, for biomedical applications, plasma source is required to be able to treat large-scale uneven substrates effectively.

For applications that require treatment of large but flat surfaces, one can easily use DBD[1.71] or barrier-free APGD[1.23,1.72] to achieve uniform treatment

with a length scale of even larger than one metre. However, for treatment of large object with uneven surfaces, the object is often too big to be placed into the electrode gap. Even when it can be placed into the gap, it is impossible to achieve a uniform treatment due to its uneven surfaces.

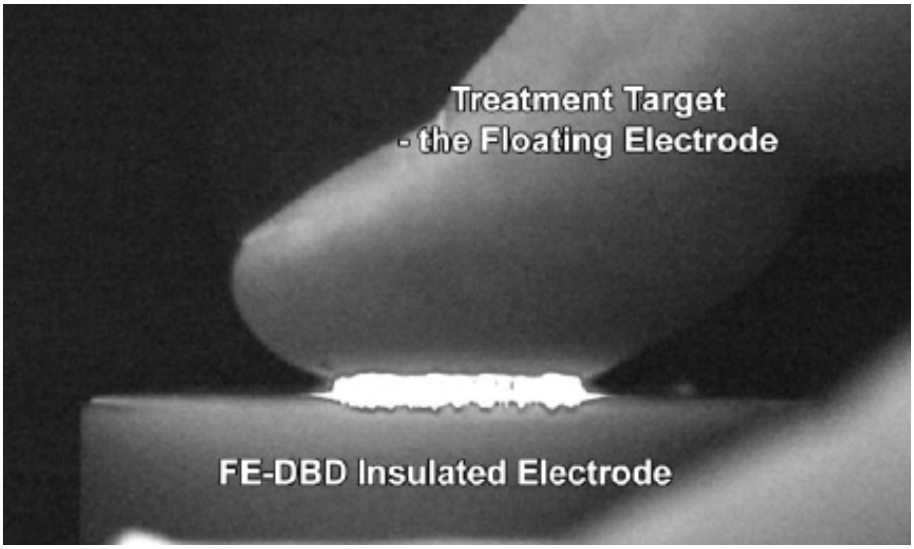

Fig 1-4: A picture of a floating-electrode DBD[1.54].

It seems that there are three different ways to realise large-scale treatment of uneven surfaces. The first one is DBD with uneven substrate (e.g. tissue) as one electrode and the corresponding plasma source is called floating-electrode DBD[1.54], which is shown in figure 1-4. This plasma source employs a powered metal electrode covered by a dielectric material and a human thumb or living tissue as the counter electrode. This human thumb is electrically floating. When it is close to the other electrode, plasma can be produced directly on the surface of the human tissue upon certain applied voltage. The typical distance between the dielectric-covering powered electrode and the human floating electrode is less than 3 mm and atmospheric air is the gas medium[1.54]. Because of the existence of the dielectric barrier, discharge current is limited to a small value which is safe to human. This floating-electrode DBD has been used for applications such as bacteria

sterilisation and blood coagulation, and effective treatment results were reached[1.54,1.73,1.74]. Another plasma source, the so-called 'plasma dispenser', can also be classified into this category[1.58].

The advantages of the floating-electrode DBD are obvious. This plasma source is easy to cover a large surface and the use of air as the working gas makes it cost-effective. On the other hand, its disadvantages are also clear. Because of its very small gas gap, this source can only be used to treat mildly uneven surfaces, leaving the majority of the targeted applications unattended. Moreover, judging from the discharge images and its current waveform, it is clear that the discharge is essentially not a glow discharge, but an unstable discharge with many streamers distributing randomly in the gap. Although these phenomena are normal for an air DBD discharge, it is unclear whether these filaments may lead to uncontrolled (hence difficult to reproduce) dose distribution on the tissue surface.

The second way to realise large-scale treatment of uneven surfaces relies on afterglow. It is characterised by the generation of a plasma in an upstream electrode region and then a transportation of the mostly uncharged plasma species to a downstream application region by a gas flow. In other words, it relies on the gas flow to convey the reactive species to the area of treatment. Several plasma sources with quite distinct structures fall into this category. They include parallel-plate type with the direction of gas flow either perpendicular to that of the externally applied electric field[1.75-1.77] or parallel to that of the electric field[1.29,1.78], pin-to-pin plasma brush[1.79,1.80] and some types of plasma jets[1.81,1.82]. In these cases, the electrons and ions are most likely trapped in the upstream electrode gap, and the treatment efficacy relies on uncharged plasma species and photons in the form of an afterglow. Considering the short-lives of some reactive plasma species as well as the distance between the plasma generation and application regions, the treatment efficacy may be compromised due to recombination of short-lived plasma

species.

Atmospheric pressure plasma jets, an important group of atmospheric pressure plasma sources, are known to be a kind of effective localised treatment tools for biomedical applications[1.81]. By appropriate designs, plasma jet can generate a plasma plume up to a few centimetres long, so it is possible to use a plasma jet to treat three-dimensional objects. Moreover, using the plasma jet, plasma species can be produced directly onto the surface of the object to be treated[1.83]. To overcome its inherent small plasma coverage, individual plasma jets can be arrayed up to form a larger plasma source. This could be the third way to realise large-scale treatment of uneven surfaces, with clear advantages over the other two ways. The parallelisation of plasma jets will be discussed in Chapter 4 ~ 6. As more and more plasma jets are packed together, issues such as plasma stability, processing uniformity, plasma reactivity as well as scalability need to be investigated. These will be discussed.

1.4 Scope of the thesis

This thesis provides an experimental study of the development of large-scale atmospheric pressure plasma sources for treatment of uneven surfaces. The plasma produced by these sources is spatially extended, i.e. the plasma is not confined in but extended spatially from its generation region. The intended applications mainly are sterilisation and decontamination of surgical instruments and/or living tissues. Further to this, the plasma sources can be used in plasma wound healing and blood coagulation. The underlying requirements of these applications are the ability to treat three-dimensional objects at a downstream gas temperature lower than 70 °C, as well as excellent plasma stability, reactivity and uniformity.

Plasma biomedical applications are of significant importance and the

field has been a hot research area since the late 1990's. These researches can be of great benefit to modern medicine. With this great potential, however, the plasma sources suitable for treating 3D objects are currently rare.

This thesis explores two possible routes to realise its goal. One is through a spatially extended DBD plasma and the other is based on single plasma jet and plasma jet arrays. The plasma diagnostics involved in this research are electrical measurement, fast imaging, optical emission spectroscopy and mass spectrometry.

1.5 Organisation of the thesis

In Chapter 1, brief introduction is given to the history of gas plasma research, low-pressure gas discharge, atmospheric pressure glow discharge and its biomedical applications. This outlines the background of this research and its significance.

Chapter 2 provides a review of plasma diagnostics used in this thesis. These include electrical measurement, fast imaging, optical emission spectroscopy and mass spectrometry.

In Chapter 3, experimental characteristics of an atmospheric pressure 'plasma curtain' are presented. Electrical parameters and images are analysed to demonstrate the streamer-free uniformity of the plasma curtain and the presence of two operating modes.

Chapter 4 discusses single APGD jet. First, classification and review of current APGD jets are given. The jets are classified into 9 groups in terms of their generic jet structures. Special attention is paid to whether the jet structure is appropriate for parallelisation. This is further investigated by a dedicated comparison of three selected single jets to bring out the best design. In three different scenarios, namely without a downstream electrode, with a grounded downstream electrode and with a dielectric downstream substrate,

the configuration of a powered capillary electrode and a grounded ring electrode, the so-called 'capillary-ring plasma jet', is shown to offer distinct advantages.

To investigate the parallelisation of single plasma jets, a 1D array of atmospheric plasma jets is proposed in Chapter 5. The 1D plasma jet array features individual ballasts, which effectively helps to achieve jet-to-jet uniformity by providing negative feedback to the applied voltage. Electrical measurements, fast imaging and optical emission intensities all support a robust temporal and spatial jet-to-jet uniformity, both for treating a flat surface and a sloped surface.

The parallelisation is advanced in Chapter 6 to introduce a 2D array of atmospheric plasma jets. It employs the capillary-ring plasma jet as its elemental jet. It is found that a built-in feedback control mechanism exists. This helps the jet array achieve uniformity even without using ballasts. This uniformity is established by analysing emission intensities. The 2D plasma jet array is more densely designed with the combined plasma area taking up to 60% of the cross-sectional area of the jet-holding unit. Bacteria inactivation experiments reveal that the impact of the bactericidal effect is much larger than the array's physical size. This correlates to a sterilisation area of 18.6 cm^2 by a 37-jet array when the physical size of the 2D jet array is about 4.9 cm^2. The discussion proves the 2D plasma jet arrays are practical large-scale atmospheric pressure plasma sources with ability to treat three-dimensional objects.

Chapter 7 focuses on a spatially separated dual-frequency plasma jet, for which a RF plasma is produced in the upstream region and kilohertz frequency is used to draw the plasma to the downstream. It demonstrates that the combination of the two frequencies can control plasma intensity and plume length in a separated fashion. The dual-frequency plasma jet is able to produce a plume much longer than the RF plasma jet and with much higher

reactive species production.

Finally, major conclusions of the thesis are given and future work is discussed in Chapter 8.

1.6 Contributions of the thesis

Over the thesis period of 36 months, 5 journal papers have been published. The work has been presented at leading international conferences in 12 conference contributions. The key contributions reported in this thesis are summarised as follows:

1. Cold atmospheric pressure slot plasma jet:

This work is detailed in Chapter 3. The uniformity of the spatially extended plasma curtain is proved by 10 ns exposure images and this device is the only one among all the published slot-shaped plasma jets that has been specifically shown for its plasma uniformity. Part of the results in this chapter were reported in 'Atmospheric dielectric-barrier discharges scalable from 1 mm to 1 m', J. L. Walsh, Z. Cao and M. G. Kong, *IEEE Trans. Plasma Sci.*, **36**, 1314 (2008)

2. Advantages of capillary-ring plasma jet:

This work is detailed in Chapter 4. This is the first reported study on a direct comparison of three common atmospheric pressure plasma jets and the advantages of the proposed capillary-ring plasma jet are explained. Many of the results in this chapter were reported in the section 2 of 'Spatially extended atmospheric plasma arrays', Z. Cao, Q. Nie, D. L. Bayliss, J. L. Walsh, C. S. Ren, D. Z. Wang and M. G. Kong, *Plasma Sources Sci. Technol.*, **19**, 025003 (2010)

3. 1D array of atmospheric pressure plasma jets:

This work is detailed in Chapter 5. The reported 1D plasma jet array employs ballast resistors to effectively achieve excellent temporal and spatial jet-to-jet uniformity and it is the first reported jet array which shows applicability for treating 3D objects. Most of the results in this chapter were published in 'Atmospheric plasma jet array in parallel electric and gas flow fields for three-dimensional surface treatment', Z. Cao, J. L. Walsh, and M. G. Kong, Ap*pl. Phys. Lett.*, **94**, 021501 (2009)

4. 2D arrays of atmospheric pressure plasma jets:

This work is detailed in Chapter 6. This densely constructed 2D plasma jet array is shown to achieve excellent uniformity, stability and reactivity with ability to treat three-dimensional objects. The plasma source has been shown clearly to be a practical choice for large-scale biomedical applications. Most of the results in this chapter were published in the section 3 of 'Spatially extended atmospheric plasma arrays', Z. Cao, Q. Nie, D. L. Bayliss, J. L. Walsh, C. S. Ren, D. Z. Wang and M. G. Kong, *Plasma Sources Sci. Technol.*, **19**, 025003 (2010) and 'A Two-dimensional cold atmospheric plasma jet array for uniform treatment of large-area surfaces for plasma medicine', Q. Nie, Z. Cao, C. S. Ren, D. Z. Wang and M. G. Kong, *New Journal of Physics*, **11**, 115015 (2009)

5. Dual-frequency plasma jet:

This work is detailed in Chapter 7. This is the first reported research for a spatially separated dual-frequency atmospheric plasma. The combination of the two frequencies can effectively tune the plasma density and plume. Most of the results in this chapter were published in 'A Cold Atmospheric Plasma Jet Controlled with Spatially Separated Dual Frequency Excitations', Z. Cao,

Q. Nie and M. G. Kong, *J. Phys. D: Appl. Phys.*, **42**, 222003 (2009)

References

[1.1] J. R. Roth, Industrial Plasma Engineering, Volume 1, Principles, (IOP Publishing Ltd, 1995).

[1.2] Y. P. Raizer, Gas Discharge Physics, (Springer, 1991).

[1.3] A. Lieberman and A. J. Jichtenberg, Principles of Plasma Discharge and Materials Processing, (John Wiley & Sons, 2005).

[1.4] S. Kanazawa, M. Kogoma, T. Moriwaki and S. Okazaki, J. Phys. D-Appl. Phys. 21, 838 (1988).

[1.5] L. G. Christophorou and J. K. Olthoff, Fundamental Electron Interactions With Plasma Processing Gases, (Kluwer Academic/Plenum Publishers, 2004).

[1.6] E. E. Kunhardt, IEEE Trans. Plasma Sci. 28, 189 (2000).

[1.7] M. G. Kong and X. T. Deng, IEEE Trans. Plasma Sci. 31, 7 (2003).

[1.8] R. J. Goldston and P. H. Rutherford, Introduction to Plasma Physics, (IOP Publishing Ltd, 1995).

[1.9] F. Iza and J. A. Hopwood, IEEE Trans. Plasma Sci. 32, 498 (2004).

[1.10] J. P. Boeuf, J. Phys. D-Appl. Phys. 36, R53 (2003).

[1.11] M. Ueda, L. A. Berni, G. F. Gomes, A. F. Beloto, E. Abramof and H. Reuther, J. Appl. Phys. 86, 4821 (1999).

[1.12] M. Kondo and A. Matsuda, Thin Solid Films 383, 1 (2001).

[1.13] R. Bussiahn, S. Gortchakov, H. Lange and D. Uhrlandt, J. Appl. Phys. 95, 4627 (2004).

[1.14] J. Opretzka, J. Benedikt, P. Awakowicz, J. Wunderlich and A. von Keudell, J. Phys. D-Appl. Phys. 40, 2826 (2007).

[1.15] F. Iza, G. J. Kim, S. M. Lee, J. K. Lee, J. L. Walsh, Y. T. Zhang and M. G. Kong, Plasma Process. Polym. 5, 322 (2008).

[1.16] F. Massines, A. Rabehi, P. Decomps, R. B. Gadri, P. Segur and C. Mayoux, J. Appl. Phys. 83, 2950 (1998).

[1.17] M. Laroussi, I. Alexeff, J. P. Richardson and F. F. Dyer, IEEE Trans. Plasma Sci. 30, 158 (2002).

[1.18] M. Thiyagarajan, I. Alexeff, S. Parameswaran and S. Beebe, IEEE Trans. Plasma Sci. 33, 322 (2005).

[1.19] J. Park, I. Henins, H. W. Herrmann, G. S. Selwyn and R. F. Hicks, J. Appl. Phys. 89, 20 (2001).

[1.20] X. H. Yuan and L. L. Raja, IEEE Trans. Plasma Sci. 31, 495 (2003).

[1.21] J. J. Shi and M. G. Kong, J. Appl. Phys. 97, 023306 (2005).

[1.22] J. J. Shi and M. G. Kong, IEEE Trans. Plasma Sci. 33, 624 (2005).

[1.23] J. L. Walsh, J. J. Shi and M. G. Kong, Appl. Phys. Lett. 89, 161505 (2006).

[1.24] F. Iza, J. L. Walsh and M. G. Kong, IEEE Trans. Plasma Sci. 37, 1289 (2009).

[1.25] D. W. Liu, J. J. Shi and M. G. Kong, Appl. Phys. Lett. 90, 041502 (2007).

[1.26] J. L. Walsh and M. G. Kong, Appl. Phys. Lett. 91, 221502 (2007).

[1.27] S. E. Babayan, J. Y. Jeong, V. J. Tu, J. Park, G. S. Selwyn and R. F. Hicks, Plasma Sources Sci. Technol. 7, 286 (1998).

[1.28] S. E. Babayan, J. Y. Jeong, A. Schutze, V. J. Tu, M. Moravej, G. S. Selwyn and R. F. Hicks, Plasma Sources Sci. Technol. 10, 573 (2001).

[1.29] G. R. Nowling, S. E. Babayan, V. Jankovic and R. F. Hicks, Plasma Sources Sci. Technol. 11, 97 (2002).

[1.30] J. Y. Jeong, S. E. Babayan, V. J. Tu, J. Park, I. Henins, R. F. Hicks and G. S. Selwyn, Plasma Sources Sci. Technol. 7, 282 (1998).

[1.31] F. Massines and G. Gouda, J. Phys. D-Appl. Phys. 31, 3411 (1998).

[1.32] G. S. Selwyn, H. W. Herrmann, J. Park and I. Henins, Contrib. Plasma Phys. 41, 610 (2001).

[1.33] Y. Sawada, S. Ogawa and M. Kogoma, J. Phys. D-Appl. Phys. 28, 1661 (1995).

[1.34] J. R. Roth, D. M. Sherman and S. P. Wilkinson, AIAA J. 38, 1166 (2000).

[1.35] E. Moreau, J. Phys. D-Appl. Phys. 40, 605 (2007).

[1.36] S. J. Park, J. Chen, C. Liu and J. G. Eden, Appl. Phys. Lett. 78, 419 (2001).

[1.37] P. von Allmen, D. J. Sadler, C. Jensen, N. P. Ostrom, S. T. McCain, B. A. Vojak and J. G. Eden, Appl. Phys. Lett. 82, 4447 (2003).

[1.38] J. G. Eden, S. J. Park, N. P. Ostrom, S. T. McCain, C. J. Wagner, B. A. Vojak, J. Chen, C. Liu, P. von Allmen, F. Zenhausern, D. J. Sadler, C. Jensen, D. L. Wilcox and J. J. Ewing, J. Phys. D-Appl. Phys. 36, 2869 (2003).

[1.39] S. J. Park, J. G. Eden, J. Chen and C. Liu, Appl. Phys. Lett. 85, 4869 (2004).

[1.40] S. J. Park, K. F. Chen, N. P. Ostrom and J. G. Eden, Appl. Phys. Lett. 86, 111501 (2005).

[1.41] J. G. Eden, S. J. Park and K. S. Kim, Plasma Sources Sci. Technol. 15, S67 (2006).

[1.42] J. G. Eden, Proc IEEE 94, 567 (2006).

[1.43] K. F. Chen, N. P. Ostrom, S. J. Park and J. G. Eden, Appl. Phys. Lett. 88, 061121 (2006).

[1.44] J. C. T. Eijkel, H. Stoeri and A. Manz, J. Anal. At. Spectrom. 15, 297 (2000).

[1.45] O. Sakai, T. Sakaguchi and K. Tachibana, J. Appl. Phys. 101, 073304 (2007).

[1.46] T. Sakaguchi, O. Sakai and K. Tachibana, J. Appl. Phys. 101, 073305 (2007).

[1.47] K. Becker, A. Koutsospyros, S. M. Yin, C. Christodoulatos, N. Abramzon, J. C. Joaquin and G. Brelles-Marino, Plasma Phys. Controlled Fusion 47, B513 (2005).

[1.48] R. M. Sankaran, D. Holunga, R. C. Flagan and K. P. Giapis, Nano Lett. 5, 537 (2005).

[1.49] M. G. Kong, G. Kroesen, G. Morfill, T. Nosenko, T. Shimizu, J. van Dijk and J. L. Zimmermann, New J. Phys. 11, 115012 (2009).

[1.50] M. Laroussi, IEEE Trans. Plasma Sci. 24, 1188 (1996).

[1.51] K. Kelly-Wintenberg, T. C. Montie, C. Brickman, J. R. Roth, A. K. Carr, K. Sorge, L. C. Wadsworth and P. P. Y. Tsai, J. Ind. Microbiol. Biotechnol. 20, 69 (1998).

[1.52] H. W. Herrmann, I. Henins, J. Park and G. S. Selwyn, Phys Plasmas 6, 2284 (1999).

[1.53] M. Laroussi, IEEE Trans. Plasma Sci. 30, 1409 (2002).

[1.54] G. Fridman, G. Friedman, A. Gutsol, A. B. Shekhter, V. N. Vasilets and A. Fridman, Plasma Process. Polym. 5, 503 (2008).

[1.55] X. T. Deng, J. J. Shi and M. G. Kong, IEEE Trans. Plasma Sci. 34, 1310 (2006).

[1.56] T. C. Montie, K. Kelly-Wintenberg and J. R. Roth, IEEE Trans. Plasma Sci. 28, 41 (2000).

[1.57] B. J. Park, D. H. Lee, J. C. Park, I. S. Lee, K. Y. Lee, S. O. Hyun, M. S. Chun and K. H. Chung, Phys Plasmas 10, 4539 (2003).

[1.58] G. E. Morfill, T. Shimizu, B. Steffes and H-U. Schmidt, New J. Phys. 11, 115019 (2009).

[1.59] X. T. Deng, J. J. Shi and M. G. Kong, J. Appl. Phys. 101, 074701 (2007).

[1.60] D. L. Bayliss, J. L. Walsh, G. Shama, F. Iza and M. G. Kong, New J. Phys. 11, 115024 (2009).

[1.61] M. Vleugels, G. Shama, X. T. Deng, E. Greenacre, T. Brocklehurst and M. G. Kong, IEEE Trans. Plasma Sci. 33, 824 (2005).

[1.62] X. T. Deng, J. J. Shi, H. L. Chen and M. G. Kong, Appl. Phys. Lett. 90, 013903 (2007).

[1.63] T. Shimizu, B. Steffes, R. Pompl, F. Jamitzky, W. Bunk, K. Ramrath, M. Georgi, W. Stolz, H-U. Schmidt, T. Urayama, S. Fujii and G. E. Morfill, Plasma Process. Polym. 5, 577 (2008).

[1.64] S. Perni, G. Shama and M. G. Kong, J. Food Prot. 71, 1619 (2008).

[1.65] G. Li, H. P. Li, L. Y. Wang, S. Wang, H. X. Zhao, W. T. Sun, X. H. Xing and C. Y. Bao, Appl. Phys. Lett. 92, 221504 (2008).

[1.66] 67. A. Shashurin, M. Keidar, S. Bronnikov, R. A. Jurjus and M. A. Stepp, Appl. Phys. Lett. 93, 181501 (2008).

[1.67] I. E. Kieft, D. Darios, A. J. M. Roks and E. Stoffels, IEEE Trans. Plasma Sci. 33, 771 (2005).

[1.68] S. Yonson, S. Coulombe, V. Leveille and R. L. Leask, J. Phys. D-Appl. Phys. 39, 3508 (2006).

[1.69] M. Laroussi and F. Leipold, Int. J. Mass Spectrom. 233, 81 (2004).

[1.70] S. Perni, G. Shama, J. L. Hobman, P. A. Lund, C. J. Kershaw, G. A. Hidalgo-Arroyo, C. W. Penn, X. T. Deng, J. L. Walsh and M. G. Kong, Appl. Phys. Lett. 90, 073902 (2007).

[1.71] J. L. Walsh, Z. Cao and M. G. Kong, IEEE Trans. Plasma Sci. 36, 1314 (2008).

[1.72] S. Y. Moon, W. Choe and B. K. Kang, Appl. Phys. Lett. 84, 188 (2004).

[1.73] G. Fridman, M. Peddinghaus, H. Ayan, A. Fridman, M. Balasubramanian, A. Gutsol, A. Brooks and G. Friedman, Plasma Chem. Plasma Process. 26, 425 (2006).

[1.74] G. Fridman, A. D. Brooks, M. Balasubramanian, A. Fridman, A. Gutsol, V. N. Vasilets, H. Ayan and G. Friedman, Plasma Process. Polym. 4, 370 (2007).

[1.75] J. Park, I. Henins, H. W. Herrmann, G. S. Selwyn, J. Y. Jeong, R. F. Hicks, D. Shim and C. S. Chang, Appl. Phys. Lett. 76, 288 (2000).

[1.76] A. P. Yalin, Z. Q. Yu, O. Stan, K. Hoshimiya, A. Rahman, V. K. Surla and G. J. Collins, Appl. Phys. Lett. 83, 2766 (2003).

[1.77] E. Panousis, F. Clement, J-F. Loiseau, N. Spyrou, B. Held, M. Thomachot and L. Marlin, Plasma Sources Sci. Technol. 15, 828 (2006).

[1.78] M. Iwasaki, H. Inui, Y. Matsudaira, H. Kano, N. Yoshida, M. Ito and M. Hori, Appl. Phys. Lett. 92, 081503 (2008).

[1.79] Q. S. Yu, C. Huang, F. H. Hsieh, H. Huff and Y. X. Duan, Appl. Phys. Lett. 88, 013903 (2006).

[1.80] Y. X. Duan, C. Huang and Q. S. Yu, Rev. Sci. Instrum. 78, 015104 (2007).

[1.81] M. Laroussi and X. Lu, Appl. Phys. Lett. 87, 113902 (2005).

[1.82] R. E. J. Sladek and E. Stoffels, J. Phys. D-Appl. Phys. 38, 1716 (2005).

[1.83] J. L. Walsh, J. J. Shi and M. G. Kong, Appl. Phys. Lett. 88, 171501 (2006).

Chapter 2
Review of Plasma Diagnostics

2.1 Introduction

It is important to understand the characteristics of plasma qualitatively and when possible to measure key plasma parameters quantitatively. Various plasma diagnostics methods have been developed in the past, mostly for low-pressure gas plasmas. Perhaps the most noticeable is the *Langmuir probe*, which was developed by Irving Langmuir in the 1920's[2.1]. Langmuir probe is extensively used for measuring key plasma parameters, such as plasma potential, electron kinetic temperature and electron density of low-pressure plasma[2.2]. The theory of the Langmuir probe assumes the absence of collisions of charged particles in the probe sheath, so the measurement can reflect the genuine characteristics of the plasma. This requires that the ion mean free path is larger than the sheath thickness. However at atmospheric pressure, the ion mean free path is typically less than a micrometer while the sheath thickness is a few hundred micrometers[2.3,2.4]. Therefore collisions in the sheath are inevitable. As a result, the existing Langmuir theory is not applicable to APGD. While there have been attempts to extend the use of the Langmuir probe to APGD, it is fair to say that a great deal of progress is needed before the Langmuir probe becomes an acceptable diagnostic tool for atmospheric plasma[2.5].

A common diagnostic for atmospheric plasmas is optical emission spectrometry (OES). OES is the spectroscopic technique to measure emission

radiation from atoms, molecules and ions. It can be used to assess the amount of the excited species both qualitatively and quantitatively. Stark broadening[2.6] and line ratios technique[2.7] are both based on OES and they can be used to measure the mean electron density. It is also possible to introduce a light into atmospheric plasma for absorption spectroscopy, for example two-photon absorption laser-induced fluorescence spectroscopy (TALIF) for measuring ground-state oxygen atoms[2.8,2.9]. Apart from spectroscopic diagnostics, some diagnostics are based on the effects of free charges on electromagnetic radiation. For example, laser Thomson scattering examines the scattering of laser light from electrons for direct and simultaneous measurement of both electron density and electron temperature[2.10,2.11]. Interferometry measures the refractive properties of a plasma which depends on the plasma characteristics including the plasma density and collision frequency[2.12].

Although the above mentioned methods are available, in reality they are not always feasible. Stark broadening is only useful for plasma with an electron density higher than 10^{13} cm^{-3}[2.7]. Given that 10^{13} cm^{-3} is normally higher than the electron densities of APGDs, Stark broadening is in general unsuitable for the plasma sources reported in this thesis. The line ratios method is developed based on collisional-radiative models[2.7]. However this method entirely relies on the completeness and accuracy of the collisional-radiative model used and for atmospheric plasmas it is at present only applicable for pure argon[2.7]. In general, Thomson scattering is the most accurate method to measure electron density and electron temperature, but it suffers from weak signal-to-background ratio[2.10]. Interferometry may also require electron density to be sufficiently large, i.e. higher than 2×10^{12} cm^{-3}[2.13]. In addition, the volume of the plasma has to be large when using millimetre wave interferometry[2.12].

This chapter provides a brief review of some of the commonly used

diagnostics for APGDs. These diagnostics include electrical measurement which will be covered in section 2.2, fast imaging in section 2.3 and optical emission spectroscopy in section 2.4. In section 2.5, a novel mass spectrometry for measurements of atmospheric plasma will be introduced and discussed.

2.2 Electrical measurements

2.2.1 Voltage measurement

Voltage measurement for atmospheric plasmas is usually done by using a voltage probe and an oscilloscope. The voltage probe makes a physical and electrical connection between an electrode and an oscilloscope, and it combines with the oscilloscope to form a measurement system. Figure 2-1 shows an equivalent circuit for using a voltage probe to make a measurement. The voltage probe can be best described as a probe resistance R_p in parallel with a probe tip capacitance C_p when the probe is attached to the circuit. Ideally, the impedance of the probe is very large, so the probe does not draw any electrical current from the power source E and it can have a genuine value for the voltage drop on the load R_L. However, because of the existence of R_p and C_p, the measured value of the voltage on the load can deviate from its true value. For an AC excitation at a high frequency, the reactance of the tip capacitor tends to be small, and so more current is drawn by the probe. It is therefore advisable to use a voltage probe with a high probe resistance R_p and a low probe tip capacitance C_p. The existence of the C_p affects the bandwidth of the probe.

It is the bandwidths of both the probe and the oscilloscope that determine the overall bandwidth of the measurement system. It is therefore important to use a probe matched to the oscilloscope. For the measurement of a sinusoidal signal, the bandwidth of the measurement system needs to be

higher than the signal frequency. If measuring a non-sinusoidal signal, it is recommended to have the system bandwidth five times higher than the signal frequency.

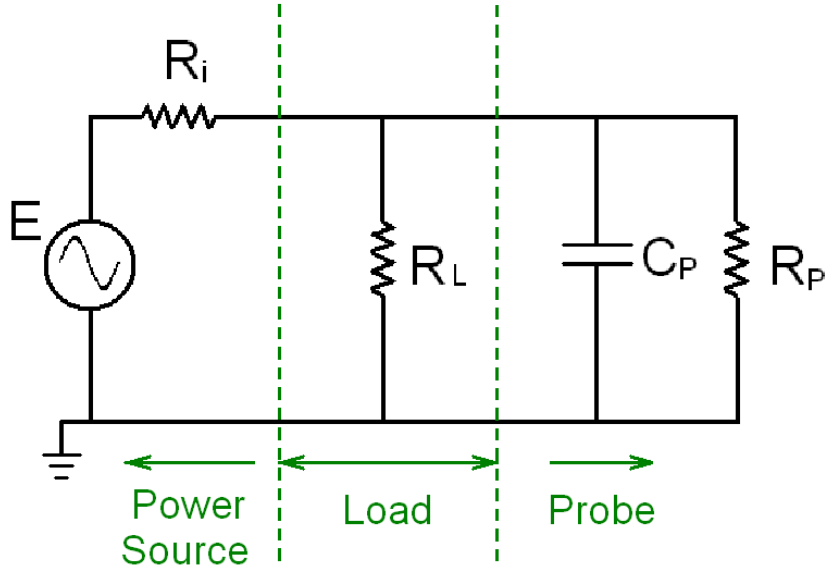

Fig 2-1: An equivalent circuit for voltage measurement using a voltage probe.

For the experiments reported in this thesis, the generation of plasma needs at least a few hundred volts. A high voltage probe, Tektronix P6015A, is used. This probe has a bandwidth of 75 MHz and a typical rise time of 4 ns. The maximum frequency measured throughout in all experiments is less than 6 MHz, which is well within the probe's bandwidth. The voltage probe has a probe resistance of 100 MΩ and a tip capacitance of 3 pF. The plasma impedance (R_L) typically ranges between tens of kΩ up to a few MΩ. The probe's maximum measurable voltage is 20 kV which offers a considerable margin over the range of the voltage measured in the studies reported here.

2.2.2 Current measurement

Generally speaking, two methods of current measurement are considered. One is to add a resistor in series with the gas gap and measure the voltage

drop on that resistor using a voltage probe (voltage probes). Since the current of a DBD is normally in the milliampere range and the added resistor should be sufficiently small not to influence the discharge, the voltage drop on that resistor tends to be too small and the signal-to-background ratio is poor.

The other method is to use a current probe (also called current transformer). Current probe is a coil-shaped transformer through which the current-carrying conductor is placed. This coil-shaped transformer is connected to an oscilloscope. When a current flows through the conductor, it creates a magnetic flux around the conductor. This magnetic flux field induces a voltage to the output of the probe and this voltage signal can be measured via the oscilloscope. Essentially, the current probe operates as a closely coupled transformer. The sensed conductor is the primary winding while the wound coil is the secondary winding. As a result, the output of the current probe is proportional to the current in the conductor as long as the magnetic core does not reach flux saturation. The latter can be judged by whether the product of the average current amplitude multiplied by the pulse width exceeds the saturation limit of the magnetic core. In order to improve the sensitivity when measuring a small current signal, it is advisable to loop the conductor through the probe several turns.

The current probe used in experiments is a Pearson current monitor model 2877. It has a bandwidth from 300 Hz to 200 MHz. Its maximum peak current and rms current are 100 A and 2.5 A respectively, and the saturation limit is 0.4 mA·s. For the experiments carried out for this thesis, the measured currents fall into the above ranges. When possible, the measured conductors are wound through the probe to improve sensitivity of current measurements.

2.3 Fast imaging

Gas breakdown and the generation of plasma are both transient

processes often at a time scale as short as a few nanoseconds. To better understand these transient processes, fast imaging with very short exposure time is vitally important. Domestic digital cameras can have an exposure time of a few thousandths second. However, at this time scale the light emission from the plasmas captured by the camera is normally too weak to be seen. In addition, an exposure time of one thousandth second is still too long for important transient phenomena in atmospheric pressure plasmas. For example, streamers are known to have a lifetime of only tens of nanoseconds at atmospheric pressure[2.1]. This requires an exposure time of 10 ns or less, for which domestic digital cameras are inadequate.

Intensified charge-coupled device (ICCD) is a good fast imaging tool. It comprises an image intensifier and a charge-coupled device (CCD). The image intensifier is mounted in front of the CCD and it can both magnify the light input and trigger a short shutter. The minimum exposure time of the ICCD camera used in the experiments reported here is 3 ns.

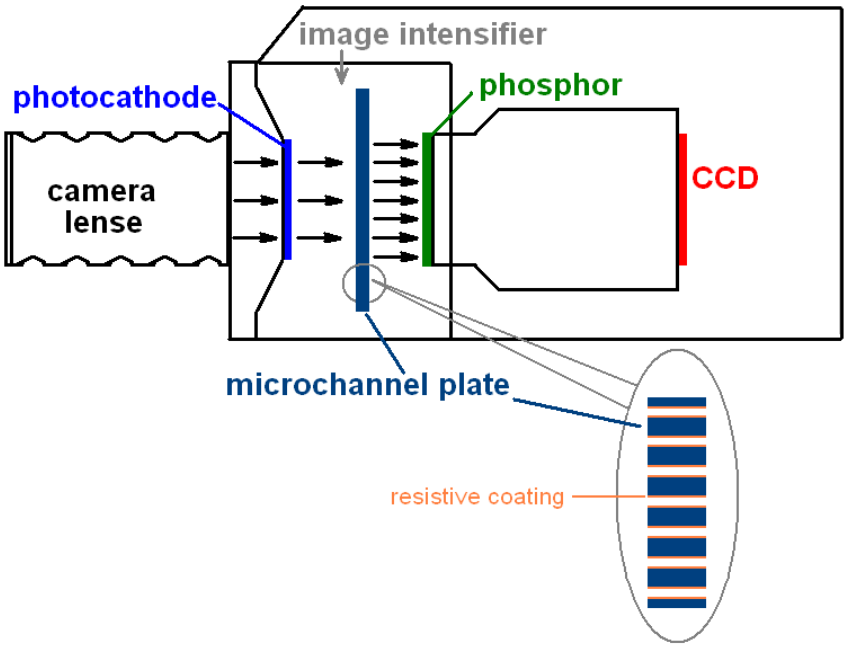

Fig 2-2: A schematic of an ICCD camera.

Figure 2-2 shows a schematic of an ICCD camera. The image intensifier

is an evacuated tube mainly consisting of three parts, namely the photocathode, the microchannel plate and the phosphor. After the input light goes through the camera lens, photons hit the photocathode and produce photoelectron emissions. An electric field exists between the photocathode and the microchannel plate, and directs those photoelectrons to move to the microchannel plate. The microchannel plate is a thin disc comprising a honeycomb of tiny glass channels with a resistive coating. A high voltage is applied across the microchannel plate and further accelerates the photoelectrons when they go through. Photoelectrons can knock secondary electrons from the channel walls and as such a multiplication process takes place. Eventually a group of electrons exit from each channel.

As these electrons hit the phosphor, light is emitted from the phosphor. The light exits from the image intensifier and is coupled to the CCD by either a fibre optic coupler or a lens. The light signals picked up by the CCD are converted to electric signals which are further transmitted to a computer for data processing.

A key advantage of the ICCD is its ability to have a very short exposure time. This is achieved by a pulse generated by an electric circuit inside the camera. This pulse is typically with very short rise and fall times in a sub-nanosecond range and by changing the value of the pulse, it can control whether the photoelectrons emitted from the photocathode can reach the microchannel plate. As a result, an effective shutter control is established. The minimum gate time (exposure time), i.e. the minimum time needed to drive the intensifier from ‘off’ to ‘on’ and to ‘off’ again, determines the minimum exposure time of the ICCD. It mainly depends on the structure of the photocathode and the pulse-generating electric circuit. The gate time can also be set to a longer time to enable images with longer exposure time. The magnification of the image intensity is achieved by tuning the voltage potential applied across the microchannel plate. This is known as the ‘gain’.

It should be noted that different models of ICCD may have a different spectral response which may affect the experimental results greatly. This is due to the different materials used for the photocathode and their thickness. ICCD should be chosen for a best wavelength response of interest. Also noted is that the different types of phosphor have different light decay times. Therefore the frame rate, i.e. how quick an ICCD is triggered, should be carefully selected. If the frame rate is so high that the light emission from the phosphor during the last frame has not decayed completely, the image is then overcounted with undesirable extra contributions. The upper limit of the frame rate may also be confined by the ability to transfer data from the CCD to a computer. This is related to the readout time of per CCD pixel and the total number of the pixels.

The ICCD camera used in the experiments reported in this thesis is Andor iStar DH720. It has 960×256 active pixels with each size being 39×39 μm^2. Its minimum gate time is 3 ns and it has a broad wavelength response from 180 ~ 850 nm. The phosphor decay time (to 10%) is 2 ms.

To gain knowledge of the evolution of a plasma, it is important to relate the time instants when the images are taken to those of the applied voltage. This is achieved by using an external trigger, i.e. the trigger signal to take an image is sent out from a function generator which also provides the excitation signal for the power supply. By this means, the trigger signal is synchronised to the applied voltage and it always triggers ICCD at the same instant relative to the applied voltage in each cycle of the applied voltage. By setting a 'delay time' to the ICCD, it is possible to trigger the camera to take image at any given instant. In our experiments, the gate time and the delay time are first selected, then the 'gain' should be properly selected so the CCD does not go into saturation. If the highest possible light intensity of a single shot is too weak, it is advisable to accumulate images over several cycles. In this case, the sampled signal of each cycle is summed on the CCD to integrate together

to a stronger intensity. In order to directly compare plasmas of different instants, it is important to choose the same 'gain' and the same gate time.

2.4 Optical emission spectroscopy

Optical emission spectroscopy is a common diagnostic used in plasma research. It provides a non-invasive method to investigate atoms, ions and molecules by analyzing emission spectra of excited plasma species. Both identification of plasma species and a quantitative estimate of their densities are possible with OES[2.6,2.7].

The emission spectrum can be explained by the atomic emission theory[2.14]. An atom consists of a nucleus and a cloud of electrons which surround the nucleus and occupy different electronic shells and orbits that define their energy levels. An atom usually stay at its ground state, i.e. the atom is at its least energetic state. At this state, all the electrons are also at their least energetic states. If a ground state atom is exposed to heat or electromagnetic radiation, or is involved in collisions with other particles (energetic electrons, excited atoms or ions), it is most likely that either the kinetic energy of the atom increases or the atom is excited to excited states. The transition of an atom from its ground state to an excited state involves an electron being promoted to a higher energy level. Because the excited state is unstable, an atom at an excited state is inclined to return to the more stable ground state or to a lesser excited state. Accordingly, the electron in the higher energy level also returns to its ground state or to an excited state of a lower energy level. This transition can be achieved either by collision with another atom or ion, or by the release of a photon. Based on the law of conservation of energy, the latter can be described as

$$\Delta E = hv \tag{2.1}$$

where ΔE is the difference between the two electron energy levels, h is

Planck's constant and v is the frequency of light. Considering

$$v = c/\lambda \tag{2.2}$$

where c is the speed of light and λ is the wavelength of the light. Equation (2.1) can be revised as

$$\Delta E = h\,c/\lambda \tag{2.3}$$

Equation (2.3) indicates that the wavelength of the emitted photon is determined by the difference between the two electron energy levels which are involved in the transition responsible for the photon emission. One transition relates to one spectral line of optical emission. Since all the electron energy levels are well-defined and the transitions between different energy levels are only allowed if they are in line with the quantum mechanical theory, each kind of atom has its own characteristic spectrum.

It should be noted that the above principles also apply to ions as ions can also be excited. In this case, photons are emitted when excited ions return to their ground state or a more stable state. Given that the atomic emission theory applies to both atoms and ions, the emission spectra include both characteristic spectra of atoms and ions. Plasma contains energetic electrons, ions and atoms, and the collisions among these particles make excitation and ionisation happen quite often. Because of this, OES can be used as a diagnostic for plasma research. Different from atomic absorption spectroscopy and atomic fluorescence spectroscopy, OES does not rely on an external radiation to acquire spectra[2.15].

A common instrument used in optical emission spectrum analysis is the spectrograph. It can separate wavelengths associated to different particles and measure the relative light intensities of every spectrum line.

Figure 2-3 shows a schematic of a spectrograph, of which the main components are indicated. First, the emission from a plasma is picked up by an optical fibre and the light is guided to pass through a slit. A collimating

mirror is then used to turn the dispersive light into a collimated light. The collimated light is dispersed into a spectrum by either a prism or a diffraction grating. If a prism is used, the collimated light undergoes refraction after it enters a prism because of the change of medium. The refraction angle of a collimated light is dependent on its frequency and this makes the collimated light dispersed after it goes out of the prism. A diffraction grating has several advantages over a prism such as better efficiency and an ability to deal with UV light, so they are more often used in spectrographs. The diffraction grating reflects rather than refracts the incident light, and disperses the light into individual wavelengths. By choosing different gratings, different wavelength ranges are selected, and the dispersed lights with individual wavelengths are focused onto different locations in a detector by a mirror. The collection of these individual spectra provides information about excited plasma particles. Traditionally photographic papers were used as detector and nowadays charged-coupled devices are normally used thus providing a computerised way to efficiently detect plasma species.

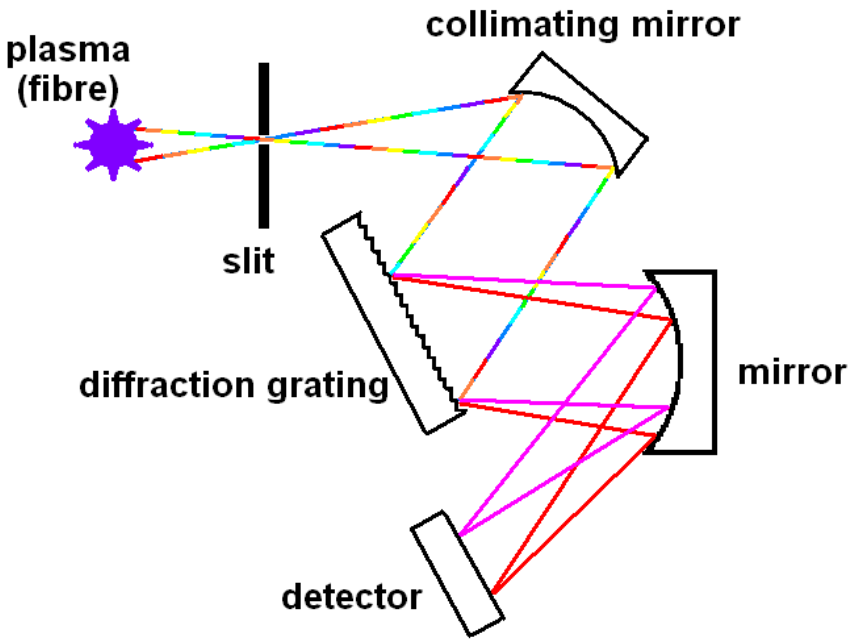

Fig 2-3: A schematic of a spectrograph.

Two different spectrographs are used in the experiments reported in this thesis, namely Andor Shamrock SR-303i spectrograph and Ocean Optics 2000 spectrometer. Shamrock SR-303i is equipped with a motorised slit and a triple grating turret. It has a focal length of 303 mm and combines with Andor iStar DH720 ICCD. The three grating options provide detection coverage of different wavelength ranges and the best resolution can be reached at 0.05 nm. Ocean Optics 2000 spectrometer has a slit with a width of 25 μm and a single grating. Its detection coverage is set to 350 ~ 1000 nm with a resolution of 1.5 nm. The detector used is a 2048-element linear silicon CCD array. Since the detection efficiency of a spectrograph is not uniform over the whole detection range due to the existence of the grating efficiency curve, the spectrograph can only provide spectral lines in relative intensity and the intensities of different spectral lines are not directly comparable. A radiometric calibration source with a continuous spectrum of known absolute spectral intensity can be used to calibrate the spectrum obtained by the spectrograph by considering the efficiency function of the spectrometer. This can provide a spectrum in absolute spectral intensity. An Ocean Optics LS-1-CAL NIST traceable white light source with known absolute intensity values at wavelengths from 300-1050 nm is used for radiometric calibration whenever it is needed in the experiments reported here.

Figure 2-4 is a typical optical emission spectrum for an atmospheric pressure helium plasma plume as an example to show typical plasma species. The spectrum is measured by using Ocean Optics 2000 spectrometer and absolute spectral intensity is obtained. The presence of helium plasma is clear as helium lines are found at 587 nm and 706 nm from the spectra. Because the plasma plume is ejected into the ambient atmosphere, the species from the atmosphere can also be found. They include atomic oxygen (645 nm, 777 nm and 845 nm), nitrogen molecular ions (391 nm and 427 nm) and nitrogen molecule (357 nm).

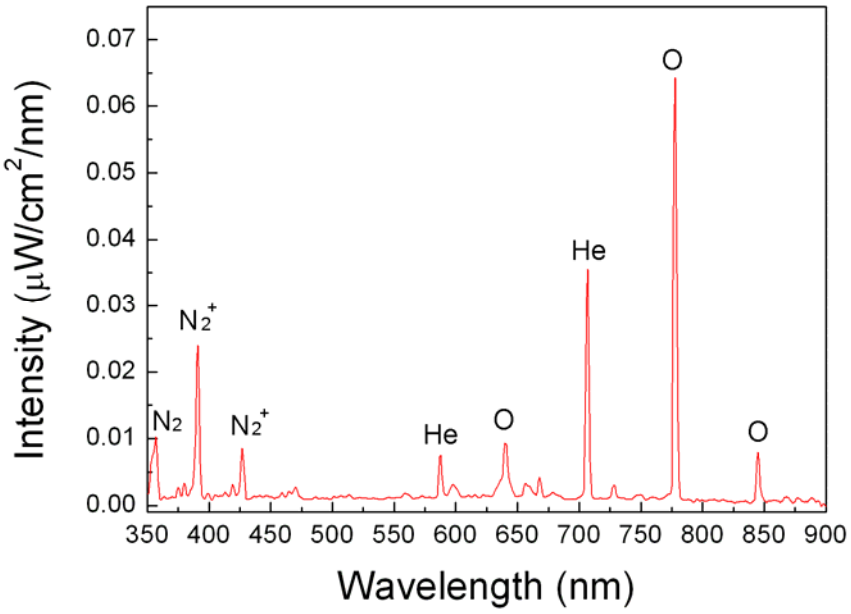

Fig 2-4: Typical optical emission spectrum for an atmospheric pressure helium plasma plume.

By knowing the spectrum of some plasma species, it is possible to obtain information about gas temperature. This is done by comparing the spectrum obtained from experiment with that from simulation (i.e. the synthetic spectrum). At atmospheric pressure, the rotational relaxation time is fast, so rotational temperature can be assumed to equal to gas temperature[2.16]. After user-specified rotational temperature is input, a simulation code (LIFBASE, a database and spectral simulation software for diatomic molecules) can provide the synthetic spectrum by calculating transition probabilities and populations of radiating species[2.17]. So the best-fit between the simulated spectrum and experimental spectrum can be used to deduce gas temperature[2.12]. The first negative system of molecular nitrogen located around 391 nm is associated with radiation transitions of nitrogen molecular ion. It is used to determine gas temperature in this thesis. Figure 2-5 shows such an example for which the experimental spectrum is found to fit the simulated spectrum well at gas temperature of 300 K.

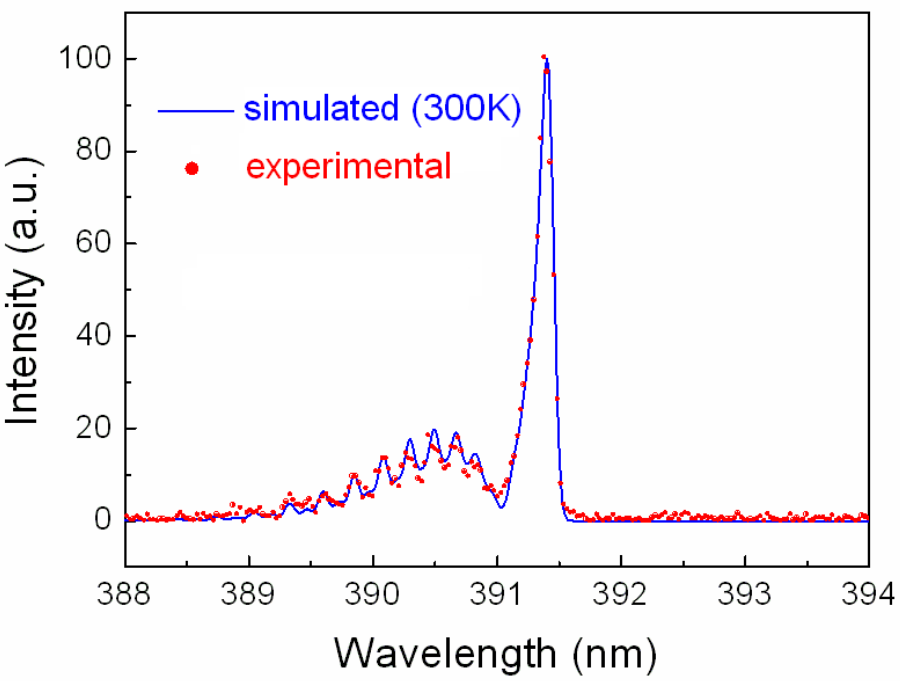

Fig 2-5: An example of deducing gas temperature by comparing experimental spectrum and simulated spectrum.

2.5 Mass spectrometry

APGD is a weakly ionised plasma and most atoms and ions are at their ground states. It is known from the discussion in the last section that the OES can only detect excited species, thus it is impossible to use OES to directly measure ground-state plasma species.

Mass spectrometry (MS) is a non-invasive analytical technique for the determination of the elemental composition of substances. It can be used to measure molecules, atoms and ions, both qualitatively and quantitatively[2.18]. Therefore MS has the advantage over OES for being able to measure heavy plasma species (other than electrons) quantitatively. Additionally, the detection limit of MS is usually 2-3 orders of magnitude better than OES[2.19]. These make MS an excellent plasma diagnostics.

It has been a long time since MS was first used as a diagnostic for plasma research[2.20]. So far most MS studies have been used for low-pressure

plasmas. In principle, a mass spectrometer consists of three parts, namely an ion source, a mass analyser and a detector. The ion source is used for ionising the sampled particles into ions, mostly by electron impact ionisation and Penning ionisation. A number of ion source technologies have been developed in the past. Similarly, different mass analysers have been developed with quite different designs. Both electric field and magnetic field can be designed to guide the ions' motion when they pass through the mass analyser and their paths are differentiated by 'mass-to-charge ratio'. More specifically, the ions in an electromagnetic field are governed by Lorentz force which can be described as

$$F = q(E + v \times B) \tag{2.4}$$

where F is the Lorentz force, q is the electric charge of the ion, E is the electric field, B is the magnetic field and v is the instantaneous velocity of the ion. Because v is much smaller than the speed of light, Newton's second law of motion is valid in this case, which gives

$$F = ma \tag{2.5}$$

where a is the acceleration. By equating the above two equations, the following is obtained

$$\frac{m}{q} = \frac{1}{a}(E + v \times B) \tag{2.6}$$

Equation (2.6) indicates that only the ions with the same mass-to-charge ratio wound have the same motion. This links to the function of the detector, being able to count the number of ions as a function of m/q, as the detector is placed to collect the ions which hit it at different places.

For mass spectrometer used for low-pressure plasma measurement, it normally uses a two-stage or three-stage differential pumping system with mass spectrometer placed in the last stage which has the lowest pressure within all stages. The pressure difference allows the plasma particles to be

extracted to a lower pressure stage and finally these species are ionised and analysed.

For the measurement of atmospheric pressure plasmas, the difference between atmospheric pressure and the required low-pressure in the last stage is so considerable that a supersonic free jet inevitably forms in the pumping system due to a great pressure gradient. If a mass spectrometer is not designed carefully, the particles in the free jet could collide with each other and this affects the mass spectrometer results dramatically. Special arrangement has to be implemented.

Figure 2-6 shows a schematic of a three-stage differential pumping mass spectrometer system developed in Ruhr-Bochum University, which has a special rotating chopper design to increase the signal-to-background ratio[2.21,2.22]. This system was used to measure densities of plasma species to be discussed in Chapter 4.

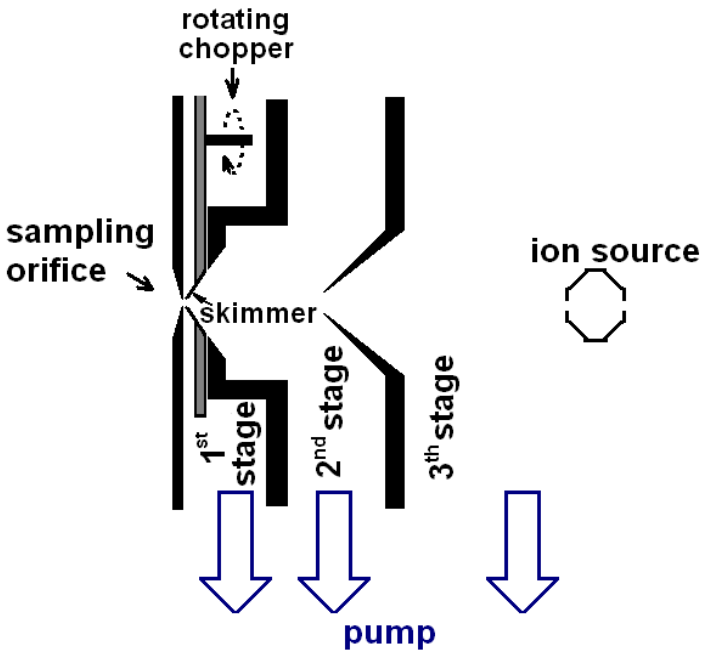

Fig 2-6: A schematic of a three-stage differential pumping mass spectrometer system with a rotating chopper design[2.21,2.22].

The system has three differential pumping stages with the ion source in

the line of sight with the sampling orifice. The orifice has a diameter of 100 μm. The atmospheric plasma to be measured is placed to the orifice. Different pumps are used to pump down the pressure in the 1st stage, 2nd stage and 3rd stage respectively. Due to the great pressure gradient, a free jet is formed inside the pumping system. This system places a chopper in the 1st pumping stage as indicated in figure 2-6. This chopper has a 2 mm long conical skimmer embedded in a 1.5 mm thick metal disk[2.21]. The disk is rotated by an ultrahigh vacuum motor at 14.3 Hz and this allows the chopper to block the sampling at most of the time and only open it periodically. The design of this skimmer ensures that the free jet is formed directly in the 2nd pumping stage while its leakage to the 1st pumping stage is very few. Meanwhile, the pump in the 1st stage still works to ensure a relative low pressure which helps to maintain the low pressure in the 2nd stage. The typical pressures in the 1st, 2nd and 3rd pumping stages are 25 Pa, 2×10^{-2} Pa and 2.8×10^{-5} Pa. Under this condition, very few collisions between the sampled particles and background particles occur. The sampled signal and background noise are measured when the sampling is opened and blocked respectively and a high signal-to-background ratio can be achieved.

Three factors are believed to cause distortion to the results of this mass spectrometer measurement and they have to be considered in calibration. The first factor is composition distortions, which arise from the operation conditions of the differential pumping system. An overview of this issue can be found in a review paper[2.23]. One major composition distortion is radical diffusion in the free jet. The behaviour of radical diffusion is that lighter particles are more likely to diffuse radically than the heavier particles when they travel downstream. Consequently, the percentage of heavier particles occupied in those detected by the mass spectrometer is overcounted while that of lighter particles is underestimated. The radical diffusion can be calibrated by using a reference material as similar as possible in both composition and

behaviour to the sampled particle[2.19,2.22]. For instance, an atmospheric helium/oxygen plasma plume, if measured by a mass spectrometer, tends to have an overcounted result for oxygen-containing particles. The calibration uses a small amount of neon (atomic weight 20) or methane (molecular weight 16) for calibrating atomic oxygen (atomic weight 16) and a small amount of argon (atomic weight 40) for calibrating ozone (molecular weight 48). The calibration is conducted by comparing the signal intensity of the calibration particles to that of sampled particles. Knowing the density of the calibration particles, density of sampled particles can be estimated. This calibrated result significantly mitigates the distortion although a method error still exists.

Two other distortion factors arise from the mass spectrometer itself. The first one is the ionisation possibilities of the particles when they go through the ion source and the other is the transmission function of the mass spectrometer. These can also be taken into consideration in the calibration.

2.6 Summary

This chapter provides a brief review of common plasma diagnostics used for APGDs, especially those relevant to the work of this thesis. It is only with these diagnostics that a good understanding of the behaviours and characteristics of the plasma sources is possible.

Four diagnostics are introduced in this chapter, namely electrical measurement, fast imaging, optical emission spectroscopy and mass spectrometry. Electrical measurement can provide temporal descriptions of plasmas and they are also used to monitor voltage and current. Fast imaging enables short exposure images which uncover the dynamic evolution of plasmas in detail. Both optical emission spectroscopy and mass spectrometry provide a non-invasive method to identify plasma species. Emission spectra

can be obtained by OES and they are signatures of excited atom and ions. MS is able to provide measurements on atoms, ions and molecules, no matter whether they are excited, based on mass-to-charge ratio.

References

[2.1] Y. P. Raizer, Gas Discharge Physics, (Springer, 1991).

[2.2] J. R. Roth, Industrial Plasma Engineering, Volume 2, Applications to Nonthermal Plasma Processing, (IOP Publishing Ltd, 2001).

[2.3] F. Iza, G. J. Kim, S. M. Lee, J. K. Lee, J. L. Walsh, Y. T. Zhang and M. G. Kong, Plasma Process. Polym. 5, 322 (2008).

[2.4] J. J. Shi and M. G. Kong, Phys. Rev. Lett. 96, 105009 (2006).

[2.5] O. Sakai, Y. Kishimoto and K. Tachibana, J. Phys. D-Appl. Phys. 38, 431 (2005).

[2.6] L. F. Dong, J. X. Ran and Z. G. Mao, Appl. Phys. Lett. 86, 161501 (2005).

[2.7] X. M. Zhu, Y. K. Pu, N. Balcon and R. Boswell, J. Phys. D-Appl. Phys. 42, 142003 (2009).

[2.8] K. Niemi, V. Schulz-von der Gathen and H. F. Dobele, Plasma Sources Sci. Technol. 14, 375 (2005).

[2.9] V. Schulz-von der Gathen, L. Schaper, N. Knake, S. Reuter, K. Niemi, T. Gans and J. Winter, J. Phys. D-Appl. Phys. 41, 194004 (2008).

[2.10] S. G. Belostotskiy, R. Khandelwal, Q. Wang, V. M. Donnelly, D. J. Economou and N. Sadeghi, Appl. Phys. Lett. 92, 221507 (2008).

[2.11] A. Kono and K. Iwamoto, Jpn. J. Appl. Phys. Part 2 - Lett. Express Lett. 43, L1010 (2004).

[2.12] S. Q. Luo, C. M. Denning and J. E. Scharer, J. Appl. Phys. 104, 013301 (2008).

[2.13] R. F. Smith, J. Dunn, J. Nilsen, V. N. Shlyaptsev, S. Moon, J. Filevich, J. J. Rocca, M. C. Marconi, J. R. Hunter and T. W. Barbee, Phys. Rev. Lett. 89, 065004 (2002).

[2.14] M. Cullen, Atomic Spectroscopy in Elemental Analysis, (Blackwell Publishing Ltd., 2004).

[2.15] E. D. Metcalfe, Atomic Absorption and Emission Spectroscopy, (John Wiley & Sons, 1987).

[2.16] C. O. Laux, T. G. Spence, C. H. Kruger and R. N. Zare, Plasma Sources Sci. Technol. 12, 125 (2003).

[2.17] http://www.sri.com/psd/lifbase/.

[2.18] E. de Hoffmann and V. Stroobant, Mass Spectrometry : Principles and Applications, (John Wiley, 2007).

[2.19] R. K. Marcus and J. A. C. Broekaert, Glow Discharge Plasmas in Analytical Spectroscopy, (John Wiley & Sons, 2003).

[2.20] R. Hippler, S. Pfau, M. Schmidt and K. H. Schoenbach, Low Temperature Plasma Physics, (Wiley-CDH, 2001).

[2.21] J. Benedikt, D. Ellerweg and A. von Keudell, Rev. Sci. Instrum. 80, 055107 (2009).

[2.22] D. Ellerweg, J. Benedikt, A. von Keudell, N. Knake and V. Schulz-von der Gathen, New J. Phys. 12, 013021 (2010).

[2.23] E. L. Knuth, Combust. Flame 103, 171 (1995).

Chapter 3
APGD Slot Jet

3.1 Introduction

One of the key development issues for atmospheric pressure plasma sources is to increase the size of the plasma coverage for large-scale industrial applications. The research led by Roth at the University of Tennessee in the middle 1990's appears to be the earliest attempt to scale up APGD[3.1]. Their plasma sources are based on large-scale parallel-plate DBD discharge for *in situ* treatment of flat materials such as polymer sheets. Figure 3-1 shows a picture of their plasma source working in helium. It is found that uniform helium atmospheric plasma, seen from naked eyes, is produced in a 2.5 cm gap with the diameter of the electrode being 19 cm. If air is used as the working gas, the gap has to be greatly reduced to less than 5 mm to avoid filaments[3.1,3.2]. It should be noted that the claimed uniformity of the plasma was ascertained from visible luminosity of the plasma and its effect on workpieces at the microscopic scale, rather than more direct evidence such as nanosecond exposure images. Similar plasma sources were later proposed by others[3.3,3.4], and a roll-to-roll plasma source, as a route to continuous treatment of polymer films, was proposed by Roth[3.1]. Due to the relative small gap distance, this kind of parallel-plate DBD plasma source is only appropriate for treating thin and flat objects, such as polymer sheets.

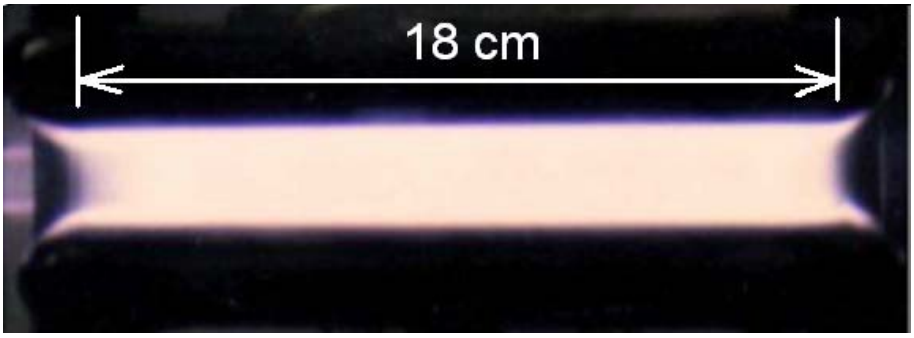

Fig 3-1: Picture of a large-scale atmospheric pressure plasma source proposed by Roth[3.1,3.2].

Another strategy for fulfilling large-scale plasma coverage is to build a plasma source and operate it in afterglow mode. This overcomes the problem of the small gap associated with the aforementioned *in situ* treatment. One of the earliest attempts in this direction is the plasma source developed by Park *et al.*, as shown in figure 3-2[3.5]. This plasma source consists of two parallel planar metal electrodes of 10×10 cm^2 which are typically separated by quartz spacers of 0.16 mm thick. Plasma excited at 13.56 MHz is generated between the parallel planar electrodes and a large gas flow rate is needed to bring out the plasma to the downstream region where sample is treated. The working gas is typically a helium flow of 50 standard litres per minute (slm) mixed with oxygen of 500 standard cubic centimetres per minute (sccm), equivalent to 5.21 m/s[3.5].

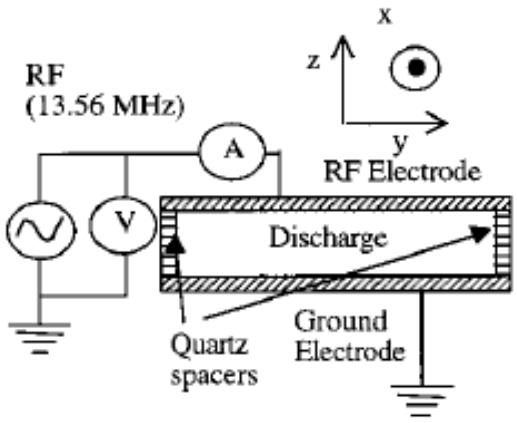

Fig 3-2: Schematic of the atmospheric pressure plasma source developed by Park *et al.*[3.5].

Other large-scale plasma sources featuring afterglow treatment include RF-driven hollow slot[3.6-3.8], kilohertz-excited DBD reactor[3.9], and DC-excited plasma brush[3.10-3.12]. The RF-driven hollow slot generates plasma between its two or three upstream long electrodes, and this RF plasma is then blown by gas convection out of its generation region, through a long slot formed between electrodes. The gap of this slot is typically less than 1 mm and its length is up to 0.5 m. With an appropriate gas flow rate, a curtain of plasma is formed between the slot exit and the downstream substrate. Typically the RF electric field is perpendicular to the direction of the gas flow field. Coupled by the electron and ion trapping by the RF field[3.13], this means that it is difficult to drive the upstream plasma to the downstream substrate and a very high gas flow rate is usually necessary (the gas velocity at the slot exit is 3.33 ~ 16.67 m/s). The DC plasma brush follows a similar design in which two rod electrodes are used to generate a plasma upstream in DC and a high gas flow field forces the upstream plasma towards a downstream substrate. In doing so, a plasma brush is formed. Again the electric field of the plasma excitation is perpendicular to the direction of the gas flow field, making it necessary to use high flow rates. Such plasma sources with their electric field and the gas flow field at 90° to each other are known as the cross-field plasma sources[3.14]. The above plasma sources all highly rely on the high gas flow to transport the reactive species to the downstream application region and the plasma plume is often very short. These impose some practical limitations.

It is desirable to generate large-scale plasma which can be produced directly onto the object to be treated, no matter whether the object is of planar or 3D structure. To address the need of cross-field plasma sources for high gas flow rate and short electrode-to-sample distance, electrodes may be configured so that the electric field is aligned in the same direction as the gas flow field. Such plasma sources are known as the linear-field devices[3.14].

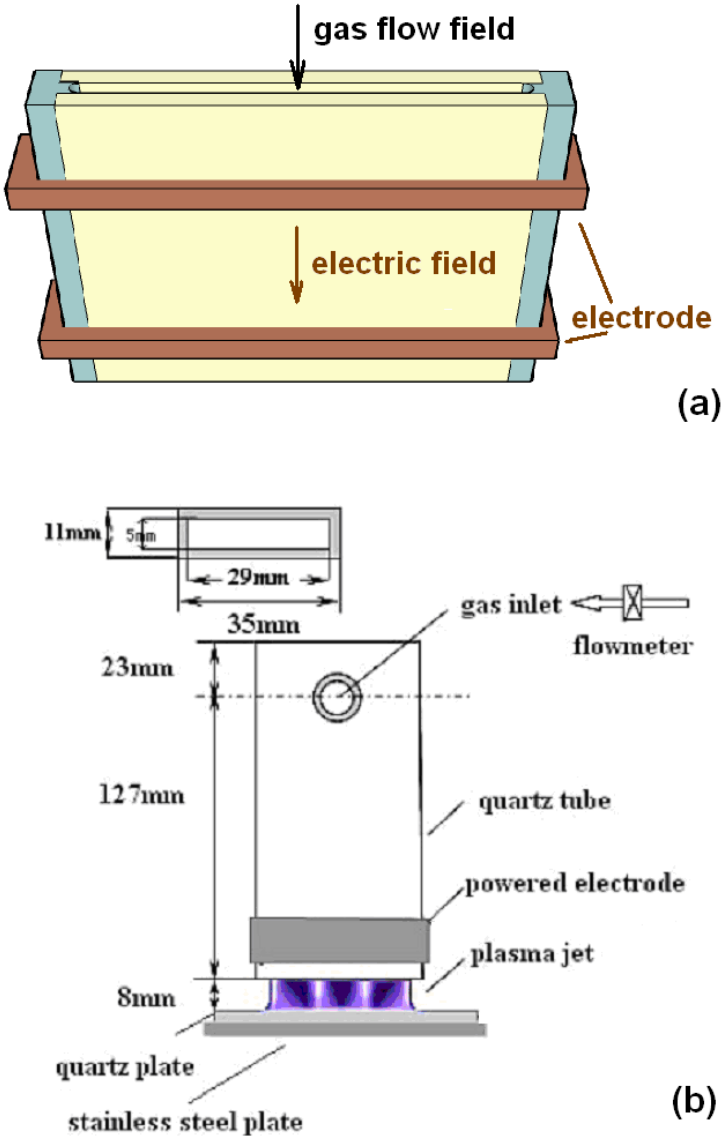

Fig 3-3: Schematic of (a) a slot plasma jet with arrows indicating the direction of the gas flow field and that of the electric field; (b) a slot plasma jet proposed by Nie[3.15].

One such example is schematically shown in figure 3-3a, and it is referred as slot plasma jet in this thesis. The slot plasma jet has a rectangular cross-sectional area with the long side being at least several centimetres. Therefore treatment of a large substrate surface would require the device to be moved in one direction only. From literature, the only plasma source of this kind appears to be the one proposed by Nie[3.15]. This source consists of a cubic quartz tube with a hollow cross-sectional area of 5×29 mm^2 and two

metallic electrodes (see figure 3-3b). One electrode is wrapped around the quartz tube and is connected to a 45 kHz AC power supply. The other electrode, a steel plate covered by a quartz substrate, is grounded and placed 8 mm away from the tube nozzle. This design was a good initiative but the focus was mainly on different plasma modes (i.e. a diffuse mode, a self-organised mode and a completely disordered mode) rather than the characteristics of the spatially extended plasma. More studies are needed, especially for the uniformity of the spatially extended plasma. The uniformity is believed to be a vital factor for reliable treatment of potentially three-dimensionally structured samples.

In this chapter, an experimental study of an atmospheric pressure glow discharge slot jet is reported. This slot plasma jet differs with those published slot jets in having a three-electrode design. The design is detailed in section 3.2. Its electrical, optical and spectral characteristics are introduced in section 3.3 with detailed discussion on plasma uniformity and plasma modes. The shortcomings of this slot plasma jet are briefly discussed in section 3.4. Finally, a summary is given in section 3.5.

3.2 Design and experimental setup

A picture of a prototype atmospheric pressure slot plasma jet is showed in figure 3-4. Basically the slot jet device can be divided into two parts. The upstream part of the device is a dielectric cassette with a gas cavity inside. It has a round gas inlet channel through which the plasma-forming gas is fed. The function of the gas cavity is to make the gas flow evenly across the entire width of the slot. This is critical for the uniformity of the sheet plasma produced. The design of the cavity channel and the possibility to integrate a porous material into the cavity help the horizontal uniformity of the gas flow.

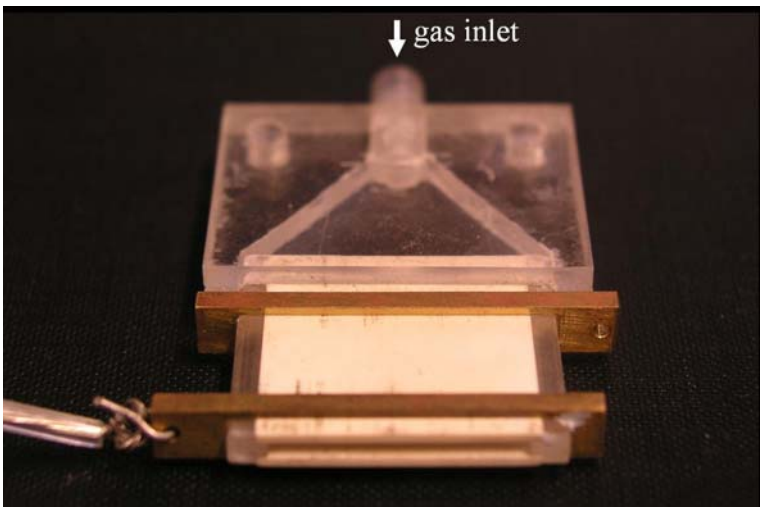

Fig 3-4: Picture of an atmospheric pressure slot plasma jet.

The downstream part of the slot jet is where the electrode region is. Here two parallel ceramic sheets are separated by insulation spacers introduced to the side edge of the ceramic sheets to form a gas channel slot of a rectangular cross-section. One end of the ceramic sheets are inserted into the upstream gas cavity and sealed, so the plasma-forming gas is fed evenly through the gap between the ceramic sheets. Different gap distances are investigated and normally a gap distance of 1.7 mm is found to result in the most uniform plasma. For the prototype device reported here, its width is 25.4 mm and its gas channel has a hollow cross-sectional slot area of 25.4×1.7 mm^2 at the exit point of the gas flow.

Two copper electrodes are wrapped tightly around the outside of the ceramic sheets as shown in figure 3-5. The copper electrode near the outlet of the slot jet is connected to an AC power supply at 30 kHz and an amplitude adjustable up to 5 kV. The distance between the edge of this electrode to the jet outlet is fixed to 3 mm. The other copper electrode can be grounded or floating, and the distance between these two electrodes is nominally set to 13 mm.

The third electrode, a grounded copper plate covered by a plasma-facing

ceramic sheet is placed 8 mm away from the slot nozzle. It combines with the other two electrodes to form a three-electrode system. Therefore there are two discharge regions. One is inside the slot gas channel and between the two copper electrodes, and it is referred as the upstream discharge region in the following discussion. The downstream discharge region occupies the gas channel between the copper electrode near the nozzle (the powered electrode) and the downstream ceramic sheet. Both discharges generated in these regions are DBD because of the use of ceramic sheets. The directions of the gas flow and the electric field are the same. As indicated by the insert in figure 3-5, the insulation spacer has a curved gas-facing surface to mitigate possible localised gas flow field and localised electric field which may disturb the uniformity of the downstream plasma curtain.

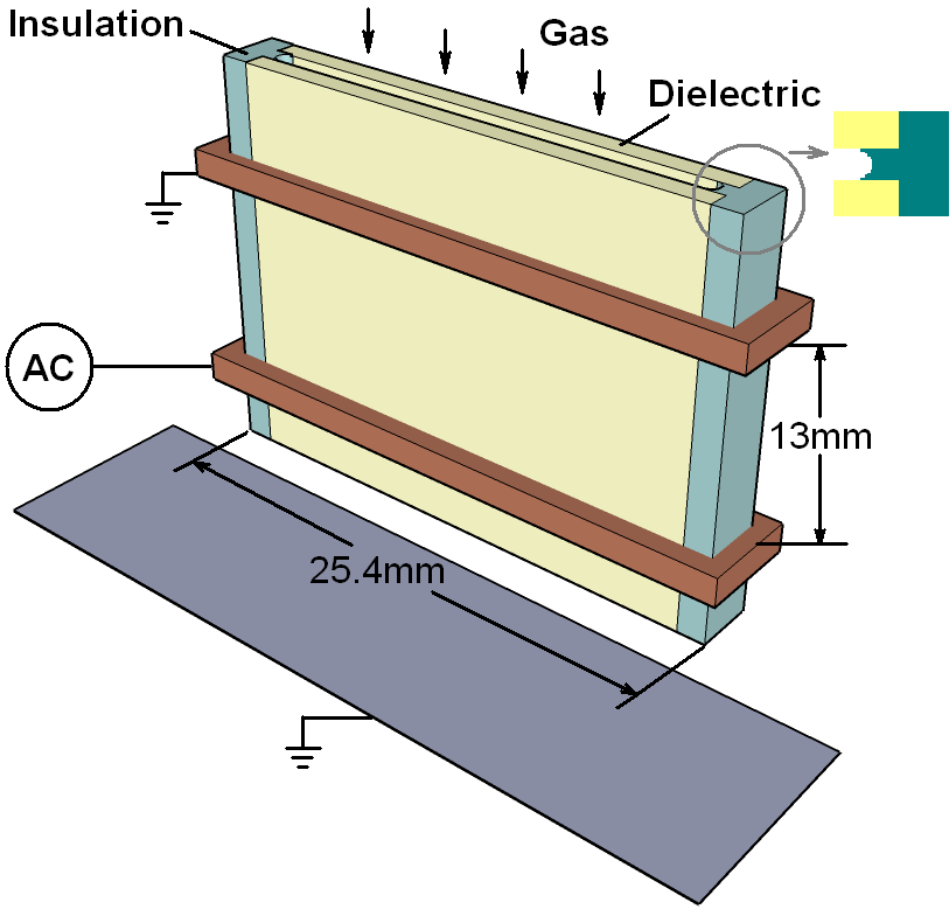

Fig 3-5: Schematic of a three-electrode slot plasma jet.

In the experiments reported here, a Tektronix P6015A voltage probe and two Pearson 2877 current probes are used to measure the electrical parameters. Currents are measured for both the upstream and downstream discharge regions simultaneously and their waveforms are recorded by a Tektronix DPO4104 oscilloscope. Both a domestic camera and an Andor DH720 ICCD camera are used for imaging. An Andor Shamrock SR-303i spectrograph with a grating of 1200 is used for taking broad spectra and a grating of 2400 is used for measurements of specific spectral lines. A helium flow of 25 slm (99.996%) is used unless otherwise stated.

3.3 Characteristics of the slot plasma jet

3.3.1 Electrical measurements and two modes

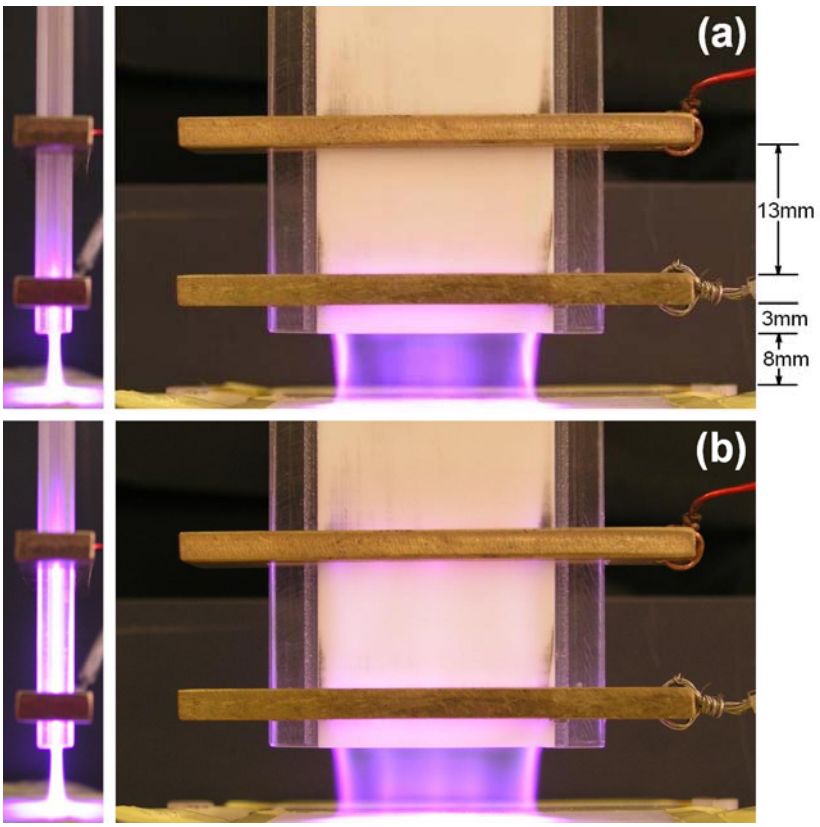

Fig 3-6: Pictures of the slot plasma jet with (a) plasma only presented in the downstream discharge region; (b) plasmas presented both in the upstream discharge region and the downstream discharge region.

The appearances of the slot plasma jet in working condition, taken by a domestic camera, are shown in figure 3-6. Depending on the amplitude of the applied voltage, the slot plasma jet can operate either with only the downstream discharge (as figure 3-6a with a peak applied voltage, V_p, = 2.75 kV) or with both the upstream and downstream discharges (as figure 3-6b with V_p = 4.5 kV). From the side view in the left-hand side of the pictures, it is clear whether a plasma is present in the upstream region. The plasma in the downstream plasma region is characterised by a sheet-like plasma with an area of 25.4×8 mm^2. This is referred as the *plasma curtain* in this thesis. The plasma curtain is bright, stable and uniform when seen with naked eyes.

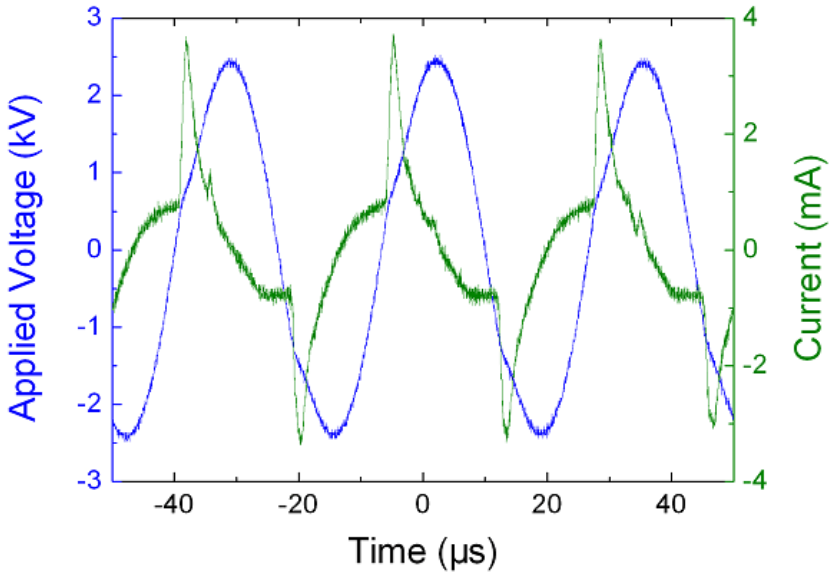

Fig 3-7: Voltage and current waveforms of a two-electrode slot jet shortly after the downstream plasma curtain forms.

Firstly we consider the case where the upstream ground electrode is removed. Figure 3-7 shows typical voltage and current waveforms of the two-electrode slot plasma jet. The peak applied voltage V_p is 2.5 kV, corresponding to a condition immediately after the gas breakdown in the downstream discharge region. A uniform plasma curtain is established. The voltage and current waveforms reflect a typical DBD with the discharge

current leading the applied voltage by approximately π/2 in phase. There is mainly one current pulse in each half cycle of the applied voltage suggesting the absence of multiple discharge events per half cycle and possibly the absence of streamers.

With increasing applied voltage, the amplitude of the current is seen to increase and the plasma curtain becomes more intense. Figure 3-8 shows the peak-peak current and the dissipated power as a function of the applied voltage. It is found that the dissipated power increases monotonically from 0.27 W at V_p = 2.5 kV to 0.88 W at V_p = 4.5 kV. As more power is coupled into the plasma, the ionisation degree is expected to increase which in turn produces a visually brighter plasma. The highest voltage for maintaining a stable plasma is about 4.5 kV and it is indicated in figure 3-8.

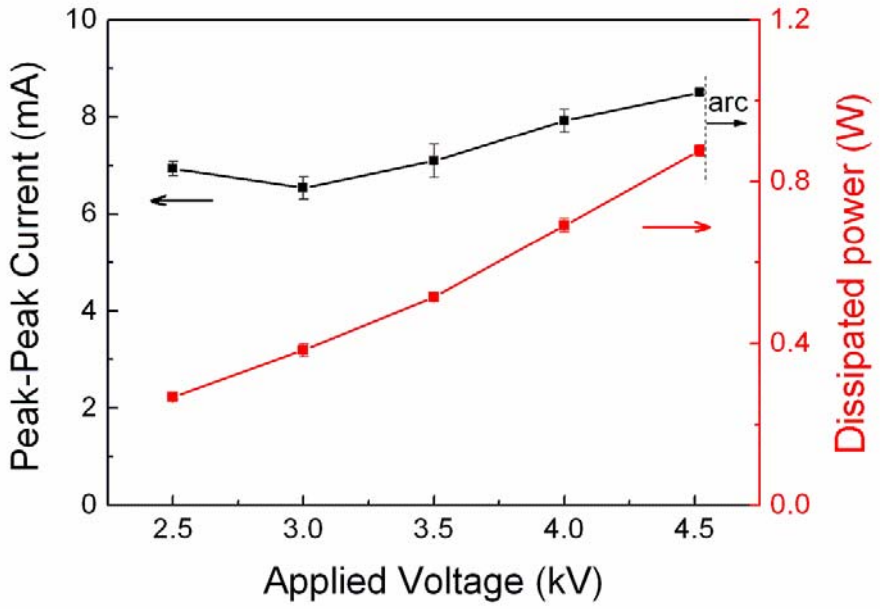

Fig 3-8: The peak-peak current and the dissipated power as a function of the applied voltage for the two-electrode slot jet.

We now consider the slot plasma jet with its most upstream electrode grounded. Depending on whether plasma is generated in the upstream discharge region, two operating modes of the slot plasma jet, namely a single discharge mode (SD mode) and a dual discharge mode (DD mode), are

observed. In the SD mode, only a downstream plasma curtain is present but no plasma exists in the upstream region, while in the DD mode plasmas are generated in both the downstream and upstream region. The pictures in figure 3-6 are representative for these two operating modes.

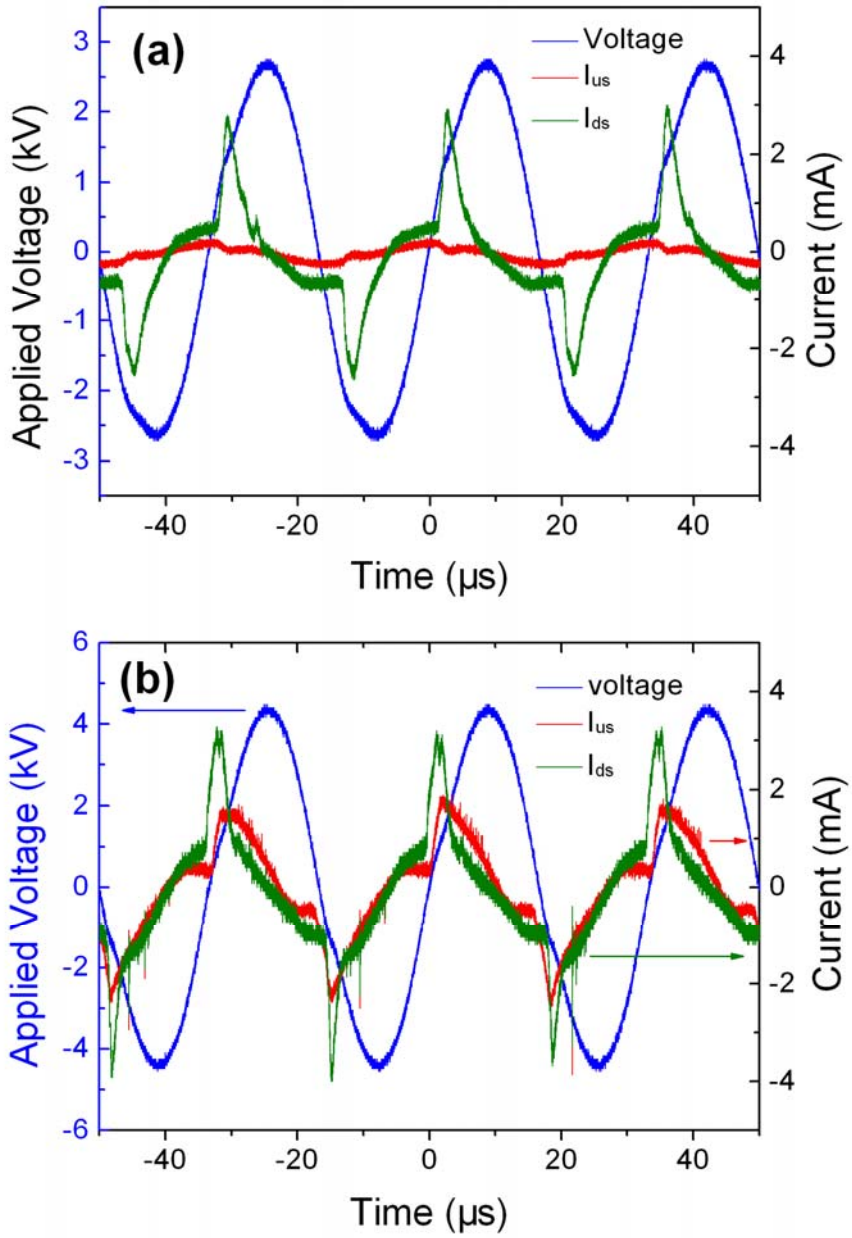

Fig 3-9: Current and voltage traces of the slot jet, in (a) single discharge mode and (b) dual discharge mode.

The current and voltage traces in the SD mode and the DD mode are showed in figure 3-9 under the same condition as that in figure 3-6. From

these traces, temporal characteristics of the discharges in the two discharge regions are revealed. I_{us} and I_{ds} are used here for the current flowing from the power electrode to the upstream ground electrode and to the downstream ground electrode, respectively. In the SD mode, I_{ds} is characterised by one large spike per half cycle of the applied voltage. This current spike is largely the conductive current of a significant discharge event, and the more gradual current component of much lower amplitude, onto which the large current spike is added, represents a displacement current. Since no discharge occurs in the upstream region, there is only displacement current in I_{us}, which is largely sinusoidal. The minor distortion is due to dynamics of the accumulated charges on the surface of the two upstream ceramic sheets.

In the DD mode, the current traces of both I_{us} and I_{ds} are dominated by one big spike every half cycle of the applied voltage. The instants for the onset of the two discharges are slightly different in the positive half cycle of the applied voltage in that the plasma in the downstream region occurs earlier than the one in the upstream region.

Figure 3-10 shows the peak-peak current as a function of the applied voltage for the three-electrode slot jet when increasing V_p from 1.25 kV to 5.25 kV with a step of 0.25 kV. The red and blue lines represent I_{ds} and I_{us} respectively. With increasing V_p, the breakdown of the downstream region occurs at V_p = 3.0 kV and immediately after the breakdown V_p drops to 2.5 kV which is enough to sustain the discharge. The dashed line shows the transition region. The breakdown of the upstream discharge region occurs at a higher applied voltage of V_p = 3.5 kV. In the graph, the pre-breakdown region, the SD mode, and the DD mode are clearly marked. The error bars shown in the graph indicate that the amplitudes of the currents change moderately with time and this may be due to the interaction between the two discharges of different regions. This interaction tends to be stronger at large applied voltage. In the pre-breakdown region where V_p < 3.0 kV, the CVC of both discharge

regions are linear and go through the origin when extending to low voltage, suggesting a pure capacitive characteristic. In the SD mode region of 2.5 kV < V_p < 3.5 kV, as the plasma only appears in the downstream region, I_{ds} is much bigger than I_{us}. In the DD mode region of V_p > 3.5 kV, after an abrupt increase in amplitude immediately after the breakdown, I_{us} increases faster than I_{ds}. The appearance of the upstream discharge lowers the increase of I_{ds} and thus keeps the downstream plasma curtain remaining stable even when V_p reaches 5.25 kV, a voltage nearly 20% higher than the highest possible applied voltage in the two-electrode slot jet case (see figure 3-8).

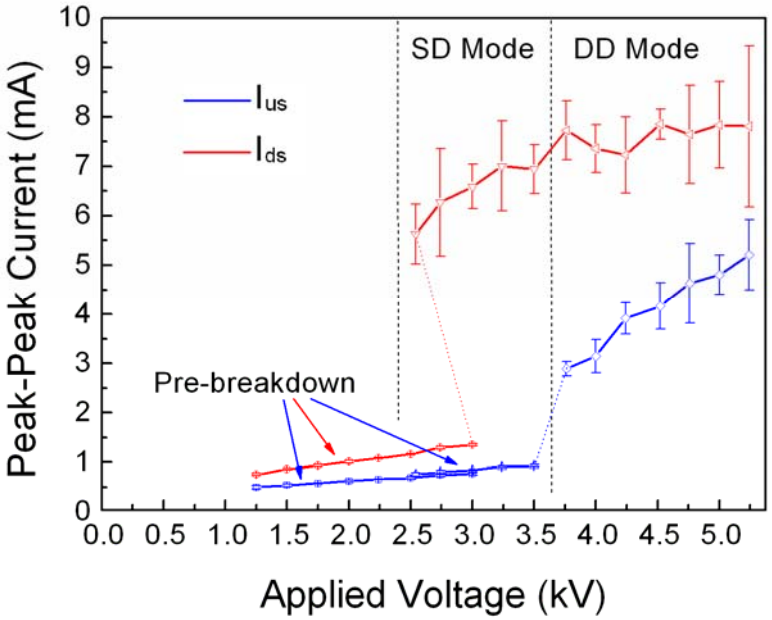

Fig 3-10: The peak-peak current as a function of the applied voltage for the three-electrode slot plasma jet.

The dissipated power of the two plasma regions as a function of the applied voltage of the slot jet is presented in figure 3-11, in which similar trends to the CVC in figure 3-10 are observed. However two differences should be noted. Firstly, there is an obvious drop for the dissipated power of the plasma curtain after the transition from the SD mode to the DD mode. Secondly, the dissipated power for both regions increases monotonously in the DD mode. The first difference clearly shows the appearance of the

discharge in the upstream region changes the original trend of the increase of power consumption in the downstream plasma curtain. Therefore the slot jet in the three-electrode configuration has a much broader operation range and works at a much higher voltage than the two-electrode slot jet. The monotonous increase of the downstream power consumption in the DD mode is likely to contribute to a similar monotonous increase of the reactive species produced. The advantage of the three-electrode slot jet over two-electrode slot jet is more than a broader operation range. As a second plasma appears in the upstream of the plasma curtain, the electrons produced in the upstream may contribute as seed electrons to the downstream discharge, and also the reactive species produced in the upstream discharge region can be blown to the downstream application region by the gas flow thus adding to the concentrations of radicals. The three-electrode slot jet is more effective in production of reactive plasma species than its two-electrode counterpart even when the former is operated at lower power dissipation.

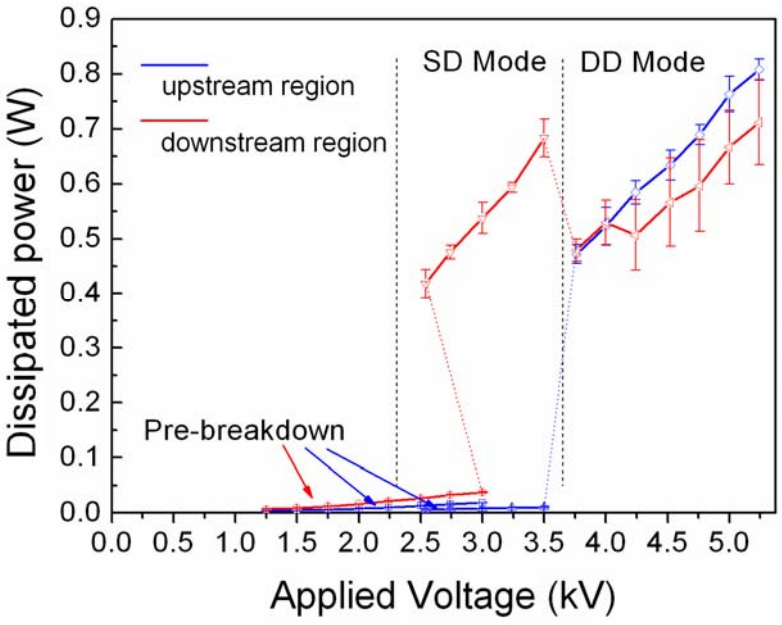

Fig 3-11: Dissipated power as a function of the applied voltage for the three-electrode slot jet.

3.3.2 Dynamics

From an application point of view, it is of interest to investigate whether the plasma is uniform and how it develops in the downstream discharge region where the sample is placed. To this end, fast imaging using an ICCD camera is used.

Figure 3-12 shows the evolution of the downstream plasma when V_p = 3.75 kV and the helium flow rate is 15 slm. The slot jet is in the DD mode. The images in figure 3-11a and 3-11b are in the positive half cycle and negative half cycle respectively. Each image is taken in a single shot with an exposure time of 1 μs and all the images are consecutive with a total time of 10 μs in the same half cycle. In the graph, the positions of the ceramic sheets and the ground electrode are indicated. All the images are normalised to the same intensity range so they are directly comparable. It is found that the plasma occupies the downstream discharge region only for 3 ~ 4 μs. This is consistent with the width of the current pulse. Light emission can be seen near the surface of the downstream ceramic sheet for a few μs after the downstream plasma is quenched. This suggests that excitation happens in the gap for a longer time scale and some plasma species can cause photon emission when they arrive at the surface of the downstream ceramic sheet. The highest light intensity in the positive half cycle is found to be 56% higher than the highest light intensity in the negative half cycle. This is because the light emission seen from the images of the positive half cycle is from the negative glow region of the plasma. It is known that the negative glow is the brightest region of a glow discharge, and the highest light emission seen from a negative half cycle is possible from the anode glow, which is darker than the negative glow.

The uniformity of the plasma curtain in these images as a microsecond scale is reasonably good, especially in the negative half cycle. The gas velocity here is 5.72 m/s. Better uniformity is observed at higher flow rates.

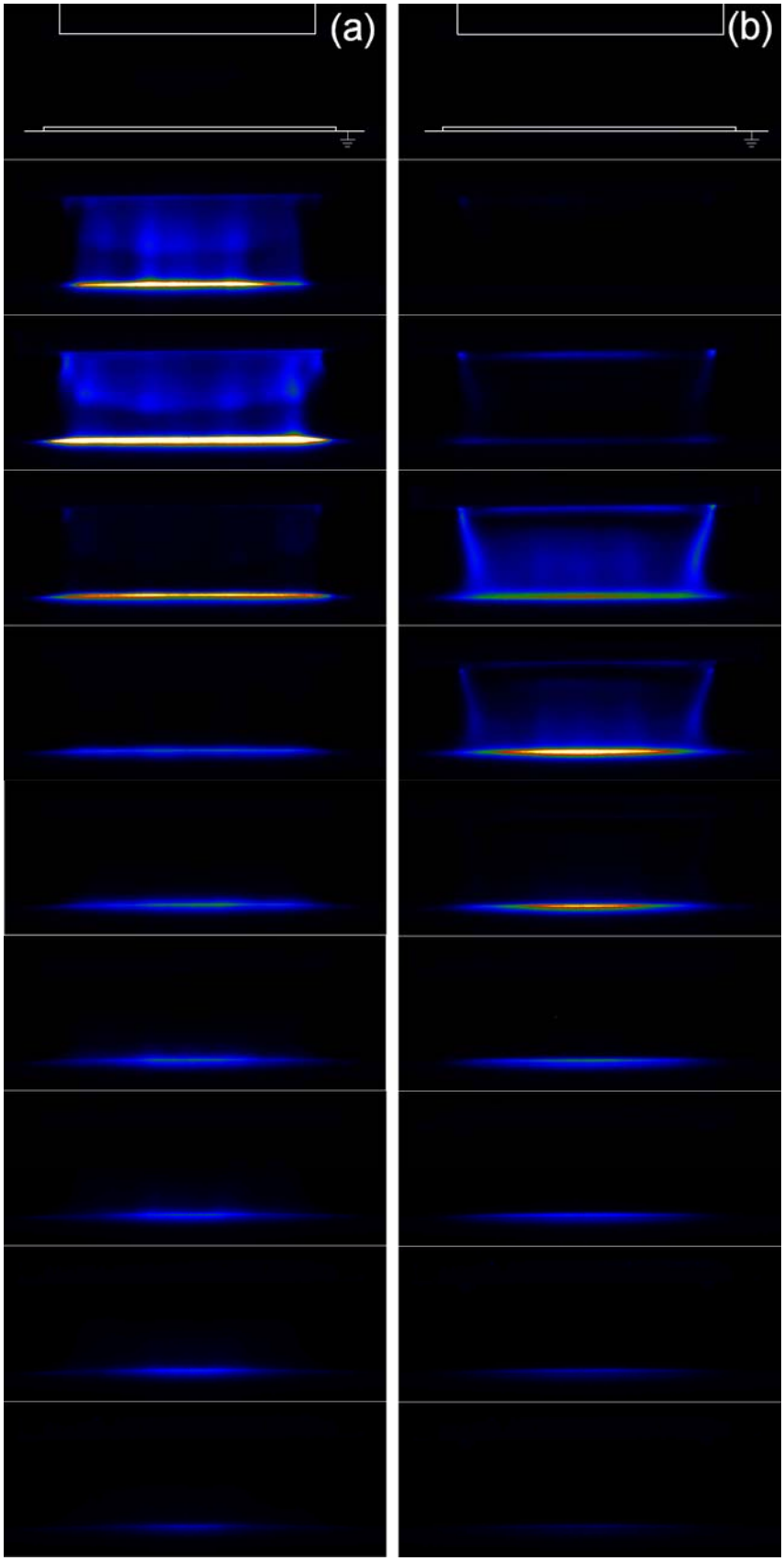

Fig 3-12: Evolution of the downstream plasma in (a) the positive half cycle, (b) the negative half cycle of the applied voltage. The gas flow rate is 15 slm.

Figure 3-13 shows an image taken when the current reaches its peak in the positive half cycle and with an exposure time of 1 μs. The flow rate in this case is 25 slm. It is clear that better uniformity is achieved than its counterpart in the 15 slm case.

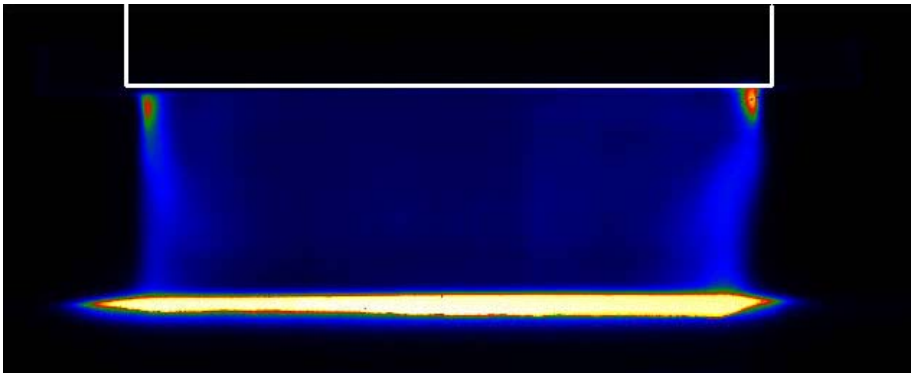

Fig 3-13: Image of the plasma curtain taken during the positive current peak. Exposure time is 1 μs and the helium flow rate is 25 slm.

Exposure time of 1 μs is too long to establish possible non-uniformity, for example, caused by streamers. To this end, images with 10 ns exposure time are taken under the same condition as those in figure 3-12. Figure 3-14 corresponds to the instant when the current reaches its peak in the positive half cycle. It is clear that the plasma curtain is free of any obvious streamers and is spatially glow-like across the width of the 25.4-mm-wide slot jet. The uniformity is further confirmed for a slot jet of 50 mm wide (data not shown). This genetic characteristic is highly desirable for applications demanding a streamer-free treatment.

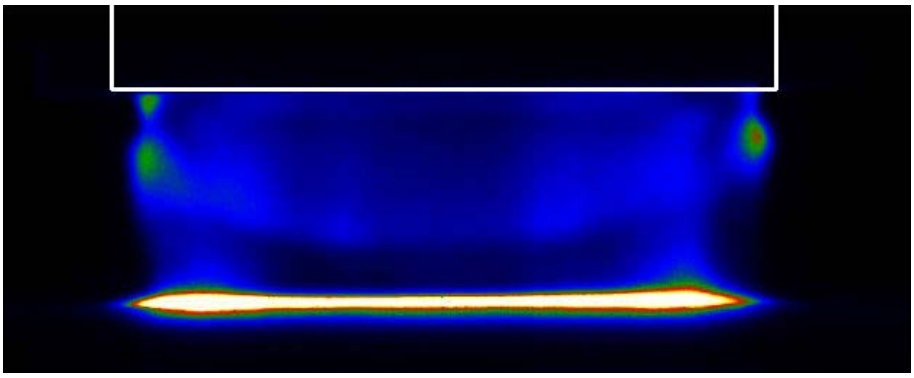

Fig 3-14: Image of the plasma curtain taken during the positive current peak. Exposure time is 10 ns and the helium flow rate is 15 slm.

3.3.3 Optical emission spectrum

Optical emission spectrum provides information of plasma species. In the experiments reported here, the emission spectrum is obtained from the downstream plasma near the downstream ceramic surface. Figure 3-15 shows the spectra from 200 nm to 800 nm taken at V_p = 2.75 kV (the SD mode) and V_p = 4.5 kV (the DD mode) respectively with the same optical setup and a fixed fibre-to-plasma distance. Emission lines of helium, nitrogen and oxygen species as well as OH radicals are found in the spectra. This is consistent with the experimental condition that the plume of the helium plasma curtain plunges into the ambient air in the downstream region and causes ionisations and excitations of air molecules. Specifically, N_2 bands are found at 316, 337, 357, 375, 380, 405 and 715 nm; N_2^+ bands at 353, 391, 427 and 470 nm; helium line at 706 nm; atomic oxygen line at 777 nm. At 309 nm, OH line is found. The overall spectrum is similar for the two modes, while higher emission intensities are always obtained in the DD mode. Detailed spectroscopic measurements focusing at 337, 706 and 777 nm with a grating of 2400 are shown in figure 3-16, in which results are obtained from 5

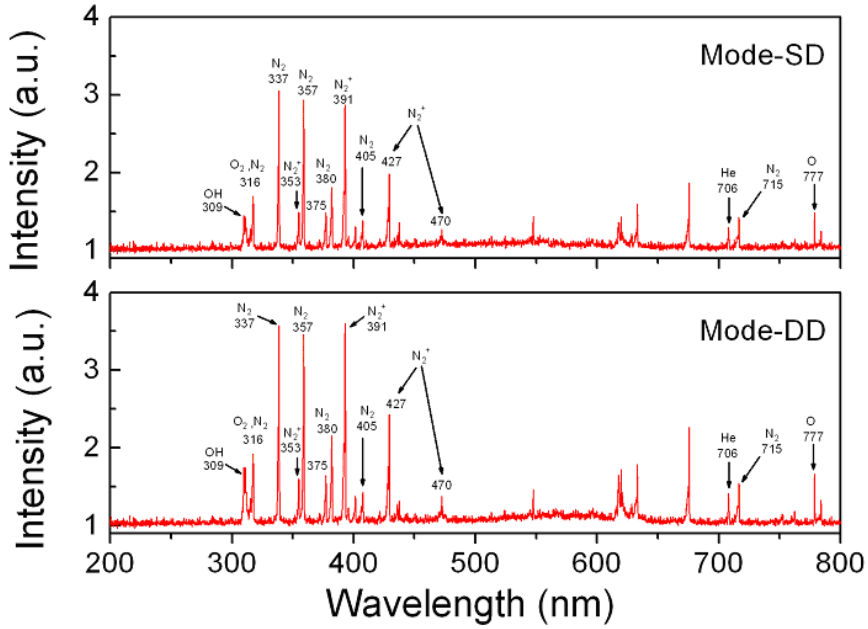

Fig 3-15: Overall spectra of the slot jet.

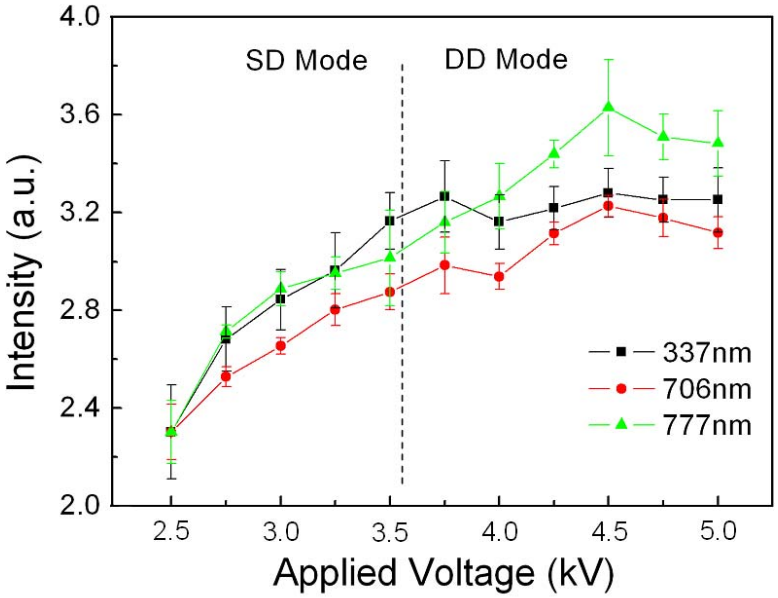

Fig 3-16: Optical emission at 337 nm, 706 nm and 777 nm as a function of the applied voltage.

independent measurements for each point. It is of interest to note the highest intensity of each spectral line does not appear at the highest applied voltage. Instead they occur at V_p = 4.5 kV. When V_p < 4.5 kV, the emission intensities of 706 and 777 nm increase monotonically with the applied voltage.

3.3.4 Temperature

Atmospheric pressure helium plasmas tend to have a low gas temperature and this is desirable for biomedical applications. The gas temperature of the atmospheric helium plasma jets reported elsewhere is found near room temperature and this is a reference point for the slot plasma jet discussed here. Temperature measurements are carried out using two methods. First, a temperature strip is used and placed at 8 mm away from the slot nozzle and the measured gas temperature is shown in figure 3-17. It is found that the gas temperature increases from 24 °C to 28 °C with the increase of V_p from 2.5 kV to 5 kV. The second method is to obtain the

rotational temperature of the plasma by comparing experimental and simulation results of the emission spectrum at specific wavelengths. This is because rotational relaxation is fast at atmospheric pressure. As a result, rotational temperature may be used to approximate gas temperature[3.16]. The insert in figure 3-17 shows a comparison at V_p = 4.5 kV, in which experimental result of the first negative system of molecular nitrogen at 391 nm matches the simulation result well at 300±10 K. Together with the measurement obtained with the temperature strip, this confirms that the gas temperature of the plasma curtain is very close to room temperature.

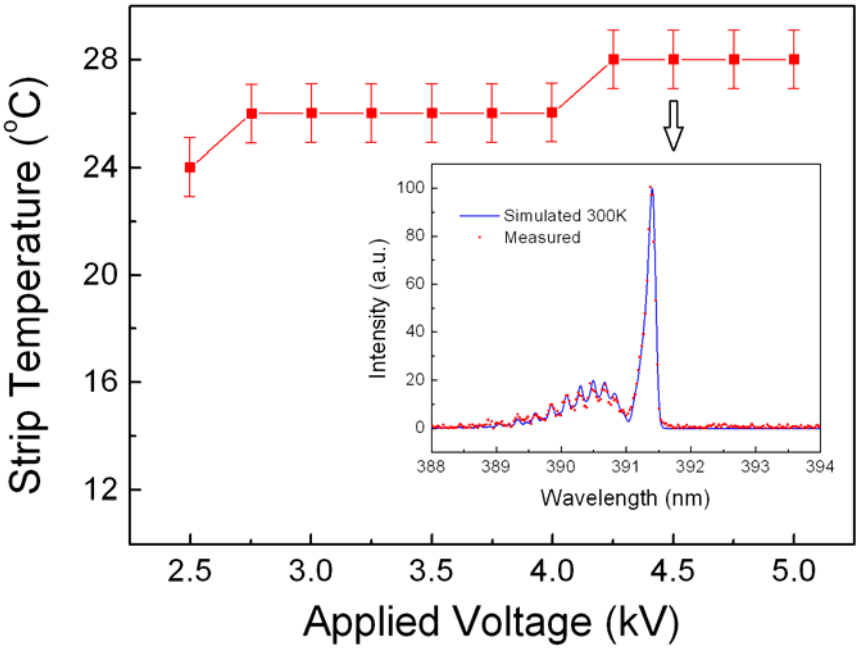

Fig 3-17: Gas temperature measurement for the plasma curtain at the downstream region near the downstream ceramic sheet.

3.4 Shortcomings

There are a few shortcomings which may limit the widespread use of the APGD slot jet reported in this chapter. First, the nozzle-to-sample distance is 8 mm and this may be too small for some applications. A larger nozzle-to-sample distance is possible. However this implies an increase in the helium flow rate above 15 slm. Second, in order to further enhance the

reactivity of the plasma curtain, it is desirable to mix molecular gas such as oxygen into the helium carrier gas. It is found that the uniformity of the downstream plasma curtain may be significantly compromised if a small amount of oxygen (i.e. > 0.1%) is mixed into the helium. It is known that the production of oxygen atoms may be optimised around O_2/He mixing rate of 0.5%[3.17,3.18]. The last but not the least, it is found that the uniformity of the downstream plasma curtain relies markedly on the uniformity of the electric field between the powered electrode and the downstream ground electrode. If an uneven object is placed between these two electrodes, the electric field will be affected, thus affecting the uniformity of the downstream plasma curtain.

3.5 Summary

In this chapter, a spatially extended atmospheric pressure slot plasma jet is presented as a route to large-scale plasmas. The slot plasma jet presented is able to produce a 25-mm-wide spatially extended plasma curtain with a typical plume length of 8 mm. It features a three-electrode configuration with two possible operation modes, namely the single discharge mode and the dual discharge mode, as well as a streamer-free uniformity of the downstream plasma curtain.

Electrical measurements demonstrate the operation range of the two modes and it shows the upstream plasma contributes to the stability of the downstream plasmas curtain by limiting the increase of the power consumption in the downstream region. The evolution and uniformity of the downstream plasma curtain are revealed by fast imaging. Its homogeneous character is confirmed by 10 ns exposure image. Both the overall spectrum from 200 ~ 800 nm and intensities of specific spectral lines are studied. It confirms the existence of reactive species in the downstream application region. The gas temperature of the plasma near the downstream electrode is

measured by two different methods, which both confirm a room temperature.

Although the three-electrode slot plasma jet is capable of producing a spatially extended cold plasma curtain with excellent uniformity and stability, this excellent uniformity is only sustainable when a largely flat surface is treated. To a certain extent, this compromises a full realisation of the objective of this thesis for achieving a capability to treat three-dimensional objects. As a result, new strategies are needed. In the following chapters, the parallelisation of plasma jets, i.e. the plasma jet arrays, will be studied and discussed.

References

[3.1] J. R. Roth, S. Nourgostar and T. A. Bonds, IEEE Trans. Plasma Sci. 35, 233 (2007).

[3.2] J. R. Roth, J. Rahel, X. Dai and D. M. Sherman, J. Phys. D-Appl. Phys. 38, 555 (2005).

[3.3] S. Y. Moon, W. Choe and B. K. Kang, Appl. Phys. Lett. 84, 188 (2004).

[3.4] M. H. Jung and H. S. Choi, Thin Solid Films 515, 2295 (2006).

[3.5] J. Park, I. Henins, H. W. Herrmann, G. S. Selwyn, J. Y. Jeong, R. F. Hicks, D. Shim and C. S. Chang, Appl. Phys. Lett. 76, 288 (2000).

[3.6] A. P. Yalin, Z. Q. Yu, O. Stan, K. Hoshimiya, A. Rahman, V. K. Surla and G. J. Collins, Appl. Phys. Lett. 83, 2766 (2003).

[3.7] A. Sharma, A. Pruden, Z. Q. Yu and G. J. Collins, Environ. Sci. Technol. 39, 339 (2005).

[3.8] R. Rahul, O. Stan, A. Rahman, E. Littlefield, K. Hoshimiya, A. P. Yalin, A. Sharma, A. Pruden, C. A. Moore, Z. Yu and G. J. Collins, J. Phys. D-Appl. Phys. 38, 1750 (2005).

[3.9] E. Panousis, F. Clement, J-F Loiseau, N. Spyrou, B. Held, M. Thomachot and L. Marlin, Plasma Sources Sci. Technol. 15, 828 (2006).

[3.10] Q. S. Yu, C. Huang, F. H. Hsieh, H. Huff and Y. X. Duan, Appl. Phys. Lett. 88, 013903 (2006).

[3.11] C. Huang, Q. S. Yu, F. H. Hsieh and Y. X. Duan, Plasma Process. Polym. 4, 77 (2007).

[3.12] Y. X. Duan, C. Huang and Q. S. Yu, Rev. Sci. Instrum. 78, 015104 (2007).

[3.13] D. W. Liu, J. J. Shi and M. G. Kong, Appl. Phys. Lett. 90, 041502 (2007).

[3.14] J. L. Walsh and M. G. Kong, Appl. Phys. Lett. 93, 111501 (2008).

[3.15] Q. Y. Nie, C. S. Ren, D. Z. Wang, S. Z. Li, J. L. Zhang and M. G. Kong, Appl. Phys. Lett. 90, 221504 (2007).

[3.16] C. O. Laux, T. G. Spence, C. H. Kruger and R. N. Zare, Plasma Sources Sci. Technol. 12, 125 (2003).

[3.17] S. Perni, G. Shama, J. L. Hobman, P. A. Lund, C. J. Kershaw, G. A. Hidalgo-Arroyo, C. W. Penn, X. T. Deng, J. L. Walsh and M. G. Kong, Appl. Phys. Lett. 90, 073902 (2007).

[3.18] X. T. Deng, J. J. Shi, H. L. Chen and M. G. Kong, Appl. Phys. Lett. 90, 013903 (2007).

Chapter 4
Single APGD Jet

4.1 Introduction

Atmospheric pressure plasma jets are a kind of atmospheric discharge sources which are so named because of their production of jet-like plasma. Normally a noble gas is fed through a housing tube and ionised in the strong electric field set up by one or more electrodes. The plasma species are flushed by the flow of the carrier gas out of the tube nozzle and thus brought in contact with the ambient environment. By doing so, a jet-like plasma plume is formed outside of the housing tube[4.1]. Atmospheric pressure plasma jets have attracted much attention for the past ten years and are well-known for their widespread use in various biomedical applications, such as sterilisation, protein removal and teeth bleaching[4.2-4.4]. This is mainly because the plasma chemistry achieved in the plume can produce abundant chemically reactive species at low gas temperature. Also, the plasma generation region of an APGD jet is spatially separated from the usually downstream application region thus providing a good level of plasma insusceptibility to variations in geometrical and material characteristics of different biomedical samples, for instance, bloods, body fluids, bones, plastic and metallic implants. Their plume length is typically of a few centimetres long, well-suited for treating large geometrically complex objects without compromising the plasma stability. Furthermore, the plasma plumes are normally of a few millimetres in diameter so the plasma can access to small cavities and the inner surfaces of

tiny tubular objects such as catheters.

In this chapter, a review of single atmospheric plasma jets is given in section 4.2. Plasma jets reported so far in literature are classified into nine categories based on their different structures. Comments will be given on whether each category of plasma jets may be appropriate for parallelisation, as the idea of parallelizing jets will be developed in the following chapters for constructing plasma array sources. A dedicated assessment of generic requirements of single atmospheric plasma jets for use in plasma array will be also given. Following an introduction of experimental setup in section 4.3, recommendations from the assessment will be used in section 4.4 to study three types of single plasma jets as possible elemental components for use in an atmospheric plasma array. These jets will be contrasted to highlight the benefits of the use of capillary electrodes also as the gas feed channel. The best-performing jet structure will be shown to have a capillary electrode combined with a concentric ring electrode placed downstream by means of electrical and optical characterisations as well as microbiology experiments. Finally, conclusions will be summarised in section 4.5.

4.2 Review of common single APGD jets

APGD jets started to be an active research topic in 1990's[4.5]. Since then electrical excitations at frequencies from DC up to microwave have all been used to drive atmospheric pressure plasma jets. However, the discussion here is not intended as an exhaustive review of all current APGD jets but an attempt to categorise some of the commonest single plasma jets and their main features in the context of their suitability for use in a plasma jet array for processing applications. The analysis focuses on electrode structures and their implications to how easily different atmospheric plasma jets may be parallelised to form an array. In terms of the electrode structure with regard to the gas flow, most plasma sources can be classified either as a cross-field

device or as a linear-field device[4.6]. A comparison study between cross-field plasma jets and linear-field plasma jets suggests that linear-field plasma jets are much more intense than cross-field plasma jets in the downstream region, so they are in general more suited for downstream processing applications[4.6].

The discussion presented here will be restricted to capacitively coupled plasma jets because their heat generation is much lower than inductively coupled plasmas, but we will comment on the latter when appropriate. The jets discussed here are those with a cylindrical structure.

Figure 4-1a and 4-1b show two similar types of atmospheric plasma jets both employing a central rod electrode and a concentric outer tube as the counter electrode. The electrode unit is cylindrical, and the annular space between them is used to flow the carrier gas. Plasma can be struck between the two electrodes at frequencies from dc up to megahertz, and is transferred to downstream by the gas flow. A downstream ground electrode is sometimes used to assist the plasma transfer by setting up an axially directed electric field. Type *a* jets do not have dielectric barriers[4.7-4.21], whereas type *b* jets do in the form of either a gas-confinement dielectric tube attached to the inner wall of the outer electrode or a dielectric coating to the inner electrode[4.5,4.6,4.22-4.56]. In general, these are cross-field jets. This tends to confine the plasma in the electrode region and to restrict the extension of the plasma jet towards the downstream region. To force the usually localised plasma out of the electrode region, the outer electrode of type *a* jets is sometimes pitched towards the axis to form a small nozzle and to set up an axial component of the electric field[4.9,4.10,4.18,4.21]. Similar arrangements are made for type *b* jets, for example with the gas confinement tube having a reduced radius towards its nozzle[4.22,4.24,4.36,4.40,4.47,4.50-4.52,4.54,4.56]. This is useful to extend a plasma jet into the downstream region. However it also introduces a drawback of decreasing the cross-sectional area of the plasma plume in proportion to the physical dimension of the cross section of the tube structure.

It is worth mentioning that in the case of a powered inner electrode the outer (grounded) electrode is sometimes removed in type *b* jets[4.35,4.37,4.42,4.47,4.50-4.52,4.56].

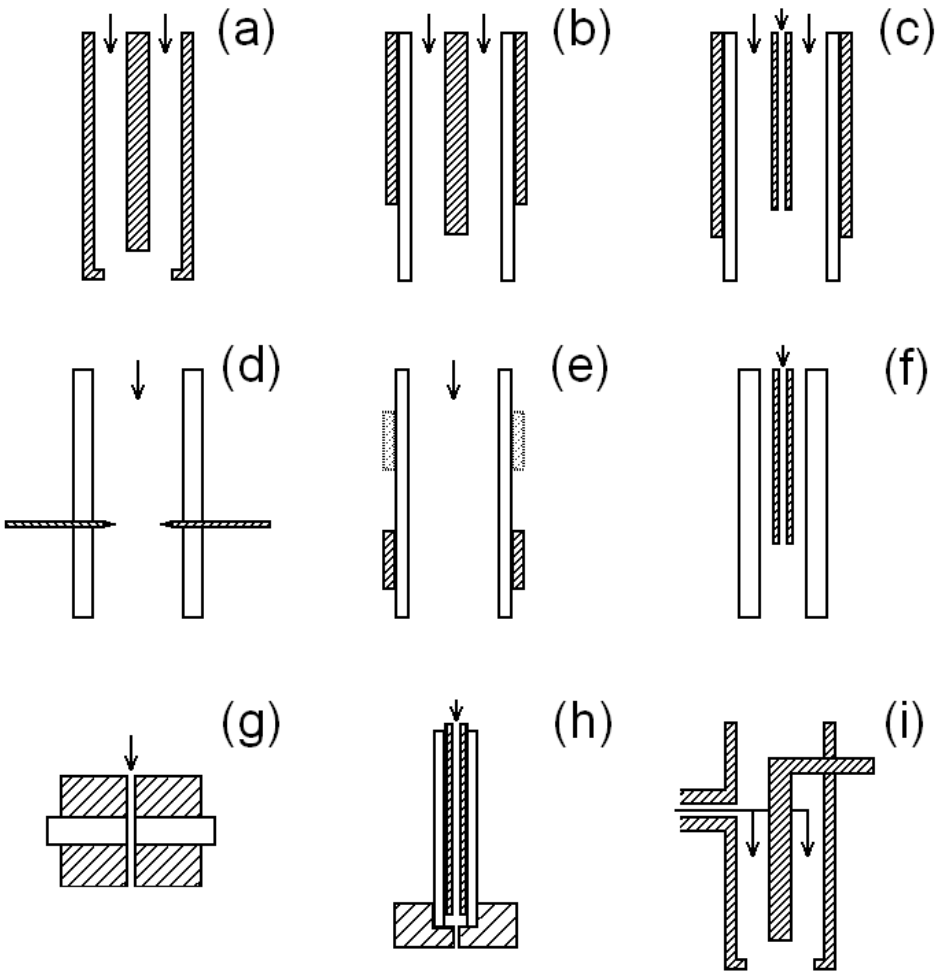

Fig 4-1: Schematics of some atmospheric plasma jets with the shaded regions indicating electrodes and the white region indicating dielectrics. Blocks in light colour in (e) indicate the possibility of a second ring electrode, and arrows indicate the direction of the gas flow.

A variation to type *a* and *b* replaces the solid inner electrode with a capillary electrode through which to feed a second gas flow in addition to the main gas flow through the annular space between the inner and outer electrodes, and it is shown in figure 4-1c[4.57-4.65]. The gas flowing in the capillary channel is usually reactive (e.g. oxygen-containing) whereas that in

the annular channel is often inert. They mix in the space near the capillary nozzle. While type *c* jets are still cross-field devices with their electric field being largely radial in the electrode region, their plasmas tend to be near the tip of the capillary electrode. Type *c* jets offer greater scope of enhancing reaction chemistry and this may allow more reactive species being delivered to a downstream sample. They are useful as an elemental jet for use in an array, and are worth being studied further to bring out their benefits when used in a plasma jet array.

A radically different cross-field configuration is used in type *d* jets as shown in figure 4-1d, where two rod or pin electrodes are brought to be very close to each other so that an intense plasma is struck between them[4.66,4.67]. The two rod electrodes are aligned in the same direction and are perpendicular to the direction of the gas flow which is confined within a dielectric tube structure. The discharge generated between the two rod electrodes is blown by the gas flow to spread into the downstream region. This downstream plasma transfer is accompanied with a horizontal expansion which is perpendicular to the gas flow direction, and this increases the plasma region on a cross-section plane but may dilute the concentrations of reactive species. The effectiveness of type *d* jets for downstream processing is likely to depend on the extent of their horizontal span and the plasma reactivity on the sample surface.

A very different category of atmospheric plasma jets to those in figure 4-1a ~ 4-1d discards the use of a central electrode and employs a gas confinement tube wrapped with one or more ring electrodes as shown in figure 4-1e[4.1,4.3,4.6,4.26,4.68-4.88]. These jets are known as linear-field plasma jets and their denser plasma in the downstream region suggests that they are in general more suited for downstream processing applications. Plasmas produced by type *e* jets tend to spread around the ring electrodes and within the electrode region they are normally weaker than cross-field jets due to

larger inter-electrode distances[4.6]. If electrons in the electrode region can be used as seeds to enhance effectively the jet in the downstream region, cross-field devices may become a stronger electron source than linear-field devices. This possibility will need to be examined and confirmed in future. Most type *e* jets are excited at frequencies from 1 kHz to megahertz. They can also be excited at higher frequencies, when their structure could be modified slightly with the ring electrode extended to form a cylindrical metallic enclosure and the dielectric tubing removed. The modified structure can be excited either inductively[4.68] or by microwave[4.70,4.72,4.89], some of which have been used for bacterial inactivation and wound healing[4.89].

Figure 4-1f shows another linear-field jet configuration, type *f* plasma jets, which employ a metallic capillary both as an electrode and as a gas flow channel[4.27,4.90-4.100]. A concentric dielectric tube is added to enclose and insulate the capillary electrode, and its inner diameter is usually larger than the outer diameter of the capillary. With the downstream sample usually earthed, the electric field is largely in the axial direction and type *f* jets are essentially linear-field plasma devices. They should be compared to type *c* jets which also employ a capillary electrode. However the use of a concentric counter electrode in type *c* jets sets up a predominately radially directed electric field, making them a cross-field device with the drawback of confining the plasma to the electrode region. Therefore despite both employing a capillary electrode, type *c* and type *f* jets support very different plasma jets. The dual use of the capillary as an electrode and the gas channel enables a streamline electrode design with little need to add other components to the outside of the tubing structure. This is useful to minimise unnecessary radial space of a single jet structure and so maximise the total plasma region when used in an atmospheric plasma jet array. It is worth mentioning that plasma sources studied in [4.90,4.92] share some characters with spatially confined plasmas and are therefore not strictly plasma jets. They are not the

most effective for downstream processing, but are considered here for completeness of discussion.

Figure 4-1g shows a simple linear-field configuration of type *g* jets with a hole through a dielectric plate sandwiched between two planar electrodes[4.2,4.101-4.110]. The hole facilitates gas flow, and upon the application of a high voltage across the two electrodes a plasma is struck. The plasma is extended as a plume to the downstream region. Parallelisation of type *g* jets into an array may be achieved by drilling many holes through the electrode sandwich, and the electrode connection is simply via the two plate electrodes. There are a few studies of parallel operation of type *g* jets at atmospheric pressure[4.104]. These studies are at present limited to relatively small number of constituent jets with small overall cross-sectional area.

The above discussion of type *a* ~ *g* jets illustrates how the electric field and the gas flow field may combine to influence the character of a single plasma jet in both the electrode region and the downstream region where processing applications take place. A general conclusion is that the cross-field configuration tends to produce a more intense plasma in the electrode region whereas the linear-field configuration is likely to support a stronger plasma in the downstream region[4.6]. A strong downstream plasma is ultimately the objective for processing applications, whereas an intense plasma in the electrode region could potentially be used as a source of seed electrons and reactive species for the downstream plasma. It is therefore logical to explore the possibility of whether the two distinct configurations could be hybridised to support a strong plasma in both the electrode and downstream regions. There have been interesting attempts in this direction, for example a pitched or tapered terminal to form a small nozzle of reduced diameter in type *a* and *b* jets[4.14,4.18,4.36]. Figure 4-1h shows examples where the inner electrode produces an intense plasma near its tip and the outer electrode is moved downwards towards the downstream region[4.111-4.114]. This enhances the axial

component of the electric field and in turn it elongates the plasma to the downstream region. While type *h* jets are relatively few and under-studied, the strategy of hybridisation is beneficial and should be explored further for their use in plasma jet arrays. It is worth noting that some type *h* jets support striations[4.113], similar to those observed in a long plasma channel formed between a pin and metal plate[4.115,4.116]. Striation is a result of nonlinear interactions in discharges and may be indicative of high plasma densities[4.117]. It is therefore of interest to study if hybrid electrode configurations may produce strong plasma jets.

Of all single jets reported so far, some employ radial channels to facilitate gas flow and electrical connection as illustrated in figure 4-1i. While these may be sensible arrangements for single jets, they are undesirable for use in a jet array because such radial structures increase the non-plasma region on the cross-section plane of the jet array and decrease the jet density.

From the above appraisal of the nine types of atmospheric plasma jets in figure 4-1, we propose to consider hybrid electrode configurations so as to take advantages of both linear-field and cross-field devices. Therefore they form the basis for the work described in the following sections. It is also clear that capillary electrode structures facilitate streamline jet designs with the capillary acting both as an electrode and as the gas inlet channel. In order to further reduce the non-plasma region, it is desirable to minimise heat generation by the plasma jet and hence remove the need for water cooling. To this end, we consider kHz excitation for this study. It is known that high frequency APGDs at megahertz and higher tend to generate more heat than their low-frequency counterparts.

4.3 Experimental setup

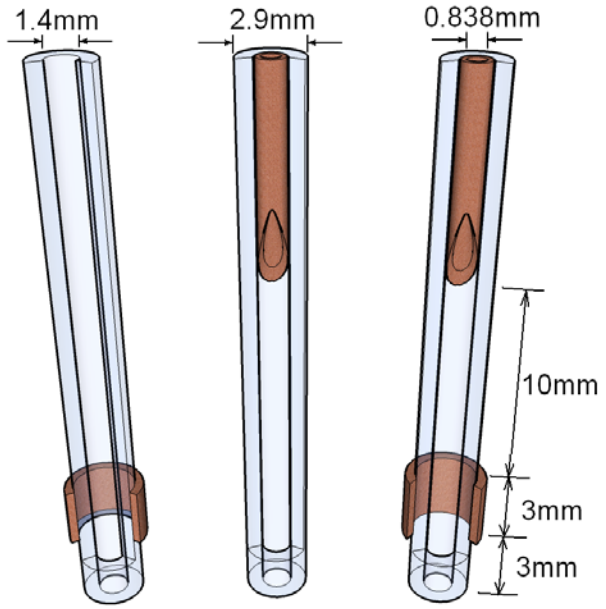

Fig 4-2: Schematics of the ring, the capillary, and the capillary-ring electrode configurations. The capillary and the downstream ring electrodes are in brown, and the dielectric tube is in light colour.

Three different plasma jets are considered here and their half-exposed schematics are shown in figure 4-2. The configuration on the right side of the figure has a hybrid electrode structure consisting of a central capillary electrode enclosed tightly within a concentric dielectric tube and a concentric ring electrode placed downstream away from the capillary. The capillary is recessed within the dielectric tube, and the tube is extended so that the ring electrode with a width of 3 mm can be wrapped around the tube near the tube nozzle. The distance between the ring electrode and the tube nozzle is 3 mm, and the axial distance between the capillary tip and the ring electrode is 10 mm. For ease of reference, it is referred to as the *capillary-ring jet*. To provide an appropriate reference for its characterisation, the capillary-ring jet is compared with two other electrode structures, both employing the same dielectric tube with either the capillary or the ring electrode connected to the power supply. These are essentially single electrode devices and are referred

to the *capillary jet* and the *ring jet*, as shown schematically in the middle and left part of figure 4-2, respectively. For the single electrode devices, the position of their electrodes is the same as that of the capillary-ring jet for a fair comparison.

The capillary electrode is made of stainless steel with its inner and outer diameter being 0.838 mm and 1.27 mm, respectively. The tube is made of quartz glass with an inner diameter of 1.4 mm and an outer diameter of 2.9 mm. Therefore the annular gap between the quartz tube and the capillary is about 65 μm. Helium (99.996%) is used as the carrier gas and it is fed through the capillary electrode at a flow rate between 2 and 4 slm. At 4 slm, the gas flow rate corresponds to a linear gas velocity of 121 m/s and 43 m/s within the capillary and the quartz tube respectively, and the corresponding Reynolds numbers for the above cases are 859.3 and 514.4, both well within the laminar flow range[4.118].

The jets are powered by an AC power supply at a frequency of 30 kHz and an amplitude adjustable up to 5 kV. Voltage is measured by a Tektronix P6015A voltage probe, and current signals are measured by two Pearson 2877 current probe. Both voltage and current signals are recorded by a Tektronix DPO4104 oscilloscope (1 GHz bandwidth and 10 mega-bit sample record length). Unless otherwise stated, plasma images are taken with an Andor DH720 ICCD camera. Spectroscopic signals are measured via an Andor Shamrock SR-303i spectrograph and a fibre which is placed very close to the plasma. The spatial resolution of the optical measurement along the length of the plasma jet is 1.4 mm. Broad spectra are obtained with an Ocean Optics 2000 spectrometer. Absolute emission intensity calibration is performed using an Ocean Optics LS-1-CAL NIST traceable white light source in the 350 ~ 1000 nm range.

4.4 Characterisation of three elemental jets

4.4.1 Free-burning mode

We first consider the three atmospheric plasma jets in their free-burning modes in order to highlight more clearly their relative merits without the complication of jet-substrate interactions. In the free-burning mode, there is no substrate placed in the path of the plasma plume.

For all three jets, the helium carrier gas becomes ionised (above certain applied voltages) and then with further increase in the applied voltage the plasma can be extended from the tube nozzle to form a free-burning plasma plume. The plume is of a purple-like colour. By taking photos for the light-emitting plume, the plume length can be measured.

The plume length is found to increase monotonically with the applied voltage at any given gas flow rate considered. Figure 4-3a shows the plume length of all three plasma jets as a function of the applied voltage at a fixed helium flow rate of 4 slm, whereas figure 4-3b shows the voltage dependence of the capillary-ring jet length at different helium flow rates when the capillary is the powered electrode. The first points of each curve in figure 4-3 correspond to an operation condition shortly after the plasma jet extends out of the quartz tube, whereas their last points indicate the maximum voltage above which the plasma jet becomes unstable. In the case of the ring jet and the capillary jet, the ring electrode or the capillary electrode is connected to the power supply. It is evident from figure 4-3a that above 3 kV the capillary jet has a longer plume length than the ring jet. At 4 kV, the capillary jet length is 20 mm whereas the ring jet length is 16 mm. It is interesting to note that the capillary jet is ignited around 2.5 kV and the ring jet needs about 3 kV for ignition. In other words, the capillary jet is triggered at a lower applied voltage and, once generated, has a longer plume length than the ring jet. This is likely to be due to a greater field enhancement at the tip of the capillary

electrode that sets up a much stronger electric field than that established by the ring electrode. The gradual structural change of the ring electrode discourages a sensitive dependence of its electric field on the applied voltage and results in a weak field enhancement. This makes the ring electrode less effective in terms of triggering plasma ignition. On the other hand, the ring jet is less susceptible to fluctuations in the applied voltage thus helping achieve better reproducibility or reliability of the processing efficacy. Differences in characteristics of the ring jet and the capillary jet therefore match them to requirements of different applications.

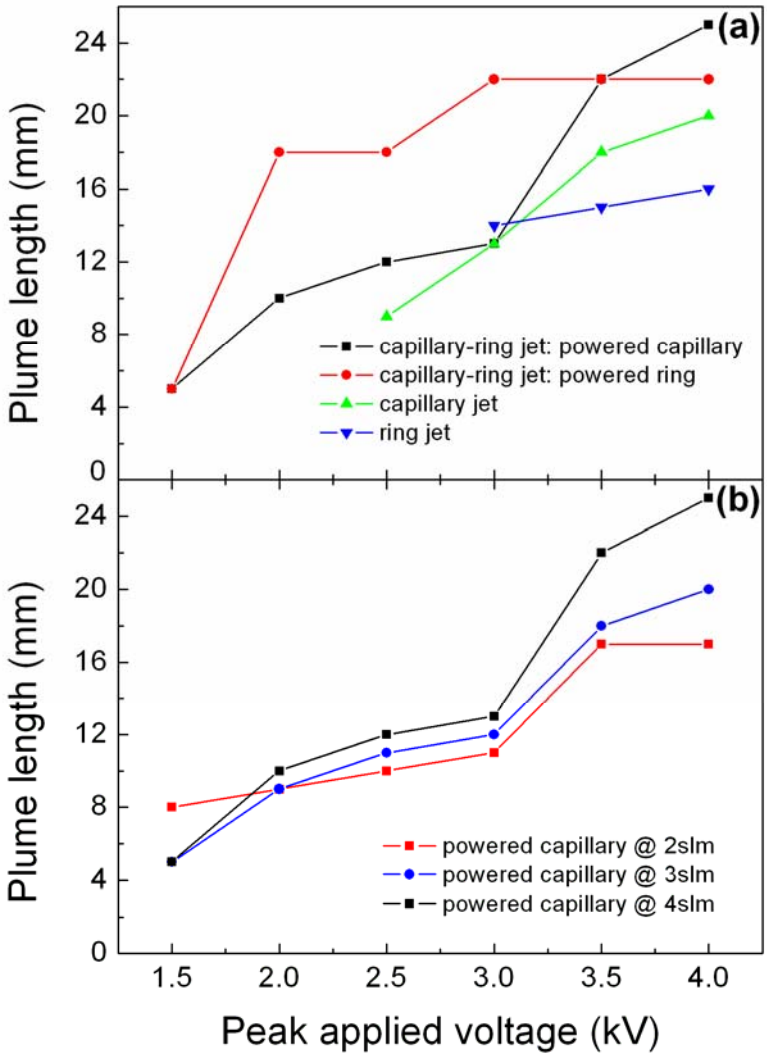

Fig 4-3: Voltage dependence of the plume length of (a) the ring, the capillary and the capillary-ring jets, all with a helium flow rate of 4 slm; and (b) the capillary-ring jet at different helium flow rates. All in their free-burning mode without any downstream substrate.

For the capillary-ring jet, either the capillary or the ring electrode may be powered, and the other electrode is grounded. In both cases, the plasma ignition voltage is seen in figure 4-3a to reduce to below 1.5 kV. This is much lower than those for the ring jet and the capillary jet, suggesting a much elevated local electric field at a given applied voltage. This is largely because the single-electrode cases have a floating ground of an uncertain physical location and its inter-electrode distance is likely to be larger than that of the capillary-ring jet. In general, the capillary-ring jet has a longer jet plume length than the two single-electrode jets at a given applied voltage. Ignition at a lower voltage and a generally longer plume length make capillary-ring jet more attractive than the two single-electrode jets.

To understand its plasma dynamics, the capillary-ring jet is imaged at different values of the applied voltage using the Andor DH720 ICCD camera with an exposure time of 33.3 μs, which is equal to one cycle of the applied voltage. Figure 4-4 shows the case of the powered capillary electrode, from which it is clear that a localised plasma is first initiated near the capillary tip at a peak applied voltage of V_p = 0.85 kV (marked with a red circle). A small increase of the peak applied voltage to 1.0 kV is seen to extend this plasma to the ring electrode, when its strongest emission still remains near the capillary tip. At 1.3 kV, a second strong emission region appears near the ring electrode and there are now two separate regions of strong emission. This second area of strong optical emission could be the signature of a second plasma as it is mainly supported by the ring electrode, and the plasma intensity between the two areas of strong optical emission is weak. However it is also unlikely to have been triggered by the ring electrode alone, because it occurs at V_p = 1.3 kV well above V_p = 1.0 kV when the first plasma reaches the ring electrode. In fact as the applied voltage is increased to 1.0 kV, the first plasma already bridges across the distance between the capillary and the ring electrodes and the electrode sheath may well have formed at each electrode in

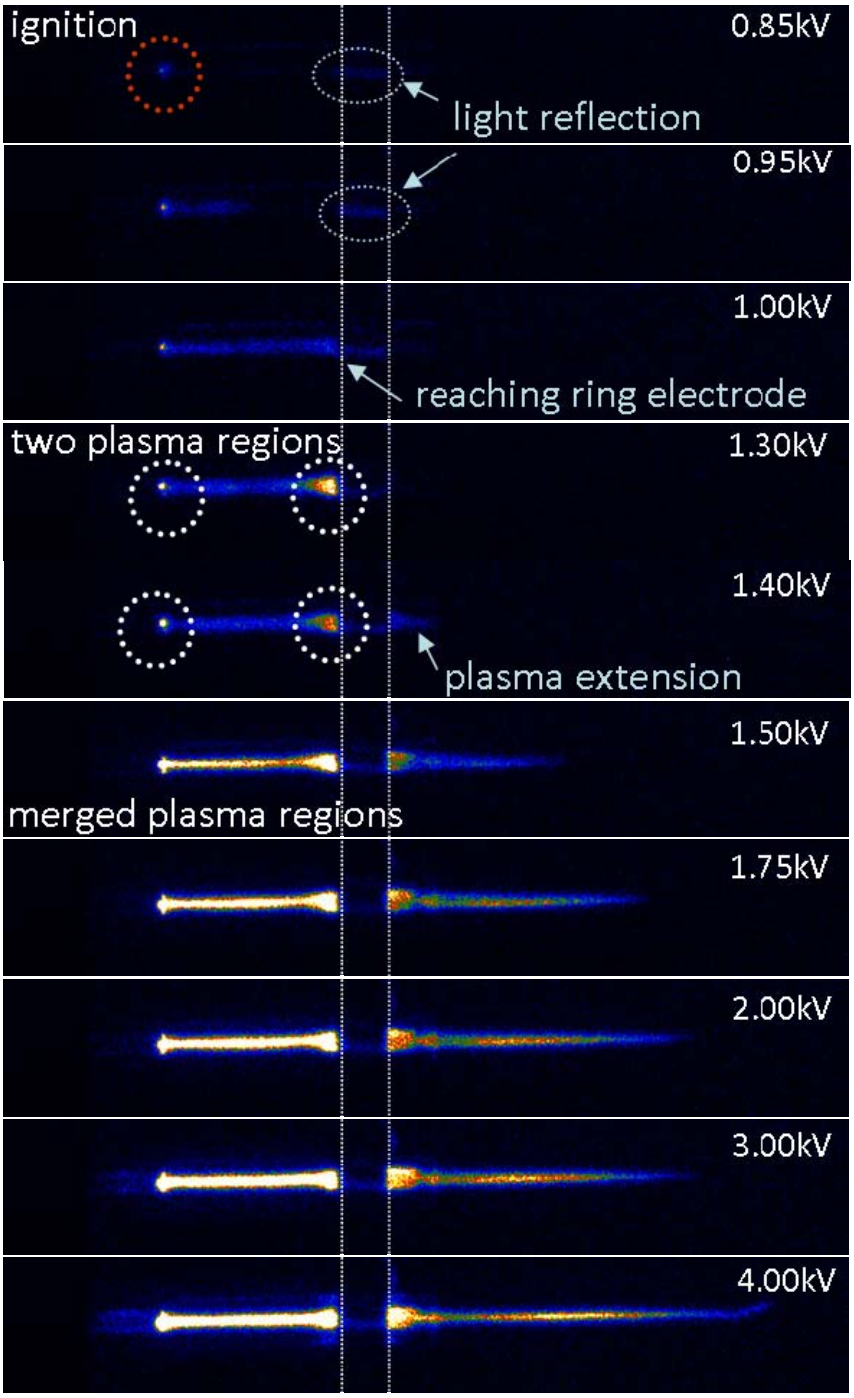

Fig 4-4: Images of the capillary-ring plasma jet in the free-burning mode at a 4 slm helium flow, with the two vertical lines through all images indicating the two boundaries of the ring electrode. The peak applied voltage varies from 0.85 kV when the plasma is ignited at the capillary tip (circled in red), through 1.3 kV, when the ring electrode starts to support a strong second plasma region (circled), and 1.5 kV when the two strong plasma regions merge into one, finally to 4.0 kV after which the plasma plume becomes unstable. The light from the ring electrode when V_p = 0.85 ~ 0.95 kV is the reflection of the plasma light emission near the capillary. Exposure time is 33.3 μs.

alternation[4.119,4.120]. Large electric field in the sheath region near the ring electrode could then trigger the second plasma. In other words, it is likely that the first plasma precipitates the second. It is however clear that the difference in geometric characters of the capillary and the ring electrodes results in a first plasma being ignited near the capillary tip and subsequently the first plasma precipitating a second plasma near the ring electrode.

Figure 4-4 shows that the two plasmas merge together into one around V_p = 1.5 kV, when the merged plasma also extends out of the tube nozzle into the downstream region. Afterwards, as the applied voltage increases, the plasma plume length is seen to be generally proportional to the applied voltage. Figure 4-3b suggests that the helium flow rate affects only slightly the plume length. It is of interest however to note in figure 4-3b that the plume length increases significantly after V_p = 3.0 kV, indicating two distinct operation regimes or modes. Atmospheric plasma jets are recently shown to have three different modes, a chaos-like mode of very low discharge current, a bullet mode where the plasma plume travels in physically discrete clusters on a nanosecond scale, and a continuous mode of high current where the plasma plume is seen to travel in one continuous cluster on a nanosecond scale[4.121]. Nanosecond images of the capillary-ring plasma jet show that the plasma plume is in the bullet mode for $V_p \leq$ 3.0 kV and in the continuous mode for $V_p >$ 3.0 kV, as demonstrated in figure 4-5, in which 10 ns exposure images are taken for V_p = 2.75 kV and V_p = 3.25 kV respectively after plasma plume extends from the nozzle. The time interval of the adjacent images in each case is 0.1 μs. Their intensities are normalised into the same range for comparison. The shapes of the plasma plume are clearly different in these two cases, although the difference of the applied voltages is only 0.5 kV. As the applied voltage increases, the continuous mode is more intense with greater power consumption, and the transition from the bullet to the continuous mode is responsible for the sudden increase in the plume length after V_p = 3.0 kV as

seen in figure 4-3b.

One remaining issue in figure 4-3a is that the plume length of the capillary-ring jet appears to be longer when the ring electrode is powered and when V_p < 3.5 kV. Since the ring electrode is placed closer to the tube nozzle than the capillary electrode, it is easier for the plasma generated near the ring electrode to extend out of the quartz tube. However this length benefit does not support the use of a powered ring electrode, because the capillary-ring jet is seen to be more intense when the capillary electrode is powered (data not shown). When a downstream ground electrode is introduced, the use of the powered capillary electrode is also able to drive more electrons to downstream, and this will be further discussed in section 4.4.2. Therefore for a strong downstream plasma, the above discussion suggests that it is advantageous to use the capillary-ring jet with a powered capillary electrode and a grounded ring electrode.

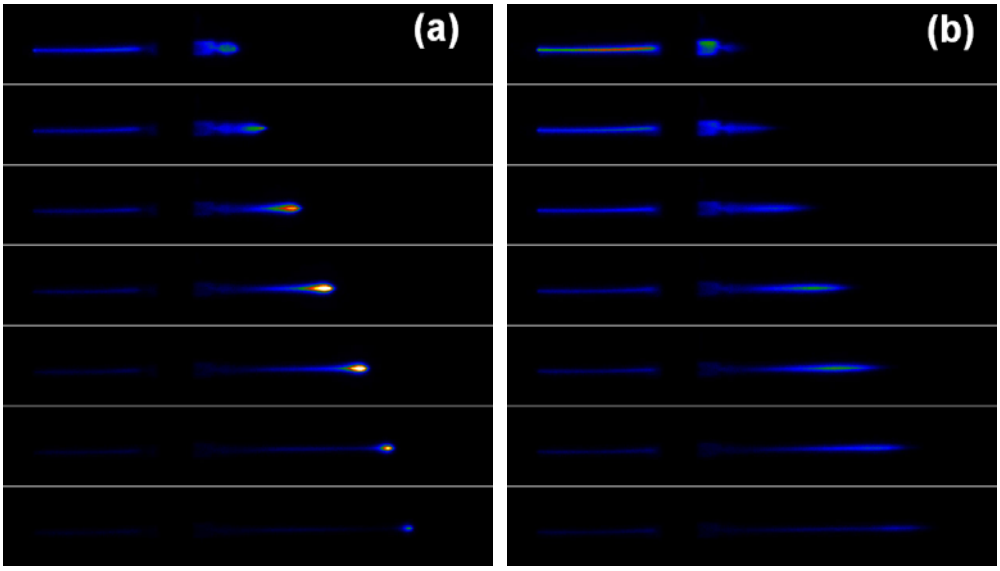

Fig 4-5: Images of the plasma plume extending out of the capillary-ring jet nozzle, in (a) the bullet mode, V_p = 2.75 kV; (b) the continuous mode, V_p = 3.25 kV. The exposure time is 10 ns.

It is worth noting that the plume length with a powered ring electrode remains at about 22 mm in the 3 ~ 4 kV range in figure 4-3a, suggesting a

levelling-off of the mechanism that is responsible for extending the plume length. As the ring electrode has a gradual curvature without any sharp features, its field enhancement is not significant and it supports a spatially spread plasma around itself. This is similar to the relatively insensitive voltage dependence of the ring jet length, as seen in blue in figure 4-3a. It should be noted that for the capillary-ring jet with its capillary electrode powered, the plume length is longer than 22 mm when V_p > 3.5 kV. This is long enough for most processing applications even for objects with considerable 3D surface structures. So in terms of the plume length, the capillary-ring jet with its capillary powered is appropriate for treatment of large 3D objects.

From the above discussion, the capillary-ring jet has been shown to be a better elemental plasma jet than the two single-electrode jets in the free-burning mode. To bring out its best performance, the capillary electrode of the capillary-ring jet should be powered and its ring electrode grounded. This electrode connection remains in the following discussion.

4.4.2 Effects of a downstream ground electrode

With the understanding of the capillary-ring jet in the free-burning mode, it is now important to characterise its behaviours with a downstream ground electrode because in a processing scenario a sample is usually placed downstream and electrically grounded. To this end, a grounded plate electrode is introduced to mimic the processing scenario. Specifically it is placed at 10 mm downstream from the tube nozzle and hence the plasma plume length is fixed to 10 mm. Optical emission intensity at the plume contact point on the downstream electrode is used as an indirect indicator of the processing efficacy, and to make this more generic the wavelength-integrated optical emission from 350 to 1000 nm is considered. To confirm the conclusion of

section 4.4.1 that the capillary-ring jet is the most effective, its comparison with the two single electrode jets is considered here with the same downstream electrode.

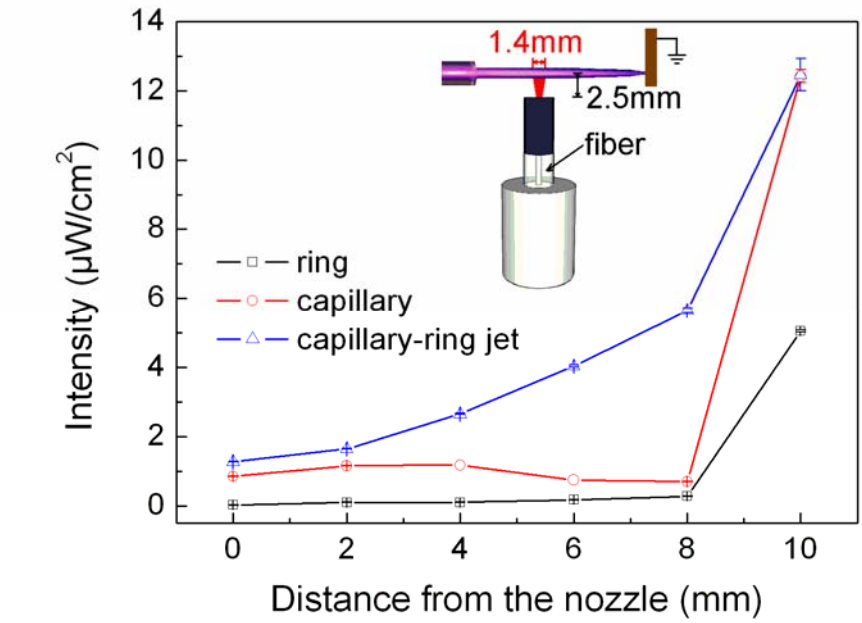

Fig 4-6: Optical emission intensity of the three jets with a downstream ground electrode at 10 mm from the tube nozzle, as a function of the distance from the nozzle. The capillary-ring jet has its capillary electrode powered and its ring electrode grounded. The insert shows a home-made optical scanning device that measures the wavelength-integrated absolute emission intensity (350 ~ 1000 nm) with a spatial resolution of 1.4 mm along the plasma length.

Figure 4-6 shows the wavelength-integrated emission intensity of each of the three plasma jets measured with a home-made scanning device along the length of a plasma plume with a spatial resolution of 1.4 mm. For any point along the length of a plasma plume before its contact point on the downstream electrode, the capillary-ring jet is found to have the greatest optical emission intensity whereas the ring jet has the weakest. This is consistent with the observations in the free-burning mode. On the surface of the downstream ground electrode, all three jets are found to converge to a small spot and the emission intensity of the capillary-ring jet is very similar to

that of the capillary jet. However the overall intensity of the capillary-ring jet is far stronger over the 10 mm length between the tube nozzle and the downstream electrode. This is reflected in its much larger intensity at all points prior to the contact point on the downstream ground electrode. It is therefore clear that the capillary-ring configuration is the most powerful both with a downstream ground electrode and in the free-burning mode.

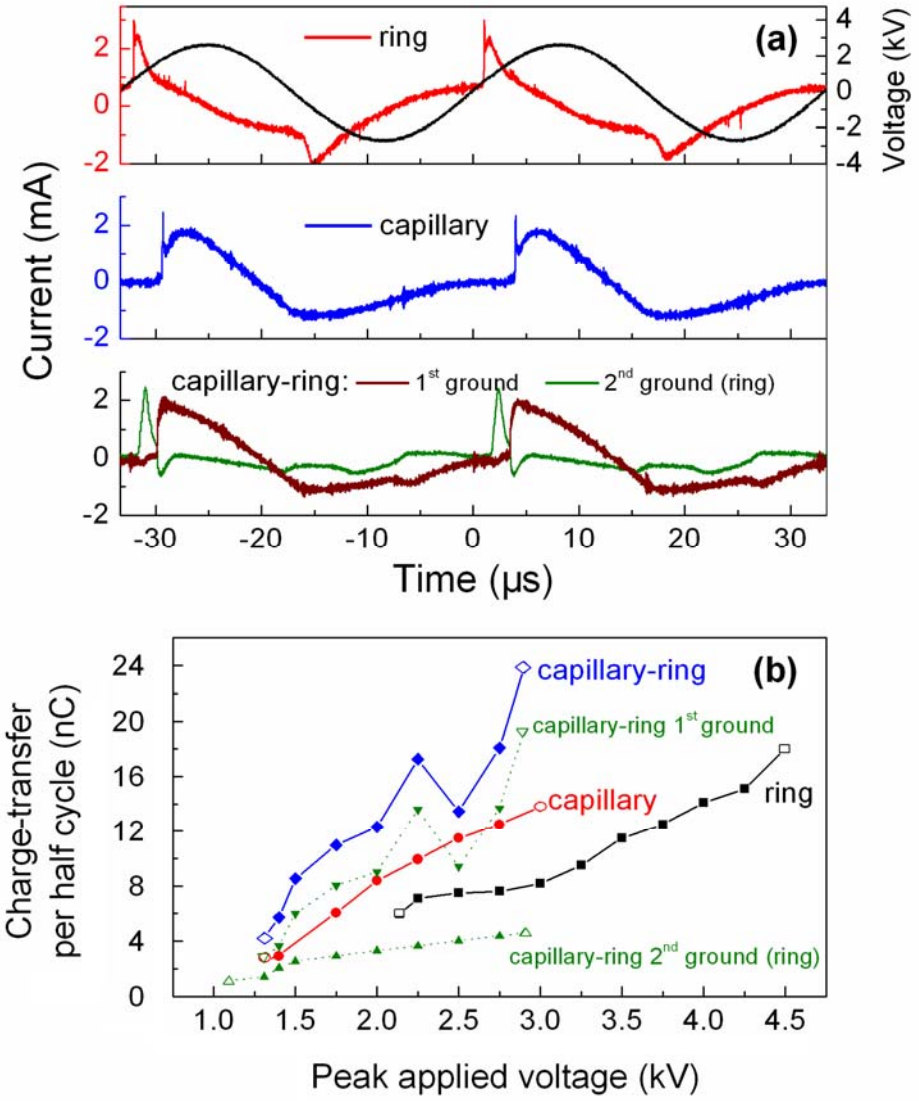

Fig 4-7: (a) Current and voltage waveforms of the three jets with the capillary-ring jet having two currents that flow to its two ground electrodes (e.g. the downstream plate as the first and the ring as the second); (b) charge transfer per half cycle as a function of the applied voltage. All measured at 4 slm.

Figure 4-7a shows the discharge currents of the three jets at an applied voltage of V_p = 2.75 kV. For all three cases, the (main) discharge current is measured between the powered electrode and the downstream ground electrode, whereas for the capillary-ring jet there is a second current flowing to the grounded ring electrode and this is also measured. All three cases have one current pulse every half cycle of the applied voltage, similar to the case of dielectric barrier discharges[4.122] though the capillary plasma jet is not a dielectric barrier discharge (its dielectric tube does not insulate any electrode). For the ring-electrode jet, the discharge current has a large pulse of 3 mA lasting for about 2 μs in the positive half-cycle of the applied voltage, and a smaller negative current pulse of 2 mA lasting for about 3 μs. The positive pulse is spikier than the negative pulse. In the case of the capillary jet, there is a positive current pulse and a negative current pulse. The positive current pulse is preceded by a narrow and sharp spike of 2.2 mA in magnitude, suggesting a very quick discharge event. This rapid discharge event is followed by a more gradual current pulse of 2 mA in magnitude and about 7 μs in duration. Similar to the case of the ring jet case, the negative current pulse of the capillary jet is much more gradual, lasting for one entire half cycle of the applied voltage. With the capillary-ring electrode structure, the main current to the downstream ground electrode is similar to that of the capillary jet case but without the preceding narrow current spike. In other words, it has a large and broad positive current pulse of 2.0 mA and a much smaller negative current pulse expanding over the entire negative half-cycle of the applied voltage. The second current flowing to the grounded ring electrode has a sharp positive pulse of 2.2 mA in magnitude and 2.5 μs in duration, and this is similar to the positive current pulse of the ring jet. However unlike the ring jet, there is not any clear peak in the negative half-cycle of the applied voltage for the capillary-ring jet.

Differences in temporal features of the discharge currents in figure 4-7a

offer no direct indication of the extent of gas discharge in the three plasma jets. To this end, the total charge transfer over one half cycle is estimated by integrating the discharge current for three consecutive cycles of the applied voltage. The results are shown in figure 4-7b. The first point of each curve is the plasma ignition point whereas the last point indicates the onset of unstable plasma. It is clear that the capillary-ring electrode structure facilitates up to 24 nC charge transfer per half cycle at V_p = 2.75 kV. This is larger than 14 nC at V_p = 3.0 kV in the capillary jet case and 18 nC at V_p = 4.5 kV in the ring jet case, suggesting that the capillary-ring jet is more efficient in producing electrons at a lower applied voltage. Most charges, e.g. 20 nC out of 24 nC (or 83%), are carried via the downstream ground electrode, and the remaining 4 nC is passed via the grounded ring electrode. This suggests that effects of the downstream ground electrode are much greater on plasma dynamics than the ring electrode. The larger charge transfer achieved with the capillary-ring jet confirms that it is capable of producing the highest electron density of the three plasma jets considered. To provide a ball-park estimate, we consider the plasma length as 26 mm from the capillary tip to the downstream electrode and approximate its averaged diameter as 1.4 mm to obtain a plasma volume of 0.04 cm^3. With a total of 24 nC charges or $1.5x10^{11}$ electrons, a simple estimate of the space and time averaged electron density is found to be $3.7x10^{12}$ cm^{-3}. This is not unreasonable for atmospheric plasma jets at kilohertz frequencies. It is useful to compare this to the case of the capillary-ring jet with a powered ring electrode and a grounded capillary electrode. At V_p = 2.75 kV, the averaged charges transferred per half-cycle of the latter case are found to be 5.1 nC and 3.6 nC from the powered ring electrode to the downstream ground electrode and the grounded capillary electrode, respectively. Therefore the charge transfer to the downstream electrode is 59% of the total, lower than the more efficient 83% of the downstream charge transfer when the capillary electrode is powered. More

importantly, the powered ring electrode case has a much lower total charge transfer of 8.7 nC than 24 nC of the powered capillary electrode case. This corresponds to a fraction of 36% and represents a much less efficient production of the discharge plasma when the ring electrode is powered.

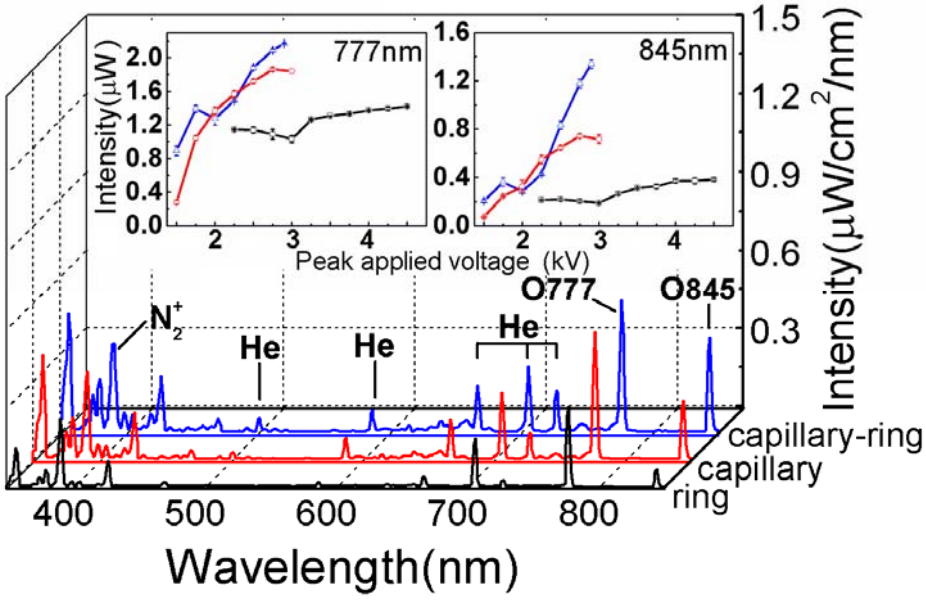

Fig 4-8: Absolute optical emission spectra of the three jets at V_p = 2.75 kV, and the insets indicate the intensities of two excited atomic oxygen lines at 777 and 845 nm. The ring, the capillary, and the capillary-ring jets are marked in black, red and blue, respectively. All measured at the contact point on a downstream ground electrode and at a helium flow rate of 4 slm.

For processing applications, the most relevant issue is the amount of reactive plasma species delivered to the sample and in our case to the downstream electrode. To this end, the optical emission spectra are measured for the plasma contact point on the surface of the downstream electrode and are shown in figure 4-8 for the case of V_p = 2.75 kV. The overall spectrum is very similar for all three jets with strong helium, oxygen and nitrogen lines, with oxygen and nitrogen lines originating from the mixing of the plasma jet plume with the ambient air. For inactivation of bacteria and biomolecules, oxygen atoms have been known to be important[4.41,4.76]. To this end, emission

intensities at the excited atomic oxygen lines of 777 and 845 nm (related to the 3P and 5P states of the oxygen atom, respectively) are plotted in the inserts of figure 4-8 as a function of the applied voltage. These voltage dependences are similar to the voltage dependences of the charge transfer in figure 4-7, suggesting that the production of excited oxygen atoms follows that of the electron concentration approximately. They also confirm that of the three jets considered the capillary-ring jet produces the largest amount of excited oxygen atoms at the lowest applied voltage.

4.4.3 Effects of a downstream dielectric substrate

In this section we will study the impact of a floating dielectric substrate on the behaviours of the plasma jets, because dielectric materials are also commonly used in many processing applications. With a dielectric substrate, one important issue is the plasma cross-sectional impact area on the surface of the downstream dielectric substrate with respect to that of the physical electrode structure. To this end, a glass plate is used as the downstream substrate to allow for optical access to the plasma impact on the surface of the downstream dielectric substrate. This plate is electrically floating and it represents dielectric materials used in many processing applications. At a helium flow rate of 4 slm and an applied voltage of V_p = 3.0 kV, the end-view images of all three jets are taken with an exposure time of 33.3 μs (equivalent to one cycle of the applied voltage) and are shown in figure 4-9. In the left column, the images are wavelength-integrated for the 300 ~ 1000 nm range. The capillary-ring jet is shown to have a light-emitting spot of 4.1 mm in diameter whereas the capillary and the ring jets have a similarly sized light emitting spot with a diameter of 2.3 ~ 2.4 mm. It is worth recalling that the inner diameter of the quartz tube is 1.4 mm, giving a plasma expansion ratio of 4.1mm/1.4mm = 2.9 for the capillary-ring jet. Bandpass-filtered end-view images are also taken. These filters have 10 nm bandpass and their central

wavelengths are 710 nm, 780 nm and 840 nm, so the images take the light emission around 706 nm from excited helium atoms and around 777 nm and 845 nm from excited oxygen atoms. For each column of wavelength-filtered images, the capillary-ring jet clearly has a bigger light-emitting spot on the substrate surface than the capillary and ring jets. This combines the wavelength-integrated result to confirm that the capillary-ring jet has the greatest area impact on a cross-sectional plane including the surface of the downstream dielectric.

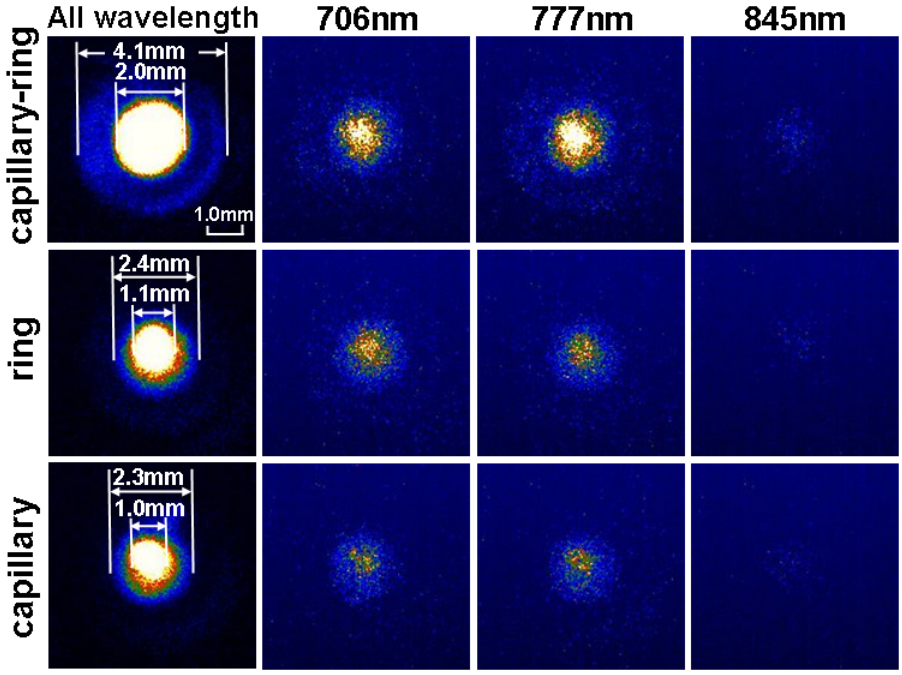

Fig 4-9: End view of the three plasma jets at V_p = 3 kV with the first column being wavelength-integrated and the remaining three columns being wavelength-filtered for 706 nm, 777 nm and 845 nm. Exposure time is 33.3 μs, equivalent to one cycle of the applied voltage at 30 kHz.

The end-view images taken in figure 4-9 have an exposure time of one voltage cycle, so it is inevitable that the images have contributions from plasma emission from the instant of its generation within the electrode region to the instant of its arrival at the downstream dielectric plate. While a sample placed on the downstream substrate receives all photons emitted by the plasma no matter where they are produced, the reactive chemical species it

collects are likely to be produced closer to the downstream substrate because of their short half-lives and because of additional reaction chemistry being introduced from the downstream ambience. To this end, it is useful to separate the optical emission produced when the plasma reaches the downstream substrate from that produced at any other times. Figure 4-10 shows a sequence of 10 ns-exposed single shot images taken from both the side view and the end view for the capillary-ring jet working at positive half cycle of V_p = 1.5 kV and 3.0 kV. Instants in μs indicated in the end view images are relative to the instant at which the first plasma starts to depart from the capillary tip. At V_p = 1.5 kV, the plasma reaches the downstream electrode at about 4.5 μs and at this point the plasma diameter is much smaller than the largest image found at 2.4 μs. The ratio of diameters in these two instants is

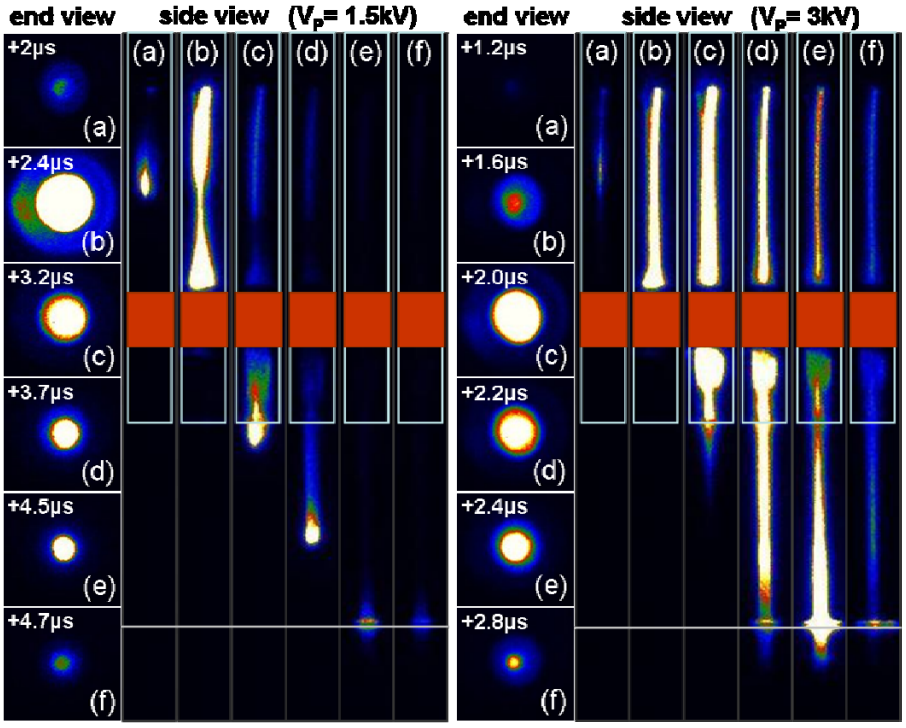

Fig 4-10: Nanosecond images of a single capillary-ring jet at V_p = 1.5 kV (left) and 3.0 kV (right), with an exposure time of 10 ns and t = 0 μs set to the instant when the plasma starts to depart from the capillary tip. Images are taken over a time scale comparable to the current pulse or above, 1 ~ 3 μs in these cases. The diameter of the plasma impact on the substrate is that of 4.5 μs and 2.2 μs for V_p = 1.5 kV and 3.0 kV respectively, smaller than those estimated from time-accumulated images in figure 4-9.

about 2.6. This becomes smaller at 1.2 in the case of V_p = 3.0 kV for which the plasma diameter is the largest at 2.0 μs and the plasma reaches the downstream electrode at 2.2 μs. Larger applied voltages appear to suppress radial expansion of the plasma and accelerate axial plasma propagation. In reality, plasma species produced near the ring electrode may still reach the sample. Therefore the actual diameter of the cross-sectional area containing many reactive plasma species may fall between the diameter of the time-accumulated optical emission in figure 4-9 and the diameter of the time-resolved optical emission in figure 4-10.

It is important to comment that reactive plasma species undergo radial diffusion and as such the spatial range of the impact of reaction chemistry may be larger than the diameter of the time-accumulated optical emission in figure 4-9. To test whether this is true, an *E. coli* bacterial inactivation experiment is carried out. *E. coli* type 1 cells are deposited on agar plates in petri dishes of 5 cm in diameter, with an initial cell concentration of 10^7 colony-forming unit (CFU) or 5.1×10^5 CFU/cm^2. The petri dishes are held on a metallic ground plate and each of the three elemental jets is held perpendicularly to an agar plate plane with a nozzle-to-surface distance of 10 mm. The peak applied voltage is 3 kV at 30 kHz, and the helium flow rate is 4 slm. Temperature of the plasma contact area is measured by burying temperature strip underneath the agar plate. Under the operating conditions considered, all temperatures at the contact points are below 45 ^{o}C during 5 minutes of plasma treatment. Control experiments are performed in ambient air, in a helium flow, and on a hot plate at 45 ^{o}C, all for 5 minutes without plasma. These are found to have little bactericidal effect. Results of *E. coli* inactivation by the three elemental jets are shown in figure 4-11, all for 5 minutes' treatment. The inactivation by the ring jet appears to be the weakest among the three jets, leaving clear underkill parts around the plasma contact point. By contrast, the result from the capillary jet has shown a clear circle on

the agar plate within which no *E. coli* colonies have survived after the treatment. The diameter of the *E. coli* inactivation zone is found to be 8 mm, and this may be used to establish the extent of the radial reach of reactive plasma species. The capillary-ring jet has a bigger reaction chemistry impact than the capillary jet. The diameter of the former is 11 mm, around 40% bigger than the latter. It should be noted that at the edge of this 11 mm diameter circle, there are some places showing inadequate inactivation. However its central part which shows clear inactivation is almost as large as the one achieved by the capillary jet, suggesting that the capillary-ring jet is most effective among the three jets for *E. coli* inactivation. The results also confirm that reactive plasma species undergo considerable radial diffusion around the plasma contact point and the spatial range of the impact of reaction chemistry is much larger than the diameter of the wavelength-integrated optical emission in figure 4-9.

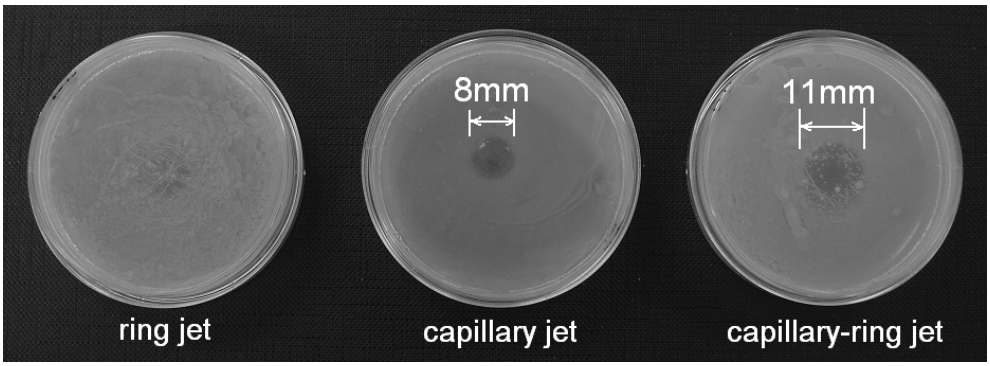

Fig 4-11: Plasma treatment of *E. coli* type 1 cells on agar plates in petri dishes for 5 minutes. For all cases, the initial *E. coli* cell density is 5.1×10^5 CFU/cm^2, V_p = 3 kV and the helium flow rate is 4 slm.

4.4.4 Absolute measurement of plasma species

Reactive species such as atomic oxygen and ozone are believed to be very important for biomedical applications of low-temperature atmospheric plasmas. From the OES results and the wavelength-filtered images discussed in the previous sections, the plasma jet is shown to produce abundant reactive

species such as atomic oxygen. However these results are qualitative rather than quantitative. Indeed, it is important to measure reactive species quantitatively for atmospheric pressure plasmas so that different plasma sources can be compared to contrast out their difference and suggest their optimisation. This task is however challenging given the complexity of laser-based plasma diagnostics. Here we consider mass spectrometry.

The experiment was carried out in Ruhr-Universität Bochum, Germany, using the three-stage differential pumping mass spectrometer system of figure 2-6. This mass spectrometer system had been used to measure a RF plasma jet, and its atomic oxygen and ozone densities measured by the system are found to be the same with that measured by TALIF[4.123].

In this experiment, a capillary-ring jet is fed with 4 slm helium and 40 sccm oxygen, and is placed vertically to the sampling orifice of the mass spectrometer. The diameter of the orifice is 100 μm. The nozzle-to-orifice distance is changed from 4 mm to 24 mm with a step of 2 mm and in each distance mass signal of atomic oxygen, ozone, oxygen and helium are detected. The applied voltage is fixed to 3.75 kV all the time no matter whether the plasma plume contacts the orifice.

Figure 4-12 shows the atomic oxygen and the ozone density as a function of nozzle-to-orifice distance. With the distance increasing from 4 mm to 24 mm, the density of both atomic oxygen and ozone undergoes an increase first and then a decrease. At 4 mm, the shortest nozzle-to-orifice distance, the atomic oxygen density is around 2.7×10^{14} cm^{-3}. Its peak density is around 4.5×10^{14} cm^{-3} when the nozzle-to-orifice distance is in the range of 10 mm to 14 mm. When the distance is bigger than 16 mm, the atomic oxygen tends to decay quickly at the orifice and its intensity is beyond detection limit at the distance of more than 20 mm.

With the nozzle-to-orifice distance increasing from 4 mm to 24 mm, the ozone density undergoes a relatively gradual increase from 4 mm to 10 mm

and a more rapid increase from 10 mm to 18 mm. The maximum ozone density is around $1.2x10^{15}$ cm^{-3} at 18 mm, and then it decreases to $9.0x10^{14}$ cm^{-3} at 24 mm.

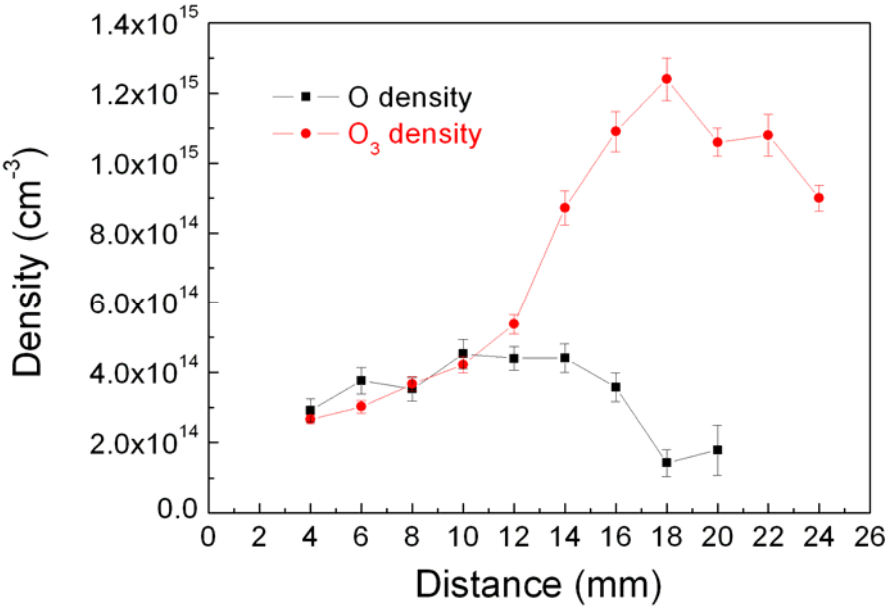

Fig 4-12: Atomic oxygen and ozone density as a function of the nozzle-to-orifice distance for a capillary-ring jet working at V_p = 3.75 kV.

Figure 4-13 shows signal intensities of helium and oxygen measured at the orifice as a function of the nozzle-to-orifice distance. It is clear that within 10 mm, both helium and oxygen intensities stay consistent, indicating that the flow field set up by the gas flow can prevent the ambient atmosphere from mixing into the plasma plume when nozzle-to-orifice distance is less than 10 mm. With the nozzle-to-orifice distance increasing from 10 mm, less helium and more oxygen are detected. This means with increasing distance, more and more oxygen from the atmosphere is able to mix into the plasma plume. It should be noted in figure 4-12 that the maximum atomic oxygen and ozone densities are detected at different nozzle-to-orifice distances, i.e. 10 mm and 18 mm respectively. Maximum ozone density happens at 8 mm distance longer then maximum atomic oxygen does. This is possibly because atomic

oxygen recombines with an increasing admixed oxygen to produce ozone ($O+O_2 \rightarrow O_3$).

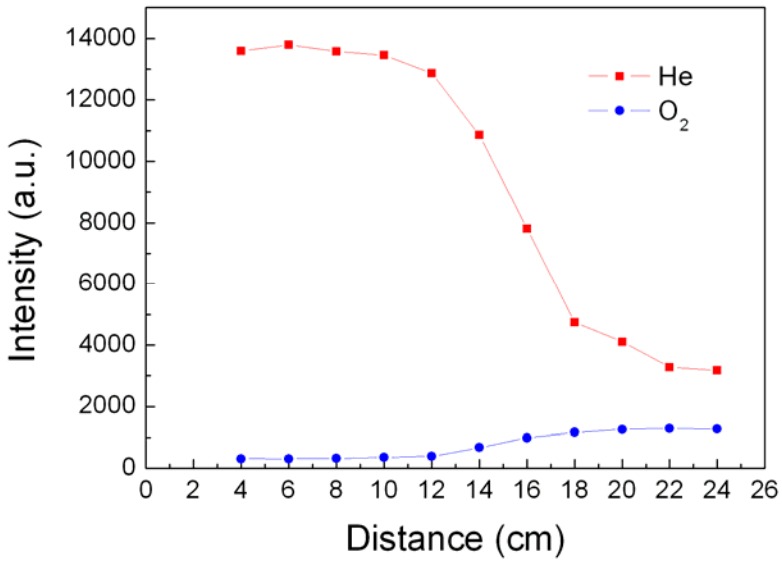

Fig 4-13: Helium and oxygen signal intensity as a function of nozzle-to-orifice distance for a capillary-ring jet working at V_p = 3.75 kV.

4.5 Summary

In this chapter a brief review on existing APGD plasma jets is first given. These jets are classified into nine categories based on their electrode structures, and then discussed in details on whether APGD jets in each category is suitable for being used in subsequent parallelisation to form plasma jet arrays.

The assessment identifies three elemental jets, namely the capillary jet, the ring jet and the capillary-ring jet, for detailed comparison. In the free-burning mode, the capillary-ring jet is found to have a longer plasma plume than the capillary jet and the ring jet. This is because the hybrid electrode configuration of the capillary-ring jet can produce a larger elevated local electric field for initiating ionisation and sustaining the resulting gas discharge. New dynamic features are uncovered in the case of the capillary-ring jet. Specifically the initial phase of its gas breakdown involves

two spatially separated plasmas. With the increase of the applied voltage, the two plasmas originally localised near the two electrodes merge into one intense plasma column. The onset of this strong plasma coincides to the formation of a plasma plume outside of the jet nozzle. It is also shown that the plasma plume is in the bullet mode when the applied voltage $V_p < 3$ kV and in the continuous mode when $V_p > 3$ kV. The transition from the bullet mode to the continuous mode also results in a significant increase in the plume length. For the capillary-ring jet, it is desirable to power the capillary electrode and ground the ring electrode for a stronger downstream plasma.

To mimic the processing of conductive materials, a downstream ground electrode is introduced at 10 mm away from the tube nozzle. The capillary-ring jet is found to produce the greatest optical emission intensity along the length of the plasma plume till the contact point on the electrode. Both charge transfers estimated and emission intensities of excited oxygen atoms demonstrate that the capillary-ring jet is able to produce the strongest plasma among the three plasma jets. The space and time averaged electron density is found to be 3.7×10^{12} cm^{-3} for the capillary-ring jet at $V_p = 2.75$ kV.

To mimic plasma treatment of dielectric materials, a glass substrate is introduced in the path of the jet plume. End-view images are used to demonstrate that the capillary-ring jet has the biggest light-emitting spot on the substrate. *E. coli* inactivation experiment confirms that reactive plasma species undergo considerate radial diffusion when they reach the dielectric substrate. The capillary-ring jet is most effective for bacterial inactivation among the three plasma jets. The diameter of its *E. coli* inactivation spot is found to be 11 mm, much larger than the diameter of its light-emitting spot.

Finally the results for an absolute density measurement of atomic oxygen and ozone produced by the capillary-ring jet are presented using MS. With the jet's operating parameters fixed but the nozzle-to-orifice distance changed from 4 mm to 24 mm, both the atomic oxygen and ozone density are

found to have a peak value. The peak atomic oxygen density is found to be $4.5x10^{14}$ cm^{-3} at 10 ~ 14 mm while the peak ozone density is $1.2x10^{15}$ cm^{-3} at 18 mm. When the nozzle-to-orifice distance is less than 10 mm, the ambient air cannot mix into the plasma plume under the experiment's conditions. The oxygen admixture from the ambient air could react with atomic oxygen to form ozone when the nozzle-to-orifice distance is larger than 10 mm.

From the standpoint of the plume length, the electron density, the emission intensities of oxygen atoms, and the radial reach of the plasma impact on different samples, the hybrid capillary-ring electrode configuration is the most appropriate structure for use in future parallelisation. It represents an excellent candidate for being used in a spatially expended atmospheric plasma array.

References

[4.1] J. L. Walsh, J. J. Shi and M. G. Kong, Appl. Phys. Lett. 88, 171501 (2006).

[4.2] M. Laroussi and X. Lu, Appl. Phys. Lett. 87, 113902 (2005).

[4.3] X. T. Deng, J. J. Shi, H. L. Chen and M. G. Kong, Appl. Phys. Lett. 90, 013903 (2007).

[4.4] H. W. Lee, G. J. Kim, J. M. Kim, J. K. Park, J. K. Lee and G. C. Kim, J. Endod. 35, 587 (2009).

[4.5] H. Koinuma, H. Ohkubo, T. Hashimoto, K. Inomata, T. Shiraishi, A. Miyanaga and S. Hayashi, Appl. Phys. Lett. 60, 816 (1992).

[4.6] J. L. Walsh and M. G. Kong, Appl. Phys. Lett. 93, 111501 (2008).

[4.7] A. Schutze, J. Y. Jeong, S. E. Babayan, J. Park, G. S. Selwyn and R. F. Hicks, IEEE Trans. Plasma Sci. 26, 1685 (1998).

[4.8] S. P. Kuo, E. Koretzky and L. Orlick, IEEE Trans. Plasma Sci. 27, 752 (1999).

[4.9] S. E. Babayan, J. Y. Jeong, A. Schutze, V. J. Tu, M. Moravej, G. S. Selwyn and R. F. Hicks, Plasma Sources Sci. Technol. 10, 573 (2001).

[4.10] G. S. Selwyn, H. W. Herrmann, J. Park and I. Henins, Contrib. Plasma Phys. 41, 610 (2001).

[4.11] E. Stoffels, A. J. Flikweert, W. W. Stoffels and G. M. W. Kroesen, Plasma Sources Sci. Technol. 11, 383 (2002).

[4.12] A. Broc, S. De Benedictis and G. Dilecce, Plasma Sources Sci. Technol. 13, 504 (2004).

[4.13] W. C. Zhu, B. R. Wang, Z. X. Yao and Y. K. Pu, J. Phys. D-Appl. Phys. 38, 1396 (2005).

[4.14] Y. H. Choi, J. H. Kim, K. H. Paek, W. T. Ju and Y. S. Hwang, Surf Coat Technol 193, 319 (2005).

[4.15] K. Niemi, V. Schulz-von der Gathen and H. F. Dobele, Plasma Sources Sci. Technol. 14, 375 (2005).

[4.16] Y. Kim, J. Park, L. A. Rosocha, H. L. Teslow and H. W. Herrmann, Appl. Phys. Lett. 87, 011502 (2005).

[4.17] S. Z. Li, J. G. Kang and H. S. Uhm, Phys Plasmas 12, 093504 (2005).

[4.18] D. Dudek, N. Bibinov, J. Engemann and P. Awakowicz, J. Phys. D-Appl. Phys. 40, 7367 (2007).

[4.19] V. Schulz-von der Gathen, L. Schaper, N. Knake, S. Reuter, K. Niemi, T. Gans and J. Winter, J. Phys. D-Appl. Phys. 41, 194004 (2008).

[4.20] S. G. Wang and J. Wan, IEEE Trans. Plasma Sci. 37, 551 (2009).

[4.21] X. Li, X. M. Tao and Y. X. Yin, IEEE Trans. Plasma Sci. 37, 759 (2009).

[4.22] P. Koulik, S. Begounov and S. Goloviatinskii, Plasma Chem. Plasma Process. 19, 311 (1999).

[4.23] J. Toshifuji, T. Katsumata, H. Takikawa, T. Sakakibara and I. Shimizu, Surf Coat Technol 171, 302 (2003).

[4.24] M. H. Guerra-Mutis, C. V. Pelaez and R. Cabanzo, Plasma Sources Sci. Technol. 12, 165 (2003).

[4.25] I. E. Kieft, E. P. van der Laan and E. Stoffels, New J. Phys. 6, 149 (2004).

[4.26] R. Foest, E. Kindel, A. Ohl, M. Stieber and K. D. Weltmann, Plasma Phys. Controlled Fusion 47, B525 (2005).

[4.27] K. Becker, A. Koutsospyros, S. M. Yin, C. Christodoulatos, N. Abramzon, J. C. Joaquin and G. Brelles-Marino, Plasma Phys. Controlled Fusion 47, B513 (2005).

[4.28] X. T. Deng, J. J. Shi, G. Shama and M. G. Kong, Appl. Phys. Lett. 87, 153901 (2005).

[4.29] S. Forster, C. Mohr and W. Viol, Surf Coat Technol 200, 827 (2005).

[4.30] Q. Chen, Y. F. Zhang, E. Han and Y. J. Ge, Plasma Sources Sci. Technol. 14, 670 (2005).

[4.31] A. Kuwabara, S. Kuroda and H. Kubota, Plasma Process. Polym. 2, 305 (2005).

[4.32] L. Xu, P. Liu, R. J. Zhan, X. H. Wen, L. L. Ding and M. Nagatsu, Thin Solid Films 506, 400 (2006).

[4.33] J. L. Zhang, H. Sun, D. Z. Wang and X. G. Wang, Thin Solid Films 506, 404 (2006).

[4.34] Y. Suga and H. Sekiguchi, Thin Solid Films 506, 427 (2006).

[4.35] X. T. Deng, J. J. Shi and M. G. Kong, IEEE Trans. Plasma Sci. 34, 1310 (2006).

[4.36] E. Panousis, F. Clement, J-F Loiseau, N. Spyrou, B. Held, M. Thomachot and L. Marlin, Plasma Sources Sci. Technol. 15, 828 (2006).

[4.37] J. Goree, B. Liu and D. Drake, J. Phys. D-Appl. Phys. 39, 3479 (2006).

[4.38] H. Yu, S. Perni, J. J. Shi, D. Z. Wang, M. G. Kong and G. Shama, J. Appl. Microbiol. 101, 1323 (2006).

[4.39] S. Shakir, S. Mynampati, B. Pashaie and S. K. Dhali, J. Appl. Phys. 99, 073303 (2006).

[4.40] W. J. Liu, Y. C. Lan, Y. C. Chen, W. C. Lo and C. H. Lin, Surf Coat Technol 201, 6530 (2007).

[4.41] S. Perni, G. Shama, J. L. Hobman, P. A. Lund, C. J. Kershaw, G. A. Hidalgo-Arroyo, C. W. Penn, X. T. Deng, J. L. Walsh and M. G. Kong, Appl. Phys. Lett. 90, 073902 (2007).

[4.42] D. B. Kim, J. K. Rhee, B. Gweon, S. Y. Moon and W. Choe, Appl. Phys. Lett. 91, 151502 (2007).

[4.43] H. Nishiyama, H. Takana, S. Niikura, H. Shimizu, D. Furukawa, T. Nakajima, K. Katagiri and Y. Nakano, IEEE Trans. Plasma Sci. 36, 1328 (2008).

[4.44] G. M. Xu, Y. Ma and G. J. Zhang, IEEE Trans. Plasma Sci. 36, 1352 (2008).

[4.45] T. L. Ni, F. Ding, X. D. Zhu, X. H. Wen and H. Y. Zhou, Appl. Phys. Lett. 92, 241503 (2008).

[4.46] Y. Noma, J. H. Choi, T. Tomai and K. Terashima, Appl. Phys. Lett. 93, 101503 (2008).

[4.47] X. P. Lu, Z. H. Jiang, Q. Xiong, Z. Y. Tang and Y. Pan, Appl. Phys. Lett. 92, 151504 (2008).

[4.48] A. Shashurin, M. Keidar, S. Bronnikov, R. A. Jurjus and M. A. Stepp, Appl. Phys. Lett. 93, 181501 (2008).

[4.49] G. L. Chen, S. H. Chen, W. X. Chen and S. Z. Yang, Surf Coat Technol 202, 4741 (2008).

[4.50] A. V. Pipa, T. Bindemann, R. Foest, E. Kindel, J. Roepcke and K-D Weltmann, J. Phys. D-Appl. Phys. 41, 194011 (2008).

[4.51] K-D Weltmann, R. Brandenburg, T. von Woedtke, J. Ehlbeck, R. Foest, M. Stieber and E. Kindel, J. Phys. D-Appl. Phys. 41, 194008 (2008).

[4.52] X. P. Lu, T. Ye, Y. G. Cao, Z. Y. Sun, Q. Xiong, Z. Y. Tang, Z. L. Xiong, J. Hu, Z. H. Jiang and Y. Pan, J. Appl. Phys. 104, 053309 (2008).

[4.53] S. J. Kim, T. H. Chung, S. H. Bae and S. H. Leem, Appl. Phys. Lett. 94, 141502 (2009).

[4.54] R. Brandenburg, H. Lange, T. von Woedtke, M. Stieber, E. Kindel, J. Ehlbeck and K-D Weltmann, IEEE Trans. Plasma Sci. 37, 877 (2009).

[4.55] H Lange, R Foest, J Schaefer and K-D Weltmann, IEEE Trans. Plasma Sci. 37, 859 (2009).

[4.56] Q. Xiong, X. Lu, J. Liu, Y. Xian, Z. Xiong, F. Zou, C. Zou, W. Gong, J. Hu, K. Chen, X. Pei, Z. Jiang and Y. Pan, J. Appl. Phys. 106, 083302 (2009).

[4.57] V. Leveille and S. Coulombe, Plasma Sources Sci. Technol. 14, 467 (2005).

[4.58] C. Cheng, L. Y. Zhang and R. J. Zhan, Surf Coat Technol 200, 6659 (2006).

[4.59] S. P. Kuo, D. Bivolaru, S. Williams and C. D. Carter, Plasma Sources Sci. Technol. 15, 266 (2006).

[4.60] J. Benedikt, K. Focke, A. Yanguas-Gil and A. von Keudell, Appl. Phys. Lett. 89, 251504 (2006).

[4.61] H. L. Long, S. Y. Shang, X. M. Tao, Y. P. Yin and X. Y. Dai, Int J Hydrogen Energy 33, 5510 (2008).

[4.62] V. Raballand, J. Benedikt and A. von Keudell, Appl. Phys. Lett. 92, 091502 (2008).

[4.63] X. H. Zhang, M. J. Li, R. L. Zhou, K. C. Feng and S. Z. Yang, Appl. Phys. Lett. 93, 021502 (2008).

[4.64] X. H. Zhang, J. Huang, X. D. Liu, L. Peng, L. H. Guo, G. H. Lv, W. Chen, K. C. Feng and S. Z. Yang, J. Appl. Phys. 105, 063302 (2009).

[4.65] M. Leduc, Sylvain Coulombe and Richard L. Leask, IEEE Trans. Plasma Sci. 37, 927 (2009).

[4.66] E. Koretzky and S. P. Kuo, Phys Plasmas 5, 3774 (1998).

[4.67] Q. Y. Nie, C. S. Ren, D. Z. Wang and J. L. Zhang, Appl. Phys. Lett. 93, 011503 (2008).

[4.68] J. Hopwood, O. Minayeva and Y. Yin, J. Vac. Sci. Technol. B 18, 2446 (2000).

[4.69] Z. Hubicka, M. Cada, M. Sicha, A. Churpita, P. Pokorny, L. Soukup and L. Jastrabik, Plasma Sources Sci. Technol. 11, 195 (2002).

[4.70] B. J. Park, D. H. Lee, J. C. Park, I. S. Lee, K. Y. Lee, S. O. Hyun, M. S. Chun and K. H. Chung, Phys Plasmas 10, 4539 (2003).

[4.71] M. Cada, O. Churpita, Z. Hubicka, H. Sichova and L. Jastrabik, Surf Coat Technol 177, 699 (2004).

[4.72] R. Stonies, S. Schermer, E. Voges and J. A. C. Broekaert, Plasma Sources Sci. Technol. 13, 604 (2004).

[4.73] M. Teschke, J. Kedzierski, E. G. Finantu-Dinu, D. Korzec and J. Engemann, IEEE Trans. Plasma Sci. 33, 310 (2005).

[4.74] M. Chichina, M. Tichy, P. Kudrna, A. Grinevich, O. Churpita, Z. Hubicka, S. Kment and J. Olejnicek, Czech. J. Phys. 56, B1212 (2006).

[4.75] A. Michels, S. Tombrink, W. Vautz, M. Miclea and J. Franzke, Spectroc. Acta Pt. B-Atom. Spectr. 62, 1208 (2007).

[4.76] X. T. Deng, J. J. Shi and M. G. Kong, J. Appl. Phys. 101, 074701 (2007).

[4.77] J. L. Walsh and M. G. Kong, Appl. Phys. Lett. 91, 221502 (2007).

[4.78] T. Nakano, IEEE Trans. Dielectr. Electr. Insul. 14, 1081 (2007).

[4.79] S. Perni, D. W. Liu, G. Shama and M. G. Kong, J. Food Prot. 71, 302 (2008).

[4.80] J. Schaefer, R. Foest, A. Quade, A. Ohl and K-D Weltmann, J. Phys. D-Appl. Phys. 41, 194010 (2008).

[4.81] Y. Nagasaki, M. Umeyama, M. Iijima, K. Kitano and S. Hamaguchi, J. Photopolym Sci. Technol. 21, 267 (2008).

[4.82] S. Perni, G. Shama and M. G. Kong, J. Food Prot. 71, 1619 (2008).

[4.83] B. L. Sands, B. N. Ganguly and K. Tachibana, IEEE Trans. Plasma Sci. 36, 956 (2008).

[4.84] B. L. Sands, B. N. Ganguly and K. Tachibana, Appl. Phys. Lett. 92, 151503 (2008).

[4.85] J. L. Walsh and M. G. Kong, IEEE Trans. Plasma Sci. 36, 954 (2008).

[4.86] R. B. Ye and W. Zheng, Appl. Phys. Lett. 93, 071502 (2008).

[4.87] W. C. Zhu, Q. Li, X. M. Zhu and Y. K. Pu, J. Phys. D-Appl. Phys. 42, 202002 (2009).

[4.88] Q. Li, J. T. Li, W. C. Zhu, X. M. Zhu and Y. K. Pu, Appl. Phys. Lett. 95, 141502 (2009).

[4.89] T. Shimizu, B. Steffes, R. Pompl, F. Jamitzky, W. Bunk, K. Ramrath, M. Georgi, W. Stolz, H-U. Schmidt, T. Urayama, S. Fujii and G. E. Morfill, Plasma Process. Polym. 5, 577 (2008).

[4.90] L. Bardos, H. Barankova and S. Berg, Surf. Coat. Technol. 97, 723 (1997).

[4.91] J. Janca, M. Klima, P. Slavicek and L. Zajickova, Surf. Coat. Technol. 116, 547 (1999).

[4.92] H. Barankova and L. Bardos, Surf. Coat. Technol. 146, 486 (2001).

[4.93] D. H. Shin, Y. C. Hong and H. S. Uhm, IEEE Trans. Plasma Sci. 34, 2464 (2006).

[4.94] Y. C. Hong, S. C. Cho, J. H. Kim and H. S. Uhm, Phys Plasmas 14, 074502 (2007).

[4.95] Y. C. Hong, S. C. Cho and H. S. Uhm, Appl. Phys. Lett. 90, 141501 (2007).

[4.96] H. Yoshiki, Rev. Sci. Instrum. 78, 043510 (2007).

[4.97] C. Richmonds and R. M. Sankaran, Appl. Phys. Lett. 93, 131501 (2008).

[4.98] S. Z. Li, W. T. Huang, J. L. Zhang and D. Z. Wang, Appl. Phys. Lett. 94, 111501 (2009).

[4.99] M. Leins, L. Alberts, M. Kaiser, M. Walker, A. Schulz, U. Schumacher and U. Stroth, Plasma Process. Polym. 6, S227 (2009).

[4.100] D. Mariotti, Appl. Phys. Lett. 92, 151505 (2008).

[4.101] A. A. H. Mohamed, R. Block and K. H. Schoenbach, IEEE Trans. Plasma Sci. 30, 182 (2002).

[4.102] R. M. Sankaran, K. P. Giapis, M. Moselhy and K. H. Schoenbach, Appl. Phys. Lett. 83, 4728 (2003).

[4.103] M. Moravej, X. Yang, G. R. Nowling, J. P. Chang, R. F. Hicks and S. E. Babayan, J. Appl. Phys. 96, 7011 (2004).

[4.104] O. Sakai, Y. Kishimoto and K. Tachibana, J. Phys. D-Appl. Phys. 38, 431 (2005).

[4.105] Y. C. Hong and H. S. Uhm, Appl. Phys. Lett. 89, 221504 (2006).

[4.106] C. X. Wang and Y. P. Qiu, Surf Coat Technol 201, 6273 (2007).

[4.107] Y. C. Hong and H. S. Uhm, Phys Plasmas 14, 053503 (2007).

[4.108] J. F. Kolb, A. A. H. Mohamed, R. O. Price, R. J. Swanson, A. Bowman, R. L. Chiavarini, M. Stacey and K. H. Schoenbach, Appl. Phys. Lett. 92, 241501 (2008).

[4.109] J. S. Sousa, G. Bauville, B. Lacour, V. Puech, M. Touzeau and L. C. Pitchford, Appl. Phys. Lett. 93, 011502 (2008).

[4.110] H. Q. Feng, P. Sun, Y. F. Chai, G. H. Tong, J. Zhang, W. D. Zhu and J. Fang, IEEE Trans. Plasma Sci. 37, 121 (2009).

[4.111] T. Yokoyama, S. Hamada, S. Ibuka, K. Yasuoka and S. Ishii, J. Phys. D-Appl. Phys. 38, 1684 (2005).

[4.112] C. Paduraru, K. H. Becker, A. Belkind, J. L. Lopez and Y. A. Gonzalvo, IEEE Trans. Plasma Sci. 35, 527 (2007).

[4.113] Y. C. Hong, H. S. Uhm and W. J. Yi, Appl. Phys. Lett. 93, 051504 (2008).

[4.114] C. Jiang, M. T. Chen and M. A. Gundersen, J. Phys. D-Appl. Phys. 42, 232002 (2009).

[4.115] Y. Yang, J. J. Shi, J. E. Harry, J. Proctor, C. P. Garner and M. G. Kong, IEEE Trans. Plasma Sci. 33, 302 (2005).

[4.116] Y. Yang, J. J. Shi, J. E. Harry, J. Proctor, C. P. Garner and M. G. Kong, IEEE Trans. Plasma Sci. 33, 298 (2005).

[4.117] M. S. Benilov, Phys Rev E. 77, 036408 (2008).

[4.118] D. F. Rogers, Larminar Flow Analysis, (Cambridge University Press, 1992).

[4.119] J. J. Shi and M. G. Kong, J. Appl. Phys. 97, 023306 (2005).

[4.120] J. J. Shi and M. G. Kong, IEEE Trans. Plasma Sci. 33, 624 (2005).

[4.121] J. L. Walsh, F. Iza, N. B. Janson, V. J. Law and M. G. Kong, J. Phys. D-Appl. Phys. 43, 075201 (2010).

[4.122] U. Kogelschatz, Plasma Chem. Plasma Process. 23, 1 (2003).

[4.123] D. Ellerweg, J. Benedikt, A. von Keudell, N. Knake and V. Schulz-von der Gathen, New J. Phys. 12, 013021 (2010).

Chapter 5
1D Array of Atmospheric Plasma Jets

5.1 Introduction

Capable of excellent plasma stability and rich reaction chemistry, atmospheric pressure plasma jets are able to treat three-dimensional objects. However they typically have a diameter of a few millimetres, and this is inadequate for many large-scale applications. An obvious solution is to group many APGD jets together to form an array of a longer length scale. There have been a few attempts in this direction. The earliest hint of relevant attempts appears to be the classic work in 1988 by Okazaki and colleagues, who employed a brush electrode constructed from 25 fine stainless-steel wires to stabilise atmospheric air plasma[5.1]. Their idea could have been extended to produce multiple plasma channels but this was not directly discussed. Subsequently it took more than 10 years before the first direct studies of plasma jet parallelisation were published. Kuo *et al.* reported in 1998 a matrix of 9 (3×3) plasma torches in atmospheric air and at 60 Hz[5.2], and proposed in 1999 that such plasma arrays could be operated in a modular fashion[5.3]. These plasma touches could be lit up simultaneously by a single power source. The author claimed that the capacitors in the electrical circuit played a crucial role because they worked as ballasts and provided feedback to the applied voltage. However with a rather high gas temperature, these plasma touches are essentially different from the low temperature plasma jets discussed in this thesis, and Kuo's work was intended for plasma stealth and

plasma-aided ignition applications rather than treating three-dimensional objects. In 2002, Hubicka *et al.* reported a linear array of 9 atmospheric plasma jets excited at 13.56 MHz[5.4]. In this work, 9 quartz tubes were each wrapped by one metal strip and the author claimed that the operation of the array was possible for treating non-flat surfaces. A linear array of 4 RF excited atmospheric plasma jets was studied in 2005 by Weltmann and colleagues[5.5]. No detailed information was given about how the 4 jets were connected electrically.

The collection of the aforementioned papers[5.2-5.6] is a fair representation of the current capability of the atmospheric plasma jet arrays, though our discussion does not cover very high frequency and microwave sources which could become an alternative[5.7]. The latter are known to be too hot for plasma medicine and the plasma-sample distance has to be increased to reduce the gas temperature. Therefore, atmospheric plasma jet arrays represent a somewhat under-studied research topic.

In this chapter, a one-dimensional atmospheric pressure plasma jet array will be reported. Following the introduction of its design and the experimental setup in section 5.2, electrical and optical characteristics of the 1D jet array will be discussed in section 5.3. Finally the conclusions will be drawn in section 5.4.

5.2 Design of 1D jet arrays

For this 1D jet array, we choose a dielectric tube wrapped with a ring electrode as the elementary unit. This is a relatively simple structure with straightforward electrical connection. Figure 5-1 shows a schematic of a 1D 10-jet array housed in an acrylic cassette having each jet compartment constructed in a tubular unit and with its own individual ballast and individual gas feed. Each tubular unit consists of a glass tube with an inner diameter of

1.5 mm and an outer diameter of 2.9 mm, and a concentric copper electrode, which wraps around the glass tube tightly working as the power electrode. The structure of a single unit is shown in the half-exposed illustration in the leftmost jet in figure 5-1. These tubular units are inserted into the acrylic housing in a line and are fixed leaving a shortest jet-to-jet insulation thickness of 0.4 mm. A 510 kΩ resistor, working as a ballast, is soldered to the copper electrode of each jet and then all the 10 ballast resistors are connected to an AC power supply. Gas is fed through a gas diffusion device which is hollow inside and can divide the total input gas into 10 identical branches to feed the 10 individual glass tubes. The design of the gas diffusion device is shown in figure 5-2. The entire array device is 3.2 cm in width from the first to the last jet.

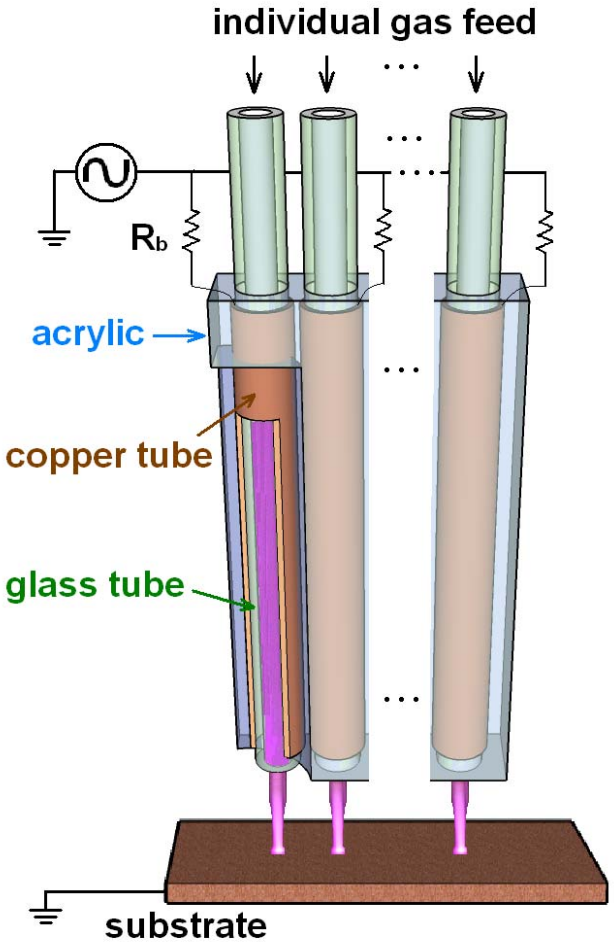

Fig 5-1: Schematic of a 1D 10-jet atmospheric plasma array with individual ballasts.

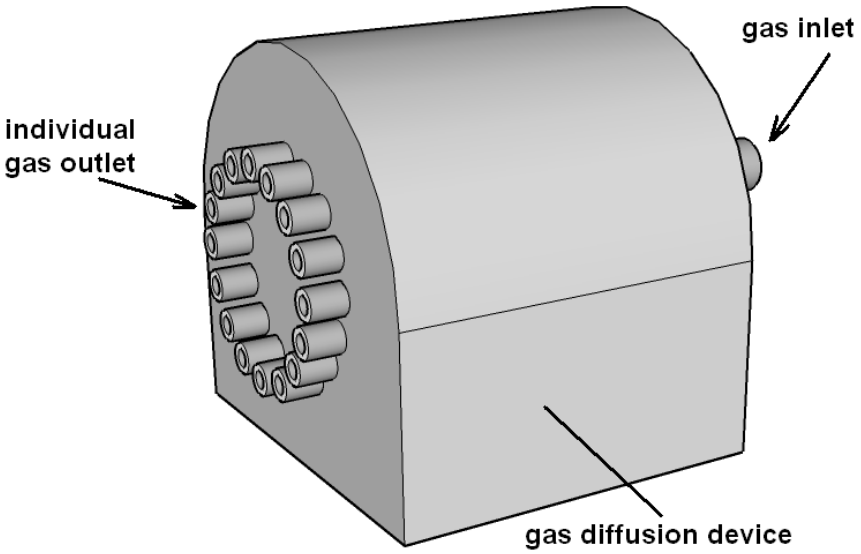

Fig 5-2: Schematic of the gas diffusion device used for feeding the 10-jet plasma array.

A total helium gas of 40 slm is nominally used for the array and the flow rate for each jet is 4 slm. This is equivalent to 37.7 m/s, well within the laminar flow limit. The jet array is driven by an AC power supply at a frequency of 30 kHz and an amplitude adjustable up to 5 kV. The voltage is measured by a Tektronix P6015A high voltage probe.

The jet array can be operated with or without a downstream ground electrode. Known from the previous discussion in Chapter 4, the electric field of this jet array is largely in the axial direction and parallel to the gas flow field. So each jet is a linear-field device. When a ground electrode is used, the total current for the jet array is measured by a Pearson 2877 current probe. Individual current for each jet can also be measured by introducing a 22 Ω resistor in series with the individual jet circuit near the ground and then monitoring the voltage fall across the resistor. Voltage and current signals are recorded using a Tektronix DPO4104 oscilloscope.

Both a domestic camera and an Andor DH720 ICCD camera are used for imaging. Spectroscopic signals are measured by an Andor Shamrock SR-303i

spectrograph with a homemade light-isolation device. To demonstrate the ability of the plasma jet array to treat 3D objects, three sloped metal substrates with a slope angle of 5°, 10° and 15° are used.

Preliminary trials have shown that it is difficult to sustain all jets simultaneously in the 1D jet array by connecting all the ring electrodes directly to one power supply (i.e. without ballasts). This could be due to each jet having an ignition voltage slightly different from one another. As a result, it is not possible to ignite all the jets at the same time. The plasma jet that is ignited first in the array undergoes a rapid reduction in its equivalent impedance before other jets are ignited and start to reduce their impedances. This further forces more current flow through the first jet thus preventing others from being ignited. Even when the other jets are eventually ignited, without ballasts it is hard to maintain spatial uniformity across the width of the jet array. When a single lumped ballast is used for the entire jet array, similarly unsatisfactory results are observed. However when each jet channel is connected to its own ballast, much better uniformity is obtained.

Here the choice of the resistor value is important, 510 kΩ is found to be appropriate for the array reported here. It can provide an effective feedback and does not weaken the discharge.

The use of individualised ballast resistor is the key for treatment of 3D objects. As the nozzle-to-object distances vary among individual jets, the jet array normally only fires in the channels of those jets with a short nozzle-to-object distance in the absence of individual ballasts. However individually connected ballast resistors can provide an appropriate voltage distribution on each jet and this approach has allowed all jets to fire simultaneously. As two examples, figure 5-3a and 5-3b are pictures of the 1D 10-jet array treating a screwdriver and a surgical tissue forceps, respectively. These tools are placed on the ground electrode, so they are grounded. It is clear that all 10 plasma jets are ignited against the very different 3D

substrates, even when different jets in figure 5-3b intercept the metallic forceps at very different nozzle-to-forceps distances. This indicates an effective self-adjustment mechanism among individual jets in the array, achieved by individualised ballast and possibly also by a spatial redistribution of surface charges on the acrylic cassette. It is worth mentioning that all APGD jets fire only when each jet is individually ballasted. The benefit of individualised ballast is similar to that for other high-pressure discharge arrays[5.2,5.8]. The above discussion demonstrates a clear robustness of the APGD array for treating intricate metallic objects.

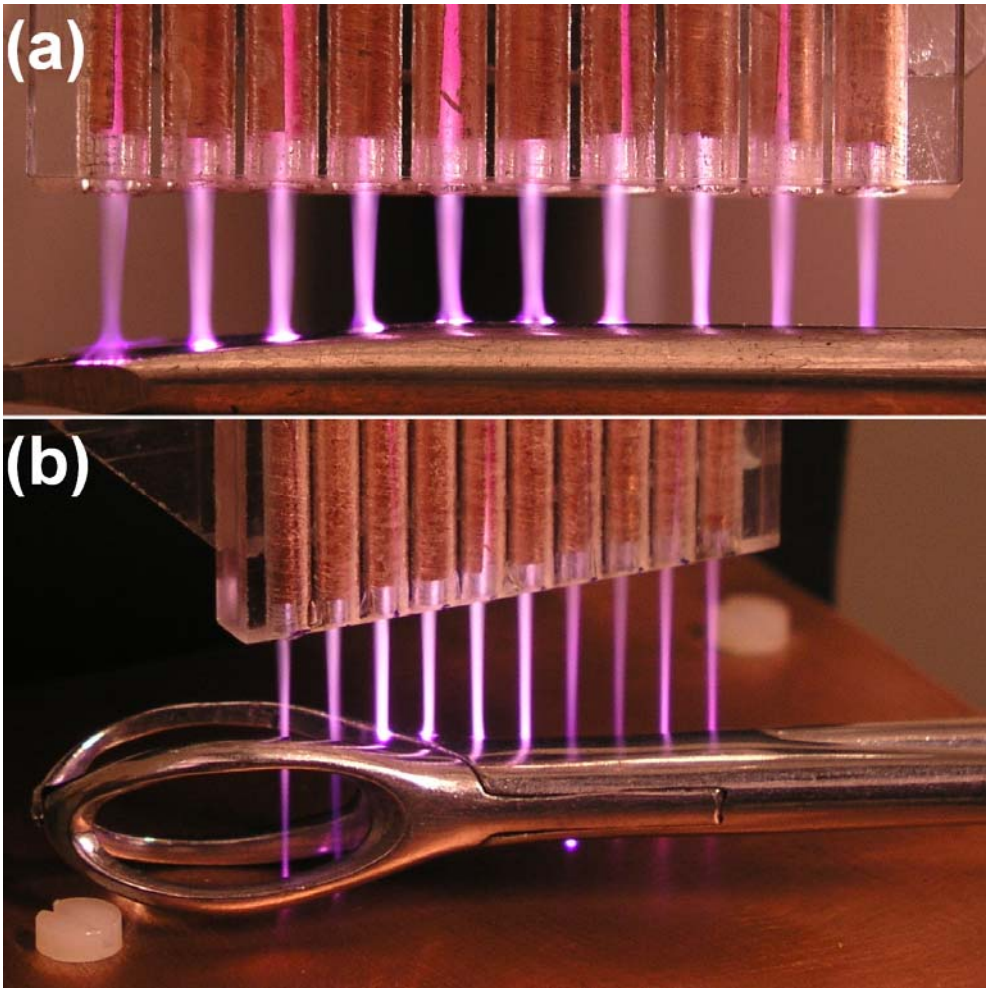

Fig 5-3: A 1D 10-jet atmospheric plasma array treating (a) a screwdriver; and (b) a surgical tissue forceps.

5.3 Electrical and optical characteristics

5.3.1 Treating flat surface

The 1D 10-jet array is first used to treat a downstream grounded metal plate as a model of flat surfaces. By naked eye, all the jets appear to fire simultaneously and with good jet-jet uniformity. Figure 5-4 shows traces of the applied voltage and the total currents of the 10-jet array when treating the surface with three different nozzle-to-substrate distances, namely 10 mm, 12 mm and 15 mm, with V_p fixed to 3.5 kV. The current traces all have a pulse in each half cycle. This peak current value decreases with the increase of the nozzle-to-substrate distance, i.e. the peak value is 27 mA for 10 mm gap distance and it decreases to 24 mA for 12 mm and 15 mA for 15 mm. This is consistent with the phenomenon observed from an equivalent single jet in that the jet plume tends to be weaker with increasing nozzle-to-substrate distance at a given applied voltage. However the provision of the ballast resistors realises the simultaneous firing of all the jets in the array.

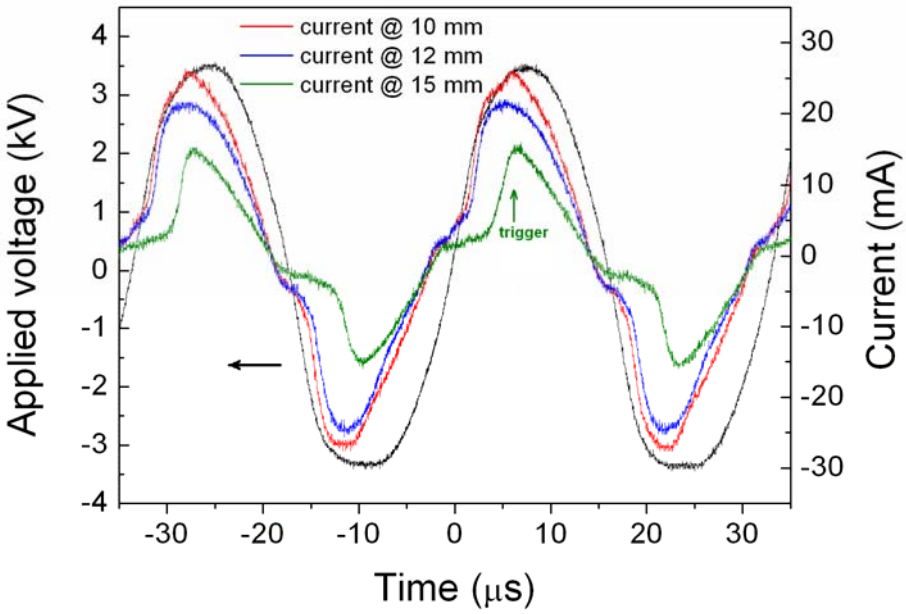

Fig 5-4: Time traces of the applied voltage (black) and the total currents of the 10-jet array when treating the surface with three different nozzle-to-substrate distances. The substrate is a flat metal substrate.

To better understand the simultaneous firing, ICCD images are shown in figure 5-5, for which V_p = 3.5 kV and the nozzle-to-substrate distance is 15 mm. The exposure time for figure 5-5a is 33.33 μs which is equal to one cycle of the applied voltage. This image indicates how the 1D plasma jet array is seen by naked eye. The 10 plasma plumes are seen to have a similar emission intensity. Figure 5-5b is taken by a single shot with an exposure time of 10 ns at the instant of the peak current in the positive half cycle, i.e. '6 μs' in the *x* axis which is indicated by the green arrow in figure 5-4. This image is representative for the operation of the jet array in nano-second scale. Clearly all 10 jets are firing together and this maintains in the other instants.

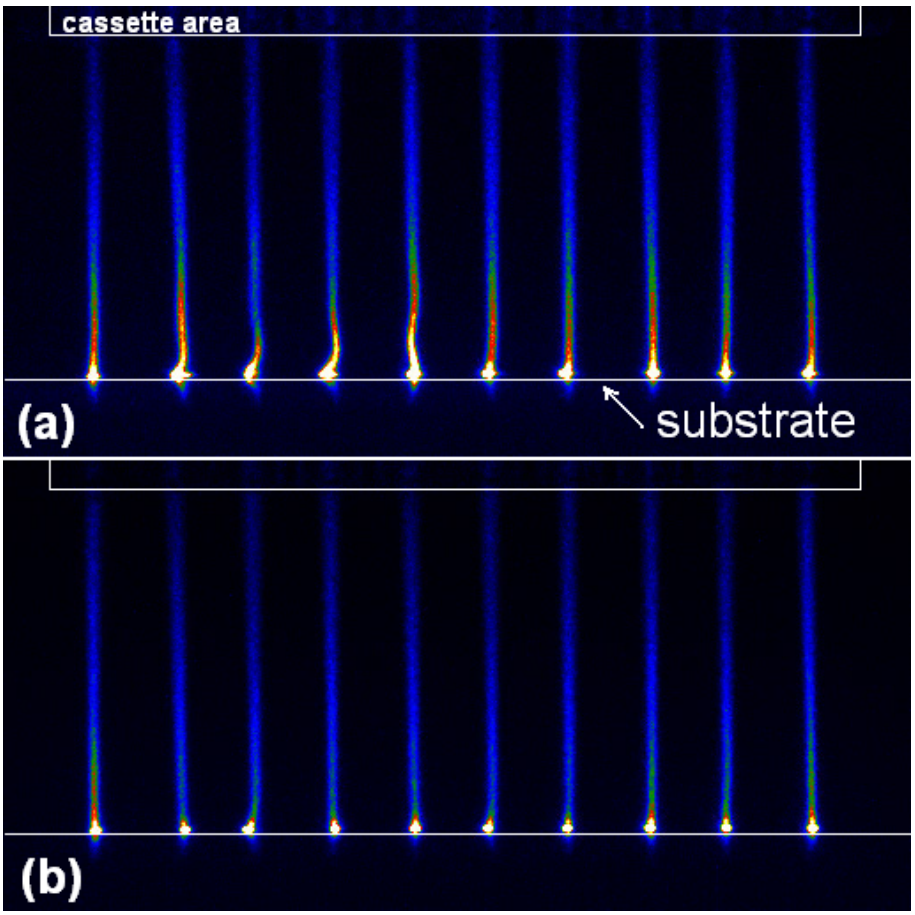

Fig 5-5: Images of the 1D 10-jet array onto a flat metal substrate with a single shot exposure time of (a) 33.33 μs and (b) 10 ns.

5.3.2 Treating sloped surface

It is worth noting the sharp contrast between the gradual surface profile of the screwdriver and the convoluted structure of the forceps in figure 5-3, highlighting the considerable potential of the 1D jet array for treating complex 3D substrates. The latter is an important indicator of the 1D jet array as a platform tool for sterilisation of diverse surgical instruments and medical devices[5.9]. To demonstrate directly its capability for treating 3D surfaces, the 1D jet array is characterised using a sloped metal plate as a 3D substrate model.

First, a metal plate sloped at 10° is used as the substrate. It is placed underneath the array nozzle with the shortest and longest nozzle-to-substrate distance being 1.0 cm and 1.6 cm respectively. This arrangement is photographed by a domestic camera with an exposure time of 1/15 s and shown in figure 5-6, with the numbers indicating individual jets. In this case, V_p = 3.4 kV and all the jets firing with fairly good uniformity are seen by the naked eyes.

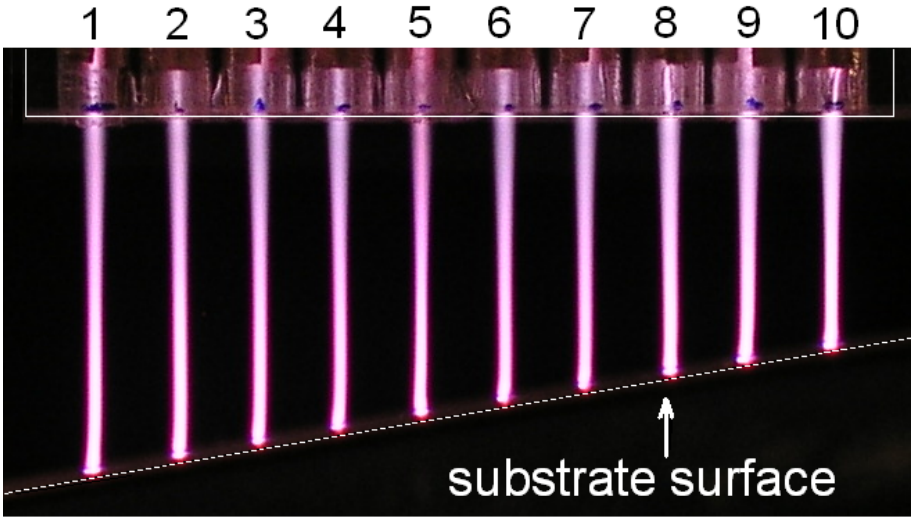

Fig 5-6: Images of the 1D 10-jet array onto a 10° sloped metal substrate with an exposure time of 1/15 s.

Figure 5-7 shows traces of the applied voltage, the total current of the

array, and the individual currents flowing through the 2nd and 7th jets, corresponding to the condition of figure 5-6. The individual currents are multiplied by 10 (the number of the jets) to allow for direct comparison to the total current and they are used as examples of the 10 individual currents without compromising the clarity of figure 5-7. The current trace shows a pulse of 25 mA in each half cycle and this current pulse lasts almost the entire half cycle. This represents a dielectric barrier discharge. All current and voltage curves in the figure are free of any obvious spikes (i.e. overcurrents), indicating a stable plasma in each channel of the jet array.

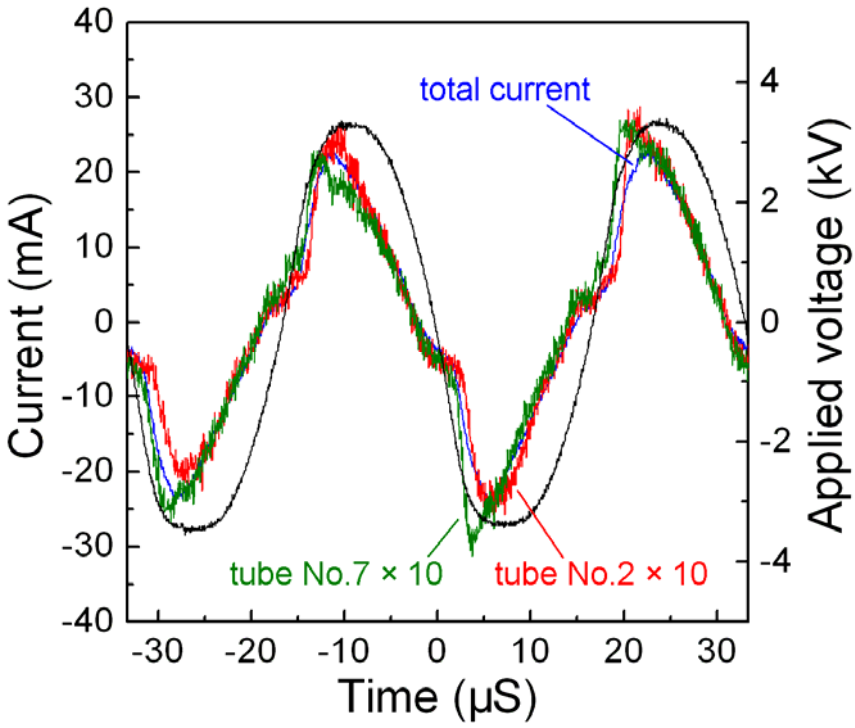

Fig 5-7: Time traces of the applied voltage (black), the total discharge (blue), and two individual jet currents (red and green). The substrate is a 10° sloped metal substrate.

The waveform of the total current is seen to map reasonably well onto the waveforms of the two individual currents, suggesting that for most of the time all 10 plasma jets are behaving similarly. Different from a typical

dielectric barrier discharge with one sharp current pulse every half cycle of the applied voltage, the discharge current of an individual jet and indeed of the entire array has a continuous waveform. It is noted that the onset time and peak value of one current pulse are slightly different from those of another. This is because the nozzle-to-substrate distance for each jet is different and the discharge tends to start from the jet with the shortest nozzle-to-substrate distance that leads to strongest induced electrical field. However, the difference between the onset instants is slight and nearly for all the time the individual current pulse overlaps. These show good similarity in the 1D jet array.

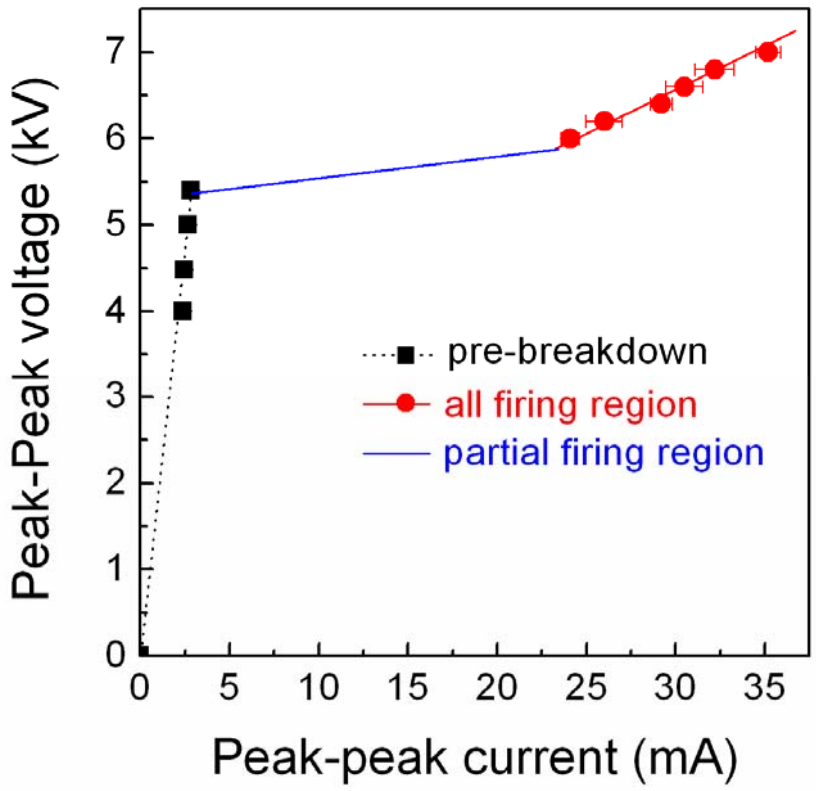

Fig 5-8: The total current dependence of the peak-to-peak voltage. The substrate is a 10° sloped metal substrate.

Relationship of the total discharge current and the applied voltage is shown in figure 5-8. The black line indicates the pre-breakdown regime.

When the peak-peak applied voltage reaches 5.4 kV, the jet array starts to fire. It is clear that there is a regime immediately after the initial gas breakdown during which not all jets are ignited, as indicated by the blue line in the figure. With increasing applied voltage, more plasma jets start to fire and the total current increases. This regime is similar to the normal mode of the glow discharge[5.10]. After the peak-to-peak applied voltage is raised to 6.0 kV, another regime with all jets firing appears as shown in red in figure 5-8. The 1D jet array has a positive differential impedance in this regime and may operate in the abnormal glow mode. Even with a positive differential impedance, not all 10 jets could fire at the same time if they were connected together and then connected to a power supply. This is different from the case of a 2x2 microhollow cathode discharge array for which ballast resistors were found unnecessary when the differential impedance was positive[5.11]. The role of individualised ballast is critical in the 1D APGD jet array of figure 5-1 and is likely to have facilitated a built-in self-adjustment mechanism in achieving simultaneous operation.

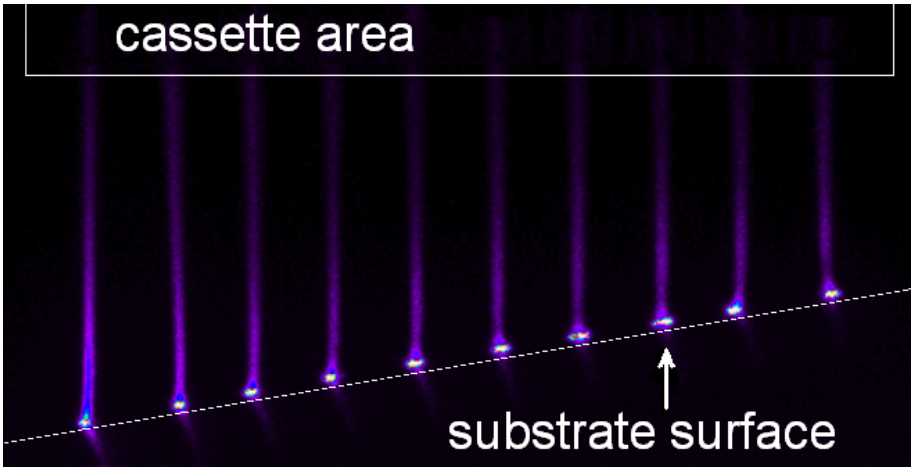

Fig 5-9: Image of the 1D 10-jet array onto a 10° sloped metal substrate with a single shot exposure time of 10 ns.

While the near identical time-dependences of the total and individual currents in figure 5-7 offer a strong indication of simultaneous firing of all

individual jets, the most direct evidence of the jet-to-jet simultaneity would need to be provided from nanosecond exposure imaging. With the slope of the metal plate at 10° and V_p at 3.4 kV, an image of the jet array with a single shot exposure time of 10 ns is taken by the ICCD camera, and it is shown in figure 5-9. Clearly all 10 jets are firing simultaneously, confirming an excellent temporal jet-to-jet synchronism. Repeated experiments at different substrate slopes of up to 15° have confirmed that excellent temporal jet-to-jet synchronism of the 1D APGD 10-jet array is maintained over a wide operating range.

Light intensity of individual jets at the substrate surface appears to be similar to each other in figure 5-9, however it is limited to the visible range of 400 ~ 700 nm of the ICCD camera outside which the emission lines of many application-significant species lie, for example the atomic oxygen lines at 777 and 844 nm, helium line at 706 nm, and nitrogen and OH lines in the 300 ~ 400 nm band. To overcome this and relate the optical emission directly to reaction chemistry, an Andor spectrograph is used to measure wavelength-integrated emission intensity from 200 to 1000 nm. Spatial separation of the light emission of one jet from that of other jets is achieved using a homemade light-isolation device shown in figure 5-10a. This light-isolation device is a cylindrical block made by black Polyvinyl chloride (PVC). It has a length of 11.7 mm and a concentric through hole. The diameter of the through hole is 0.88 mm and it is slightly larger than the diameter of the optical fibre used, which is 0.6 mm. The optical fibre is attached to the light-isolation device tightly and the other end of the light-isolation device points to a plasma at its contact point to the substrate. The distance between the light-isolation device and plasma contact point is 2.5 mm, and at this distance the device does not disturb the plasma. Given the distance between two adjacent jets being 3.5 mm, the above arrangement is able to pick up the light from one contact point and block those from the

others.

Special arrangement is made to ensure that the light-isolation device was always pointing to the contact points precisely and at the same distance. Light intensity measurement via the isolation device is made within 3.5 mm either side of the location of a firing plasma jet in dark ambience. Figure 5-10 shows that the light of a firing plasma jet collected by the isolation device falls to the background noise level within 1.75 mm away from the jet location, in other words at the midpoint to an adjacent jet of the jet array. This suggests that light emission from any source outside the 1.75 mm radius, either the remaining plasma jets in the array or otherwise, is blocked out by the isolation device thus achieving effective spatial selectivity of optical emission from different jets.

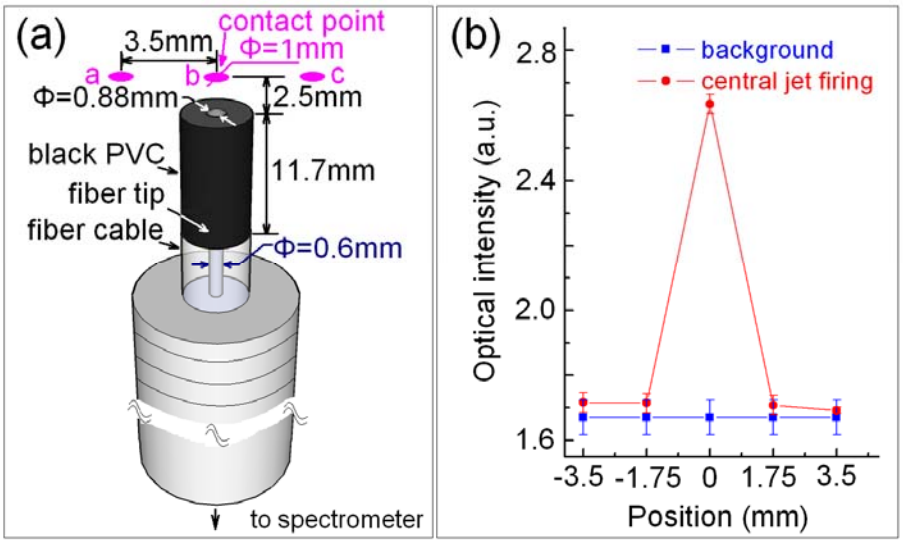

Fig 5-10: (a) Schematic of a light-isolation device and its integration to the light-collecting optical fibre cable. Label *a, b, c* mark the contact points of three consecutive plasma jets in the jet array. (b) Optical emission of one firing plasma jet measured by scanning the light-isolation device over 3.5 mm either side of the jet.

The light-isolation device is used to establish the spatial jet-to-jet uniformity of the APGD jet array in comparison with that of a single jet which needs to scan when treating a large surface area. In this case, we

consider a surface-scanning single jet with a stationary jet array. Using the isolation device, the wavelength-integrated light intensity of each jet of the APGD 10-jet array is measured at its contact point on a sloped metal substrate, and then compared to those of the single jet as the latter scans across the same substrate. The single jet scans four specific positions which correspond to the No. 1, No. 4, No. 7 and No. 10 jets in the array. Three metal substrates with a slope angle of 5°, 10° and 15° as well as a flat substrate are used. For all cases the minimum nozzle-to-substrate distance is fixed at 10 mm.

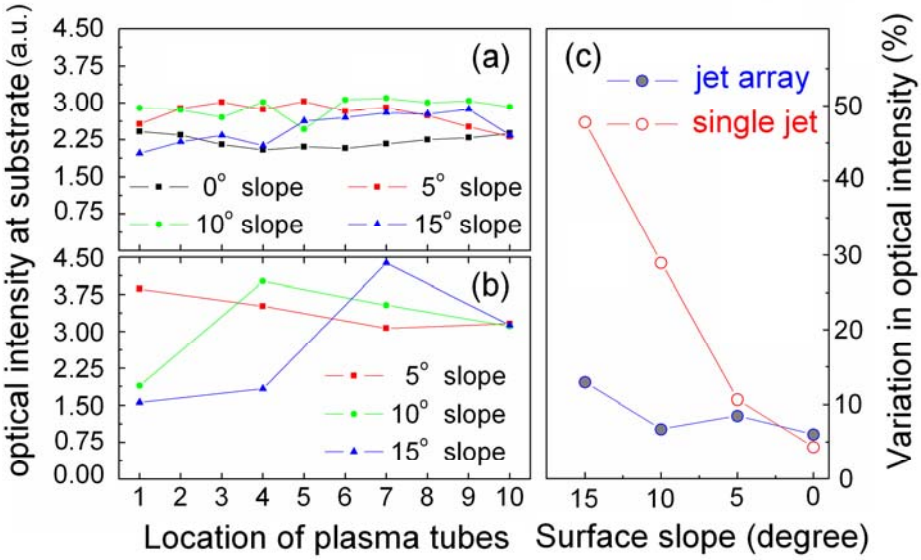

Fig 5-11: Optical emission from (a) each of the 10 jets in the jet array and from (b) a scanning single jet, as well as (c) relative standard variation of optical emission as a function of the slope of the metal substrate for the jet array (blue) and for the single jet (red).

Results are shown in figure 5-11, with the emission intensity of the jet array in figure 5-11a exhibiting a much better spatial jet-to-jet uniformity than that of the scanning single jet in figure 5-11b, particularly with sloped substrate above 5°. In the single jet case, variation in optical intensity across the sampled surface points is seen in figure 5-11c to increase from 4.0% at 0° slope to 48% at 15° slope. By contrast, the jet array has much smaller intensity variation from 6% at 0° slope to 12% at 15° slope. This

demonstrates an excellent spatial jet-to-jet uniformity of the 1D APGD jet array, a factor of 4 (= 48%/12%) better than that of the single jet in the 15° slope case. The jet array covers surface area about 10 times of that of a single-jet at any given time, and this can be easily translated into a reduction factor of 10 in processing time.

5.4 Scalability

The aforementioned 1D atmospheric pressure 10-jet array has been shown as a capable atmospheric plasma source for treating flat and three-dimensional objects with good simultaneity and uniformity. This prototype has only 10 individual channels and a length of 3.2 cm, so there is a need to increase its coverage in order to use it for large-scale applications. In principle, the 1D jet array can be extended to have many channels. However as all the channels are powered by one power supply, the capacity of the power supply could determine how many jets can be included in an array.

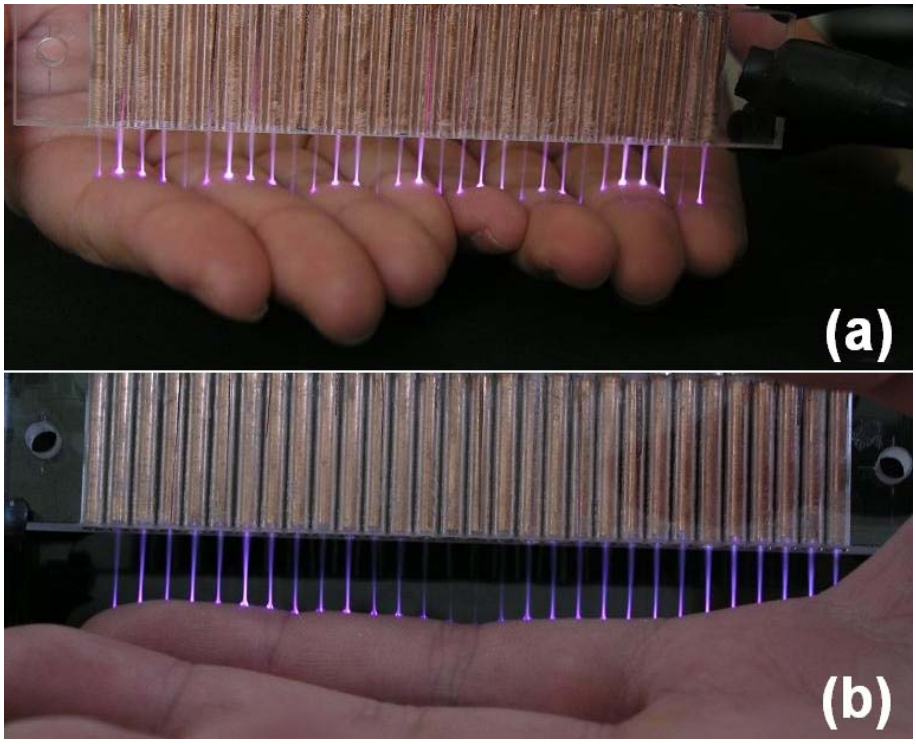

Fig 5-12: Pictures of a 1D 30-jet array treating human hands.

Figure 5-12 shows two pictures of a 1D 30-jet array treating human hands. The unit jet is geometrically the same with those in the 1D 10-jet array, so the length of this 30-jet array is around 10 cm, three times of that of the 10-jet array. For this length, a human hand can be treated with good coverage, as shown in figure 5-12a and 5-12b. Moreover, the pictures also demonstrate that the direct treatment of human living tissue and hand by the jet array is potentially safe though *in-vitro* and *in-vivo* toxicology studies are needed to confirm this. Given that atmospheric plasma has bactericidal effect, this shows great potential for this kind of 1D atmospheric plasma jet arrays to be adopted in real applications.

5.5 Summary

Inspired by the reliability of atmospheric pressure plasma jets, 1D arrays of atmospheric pressure plasma jets are investigated in this chapter. The jet array features one ballast resistor for each of the individual jets to provide negative feedback in each plasma channel. This individualised effective self-adjustment mechanism enables all jets to fire simultaneously not only against flat substrates but also against sloped substrates.

Electrical and optical characterisations of the 10-jet array are used to demonstrate its robust temporal synchronism and spatial jet-to-jet uniformity. For flat substrates, 10 ns exposure image demonstrates the simultaneous firing of all jets. For sloped substrates, there is initially a partial firing region in which not all jets fire. However after the applied voltage is increased, all the jets start to fire simultaneously. Both current waveforms of individual jets and 10 ns exposure image confirm their simultaneous firing in the array. Wavelength-integrated light intensity picked up from the contact points between the individual jets and the sloped surfaces also shows good spatial uniformity. On substrates with a slope of 5° ~ 15°, the jet array shows

consistently better spatial uniformity than its single jet counterpart that covers the area of the substrate by scanning. These highlight a high-level consistency of the 1D jet array in maintaining its plasma physical and chemical characters among its constituent jets when treating vastly three-dimensional objects.

Finally the scalability of 1D jet array is demonstrated by a 30-jet array which has a width of 10 cm. This longer 1D jet array is well suited for treating large-scale three-dimensional structures.

References

[5.1] S. Kanazawa, M. Kogoma, T. Moriwaki and S. Okazaki, J. Phys. D-Appl. Phys. 21, 838 (1988).

[5.2] E. Koretzky and S. P. Kuo, Phys Plasmas 5, 3774 (1998).

[5.3] S. P. Kuo, E. Koretzky and L. Orlick, IEEE Trans. Plasma Sci. 27, 752 (1999).

[5.4] Z. Hubicka, M. Cada, M. Sicha, A. Churpita, P. Pokorny, L. Soukup and L. Jastrabik, Plasma Sources Sci. Technol. 11, 195 (2002).

[5.5] R. Foest, E. Kindel, A. Ohl, M. Stieber and K. D. Weltmann, Plasma Phys. Controlled Fusion 47, B525 (2005).

[5.6] Z. Cao, J. L. Walsh and M. G. Kong, Appl. Phys. Lett. 94, 021501 (2009).

[5.7] T. Shimizu, B. Steffes, R. Pompl, F. Jamitzky, W. Bunk, K. Ramrath, M. Georgi, W. Stolz, H. Schmidt, T. Urayama, S. Fujii and G. E. Morfill, Plasma Process. Polym. 5, 577 (2008).

[5.8] T. Sakaguchi, O. Sakai and K. Tachibana, J. Appl. Phys. 101, 073305 (2007).

[5.9] X. T. Deng, J. J. Shi and M. G. Kong, J. Appl. Phys. 101, 074701 (2007).

[5.10] J. R. Roth, Industrial Plasma Engineering, Volume 2, Applications to Nonthermal Plasma Processing, (IOP Publishing Ltd, 2001).

[5.11] K. H. Schoenbach, R. Verhappen, T. Tessnow, F. E. Peterkin and W. W. Byszewski, Appl. Phys. Lett. 68, 13 (1996).

Chapter 6
2D Arrays of Atmospheric Plasma Jets

6.1 Introduction

A one-dimensional atmospheric pressure plasma jet array discussed in Chapter 5 requires mechanical movement in order to cover a large surface area, for example a human wound. Inevitably this increases the treatment time and may introduce variation from one treatment to the next. Further issues such as treatment uniformity also need to be addressed. One straightforward way to cover larger area is to parallelise many plasma jets to form a two-dimensional plasma array. For low temperature atmospheric plasmas, this obvious approach has so far been realised only with microplasmas confined to micrometer-scale inter-electrode space (e.g. microcavity)[6.1]. It has been shown that these microplasmas have been arrayed in hundreds, sometimes millions. These may be classified as *spatially confined atmospheric plasma* (SCAP) arrays. The elemental source of an SCAP array is microplasma, such as microhollow discharges which may be sustained at DC[6.2], RF[6.3], RF DBD[6.4] and kilohertz DBD[6.5] or microplasma generated with different electrode configurations including micro-structured electrode[6.6-6.8], coaxial-hollow micro DBD[6.9], capillary-in-hole[6.10,6.11] and microcavities[6.12-6.18]. Figure 6-1 shows an example of SCAP arrays which is proposed by Eden *et al.* to illustrate the characteristics of SCAP arrays. The design of their electrode structure suggests that these microplasmas are produced inside the microcavities and they are spatially confined. SCAP

arrays at present are used mainly for photonics applications, for instance as a flexible-sheet light source[6.19] or as a tuneable band-pass filter[6.20]. For processing applications relying on photons, an SCAP array can deliver photon fluxes to a distant sample of uneven surface and its surface processing can be effective provided absorption of photons in the atmosphere is limited. However for other applications which favour reactive plasma species for surface treatment, especially for biomedical applications, spatial confinement of the individual plasmas in an SCAP array forces reliance on an unaided and potentially ineffective diffusion of reactive species towards the sample[6.21,6.22]. Given the typical short half-lives of many reactive species, this compromises application efficacy and calls for directed delivery of reactive plasma species. Although with an additional electrode, plasma confined in a SCAP array may be extracted out of electrode confinement and thus enhance downstream diffusion of reactive species[6.4,6.23], alternative array architectures would be preferred if they could produce reactive species directly on the surface of a downstream sample.

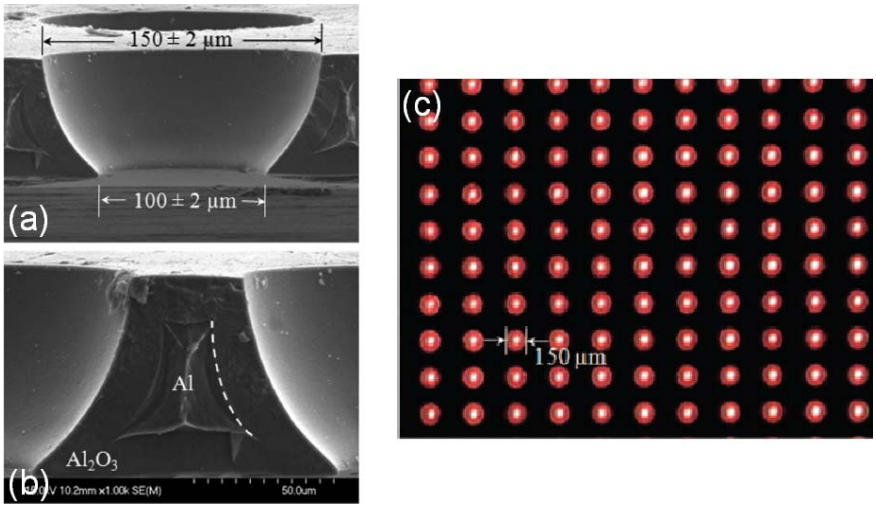

Fig 6-1: SCAP arrays proposed by Eden *et al.* (a) the cross-sectional profile of an Al_2O_3 microcavity with emitting (upper) and lower apertures of 150 and 100 µm respectively. (b) a magnified view of the region between two adjacent microcavities showing an Al electrode, separated from the microcavity by a ~17 µm thick layer of nanoporous Al_2O_3 and having an inner surface with the same profile as the microcavity. (c) an 11×10 segment of a 200×100 SCAP arrays in operating condition[6.18].

As discussed in chapter 4 and 5, atmospheric plasma jets are known to be able to produce reactive species directly on the surface of a downstream sample and even into the inner space of three-dimensional structures. When they are arrayed up in parallel, such as the 1D plasma arrays discussed in chapter 5, a shower of reactive species can be produced by the array and delivered to cover a large downstream surface. This kind of plasma array may be classified as *spatially extended atmospheric plasma* (SEAP) array, in contrast to the SCAP array.

SEAP arrays have the potential to become an enabling technology for many large-scale processing applications including plasma medicine. Stability control and spatial extension achieved with plasma jets allow for additional reactive chemistry to be introduced in a downstream region including the sample surface[6.24,6.25]. Spatial extension of SEAP arrays is therefore critical in facilitating both rich reactive chemistry and its directed delivery to a downstream 3D sample (even through a hollow structure such as surgical forceps)[6.24]. It should be noted that the physical size of the sample in the direction of the plasma jets dictates the minimum length of the plasma plume and in general an elemental jet in an SEAP array needs to be much longer than the size of a single cavity plasma in an SCAP array[6.19,6.26]. Therefore in addition to the difference in their intended applications (e.g. photonics vs surface processing), SEAP and SCAP arrays operate in different parametric spaces potentially dominated by different plasma physics. As will be shown later in this chapter, the main scientific challenge for SEAP arrays is jet-to-jet interactions and jet-to-sample interactions whereas for SCAP arrays it is plasma physics at the interface of different phases of matter and under the influence of quantum effects when the electrode gap is reduced to below one micrometer[6.19,6.26].

While immense advances have been made with the SCAP array technology[6.1,6.11,6.19,6.26,6.27], SEAP arrays are far less studied, as reviewed in

section 5.1. Notwithstanding the relevant merits of different SEAP arrays, their technical capability is at present little developed and their underpinning science is little understood. As all SEAP arrays reported so far are 1D linear arrays and require scanning to cover a substrate area, this chapter aims to introduce a 2D SEAP array employing atmospheric plasma jets. The array presented here is the first reported 2D SEAP array based on atmospheric plasma jets with the potential to treat a surface area without scanning. Our emphasis is on plasma dynamics, jet-to-jet uniformity, large-scale processing uniformity, and its capability to sustain all plasma channels when treating heavily three-dimensional objects. All these topics are important for atmospheric plasma jet arrays to be advanced towards real applications.

In this chapter, we report an experimental study of a 2D atmospheric pressure plasma jet arrays. Based on the results of detailed assessment of single atmospheric plasma jets in Chapter 3, we will discuss the design of a 2D jet array in section 6.2. Its electrical characteristics, dynamics and optical characteristics will be analysed in section 6.3-6.5 for which plasma stability, jet-to-sample interaction and jet-to-jet uniformity will be discussed. In section 6.6 bactericidal characteristics will be used to indicate the scalability of both the plasma jet array and its physical extent of reaction chemistry. Finally, section 6.7 will provide concluding remarks.

6.2 Design of 2D jet arrays

6.2.1 Technical requirements

Before a detailed description for the design of the 2D jet array, it is worth mentioning the technical requirements for SEAP arrays. Four specific features of SEAP arrays are identified to be desirable for their applications, namely jet density, jet-to-jet interaction, jet-to-sample interaction and processing uniformity.

The concept of the jet density is introduced here to indicate how tightly individual plasma jets are packed in an array onto a given cross-sectional area. We introduce the jet density as

$$\rho_j = 2R_p / d_{jj} \tag{6.1}$$

where R_p is the radius of one plasma jet and d_{jj} is the distance between two adjacent plasma jets, measured when the array fires with collimated jets without jet convergence or repulsion. Equation (6.1) assumes that the plasma jet array is composed of identical jets each placed in equal distance from its nearest neighbouring jets. It is important to emphasise that the above definition is meaningful only when jets in a jet array are all firing in collimated plasma channels, as an array of converging or repelling jets is unacceptable as a large-scale processing tool. The concept of the jet density has not been considered before in the literature[6.24], but is essential for comparing different jet arrays and estimating how much a plasma jet array must be moved to scan a given surface. While previous studies of APGD jet arrays do not always provide the value of their d_{jj}[6.25,6.28-6.30], extrapolations based on their plasma images suggest that their jet density is typically of ρ_j = 0.05 ~ 0.3. For the 1D jet array reported in Chapter 5, ρ_j = 0.35 ~ 0.43. While a large jet density is desirable, ρ_j = 1 is impractical because of the need for mechanical support to the individual jets and their thermal management.

A high jet density cannot necessarily be achieved by simply packing together more individual jets into a given space. As individual jets are brought close to each other, their interaction becomes significant and without an appropriate control this may lead to repelling or converging jets thus compromising the objective of arraying up plasma jets. Therefore jet-to-jet interactions introduce an additional limit on the maximum achievable jet density. However, it has been shown in the previous chapter that good control of jet-to-jet interactions and attainment of collimated jet array are possible in 1D plasma jet arrays, and these should be achieved also for 2D jet arrays. In

order to treat three-dimensional objects, plasma susceptibility to sample variations, e.g. jet-to-sample interaction, is also a key issue and this is related to the uniformity of plasma processing over the entire sample surface.

6.2.2 Structure of 2D jet array

A dielectric housing with hexagonally arranged through-holes is used to support unit jets and its honeycomb configuration is shown schematically in figure 6-2. Each unit jet has a capillary-ring structure of the same dimensions as described previously in Chapter 4. The inner diameter of the through-holes is slightly bigger than the outer diameter of the quartz tube so that the dielectric housing can hold individual jets tightly, and as a result all quartz tubes are mechanically held to align in parallel to each other. As indicated in the schematic, except the central hole, the holes marked with the same number are a hexagon-shaped ring and they encircle a smaller ring marked with a number that is '1' smaller than the number of the larger ring. By following this rule, more jets can be stacked onto the array which in turn can cover a bigger area. A 7-jet array will be first studied as a prototype and a 19-jet array and a 37-jet array will then be used to demonstrate the scalability.

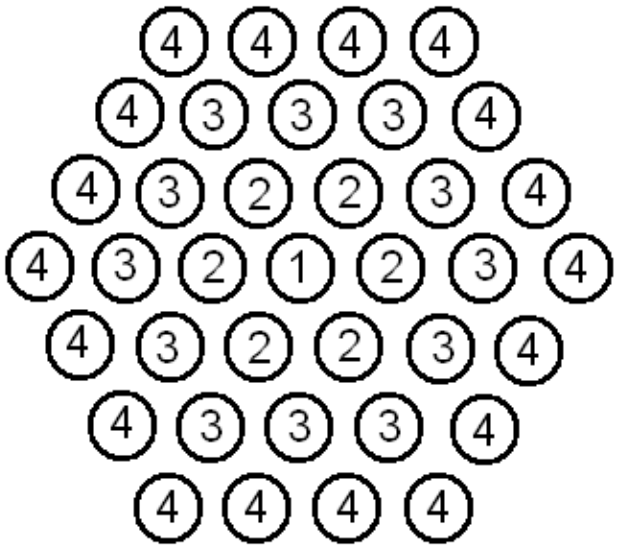

Fig 6-2: Schematic of jets arranged in a 2D jet array.

A 2D 7-jet array is shown schematically in figure 6-3 for its structural details both from the side view and the end view. The diameter of the entire array measured as the distance between the outer edges of two furthest-apart tubes in the hexagon-shaped ring is 10 mm. The quartz tubes have an inner diameter of 1.4 mm and an outer diameter of 2.9 mm respectively, and the centre-to-centre distance between two adjacent quartz tubes is 3.55 mm. Each quartz tube encloses a coaxial stainless steel capillary electrode with an inner and outer diameter of 0.838 mm and 1.27 mm respectively. As a result, the annular gap between the tube and the capillary is 65 μm. These capillary electrodes are connected to an AC power supply without external ballasts and the excitation is with an amplitude up to 5 kV and at 10 kHz (equivalent to 100 μs per cycle). Seven ring electrodes, 3 mm in length, wrap around the quartz tubes leaving a distance of 3 mm to the nozzles of the tube. These ring electrodes are all connected to ground. The tips of capillaries are 10 mm in the axial direction away from the edge of the ring electrodes.

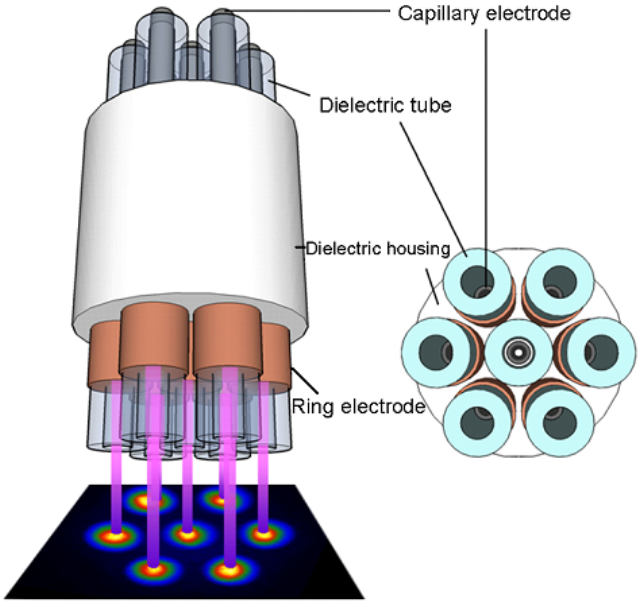

Fig 6-3: Schematic of a 7-jet array arranged in a honeycomb configuration with both the side view (left) and the end view (right). Each plasma jet delivers a jet-centric spread of reactive species on the surface of the downstream substrate. The seven circular images on the substrate are wavelength-integrated plasma emission taken with a 100 μs exposure time.

The carrier gas is fed through a gas diffusion device (see figure 5-2) and then divided into seven identical branches to feed the seven capillaries. Normally a helium (99.996%) flow of 15 slm is used and so each channel shares 2.14 slm. The gas velocity inside the capillary electrode and quartz tube is 64.8 m/s and 23.2 m/s respectively, and the corresponding Reynolds numbers for the above cases are 460.4 and 275.6, which means the gas flow is well within laminar mode. A small quantity of oxygen can also be mixed into the helium flow, and if so this will be noted in the following text.

6.3 Electrical characteristics

6.3.1 Operation range

Driven at a peak applied voltage, V_p, of 3 kV and at 10 kHz, the 7-jet array is found to fire in all seven channels simultaneously with good jet-to-jet uniformity as shown in figure 6-4 against (a) a downstream ITO (indium tin oxide) ground electrode with the ITO facing the array and placed at 10 mm from the tube nozzles; and (b) the same downstream ITO electrode floated, with its glass side facing the plasma and placed at 13 mm from the tube nozzle. Pictures of both cases have an exposure time of 0.25 s. These two substrates are used to represent metallic and dielectric samples. In figure 6-4a, each of the plasma jets is seen to form a small root on the ITO electrode and the jet root has multiple bright spots. These bright spots are found to shake, sometimes, on the ITO electrode. This is also observed in the case of single jet device in Chapter 4 when employing a downstream metallic substrate. In general, these bright spots do not cause any obvious surface damage nor any significant temperature rise of the substrate. When a dielectric substrate is used, the plasma root spreads on the dielectric surface as shown in figure 6-4b and its impact range on the substrate surface is much larger than that on a metallic substrate. In fact, the blurred purple ‘cloud’ above the dielectric

substrate in figure 6-4b hints an overlapped reaction chemistry coverage of the substrate surface. For both metallic and dielectric substrates, all seven plasmas in figure 6-4 are found to form well collimated jets and their capability to fire simultaneously is found to hold over a large range of the applied voltage and the gas flow rate. Even when a small amount of oxygen (up to O_2/He = 1.5%) is added to the helium carrier gas, the 7-jet array is found to support all seven jets.

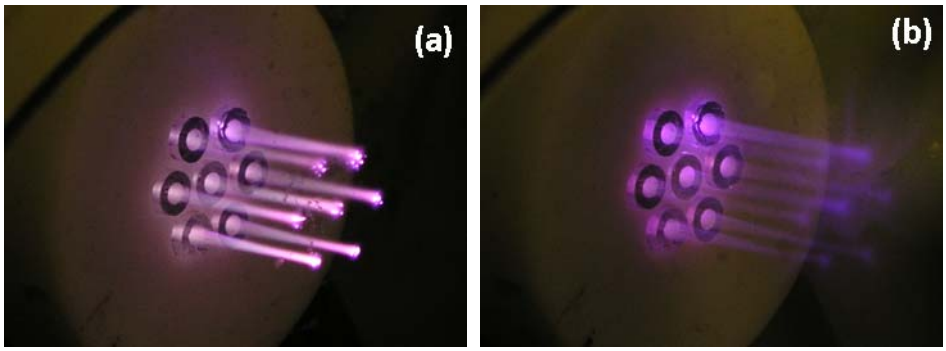

Fig 6-4: Pictures of the 2D 7-jet array in an atmospheric helium flow, at an excitation frequency of 10 kHz and a peak applied voltage of 3 kV, treating (a) an ITO electrode; (b) a glass substrate.

Figure 6-5 indicates the operation range of the 2D 7-jet array with a downstream glass substrate placed at 15 mm from the quartz tube nozzles. The black points in the figure indicate the first ignitions at the tip of capillaries (see discussion in section 6.3.2). With increasing the applied voltage, the plasmas start to extend towards the ring electrode (see figure 6-3), and eventually emerge from the tube nozzles which is indicated by the red points in figure 6-5. Further increase in the applied voltage results in all plasma plumes reaching the substrate and this is labelled by the green points in figure 6-5. Finally the blue points in figure 6-5 indicate the maximum applied voltages beyond which the plasmas become unstable. At a helium flow rate of 0.71 slm per channel, plasmas are ignited at the tips of the capillaries around 1.3 kV but cannot be extended out of the quartz tube to form plumes regardless the value of the applied voltage. With increasing

helium flow rate, it is possible to extend the plasmas to form jets in the downstream region. At 1.07 slm per channel all seven plasma jets reach the downstream substrate at an applied voltage of 1.4 kV. Too much increase in the applied voltage eventually causes the plasma jets to become unstable. Above 1.07 slm per channel, the helium flow rate changes little the plasma ignition voltage, the voltage for all jets to merge from the tube nozzle, and the voltage for them to reach the downstream substrate. However the voltage below which plasma jets remain stable decreases from 4.1 kV for 1.07 slm per channel to 2.8 kV for 2.86 slm per channel. This means that higher flow rate limits the operating range of the 7-jet array. It is also interesting to note that the plasma ignition voltage experiences a clear drop from 0.71 slm to 1.07 slm but above 1.07 slm it remains relatively unchanged. It is clear that in order to form plasma plumes, the 7-jet array should be operated at a flow rate bigger than 0.71 slm per channel. For experiments reported below, the helium flow rate is kept at 2.14 slm per channel.

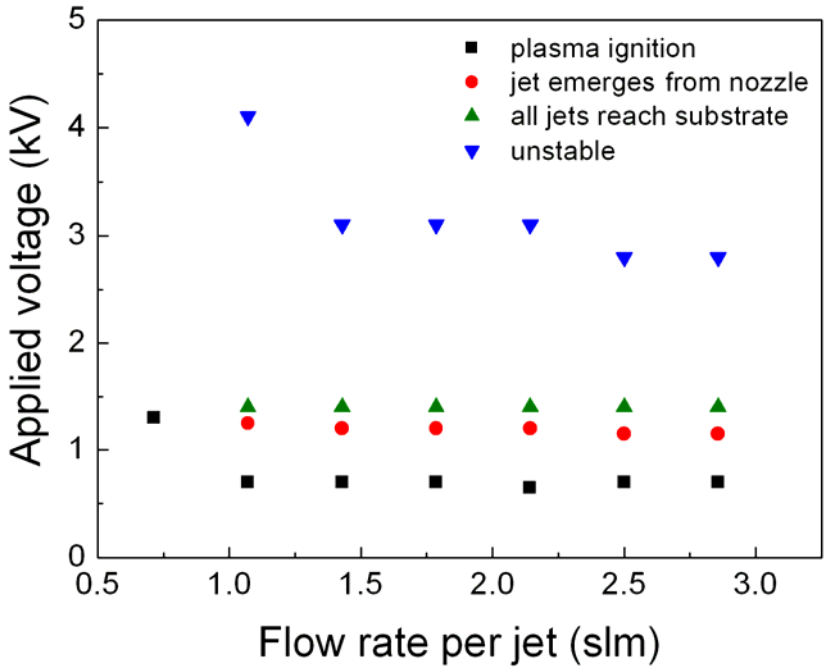

Fig 6-5: Operating conditions of the 2D 7-jet array as defined by the range of the applied voltage and the helium flow rate. A downstream glass substrate is placed at 15 mm from the jet nozzles.

6.3.2 Current, voltage and power

To demonstrate typical waveforms of the applied voltage and the total current of the 7-jet array, an ITO electrode is placed downstream 13 mm away from the quartz tube nozzles with its glass side facing the nozzles and the ITO side grounded so that the current flowing through the substrate can be measured. In this case, 10.7 sccm oxygen is mixed into the helium flow of 2.14 slm per channel (e.g. oxygen/helium = 0.5%). Figure 6-6a shows the voltage and current waveforms when V_p = 2.6 kV. This corresponds to a weak discharge, with the total measured discharge current having a peak value of around 0.08 mA in its positive half cycle and of 0.05 mA in its negative half cycle respectively. These waveforms reflect the DBD nature of the discharge.

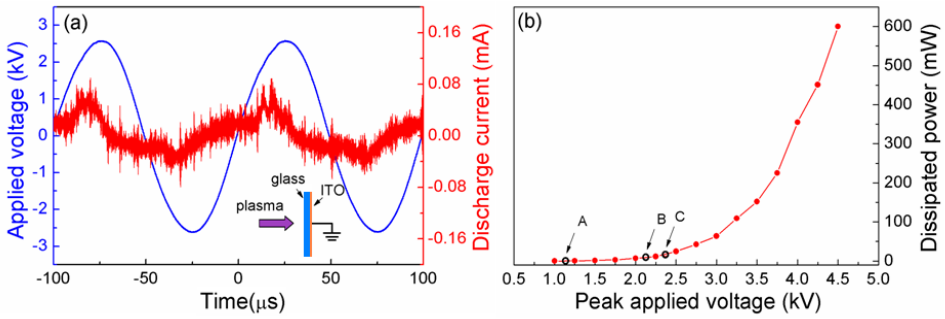

Fig 6-6: Electrical characteristics of the 7-jet array addressing an ITO substrate with its glass facing the plasma jets: (a) time traces of the applied voltage and the total discharge current; (b) the voltage dependence of the total dissipated power. Point A, B and C in (b) indicate, respectively, the ignition point for the six outer jets (simultaneous ignition), the ignition point for the central jet, and the point where all seven jets reach the downstream ITO electrode.

It is observed that the breakdown occurs in the six outer channels first and simultaneously, and then plasma ignition is triggered in the central channel. Figure 6-6b shows the evolution of the voltage dependence of the dissipated power, with point *A*, *B* and *C* representing the ignition of the six outer channels, the ignition for the central channel, and the point of all seven jets reaching the downstream ITO electrode. Point *C* corresponds to $V_p \approx 2.4$

kV, so the current trace at V_p = 2.6 kV in figure 6-6a is obtained shortly after the jets reach the substrate. Once the array-housing unit and the ITO electrode is bridged in all seven channels by the plasma jets, the dissipated power is found to increase more quickly as shown in figure 6-6b. The plasmas then become less capacitive and appear more intense to the naked eye. At V_p = 4.5 kV, the total dissipated power is 600 mW or 85.7 mW per channel. With an estimated plasma volume of 28 mm^3 per channel, this is equivalent to 3.1 W/cm^3, and is about one order of magnitude larger than the typical dissipated power density of 0.3 W/cm^3 in atmospheric helium dielectric barrier discharges sustained between two parallel plates at kHz frequencies[6.31]. This SEAP array therefore gives potentially stronger plasmas with higher plasma density than their counterparts between parallel electrodes.

Electrical characteristics of the 2D 7-jet array are in general similar to those of a comparable single jet, but they are quantitatively different. Figure 6-7 shows the increase of the dissipated power with increasing the applied voltage for two cases of one firing plasma channel, one as the central channel hosted in the 2D jet housing unit with no plasma in all other six channels and the other in a single jet housing unit. These are used to establish whether the different jet housing units may present a significant difference in their impedance in the equivalent circuit of the plasma-producing set up. Figure 6-7 also includes the case of all seven jets firing in the 2D jet-housing unit. It is evident from figure 6-7 that the power-voltage relations are very similar in the two one-channel cases, regardless of the jet-housing structure being a single-channel device or the seven channel array. An additional test is performed with all seven channels in the array structure connected to the power supply but only the central channel fed with the He-O_2 gas, and this case is found to have a very similar voltage dependence of the dissipated power to that of other single-channel cases. In the absence of plasma jets, the equivalent capacitance of the array structure should be different from that of a

single-channel device. The similarity of the one-channel cases suggests that electrical properties are dominated by the characteristics of the firing plasma jet, and that their difference from the jet-array case is mainly due to the difference in discharge properties.

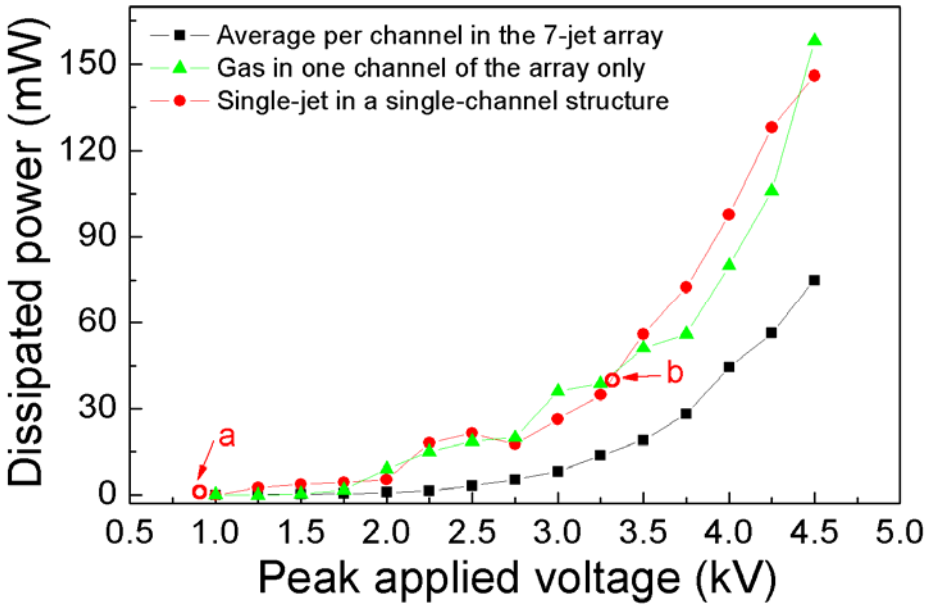

Fig 6-7: Voltage dependence of the dissipated power in one plasma channel, in the case of the seven jet array (black), gas flow and hence plasma formation only in the central channel of the array structure (green, no plasma ignited in the six outer channels), and a single plasma in a single-jet structure (red). For each channel, the helium flow rate is 2.14 slm and the oxygen flow rate is 10.7 sccm. For the single-channel structure case, point *a* indicates its ignition point and point *b* indicates the voltage at which the single plasma jet reaches the downstream electrode.

At a given applied voltage, the jet array appears to consume less electrical power per channel. For example, the one-channel cases consumed about 150 mW at V_p = 4.5 kV where the array consumes 50% less at 75 mW per channel. This is likely a result of jet-to-jet interactions. It is also worth noting that plasma ignition in the one-channel cases occurs at approximately 0.8 kV (point '*a*' in figure 6-7) and the plasma jet reaches the substrate at V_p = 3.3 kV (point '*b*' in figure 6-7). For the ease of reference, the latter is referred to as the bridging voltage at which a plasma jet starts to bridge the powered

electrode to the downstream ground electrode. In the case of the 2D jet array, the plasma ignition and bridging voltages are 1.1 kV and 2.3 kV respectively. Therefore compared to the case of one firing plasma channel, plasma ignition in the 7-jet array occurs at a higher applied voltage but its jets reach the downstream ground electrode at a lower applied voltage.

6.3.3 Effects of the excitation frequency

Excitation frequency is found to influence the operation of the 7-jet array. As shown in figure 6-8, jet-to-jet uniformity of the 2D 7-jet array is sensitively dependent on the excitation frequency, for which wavelength-integrated end-view images of the 7-jet array working in pure helium flow are seen at five different frequencies. The applied voltage is kept at 2.5 kV for all five cases and each image is accumulated over 10 frames, with each frame having an exposure time of one cycle of the applied voltage. The result shows that optical emission is quite uniform among different jets at 5 ~ 10 kHz but this uniformity deteriorates above 10 kHz. Specifically the relative standard variation in the optical emission among different jets is found to be 12.7%, 12.0%, 13.6%, 31.3% and 37.7% at 5, 8, 10, 20, and 30 kHz respectively. In fact, from the observation of this experiment at 20 kHz and 30 kHz, some channels are seen as being too short to reach the substrate which is placed 15 mm away from the nozzles. Stray capacitance is known to exist due to the structure of the jet array and at different frequencies their effective impedances to the external circuit would be different. Low excitation frequencies appear to enable better jet-to-jet uniformity in a similar way to the introduction of individual ballast[6.24]. At low frequencies, the impedance of the stray capacitance (~$1/\omega C$) is larger and is more effective in limiting current. This ballast however is built-in and capacitive, different from the added resistance used in the 1D jet array. It is likely that this built-in capacitance matches the impedance of the remainder of the circuit only at

frequencies within a certain band. Many factors may contribute to jet-to-jet interactions and hence jet-to-jet uniformity, including dynamics of surface charges on the dielectric tubes and cross talks of photons and metastables species between different jet channels. Difference in jet-to-jet uniformity in figure 6-8 is likely to be influenced strongly by dynamic redistribution and relaxation of residual charges on the surfaces of the dielectric tubes and the dielectric block, since the cross-influence between different plasma jets through metastable species (e.g. helium metastables) and photons should not change significantly over a frequency span of 5 ~ 30 kHz. Indeed at lower excitation frequencies, surface charges would have more time to redistribute over the geometric structure of the array and this may contribute to the better jet-to-jet uniformity observed. It is known that surface charges in dielectric barrier discharges are influenced strongly by excitation frequency[6.32]. Images in figure 6-8 are not normalised to the same intensity range and the absolute emission intensity is larger at higher frequencies. For example the brightest point in 30 kHz has an intensity 10 times higher than the brightest point in 5 kHz case. Considering both uniformity and plasma intensity, we believe the optimal frequency for the 7-jet array is around 10 kHz and this will be used for the following study.

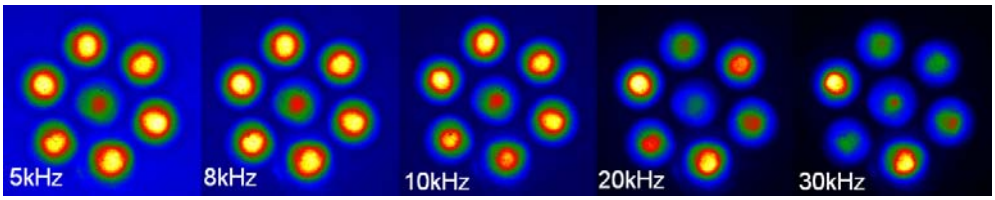

Fig 6-8: End-views of wavelength-integrated optical emission from the 7-channel jet array at five different excitation frequencies of 5, 8, 10, 20, and 30 kHz.

Because of the built-in ballast mechanism, the 7-jet array can not only fire all its seven jets together on flat surface as demonstrated previously, but also treat 3D structures with hollow features. To illustrate this, the 7-jet array

is employed to treat different uneven objects, as shown in figure 6-9 with each picture taken with a domestic digital camera with an exposure time of 0.25 s. Figure 6-9a shows a picture of the 7-jet array treating a sloped metallic surface at 10^{o}, and it is evident that all seven plasmas are firing with good jet-to-jet uniformity. To challenge the jet array with 3D structured objects, we employ the array to treat the same surgical forceps as used in figure 5-2 and the results are shown in figure 6-9b and 6-9c for two different treatment situations. The numbered circles on the right of each graph are hexagonally positioned to indicate the arrangement of the seven jets in relation to their positions on the surgical forceps. The latter are marked with a second set of numbered circles near the roots of the seven channels. In figure 6-9b, the central channel and two other channels (no. 2 and no. 3) are terminated on one tooth of the forceps with a nozzle-to-forceps distance between 5 and 8 mm. All four remaining channels (no. 4 ~ 7) terminate on the surface of the metallic supporting substrate with the same nozzle-to-forceps distance of 20 mm. In other words, the ratio of the longest discharge distance to the shortest is up to 4 (=20/5). Despite of vastly different discharge distances, all seven plasma jets are terminated without compromising plasma stability. It is clear that each channel in the jet array experiences very different jet-to-sample interactions and this scenario would usually lead to the majority of the electrical power being fed to the shortest channel where the effective impedance is the lowest and in turn the unbalanced power consumption would extinguish other channels. Built-in ballast feedback control works well here so all seven plasma jets fire together without being extinguished.

Plasma stability of the 7-jet array in figure 6-9b is found to be independent of its position relative to the forceps. Its built-in feedback function remains robust when the jet array is moved to treat the forceps from different positions. Figure 6-9c shows an example of this, where the first three channels are seen to land on the forceps again and the other four channels on

the downstream supporting substrate. It is worth noting that channel no. 6 is partly clipped by the forceps. However this is not resulting in the 6th plasma channel to terminate on the forceps completely. Instead, the unclipped part of the 6th channel is able to continue its extension towards the downstream supporting plate. This suggests that the plasma jets are robust in their insusceptibility to structural, geometrical and even material variations of the surgical forceps. Similarity between figure 6-9b and 6-9c suggests that this insusceptibility can be achieved at different treatment positions or angles of the jet array relative to the forceps.

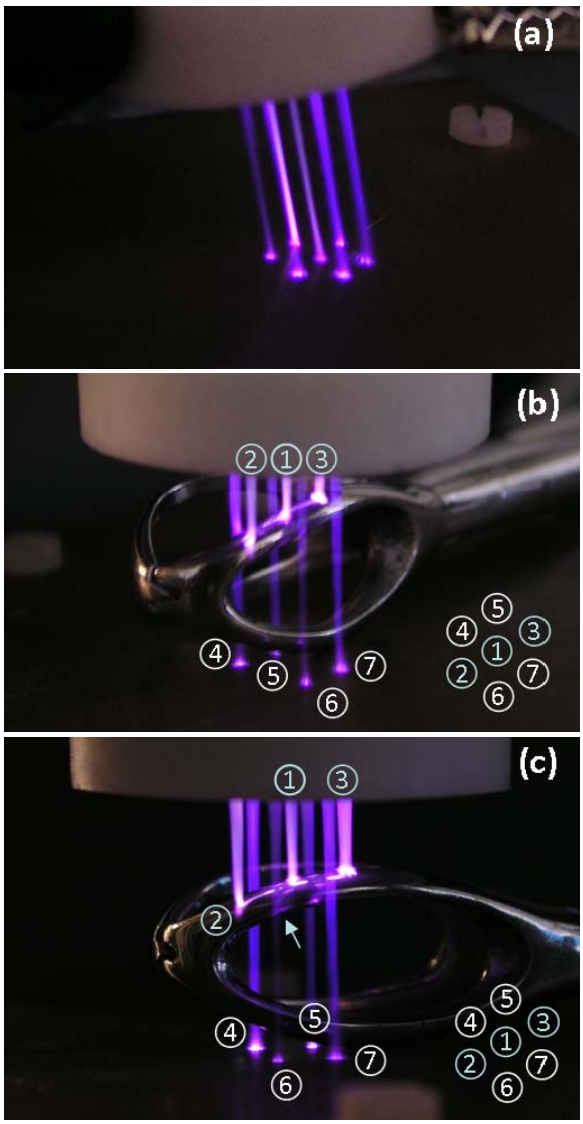

Fig 6-9: Pictures of the 7-jet array treating (a) a sloped metallic plate tiled at 10^{o}, (b) a surgical forceps, and (c) the same surgical forceps at a different position.

6.4 Dynamics

In this section, we report on the dynamics of jet-to-jet interactions and jet-to-sample interactions. To this end, we consider the mode of direct plasma-sample interaction in which the plumes of the 7-jet array contact directly a downstream ITO substrate. Nanosecond-resolved imaging is used to establish the difference between the 7-jet array and a corresponding single plasma jet described in Chapter 4, and the dynamic evolution of all the seven jets in the array. This provides a direct description of jet-to-jet interaction and the plasma stability of the jet array, both being important factors in achieving uniform treatment and ultimately processing reproducibility.

In this experiment, a ITO ground electrode is placed at 13 mm downstream from the quartz tube nozzles, with its glass side facing the 7-jet array. Oxygen is mixed into the helium with its admixture being 0.5%, i.e. a total oxygen flow of 75 sccm in a total helium rate of 15 slm. At V_p = 2.6 kV, the waveforms for the applied voltage, the total discharge current and the ICCD trigger signal are shown in figure 6-10.

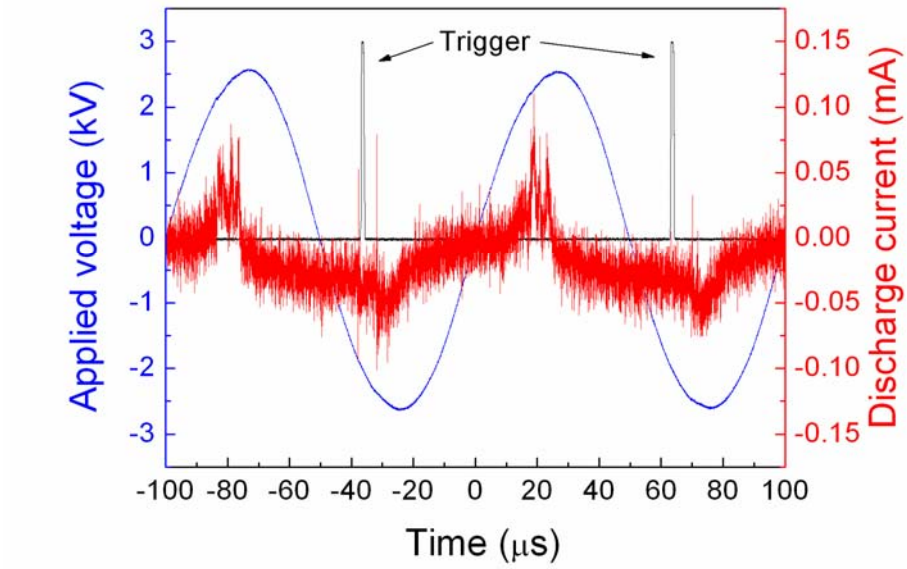

Fig 6-10: Waveforms for the applied voltage, the total discharge current and the ICCD camera trigger signal.

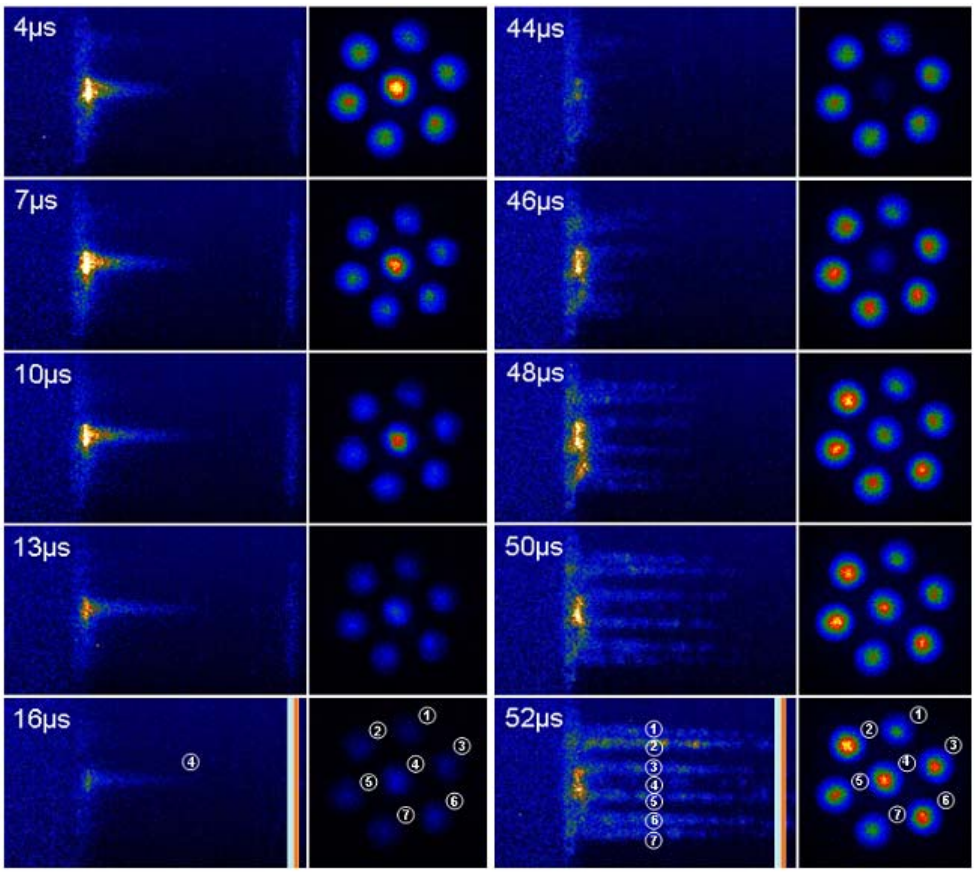

Fig 6-11: Side and end views of the 7-jet array in 10 ns exposure time. Left two columns are for a negative half-cycle of the applied voltage, whereas the right two columns are for a positive half-cycle. The grey and orange vertical lines in the '16 μs' image (in the 1st column) and the '52 μs' image (in the 3rd column) indicate the glass and the metal coating of the downstream ITO electrode.

Nanosecond images taken at different instants over one complete cycle of the applied voltage is shown in figure 6-11, in order to reveal the full course of the 7-jet array's dynamics. These side view images and end view images are normalised to their own intensity range, so that the two sets of the side views are comparable and the two sets of the end views are also comparable. In the first two columns in figure 6-11, the five side views and their corresponding end views are captured at 4 μs, 7 μs, 10 μs, 13 μs and 16 μs after the onset of the trigger when there is a pulse in the discharge current in the negative half cycle of the applied voltage. Each image has an exposure time of 10 ns. It is evident that the central channel is ignited first and it

remains by far the strongest among the seven jets. However no plasma jet ever reaches the downstream ITO electrode. These are in a sharp contrast to the 10 ns images in the last two columns of figure 6-11 for the positive half cycle of the applied voltage. These images are captured at 44 μs, 46 μs, 48 μs, 50 μs and 52 μs after the onset of the trigger signal when the downstream ground electrode is the instantaneous cathode. In this case, plasma ignition starts with the six surrounding channels and it is simultaneous in all surrounding channels (see images taken at 44 μs and 46 μs), and then ignition of the central channel follows. For the positive half cycle the central plasma jet seems to occur a bit later than those of the surrounding plasma jets. Therefore in terms of plasma generation in the central channel and its six surrounding channels, the positive and negative half cycles are quite different. Another difference is that after ignition, all seven jets reach the downstream ground electrode during the positive half cycle whereas none reaches in the negative half cycle.

The above phenomena that the arrival of all seven jets at the downstream electrode occurs in the positive half cycle are consistent with the common recognition that plasma jets are cathode-directed filaments or streamers. However, during the experiment, no plasma bullets are observed at any applied voltage in the stable operation range. This is obviously different to the case of a comparable single plasma jet, for which plasma bullets are routinely observed (figure 4-10).

Spatial uniformity of the plasma jets shown in figure 6-10 is established with an oxygen admixture of 0.5%. To evaluate whether this remains true at other O_2/He ratios, fast imaging experiments are repeated for O_2/He = 0.3% ~ 0.7%. As shown in figure 6-12a, the lowest relative standard deviation of 5% is reached at an oxygen flow rate of 75 sccm or O_2/He = 0.5%. When the O_2/He ratio changes by 0.1% to either 0.4% or 0.6%, relative standard deviation increases significantly to 12% from 5%. As the oxygen admixture

changes, the applied voltage at which to achieve the best jet-to-jet uniformity also changes and the range of its change is about 0.9 ~ 1.1 kV (marked by dots in figure 6-12a). Under the conditions for the best jet-to-jet uniformity for O_2/He = 0.3% ~ 0.7%, it is found that the highest optical emission also occurs at O_2/He = 0.5%. The maximum oxygen atom concentration of He/O_2 APGD is known to be at 0.5%. The highest optical emission at O_2/He = 0.5% in figure 6-12b is desirable for practical applications because of high oxygen atom concentration, and is shown in figure 6-12b where both wavelength-integrated intensity and wavelength-filtered intensity at 845 nm are normalised to their respective values for O_2/He = 0.5%.

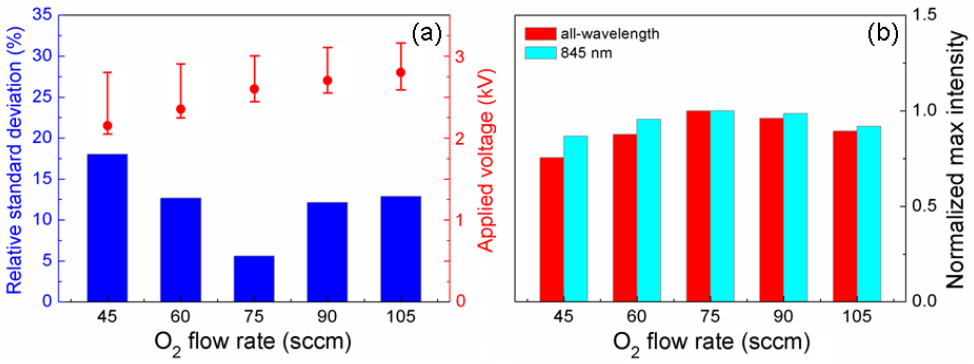

Fig 6-12: (a) Jet-to-jet uniformities measured in relative standard deviation and their applied voltage ranges; (b) normalised maximum emission intensity both wavelength-integrated and resolved at 845 nm as a function of the oxygen mixture rate.

6.5 Optical emission

Plasma dynamics of the seven jets in figure 6-11 exhibit a synchronised jet evolution, and a mirror contrast of plasma generation in the two different half cycles suggests the possibility of optical emission of each plasma channel may average out over one complete cycle to become similar to one another. This suggests that on a timescale relevant to surface processing time (e.g. many seconds to a few minutes), reaction chemistry delivered to a downstream surface by each plasma channel may have good channel-channel

uniformity. To test whether this hypothesis is true, optical emission intensity is employed as an indirect measure of reactive species and hence reaction chemistry, because of the lack of reliable density measurement techniques for relevant reactive plasma agents, including electrons, oxygen atoms, nitric oxides and OH radicals. We consider wavelength-integrated optical emission as a broad indicator of plasma species as well as wavelength-filtered emission for 706, 777 and 845 nm. Helium line at 706 nm is known to represent energetic electrons[6.33], and recently it has also been linked to energetic electrons in RF atmospheric microplasmas[6.34]. Excited atomic oxygen lines at 777 and 845 nm are relevant because of their direct link to ground-state oxygen atoms, which are important for both microbial inactivation[6.35-6.40] and protein reduction[6.41-6.43]. Without being limited to specific applications, energetic electrons and oxygen atoms are used here to represent important plasma agents for plasma medicine.

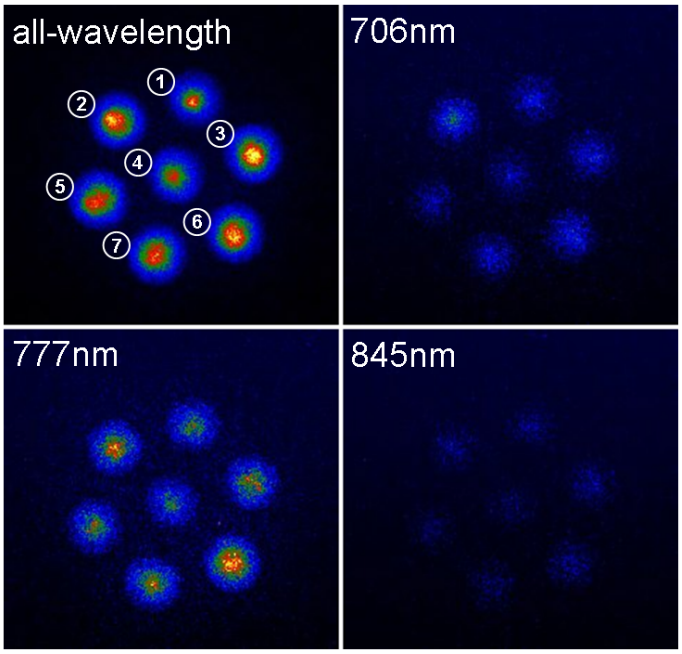

Fig 6-13: End view images of the 7-jet array taken with an exposure time of 10 ns at V_p = 2.6 kV.

First, it is of interest to see whether good uniformity of downstream reactive species can be achieved over a short timescale. Figure 6-13 shows

end view images of optical emission patterns of the 2D 7-jet array at a peak applied voltage of 2.6 kV with an exposure time of 10 ns, both wavelength integrated and filtered for 706, 777 and 845 nm. Good uniformity is evident. Detailed evaluation finds that on a 10 ns timescale the jet-to-jet variation of all wavelength emission intensity is 11.9% whereas that of wavelength-filtered emission is 6.5%, 8.5% and 3.3% at 706, 777 and 845 nm, respectively. It should be noted from figure 6-11 that jet-to-jet variations on a 10 ns scale tend to change depending on when the image is taken. Therefore the variation percentage on the 10 ns scale in figure 6-13 may not be representative of what a downstream sample may experience in terms of reaction chemistry.

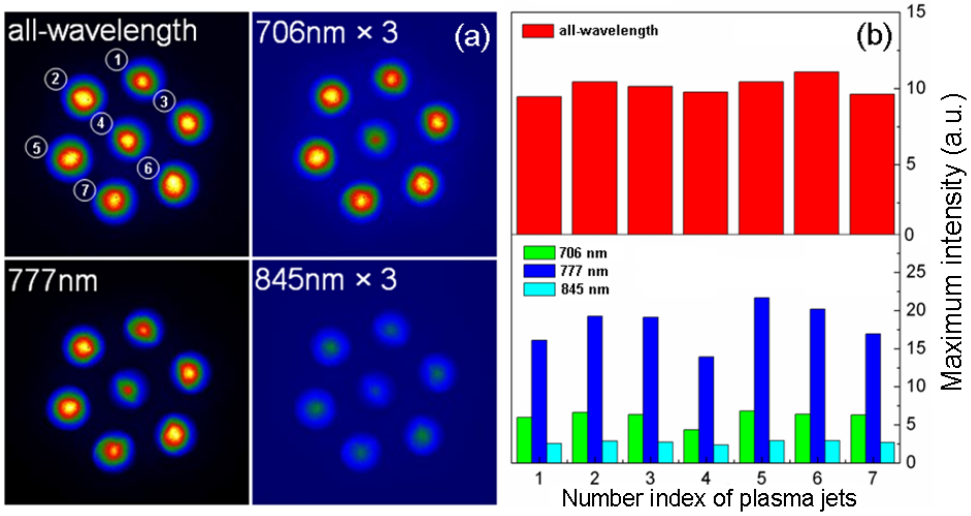

Fig 6-14: (a) End view images of the same four cases as in figure 6-13 but with 100 μs exposure time; (b) the jet-to-jet variation of the peak optical emission intensities, both wavelength-integrated and filtered for 706, 777 and 845 nm.

Figure 6-14a shows end view images of the same four cases again but with an exposure time of 100 μs, which is equivalent to one period of the applied voltage. Emission intensities at 706 nm and 845 nm are comparatively weak compared to that at 777 nm so they are multiplied by a factor of 3 to bring the emission intensities of all three cases to a similar level.

The four cases in figure 6-14a are very similar and indicate good uniformity of reactive species and electrons delivered by individual plasma jets. Figure 6-14b provides a more direct indication of the jet-to-jet uniformity, particularly in the case of wavelength-integrated optical emission and that at 845 nm. Their jet-to-jet variation is found to be 5.6% and 7.9%, respectively. On the other hand, the jet-to-jet variation at 706 nm and 777 nm is larger at 13.5% and 14.7%, respectively. In our experiments, the plasma-substrate interaction is subject to environmental interference without any control chamber and no individual ballast is used. Therefore the variations could be reduced further by, for example, individualised ballasts.

Although the intensities among different jets in the wavelength integrated image in figure 6-14 are reasonably uniform, from its wavelength-filtered images at 706 nm and 777 nm, it is clear the intensity of the central jet is lower than any surrounding jet, at about one third less intensive than the most strongly light-emitting channel in the array. When the carrier gas is changed to pure helium, the phenomenon that the central jet tends to have a lower intensity is also observed, as shown in figure 6-15, for which a glass plate is placed 15 mm from the array nozzles and the wavelength-integrated end view is taken. The central jet experiences a balanced impact of jet-to-jet interaction whereas all six surrounding jets do not. The weak optical appearance of the central channel in comparison to the six surrounding channels may be a result of the interaction among seven hexagonally placed channels.

While a marked improvement is believed to be attainable by imposing smaller fabrication tolerance for the jet array, it is also expected that individualised ballast will improve the jet-to-jet uniformity significantly. Notwithstanding improved jet-to-jet uniformity, it is important to note that uniformity requirements for many processing applications, including plasma medicine, could in practice be relaxed. In the case of biological

decontamination, an overkill by some plasma channels and a just-enough kill by others would result in the target of sterility being uniformly satisfied across the entire surface of the sample. Better inactivation efficacy achieved by an overkill for a small region of the sample surface area means a more rapid attainment of sterility, but the attained sterility is the same as the sterility achieved by just-enough inactivation elsewhere. Therefore the uniformity in processing efficacy can often be addressed with an overkill strategy, provided the overkill strategy does not cause adverse effects on the surface of the substrate, for example etching and surface roughing.

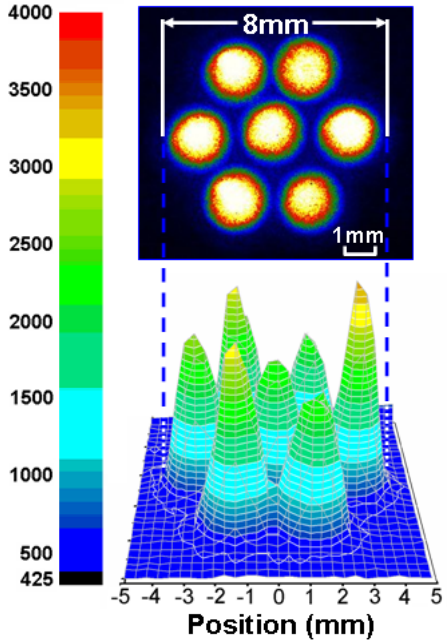

Fig 6-15: A wavelength-integrated end view image of the 2D 7-jet array with an exposure time of 100 μs in pure helium flow.

From the above discussion, good jet-to-jet uniformity of the 2D 7-jet array is well assessed from the maps of optical emission images. Better performance can be expected by using better fabrication and active feedback control. For applications in plasma medicine, an overkill strategy helps attain the processing uniformity.

6.6 Spatial reach of plasma reaction chemistry

The centre-to-centre distance between two adjacent quartz tubes of the 2D 7-jet array is 3.0 mm. Discussions of figure 4-9 and 4-10 indicate the difficulty to precisely measure the plasma diameter on the downstream ground electrode, but suggest that it would be between those estimated with time-accumulated and time-resolved optical emission. With this, the plasma spot on the downstream substrate is estimated to be between 1.4 and 1.8 mm. By using equation (6.1), this is translated into a jet density, $\rho_j = 0.47 \sim 0.60$. This represents the highest jet density compared to typically $\rho_j = 0.05 \sim 0.4$ in previously reported SEAP array studies[6.24,6.25,6.28-6.30].

In principle, it is not possible to achieve plasma uniformity with a unity jet density because space must be provided between channels for mechanical support and thermal management. Therefore it is perhaps unrealistic to expect the light-emitting parts of two adjacent plasma jets in the 2D jet array to overlap. This appears to suggest that the array would need to be moved to fully cover the surface area of a downstream sample even with a large jet density of $\rho_j = 0.47 \sim 0.60$. However, reactive species delivered by a plasma jet to the sample surface will undergo radial transport on the sample surface and as such it is possible for their impact range on the sample surface to exceed the jet-to-jet distance. If this is the case, the entire sample surface would be impinged by an overlapped shower of incoming fluxes of reactive plasma species. This may remove the need for moving the 2D jet array to achieve a complete surface coverage of a downstream sample, and is an important benefit for practical implementation of 2D jet arrays. To test whether the 2D jet array of figure 6-3 facilitates adequate spatial overlap of fluxes of reactive plasma species, we consider the uniformity of its bacterial inactivation without moving the jet array nor the bacterial sample. We use *E. coli* type 1 cells deposited on agar plates in petri dishes, with an initial cell concentration of 10^7 CFU or 5.1×10^5 CFU/cm^2. The petri dish is held on a

metallic ground electrode and the distance between the jet nozzles and agar surface is 13 mm. The peak applied voltage is 4 kV at 10 kHz, and the flow rates are 2.14 slm helium and 10.7 sccm oxygen per channel with a fixed O_2/He ratio of 0.5% according to the previously reported optimum biocidal condition[6.40,6.41]. Temperature of the plasma contact area is measured by burying a temperature strip underneath the agar. The temperature measurement suggests that the sample temperature remains below 45 ^oC for the treatments. Control experiments are performed in ambient air, in a helium/oxygen flow, and on a hot plate maintained at 45 ^oC, all for 5 minutes without plasma. These are found to have little bactericidal effect.

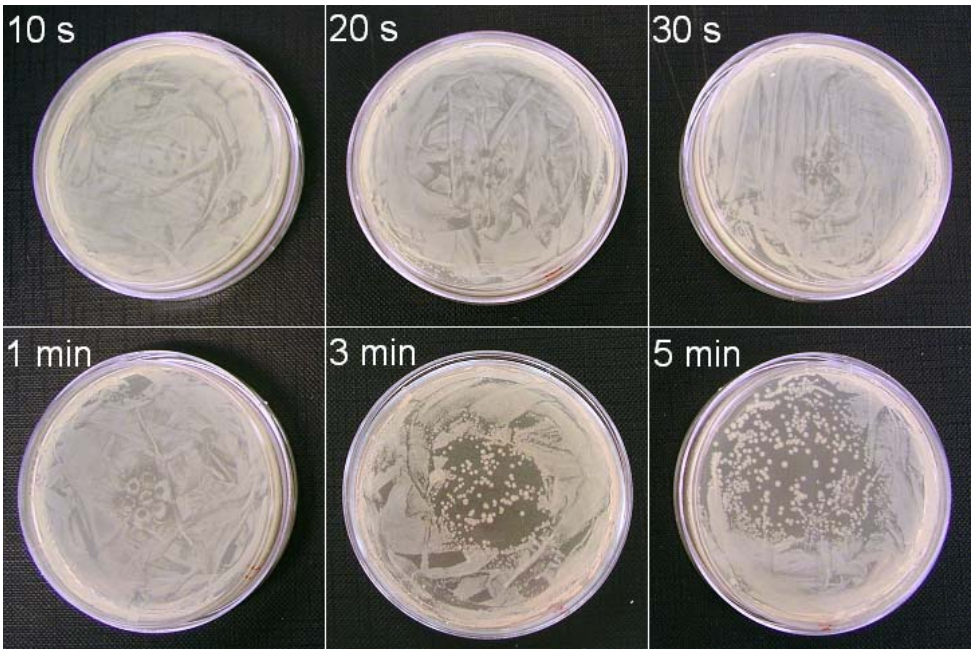

Fig 6-16: The 7-jet array treatment of *E. coli* type 1 cells on agar plates in petri dishes. For all cases, the initial *E. coli* cell density is $5.1x10^5$ CFU/cm^2, the peak applied voltage is 4 kV and the flow rate is 2.14 slm helium with 10.7 sccm oxygen per channel.

Results of *E. coli* inactivation by the 7-jet array are shown in figure 6-16 for six different treatments from 10 seconds to 5 minutes. Clearly longer treatment attains better killing result. After 10 seconds' treatment, the plasma appears to kill the *E. coli* bacteria from the plasma contact point for which the

plasma 'root' can be seen from the image. This root is seen to increase for a longer treatment. Its diameter is found to be around 1.4 mm and 1.5 mm after 30 seconds and 1 minute, respectively. When the treatment is less than 1 minute, these plasma roots are isolated separately from each other. For the 3 minutes treatment, the bactericidal impact from each jet is found to overlap with the surrounding ones, and the bacterial sample now has a circular void of ~27 mm in diameter. For treatment of 5 minutes, the central circular void is further enlarged to have a diameter of ~35 mm.

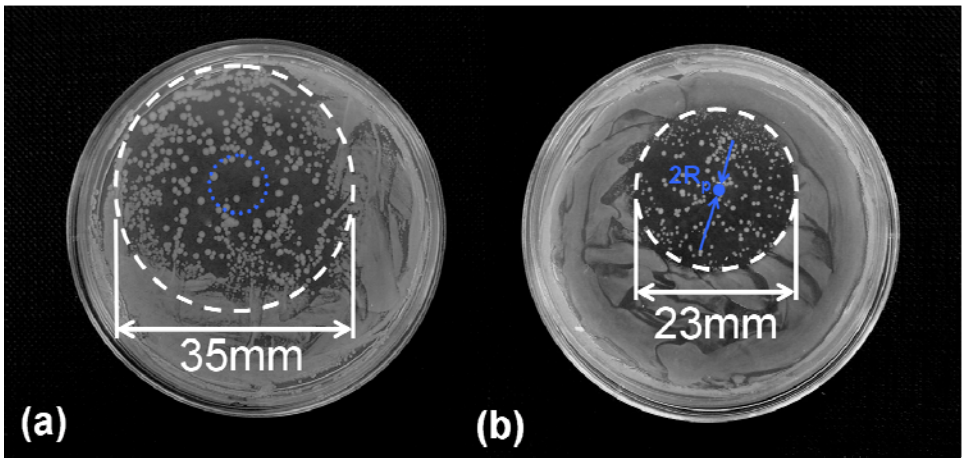

Fig 6-17: Plasma treatment of *E. coli* type 1 cells on agar plates in petri dishes using (a) the 7-jet array, and (b) a single capillary-ring plasma jet. For both cases, the initial *E. coli* cell density is 5.1×10^5 CFU/cm^2, plasma treatment time is 5 minutes, the peak applied voltage is 4 kV and the flow rates are 2.14 slm helium with 10.7 sccm oxygen per channel. The blue circle in (a) and the blue dot in (b) indicate the physical size of the 7-jet array and the size of plasma contact on agar surface respectively. The diameter of the former is 9 mm and that of the latter is 1.4 mm.

A closer view of the sample treated for 5 minutes is presented in figure 6-17a, where no obvious impact of individual plasma jets is evident and the treatment is more uniform than the jet-to-jet uniformity on the downstream glass plate (see figure 6-15). This processing uniformity confirms the possibility that the spatial impact of reactive species on the bacterial sample may accumulate to even out the uneven localisation of individual jets in the

2D array. In other words, the impact of the jets overlaps. This suggests that 2D SEAP arrays can treat a large downstream sample without a relative movement between the jet array and the sample, even though the light-emitting parts of individual plasma channels do not overlap. While further tests are needed for other microorganisms and indeed other biological contaminants, the confirmation of overlapped reaction chemistry has implications not only for practical implementation of SEAP arrays (e.g. exemption of mechanical scanning), but also for the assurance of their treatment reproducibility. The latter is important in the case of treatment of living tissues, for which dosage control is likely to be a central issue[6.44].

To introduce a more quantitative measure of the physical extent of reaction chemistry on the agar plate, we introduce the concept of the reaction chemistry impact diameter D_{imp} and for the treatment of 5 minutes in figure 6-17a D_{imp} = 35 mm. To contrast this against the single jet case, identical *E. coli* samples are treated by the unit jet of figure 6-3 sustained at V_p = 4 kV and 10 kHz. The gas is helium of 2.14 slm mixed with oxygen of 10.7 sccm (i.e. 0.5%), and the treatment time is 5 minutes. Therefore the plasma conditions are identical to those of the 2D jet array. Result of the single jet is shown in figure 6-17b with a reaction chemistry impact diameter D_{imp} = 23 mm. Therefore the impact range of the 2D SEAP array increases by 52% from that of the single jet. It is useful to note that the reaction chemistry impact diameter depends on the character of the biological contaminants and also the treatment time. For *E. coli* type 1 samples used here, plasma treatment of 3 minutes is found to result in a reduced impact diameter of 27 mm and 19 mm for the 2D array and the single jet respectively. These suggest that the increase in the impact range is 42%, smaller than that in the case of 5 minutes. Benefits in extending the physical impact range of reaction chemistry using SEAP arrays are greater with longer treatment times.

It is useful to compare D_{imp} to the size of the light-emitting part of the

plasmas. In the single jet case in a helium-oxygen flow at V_p = 4 kV, its light emitting spot on a downstream glass plate is estimated to be D_{sp} ~ 1.4 mm. For the 2D SEAP array, the light emitting spot of each jet on the same downstream glass plate is also D_{sp} ~ 1.4 mm when the gas is helium-oxygen mixture at O_2/He = 0.5%. Therefore the total area of the light emitting spots of the 2D array, S_{sp} and area of the reaction chemistry impact, S_{imp} are

$$S_{sp} = n\pi(D_{sp}/2)^2 \tag{6.2}$$

$$S_{imp} = \pi(D_{imp}/2)^2 \tag{6.3}$$

where n is the number of the jets in the array. To quantify the relationship of the reaction chemistry impact diameter D_{imp} to the effective plasma diameter, we introduce the concept of the plasma impact ratio as

$$\rho_{imp} = \sqrt{S_{imp}/S_{sp}} \tag{6.4}$$

Equation (6.4) can be simplified as

$$\rho_{imp} = D_{imp}/(\sqrt{n}D_{sp}) \tag{6.5}$$

We found ρ_{imp} = 9.4 and 16.4, respectively, for the 2D array case of figure 6-17a and the single-jet case of figure 6-17b, indicating that the impact of reaction chemistry is much larger than the actual size of the plasma root in both cases. The single-jet case represents a larger scaling ratio in plasma treatment than the array case, and suggests that the plasma impact radio of 9.4 in the 2D array is likely to decrease as the array is scaled up with more channels. The smaller scaling ratio in the 2D array case is due to the fact that the impact extent of the individual jets overlap. Figure 6-18 shows the atomic oxygen emission intensity at 777 nm on the downstream glass substrate overlaid with a circle indicating its reaction chemistry impact range of 35 mm in diameter. The top-right single jet is marked with its own reaction chemistry impact range of 23 mm in diameter, if acting along as a single jet. It is clear that the impact range of the array exceeds that of the top-right single jet and indeed those of the six surrounding jets. Hence under the same plasma

condition, the 2D array has a greater biocidal reach than that predicted from the simple superposition of all individual jets. Long-living helium metastables generated by the central jet may have diffused to the surrounding area and enhanced oxygen dissociation there via $He^*+O_2 \rightarrow O+O^*+He$ and $He_2^*+O_2 \rightarrow O+O^*+2He$, which are known to be the main pathways for production of oxygen atoms in He-O_2 atmospheric plasmas (here O and O* are the ground-state and the excited-state oxygen atoms; He* and He_2^* are excited helium atoms and metastables)[6.45]. This may be responsible for the greater reaction chemistry reach of the 2D array in figure 6-18.

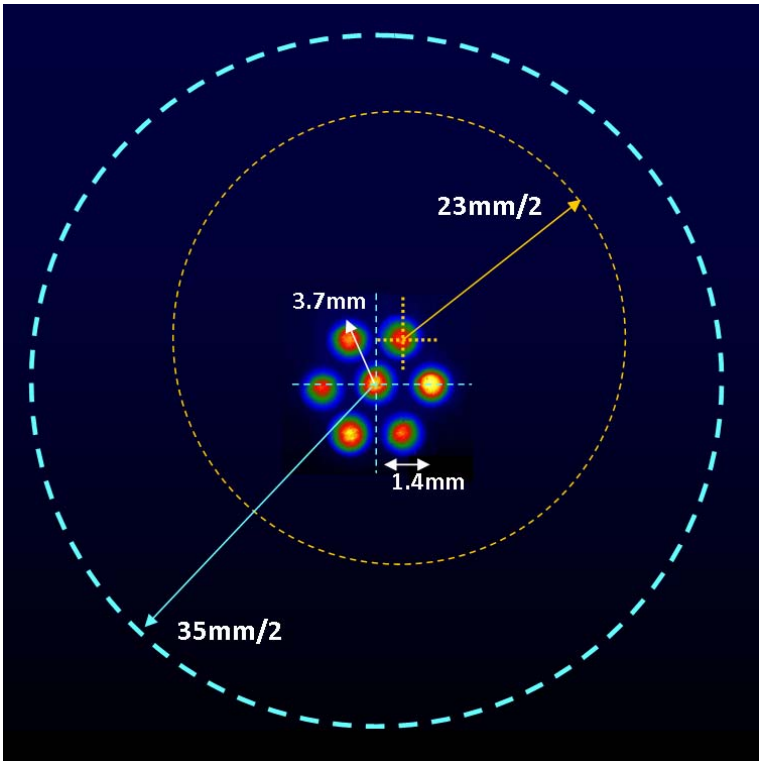

Fig 6-18: An end-view, filtered at 777 nm, of the seven plasma jets on the downstream glass plate, each having a light-emitting spot of ~1.4 mm in diameter. The effective radius of the jet array is estimated from the centre of the central jet to the outside edge of one surrounding jet, and is approximately 3.7 mm. The top-right jet is marked with its reaction chemistry range of 23 mm in diameter, if acting alone as a single jet. The reaction chemistry impact range of the array has a diameter of 35 mm from figure 6-17, and exceeds the range of the top-right single jet.

It has been demonstrated in figure 6-17 and illustrated in figure 6-18 that the spatial overlap of reaction chemistry delivered by individual plasma jets covers all the spaces between any two adjacent plasma jets and there is no untreated region on the entire surface area of the sample as long as the sample is smaller in surface area than the plasma impact range. One implication is that a more tightly packed jet array with a jet density approaching unit may not be necessary. It also implies that with further up-scaling 2D SEAP arrays it would be capable of treating a large surface without relative plasma-sample movement. This is advantageous not only for engineering simplicity but also for processing reliability. In a typical scenario of plasma medicine where an SEAP array is used to treat a chronic wound, movement by either the plasma or the patient introduces variation to the plasma-tissue interaction and in turn this may compromise the reproducibility of the plasma treatment. Minimal moving or even stationary plasma treatment has not been anticipated for plasma jets and jet arrays in the past, partly because existing SEAP arrays are either one-dimensional or with large jet-to-jet distance[6.24,6.25,6.28-6.30], but now it appears to be a distinct possibility.

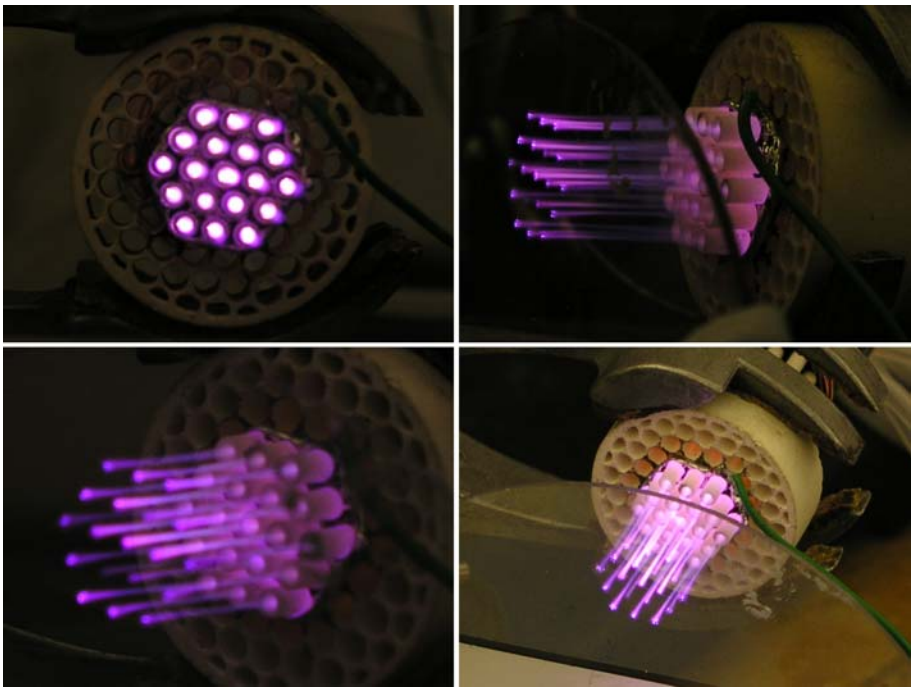

Fig 6-19: Pictures of a 19-jet array viewed from different angles.

The discussion so far in this chapter is mainly about the 2D 7-jet array as an example of the 2D SEAP array. As illustrated in figure 6-1, and explained in the above discussion, the 7-jet array can be up-scaled and practically cover a larger area. As an illustration of its scalability, figure 6-19 shows pictures of a 19-jet SEAP array from different viewing angles. It is clear that all jets are capable of addressing the downstream ITO glass with fairly good jet-to-jet uniformity and plume intensity.

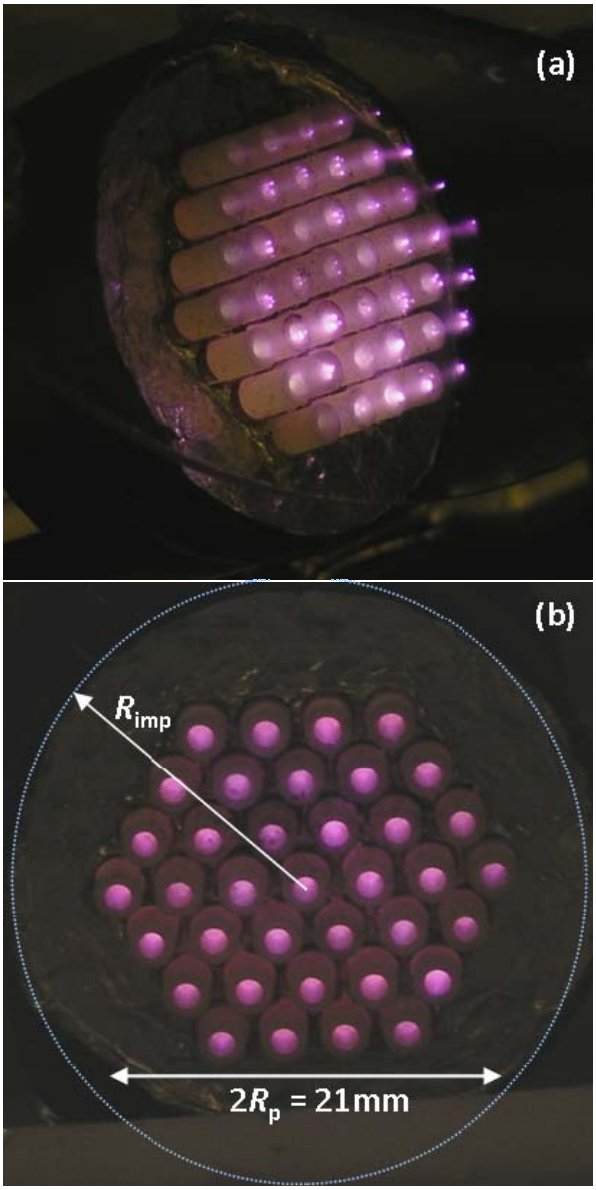

Fig 6-20: A 37-jet SEAP array viewed from (a) the side and (b) the end, both against an ITO downstream electrode. The plasma array diameter is $2R_p$ = 21 mm whereas the impact range of reaction chemistry is much larger. In the case of *E. coli* inactivation, $D_{imp} \approx 48.6$ mm.

By adding another 18 single capillary-ring jet units to the outer ring of the 19-jet array, a 2D 37-jet array is assembled and figure 6-20 shows its treatment of a downstream ITO glass. Again it is evident that the 37-jet array attains similar jet-to-jet uniformity and simultaneous jet firing to the 7-jet array. The plasma array diameter is approximately $2R_p$ = 21 mm. Using reaction chemistry impact values for the 7-jet array and the single jet from figure 6-17, the distance between the edge of the plasma diameter to the edge of the reaction chemistry range is (35mm–2x3.7mm)/2 = 13.8mm. This figure is used to approximate the extent of reaction chemistry of the 37-jet array beyond its diameter and to estimate its reaction chemistry impact range as D_{imp} = 2x13.8+$2R_p$ = 48.6 mm. This dimension is already appropriate for treating skin diseases, some open wounds, and many surgical instruments. In principle, there is no immediate limitation on how far the SEAP arrays could be scaled up to and larger SEAP arrays are certainly attainable. As their up-scaling is pursued further and further, engineering challenges, particularly power supply designs and array architectures, are expected to emerge.

6.7 Summary

Two-dimensional SEAP arrays are studied and discussed in this chapter. The 2D jet array employs capillary-ring jets as its elemental jets, and the jets are arranged in a hexagon-shaped configuration. A 7-jet array is studied as an example. It is found that the 2D 7-jet array has a built-in feedback control mechanism which is influenced by the excitation frequency. At 10 kHz, the array structure is shown to support simultaneous firing of all its seven channels against both metallic and dielectric substrates. The jet-to-jet uniformity is good and the jet density of 0.47 ~ 0.6 represents the highest of all jet arrays reported so far. The 2D jet array also shows a good level of insusceptibility to variations of the downstream samples in their physical dimensions, structural and material properties.

The 2D plasma jet array also exhibits intriguing dynamic behaviours, particularly the difference in dynamics of the central jet and that of the other jets. In the negative half cycle, only the central channel supports a plasma plume. In the positive half cycle, all channels support plasma plumes, suggesting different jet-to-jet interactions.

Optical emission captured from the end view demonstrates that a good jet-to-jet uniformity can be achieved for the 2D jet array. *E. coli* bacteria inactivation experiments confirm spatial uniformity of the plasma array treatment. It is shown that plasma species impact on a much larger surface area than the physical diameter of the plasma array and that the fluxes of reactive species of individual plasma jets overlap considerably on the substrate surface. These are desirable for achieving good processing uniformity and reproducibility.

The 7-jet array is shown to be up-scaled to a 2D 19-jet array and to a 2D 37-jet array. The reaction chemistry impact diameter of the 2D 37-jet array is estimated to be 48.6 mm, and its impact covers an area of 18.6 cm^2. This represents the largest addressable surface area of jet-based plasma sources so far and is already adequate for some applications in plasma medicine. In principle larger arrays are possible if more elemental jets are added. At some point of up-scaling however, this may be challenged by the capability limit of the power supply. To overcome this, the jet array can be operated in a modular fashion. Jet arrays, as many as needed, can operate in parallel each with its own power supply.

In summary, 2D atmospheric plasma jet arrays offer a viable option as large-scale atmospheric plasma sources well suited for many processing applications including plasma medicine.

References

[6.1] K. H. Becker, K. H. Schoenbach and J. G. Eden, J. Phys. D-Appl. Phys. 39, R55 (2006).

[6.2] K. H. Schoenbach, R. Verhappen, T. Tessnow, F. E. Peterkin and W. W. Byszewski, Appl. Phys. Lett. 68, 13 (1996).

[6.3] H. Barankova and L. Bardos, Appl. Phys. Lett. 76, 285 (2000).

[6.4] Y. B. Guo and F. C. N. Hong, Appl. Phys. Lett. 82, 337 (2003).

[6.5] I. G. Koo and W. M. Lee, Plasma Chem. Plasma Process. 24, 537 (2004).

[6.6] L. Baars-Hibbe, P. Sichler, C. Schrader, K. H. Gericke and S. Buttgenbach, Plasma Process. Polym. 2, 174 (2005).

[6.7] L. Baars-Hibbe, P. Sichler, C. Schrader, N. Lucas, K. H. Gericke and S. Buttgenbach, J. Phys. D-Appl. Phys. 38, 510 (2005).

[6.8] C. Schrader, L. Baars-Hibbe, K. Gericke, E. M. van Veldhuizen, N. Lucas, P. Sichler and S. Buttgenbach, Vacuum 80, 1144 (2006).

[6.9] O. Sakai, Y. Kishimoto and K. Tachibana, J. Phys. D-Appl. Phys. 38, 431 (2005).

[6.10] O. Sakai, T. Sakaguchi, Y. Ito and K. Tachibana, Plasma Phys. Controlled Fusion 47, B617 (2005).

[6.11] T. Sakaguchi, O. Sakai and K. Tachibana, J. Appl. Phys. 101, 073305 (2007).

[6.12] P. von Allmen, D. J. Sadler, C. Jensen, N. P. Ostrom, S. T. McCain, B. A. Vojak and J. G. Eden, Appl. Phys. Lett. 82, 4447 (2003).

[6.13] S. J. Park, J. G. Eden, J. Chen and C. Liu, Appl. Phys. Lett. 85, 4869 (2004).

[6.14] S. J. Park, K. F. Chen, N. P. Ostrom and J. G. Eden, Appl. Phys. Lett. 86, 111501 (2005).

[6.15] K. F. Chen, N. P. Ostrom, S. J. Park and J. G. Eden, Appl. Phys. Lett. 88, 061121 (2006).

[6.16] J. G. Eden, S. J. Park and K. S. Kim, Plasma Sources Sci. Technol. 15, S67 (2006).

[6.17] J. G. Eden, Proc IEEE 94, 567 (2006).

[6.18] K. S. Kim, T. L. Kim, J. K. Yoon, S. J. Park and J. G. Eden, Appl. Phys. Lett. 94, 011503 (2009).

[6.19] S. J. Park, J. Chen, C. Liu and J. G. Eden, Appl. Phys. Lett. 78, 419 (2001).

[6.20] O. Sakai, T. Sakaguchi and K. Tachibana, J. Appl. Phys. 101, 073304 (2007).

[6.21] M. Moravej, S. E. Babayan, G. R. Nowling, X. Iang and R. F. Hicks, Plasma Sources Sci. Technol. 13, 8 (2004).

[6.22] M. Iwasaki, H. Inui, Y. Matsudaira, H. Kano, N. Yoshida, M. Ito and M. Hori, Appl. Phys. Lett. 92, 081503 (2008).

[6.23] H. Barankova and L. Bardos, Surf. Coat. Technol. 163, 649 (2003).

[6.24] Z. Cao, J. L. Walsh and M. G. Kong, Appl. Phys. Lett. 94, 021501 (2009).

[6.25] Z. Hubicka, M. Cada, M. Sicha, A. Churpita, P. Pokorny, L. Soukup and L. Jastrabik, Plasma Sources Sci. Technol. 11, 195 (2002).

[6.26] J. G. Eden, S. J. Park, N. P. Ostrom, S. T. McCain, C. J. Wagner, B. A. Vojak, J. Chen, C. Liu, P. von Allmen, F. Zenhausern, D. J. Sadler, C. Jensen, D. L. Wilcox and J. J. Ewing, J. Phys. D-Appl. Phys. 36, 2869 (2003).

[6.27] W. H. Shi, R. H. Stark and K. H. Schoenbach, IEEE Trans. Plasma Sci. 27, 16 (1999).

[6.28] E. Koretzky and S. P. Kuo, Phys Plasmas 5, 3774 (1998).

[6.29] S. P. Kuo, E. Koretzky and L. Orlick, IEEE Trans. Plasma Sci. 27, 752 (1999).

[6.30] R. Foest, E. Kindel, A. Ohl, M. Stieber and K. D. Weltmann, Plasma Phys. Controlled Fusion 47, B525 (2005).

[6.31] M. G. Kong and X. T. Deng, IEEE Trans. Plasma Sci. 31, 7 (2003).

[6.32] X. T. Deng and M. G. Kong, IEEE Trans. Plasma Sci. 32, 1709 (2004).

[6.33] G. Nersisyan and W. G. Graham, Plasma Sources Sci. Technol. 13, 582 (2004).

[6.34] D. W. Liu, F. Iza and M. G. Kong, Appl. Phys. Lett. 95, 031501 (2009).

[6.35] X. Deng, J. J. Shi and M. G. Kong, IEEE Trans. Plasma Sci. 34, 1310 (2006).

[6.36] X. T. Deng, J. J. Shi, G. Shama and M. G. Kong, Appl. Phys. Lett. 87, 153901 (2005).

[6.37] T. Sato, T. Miyahara, A. Doi, S. Ochiai, T. Urayama and T. Nakatani, Appl. Phys. Lett. 89, 073902 (2006).

[6.38] H. Yu, S. Perni, J. J. Shi, D. Z. Wang, M. G. Kong and G. Shama, J. Appl. Microbiol. 101, 1323 (2006).

[6.39] M. Laroussi, C. Tendero, X. Lu, S. Alla and W. L. Hynes, Plasma Process. Polym. 3, 470 (2006).

[6.40] S. Perni, G. Shama, J. L. Hobman, P. A. Lund, C. J. Kershaw, G. A. Hidalgo-Arroyo, C. W. Penn, X. T. Deng, J. L. Walsh and M. G. Kong, Appl. Phys. Lett. 90, 073902 (2007).

[6.41] X. T. Deng, J. J. Shi, H. L. Chen and M. G. Kong, Appl. Phys. Lett. 90, 013903 (2007).

[6.42] X. T. Deng, J. J. Shi and M. G. Kong, J. Appl. Phys. 101, 074701 (2007).

[6.43] D. L. Bayliss, J. L. Walsh, G. Shama, F. Iza and M. G. Kong, New J. Phys. 11, 115024 (2009).

[6.44] M. G. Kong, G. Kroesen, G. Morfill, T. Nosenko, T. Shimizu, J. van Dijk and J. L. Zimmermann, New J. Phys. 11, 115012 (2009).

[6.45] J. L. Walsh, D. X. Liu, F. Iza, M. Z. Rong and M. G. Kong, J. Phys. D-Appl. Phys. 43, 032001 (2010).

Chapter 7
Dual-frequency Plasma Jets

7.1 Introduction

In the previous chapters we discussed low-temperature atmospheric plasmas configured as spatially extended jets as well as jet arrays in different designs. The success of spatially extended atmospheric pressure plasma jets and jet arrays can be attributed to two advantages. First, applications benefit critically from the spatial separation of the plasma generation region from the downstream processing region, thus facilitating a near-sample introduction of versatile reaction chemistry with relatively little impact on plasma stability. Second, spatial extension of those plasma sources makes them able to treat three-dimensional objects. Therefore, atmospheric plasma jet arrays offer an interesting option for treatment of large three-dimensional objects.

Atmospheric plasma jets and jet arrays are relatively new additions to the family of non-equilibrium atmospheric discharges with relatively little understanding of both their technological scope and their underpinning physics. The expanding range of their practical applications puts an increasing focus on two important long-term questions, namely whether future innovations may fundamentally improve their performance as a material processing tool and how their plasma dynamics could be tailored to control downstream reaction chemistry. While these two questions are being pursued sometimes independently, their common goal is to identify effective control strategies with which key plasma parameters can be tuned, separately

but not necessarily independently, to influence and control the functionalities of plasma processing.

The task to achieve controllable plasma processing with physical parameters is particularly challenging for non-equilibrium atmospheric discharges. This is largely due to their very high collisionality that forces a narrow parametric range within which to satisfy multiple and often conflicting requirements such as high electron density and temperature, low gas temperature, robust plasma stability, and active reaction chemistry. Many of these key plasma parameters are intertwined together in strong and sometimes unwanted cross-dependence in most current low-temperature atmospheric plasma sources. For example, an attempt to increase plasma density hence achieve more active reaction chemistry usually leads to a large increase in gas temperature and sometimes plasma instability. The need to reduce gas temperature for processing heat-sensitive materials on the other hand is often met by operating low-temperature atmospheric plasmas in a low current regime or in an afterglow mode for which reaction chemistry may be significantly compromised. It should be acknowledged that engineering solutions may mitigate some of the unwanted cross-correspondences and achieve an acceptable application efficacy for a specific application. However it is always desirable to seek a general strategy that weakens these cross-correspondences and enhances opportunities for better process control.

The jets considered in the previous chapters all employ electrical excitation in the kilohertz range (referred to as AC). This is because in comparison with radio-frequency (RF) or microwave excited jets, AC excited plasma jets tend to achieve a longer plume, which is desirable for treating three-dimensional objects, and a lower gas temperature which is necessary for treating heat-sensitive materials. By contrast, RF plasma jets tend to achieve a higher plasma density but have short plasma length and high gas temperature, both restricting their own application scopes. The results in Chapter 4 show

that the hybrid capillary-ring jet has an upstream plasma region between the capillary electrode and the ring electrode, and a downstream plasma processing region. This spatially separated structure motivates an initiative to explore dual-frequency excitations to the capillary-ring jet as an attempt to separate the control of three fundamental plasma quantities in jets, namely plasma plume length, plasma density and gas temperature. This is the focus of this chapter.

Dual-frequency excitations are known to be beneficial for low pressure capacitively coupled plasmas[7.1], but their use for atmospheric plasmas are rare and so far limited to a co-located excitation at two similar radio frequencies in the parallel-plate electrode configuration [7.2,7.3]. In the latter case, the effects of the two excitation frequencies are strongly coupled, encouraged by their co-located application. This is different from our goal of weakening and separating the cross-dependence of plasma density, plasma plume and gas temperature. The spatially separated dual-frequency excitations to be introduced are novel for non-equilibrium atmospheric plasmas in general and atmospheric plasma jets in particular.

This chapter is organised as follows. Details of the design of the spatially separated dual-frequency jet are discussed in section 7.2. Its characteristics are detailed in section 7.3 including the control of plasma plume, plasma density and gas temperature. Finally a summary is given in section 7.4.

7.2 Design and experimental setup

Figure 7-1 shows a schematic of the experimental setup and the design of the dual-frequency jet. A capillary-ring jet is used with the same capillary and ring electrodes and the same quartz tube as those described in Chapter 4. The ring electrode wraps tightly around the quartz tube and is placed 1 mm away from the tube nozzle. It is electrically grounded. The capillary electrode

is connected to a RF power supply via a matching network and the axial distance between the capillary tip and ring electrode is set to 1 mm. The frequency of the RF power supply is fixed to 5.5 MHz. The third electrode, a metal plate, is connected to an AC power supply with a frequency at 30 kHz and an amplitude up to 5 kV. It is placed some distance away from the tube nozzle to form a downstream region. As a result of the above design, the influence of the RF excitation is confined mainly in the upstream region between the capillary and ring electrodes, whereas the influence of the AC excitation is confined largely to the open downstream region between the ring and the plate electrodes. This spatially separated application of the dual frequency excitations is useful to maximise control of plasma dynamics.

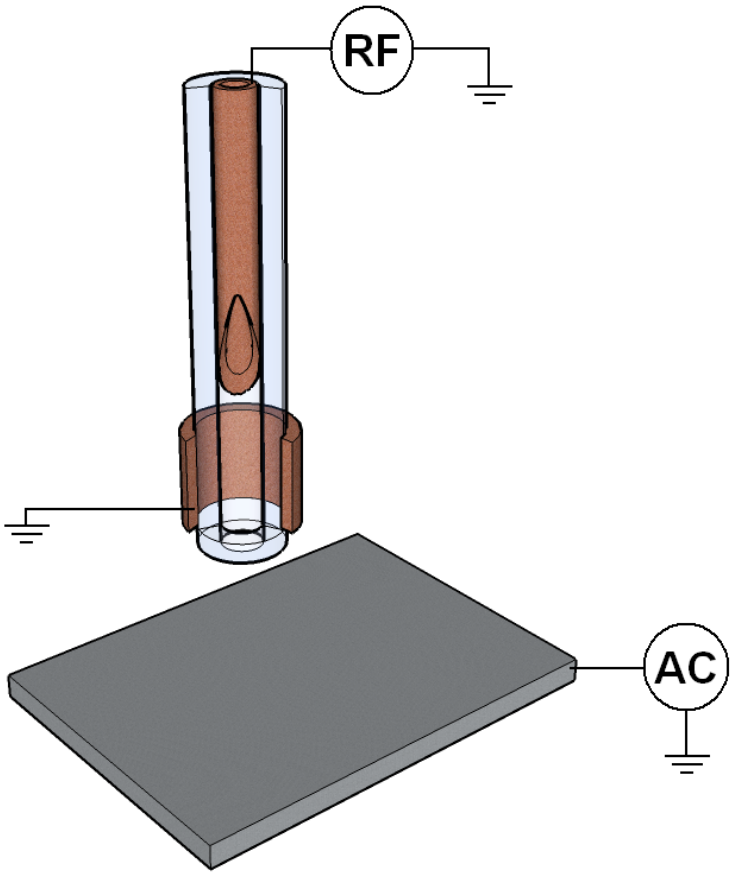

Fig 7-1: Schematic of a spatially separated dual-frequency excited jet with a capillary electrode (also doubling up as the gas inlet), a ring electrode placed near the nozzle of the gas-confinement quartz tube, and a downstream plate electrode. Also shown are power connections of the dual-frequency excitations.

For experiments reported here, a helium flow (99.996%) of 4 slm flows through the capillary electrode and then the quartz tube if not stated otherwise. The flow rate is well within the laminar flow range. Two Tektronix P6015A voltage probes are used to monitor the applied voltages to the capillary electrode and the plate electrode, respectively. Discharge current is measured by a Pearson 2877 current probe. These electrical signals are recorded by a Tektronix DPO4104 oscilloscope. Plasma images are taken with either an Andor DH720 ICCD camera or a domestic digital camera. Spectroscopic signals for optical emission used for estimating the rotational temperature are measured via an Andor Shamrock SR-303i spectrograph. Broad spectra are obtained with an Ocean Optics 2000 spectrometer with absolute emission intensity determined by using an Ocean Optics LS-1-CAL NIST traceable white light source in the 350 ~ 1000 nm range.

7.3 Characteristics of the dual-frequency jet

7.3.1 Plume length

Figure 7-2 provides an overview about how the spatially separated dual-frequency jet works. All the images have an exposure time of 33.333 μs which is equal to one cycle of the applied AC voltage, and they are normalised to the same intensity range. As a result, the intensities of these images are directly comparable. The nozzle-to-plate distances are 1.5 cm in figure (a)-(e) and 3.0 cm in figure (e), respectively. The white rectangular lines outline the positions of the quartz tube and the capillary electrode. The red square indicates the location of the ring electrode and the vertical red line indicates the plate electrode.

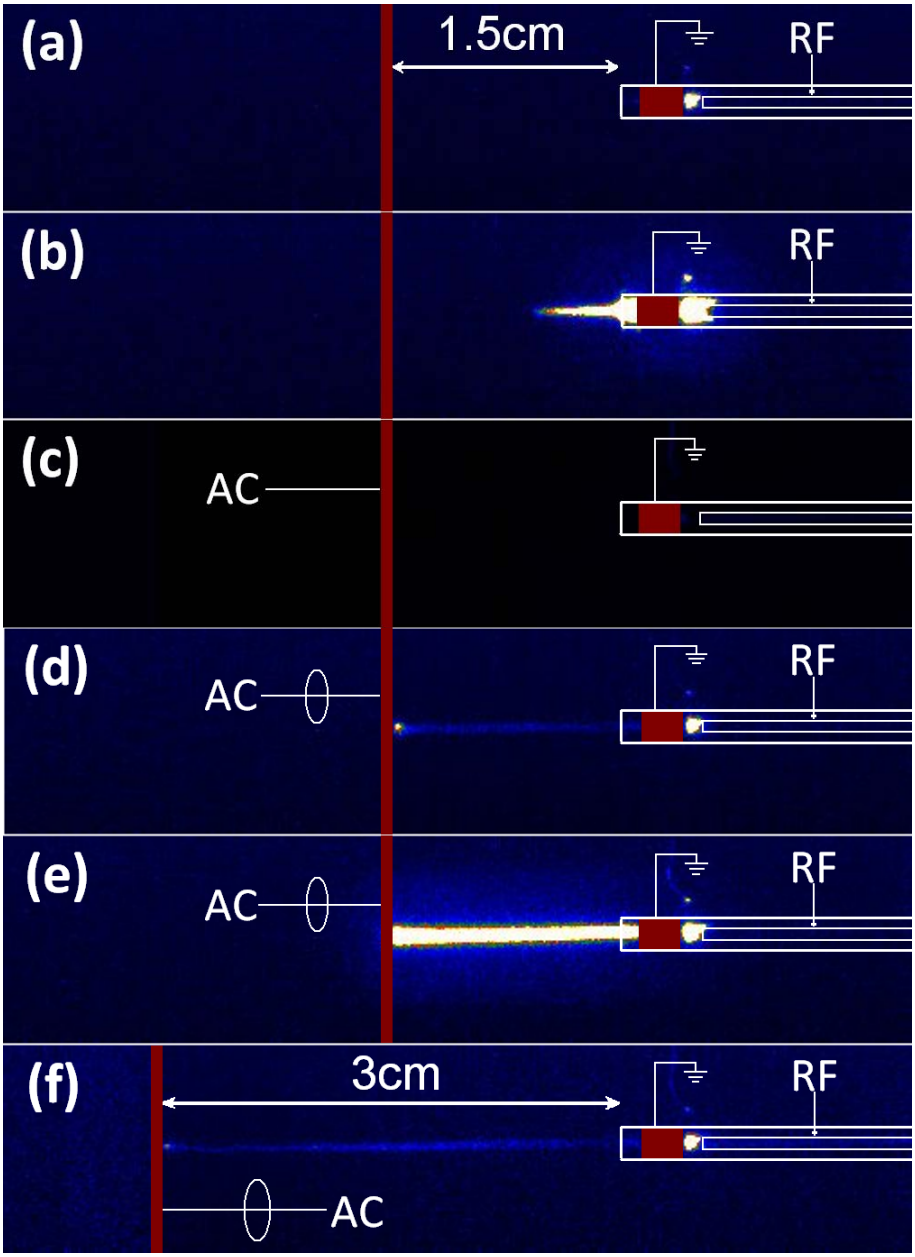

Fig 7-2: Images of the spatially separated dual-frequency. (a) V_{RF} = 1.0 kV, V_{AC} = 0 V; (b) V_{RF} = 2.0 kV, V_{AC} = 0 V; (c) V_{AC} = 6.0 kV, V_{RF} = 0 V; (d) V_{AC} = 3.0 kV, V_{RF} = 1.0 kV; (e) and (f) V_{AC} = 5.0 kV, V_{RF} = 1.0 kV with different nozzle-to-plate distances.

The first three images show the profiles of plasmas if only one frequency is applied to the jet, i.e. either the capillary or the plate electrode is powered. When the AC power supply is off, with increasing the applied RF voltage, breakdown occurs between the capillary tip and the ring electrode when the peak-peak RF voltage (V_{RF}) is higher than 1 kV. Immediately after the

breakdown, the discharge voltage is reduced to less than 600 V. Figure 7-2a shows the situation when V_{RF} = 1.0 kV. A bright plasma is located in the upstream electrode gap and it is not seen to extend downstream beyond the ring electrode. Still with AC power off, the plasma in the upstream region expands its volume and its plume extends towards the downstream region when V_{RF} is further increased. Around V_{RF} = 1.2 kV, the plume starts to extend out of the jet nozzle. Figure 7-2b shows this situation when V_{RF} reaches 2 kV. It is found that an intense plasma plume is formed and its length outside the quartz tube is about 5 mm. The plume length remains 5 mm even with further increase of the applied RF voltage due to an electron trapping mechanism for RF atmospheric plasmas[7.4]. Specifically, for V_{RF} = 2 kV, the value of the electric field strength, *E*, between the capillary tip and the downstream plate electrode is $2000/(2\times2^{0.5}\times2)$ V·cm^{-1} (according to equation $E = V/d$, where V is the applied voltage and d is the distance). Knowing that the electron mobility is 1132 cm^{2}V^{-1}s^{-2}, the electron transition time across the electrode gap of 2.0 cm (from the capillary tip to the plate) is found to be 5 μs, which is much longer than the half RF cycle of 91 ns. As a result, electrons cannot travel further to bridge the gap between the capillary tip and the downstream metal plate. This phenomenon is consistent with the typical RF jets being millimetre in length[7.5]. The bright plasma plume indicates a high plasma density. This is because the high excitation frequency makes electrons travel back and forth quite quickly and the resulting collisions lead to an intense plasma, i.e. an abundant electron source.

If the jet is only powered by AC for the plate electrode (i.e. without the RF power), it is found that the peak-peak AC voltage (V_{AC}) needs to reach more than 6 kV to trigger breakdown. This high breakdown voltage is a result of the relatively weak electric field between the plate electrode and the ring electrode. Figure 7-2c is taken at V_{AC} = 6.0 kV in which no plasma is present.

The combination of the RF and AC excitations can change the plasma

evolution remarkably. Figure 7-2d shows a situation with V_{RF} = 1.0 kV and V_{AC} = 3.0 kV, each alone being unable to extend the plasma outside the quartz tube. However a 15 mm long plasma jet is formed outside the tube with the dual-frequency excitations. A further increase of the AC voltage to V_{AC} = 5.0 kV with V_{RF} = 1.0 kV fixed is seen in figure 7-2e to significantly increase the optical emission of the plasma jet. This emission intensity is comparable to that in figure 7-2b, suggesting similar plasma density achieved to the high plasma density of the RF jet in figure 7-2b. Moreover, the dual-frequency excitations are capable to extend the plasma for a longer plume length. Still with the same applied voltages as those in figure 7-2e, i.e. V_{AC} = 5.0 kV and V_{RF} = 1.0 kV, the plume length is seen to reach 3.0 cm as shown in figure 7-2f. Compared with figure 7-2e, the plume intensity in figure 7-2f is weaker. This is because as the nozzle-to-plate distance increases the electric field induced by the AC power decreases, and as a result the ability to draw the intense plasma from the upstream region towards the downstream region becomes weaker. Experiments confirm that if a higher AC is used for the case of figure 7-2f, the intensity of the downstream plasma plume can be enhanced. In other words, the progress from figure 7-2d to figure 7-2e is repeatable.

The above illustration is a fairly representative of how dual-frequency excited jets work. It appears that the spatially separated dual-frequency excitations can control the jet plume and plasma density separately. It is of interest to see that, with the addition electrons fed from the upstream RF discharge, the long plume length of dual-frequency jet can be achieved at relatively low applied voltages. To see this more clearly, the plate electrode is placed at different downstream locations until the tip of the dual-frequency jet just touches the plate electrode. This is referred to as the longest plume length measured from the tube nozzle to the plate electrode. In figure 7-3a, the longest plume length of the RF plasma jet (V_{AC} = 0 V) is seen to increase monotonically with V_{RF} and its maximum value is about 5 mm at V_{RF} = 2.0

kV, above which the length does not change. For the dual-frequency jet case, its longest plume length is found to be much longer than that of RF jet and can reach 36 mm at V_{AC} = 6.0 kV and V_{RF} = 1.0 kV. When $V_{AC} \geq$ 5.0 kV and $V_{RF} \geq$ 1.0 kV, the longest plume length is always longer than 30 mm, which is 5 times longer than the longest plume length in RF jet case. The dependence of the plume length on V_{RF} is also different. The plume length increases quickly with the increase of V_{RF} till V_{RF} = 1.0 kV after which it undergoes much slower change. This gradual change varies from a small increase at V_{AC} = 3.0 kV to a small decrease at $V_{AC} \geq$ 5.0 kV. All these results suggest that the additional use of the AC excitation changes substantially the plasma plume length in dual-frequency plasma jets.

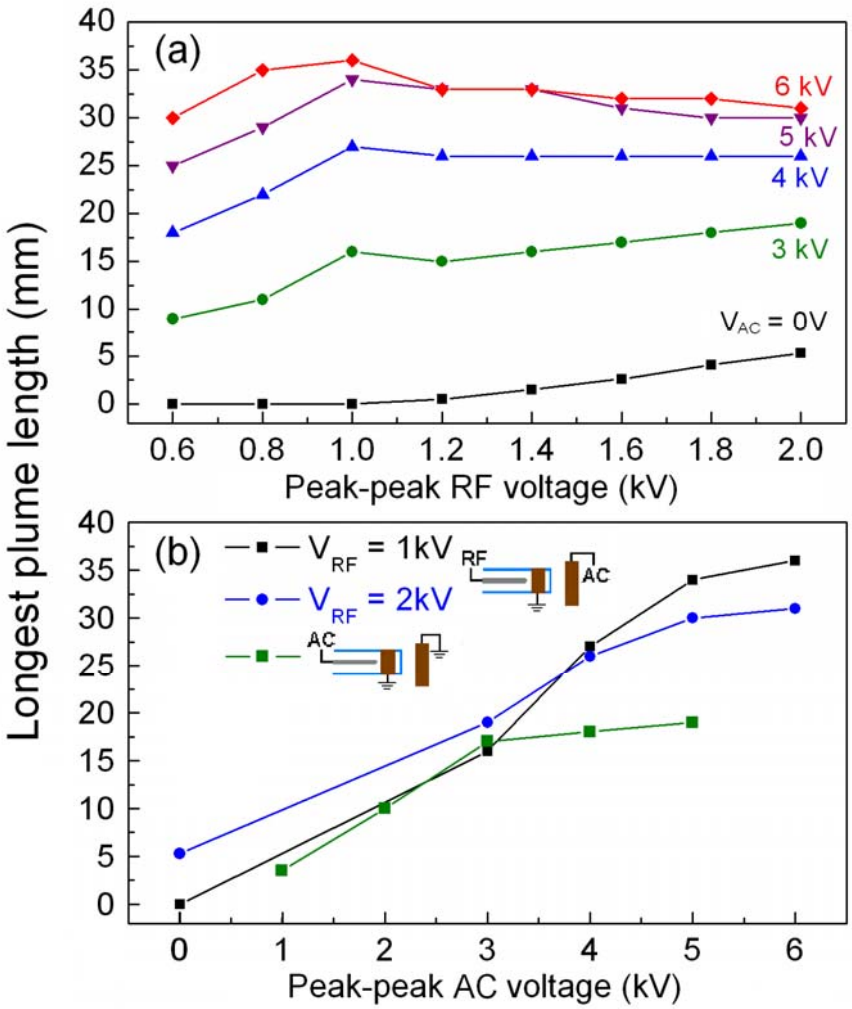

Fig 7-3: The longest plume length as a function of (a) the RF voltage and (b) the AC voltage.

It should be remarked that the downstream plate electrode is powered at AC to maximise the spatial separation of the two excitations for the dual-frequency jet. However to compare its plume length to that of a conventional AC jet, it is appropriate to power the capillary electrode at AC, as indicated in the insert of figure 7-3b. In this case, figure 7-3b shows that the maximum value of its longest plume length is 20 mm when V_{AC} = 5.0 kV. The plasma jet becomes unstable if V_{AC} is raised above 5.0 kV, and so the longest plasma plume length is about 20 mm with the AC excitation alone. With V_{RF} switched onto the capillary electrode and V_{AC} = 6.0 kV now applied to the plate electrode, the plume length increases significantly to around 31 ~ 36 mm. This is markedly higher than the maximum 20 mm of the plasma plume in the AC jet. It should be noted that although the AC excitation influences most significantly the plasma plume length, the RF excitation has its own influence. The two dual-frequency cases in figure 7-3b suggest that the plume length can be 5 mm longer at V_{RF} = 1.0 kV than at V_{RF} = 2.0 kV when V_{AC} = 6.0 kV in both cases. Also when V_{AC} is higher than 3.0 kV, the plume length at V_{RF} = 1.0 kV seems has a quicker increase than that at V_{RF} = 2.0 kV. This could be a result of stronger electron trapping in the upstream region with a larger V_{RF}[7.4].

From the above discussion, it is clear that the upstream RF discharge is a source of intense plasma, which itself cannot extend to more than 5 mm into the downstream region due to the electron trapping. The downstream AC power can draw electrons out of the upstream plasma by the electric field set up between the plate electrode and the ring electrode. The electrons generated upstream could become seed electrons to influence the downstream breakdown.

7.3.2 Voltage and current characteristics

Figure 7-4 shows typical temporal behaviours of the two applied voltages (V_{RF} = 1.0 kV, V_{AC} = 4.0 kV) and the discharge current, the latter of which is measured between the AC power supply and the ground to capture the electrical signature of the plasma jet in the downstream region. The nozzle-to-plate distance is 15 mm. The insert provides an enlarged view for the RF voltage waveform. It is clear that the discharge current is made of a slow-changing AC component superimposed with a fast-oscillating RF component. There is also a significant negative dc bias in the RF voltage and this is absent in the case of the RF jet, suggesting new physics for example an asymmetric discharge structure. These indicate a clear interaction between influences at the two excitation frequencies. In particular, the upstream discharge sustained by the RF excitation is dense and provides an additional electron source to the downstream AC-sustained discharge. This increases the plasma density in the downstream. Operating at a much lower excitation frequency, electron wall loss in AC jets is severe with little electron trapping and as a result their electron density tends to be lower than that in an RF jet.

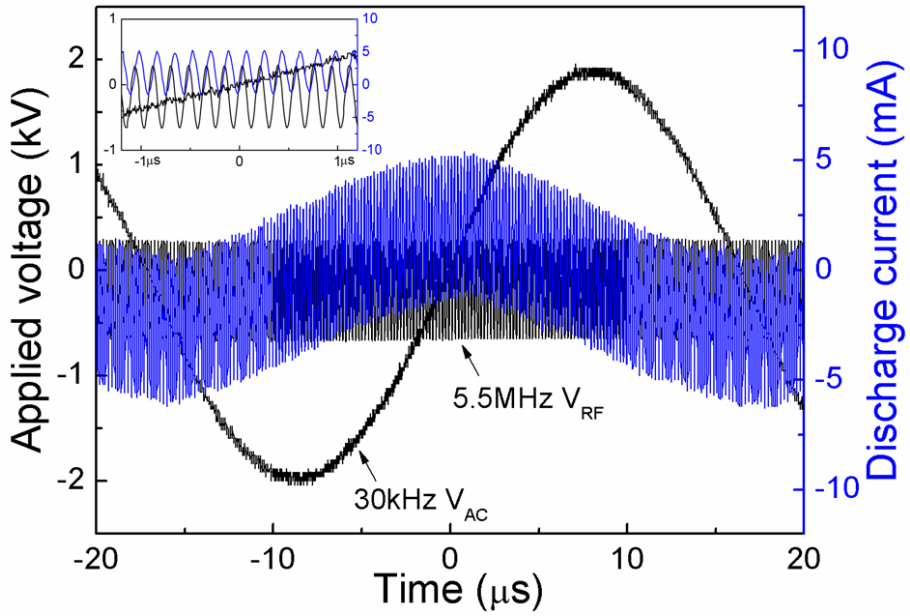

Fig 7-4: RF and AC applied voltages together with the discharge current, with the latter measured between the AC power supply and the ground.

However the reduced electron trapping also allows the AC jet to be spatially extended. With the upstream discharge providing considerable seed electrons to the downstream AC plasma jet, the plasma density of the latter is enhanced substantially along its full plume length.

7.3.3 Plasma density and gas temperature

Spatially separated dual-frequency excitations have been shown to control the plasma plume length and plasma density separately. It is now of interest to study whether it could be used to control plasma density and gas temperature separately.

Absolute wavelength-integrated optical emission intensity from 350 nm to 900 nm is measured as an indirect indicator for plasma density. It is measured by using an Ocean Optics 2000 spectrometer with an optical fibre placed close to the jet contact point on the plate electrode. More detailed spectrum in the N_2^+ first negative system from 388 nm to 392 nm is collected using an Andor Shamrock SR-303i spectrograph. It is compared with the simulation results obtained from LIFBASE software[7.6], to determine rotational temperature, T_{rot}, which is a good approximation of gas temperature[7.7].

We consider three configurations, namely two single frequency excitations at AC and RF and the dual-frequency excitations. For the dual-frequency case, both V_{RF} = 1.0 kV and V_{RF} = 2.0 kV are considered. As the plume length of the RF jet is small, the downstream plate electrode is placed 4 mm from the quartz tube nozzle for the RF jet. For the AC and dual-frequency jets, this distance is 15 mm.

Figure 7-5 shows that both the absolute emission intensity and T_{rot} as a function of the applied voltage. It is found that both the emission intensity and T_{rot} increase with the applied voltage. For the RF jet in figure 7-5a, its

emission intensity is seen to increase significantly from 0.6 μW/cm^2 at V_{RF} = 1.6 kV to 19.8 μW/cm^2 at V_{RF} = 1.8 kV, during which the corresponding T_{rot} increases from 360 K to 490 K. For the AC jet in figure 7-5b, its emission intensity undergoes a more gradual increase from 5.2 μW/cm^2 at V_{AC} = 3.0 kV to 14.9 μW/cm^2 at V_{AC} = 5.3 kV. The corresponding T_{rot} increases from 380 K to 490 K. V_{RF} = 1.8 kV and V_{AC} = 5.3 kV are near the operation upper limit above which plasma tends to be unstable, so they mark the capacities of the RF jet and AC jet respectively. The RF jet is seen to reach a higher plasma

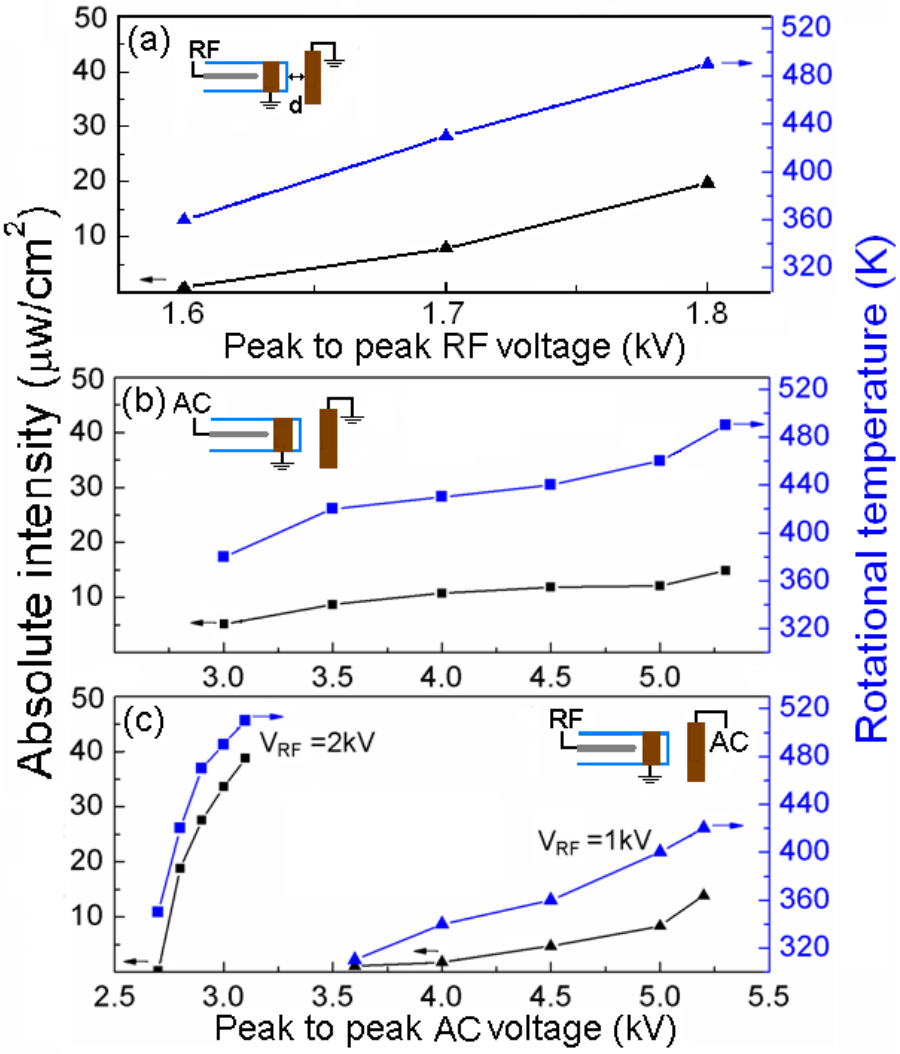

Fig 7-5: Absolute wavelength-integrated emission intensity (in black) and gas temperature (in blue) for the jet powered at (a) RF; (b) AC; and (c) dual-frequency. The plate electrode is placed 4 mm downstream from the tube nozzle for the RF case, and 15 mm for the two other cases.

density than the AC jet at the contact point, and this is consistent with the fact that RF provides a more dense plasma. The gas temperature is near 490 K for both RF and AC jets when they reach their maximum plasma density at the contact point.

For the dual-frequency jet case in figure 7-5c, a larger V_{RF} is found to substantially increase the emission intensity. At V_{RF} = 2.0 kV, an increase of V_{AC} from 2.7 kV to 3.1 kV leads to an increase of emission intensity from 0.2 μW/cm^2 to 38.8 μW/cm^2, which is 2.0 and 2.6 times of those maximum for the RF and AC jets, respectively. The T_{rot} is also seen to undergo a noticeable increase, from 350 K to 510 K, when V_{AC} increases from 2.7 kV to 3.1 kV. However, the increase of emission intensity in the dual-frequency jet is achieved at lower gas temperature. For example, the emission intensity corresponding to $T_{rot} \approx$ 400 K is similar at about 7 μW/cm^2 for both the AC and RF jets and about 15 μW/cm^2 for the dual-frequency jet. This represents a factor of 2 in the intensity ratio. At V_{RF} = 1.0 kV, the increase of emission intensity and T_{rot} is smaller than the larger V_{RF} case. However the emission intensity reaches 13.9 μW/cm^2 with T_{rot} at 420 K. This represents a similar emission intensity to the maximum achieved by the AC jet, but with the gas temperature at 50 K lower. Therefore the dual-frequency jet enables a route to separate tuning of plasma density and gas temperature. When the upstream RF operates at a high applied voltage, with relatively small change to the gas temperature, the dual-frequency jet can produce stronger plasma than its single-frequency counterparts. When the upstream RF operates at a low applied voltage, the dual-frequency jet can achieve similar plasma density to AC jet but with much smaller gas temperature.

The results in figure 7-5 focus on wavelength-integrated optical emission intensity. It is possible to strengthen the results with emission intensities of key plasma species. Figure 7-6 shows the AC voltage dependence of emission intensities of nitrogen dimer ions at 391 nm, excited helium at 706 nm, and

two excited atomic oxygen lines at 777 and 845 nm. It is evident that these important species are much more abundant at V_{RF} = 2 kV than the AC only case. Helium line at 706 nm is known to indicate energetic electrons[7.8], and its larger emission intensity in figure 7-6b supports the conclusion of larger plasma density in the dual-frequency jet derived from the wavelength-integrated emission data in figure 7-5. Also the higher emission intensities of the dual-frequency jet at 777 nm and 845 nm suggest a more active reaction chemistry in the downstream region. Finally it should be noted that the increase in the emission intensity of the dual-frequency jet from the AC case is different, particularly at 706, 777 and 845 nm. This may be indicative of changes in the electron mean energy and indeed the electron energy distribution function. However ion energy may not change much, as it is small in atmospheric plasmas[7.9].

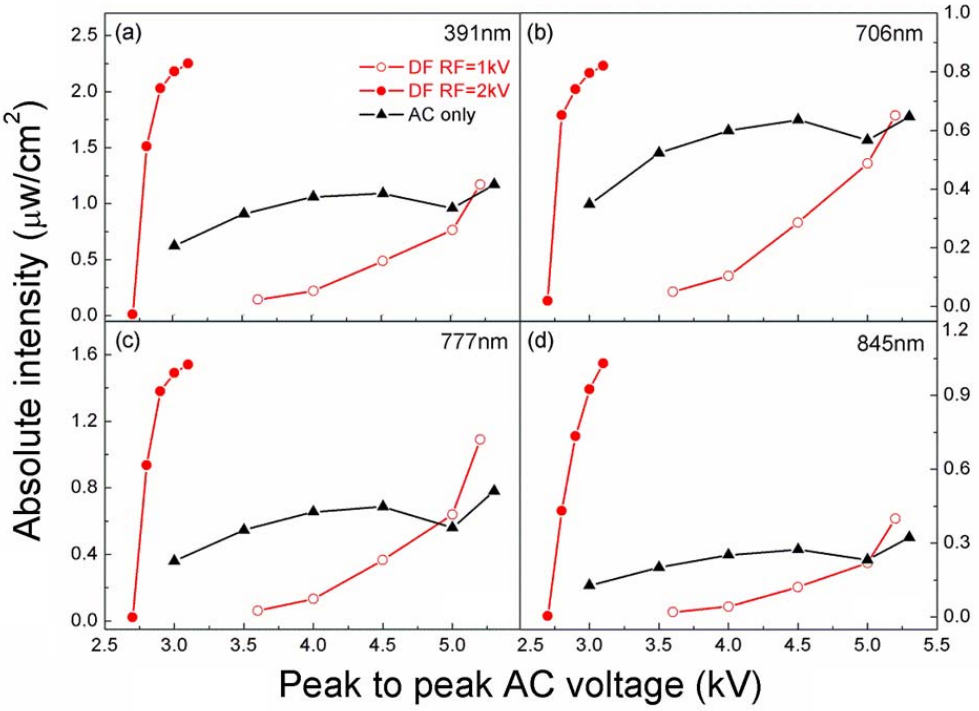

Fig 7-6: Absolute emission intensities at (a) 391 nm; (b) 706 nm; (c) 777 nm; and (d) 845 nm as a function of the AC voltage, for the three different values of the RF voltage: V_{RF} = 0 (AC only, black curve); V_{RF} = 1.0 kV (red empty circles) and V_{RF} = 2.0 kV (red solid circles).

If the applied voltage of the single-frequency jet, either RF or AC, is increased above its maximum value shown in figure 7-5, the plasma jet would become unstable. However for the dual-frequency jet, further increase in V_{AC} does not affect plasma stability but it may cause the AC voltage waveform to deviate from its nominally sinusoidal waveform because of the excessive current flowing through the transformer of the power supply. As this non-sinusoidal regime is still useful for practical applications, the wavelength-integrated emission intensity is plotted in figure 7-7 against the dissipated AC power for both the sinusoidal and the non-sinusoidal regimes. It is evident that the optical emission intensity can reach 64 $\mu W/cm^2$ and 60 $\mu W/cm^2$ for V_{RF} = 2.0 kV and V_{RF} = 1.0 kV respectively, at least 3 times of the maximum emission intensity of the single-frequency jets. This much increased optical emission is indicative of the very high plasma density that can be achieved with the dual-frequency plasma jet.

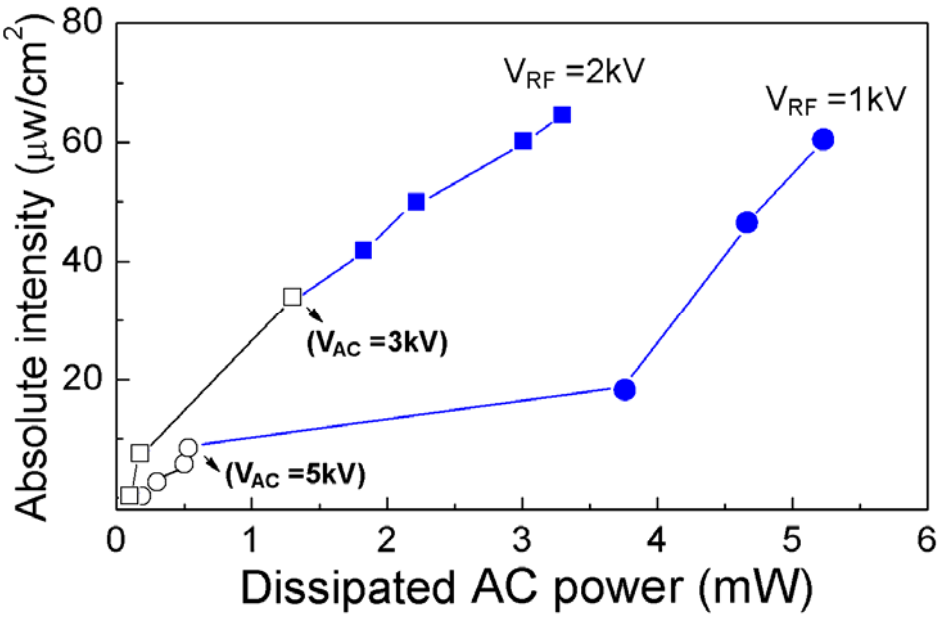

Fig 7-7: Absolute emission intensity as a function of the dissipated AC power at two values of V_{RF}. The black section has a sinusoidal current waveform, whereas the blue section has a non-sinusoidal waveform.

7.4 Summary

A spatially separated dual-frequency jet is reported in this chapter. This jet employs the capillary-ring structure with the capillary electrode connected to RF power and the ring electrode grounded. An additional electrode is placed downstream and powered by AC at kilohertz. This structure makes it possible to apply two plasma excitations at different frequencies to spatially separated locations.

Results and discussions presented in this chapter have demonstrated the distinct benefits of the dual-frequency plasma jet. In comparison with its single-frequency counterparts, the dual-frequency jet has been shown to have larger plasma density, at least 3 times that of the maximum of the RF jet. Also, the dual-frequency jet is able to achieve longer plume length than the AC jet, and at a low level of the applied voltages at which the corresponding single-frequency excitation would be unable to even strike a plasma. Clearly the dual-frequency jet captures the advantages of the RF and AC jets in a single device. Moreover, the achievement of high plasma density in the dual-frequency jet is achieved at lower gas temperature.

The interaction between the influences of the two frequency excitations is both clear and beneficial. The upstream RF discharge provides an intense source of electrons which can be drawn to the AC discharge in the downstream region for the latter to acquire higher plasma density and longer plume length without undue increase in gas temperature. Clearly the influences of the two excitations do couple together to influence plasma behaviour of the dual-frequency plasma jet.

In short, the promising possibility of separate control of different plasma parameters (e.g. plume length, plasma density and gas temperature) is demonstrated. It is clear that dual-frequency plasma jets offer enhanced plasma properties with potential for greater process control.

References

[7.1] P. C. Boyle, A. R. Ellingboe and M. M. Turner, J. Phys. D-Appl. Phys. 37, 697 (2004).

[7.2] D. O'Connell, T. Gans, E. Semmler and P. Awakowicz, Appl. Phys. Lett. 93, 081502 (2008).

[7.3] J. Waskoenig and T. Gans, Appl. Phys. Lett. 96, 181501 (2010).

[7.4] D. W. Liu, J. J. Shi and M. G. Kong, Appl. Phys. Lett. 90, 041502 (2007).

[7.5] E. Stoffels, A. J. Flikweert, W. W. Stoffels and G. M. W. Kroesen, Plasma Sources Sci. Technol. 11, 383 (2002).

[7.6] http://www.sri.com/psd/lifbase/.

[7.7] C. O. Laux, T. G. Spence, C. H. Kruger and R. N. Zare, Plasma Sources Sci. Technol. 12, 125 (2003).

[7.8] N. K. Bibinov, A. A. Fateev and K. Wiesemann, J. Phys. D-Appl. Phys. 34, 1819 (2001).

[7.9] S. M. Lee, Y. J. Hong, Y. S. Seo, F. Iza, G. C. Kim and J. K. Lee, Comput. Phys. Commun. 180, 636 (2009).

Chapter 8
Conclusions and Future Work

8.1 Main conclusions

This thesis has systematically studied the development of one class of up-scalable low-temperature atmospheric pressure plasma sources, namely the spatially extended atmospheric plasma jets and jet arrays. These plasma sources are intended for low-temperature processing of three-dimensional objects such as those relevant to medicine (e.g. living tissues and surgical instruments). Five different plasma sources have been proposed and investigated experimentally, and their relevant merits are analysed. The organisation of this thesis shows a logical development of these plasma sources and the benefits of parallelising spatially extended atmospheric plasma jets to a large-scale plasma source with distinct advantages of spatial uniformity and robust stability when treating complex 3D-shaped samples. The work detailed in this thesis has contributed to five journal publications and twelve conference presentations. The key conclusions are summarised in the following sections.

8.1.1 Atmospheric pressure slot plasma jet

Chapter 3 details the development of an atmospheric pressure slot plasma jet. It is shown that the slot plasma jet can work in two distinct modes, i.e. the single discharge mode and the dual discharge mode. For a

three-electrode slot plasma jet working in the dual discharge mode, the presence of the upstream discharge lowers the power consumption of the downstream plasma curtain. This allows the applied voltage to be raised by about 20% without unstabilising the downstream plasma curtain when compared to the two-electrode slot plasma jet case. Nanosecond-exposure images demonstrate the 25.4×8 mm^2 plasma curtain produced by the slot plasma jet is free of streamers at a helium flow of 15 slm. Abundant reactive species are found in the downstream application region and the gas temperature at the contact point with the downstream substrate is just below 30 °C. The main disadvantage of the atmospheric pressure slot plasma jet is that its plasma stability and uniformity become deteriorative when treating three-dimensional objects.

8.1.2 Single APGD jet

Common atmospheric pressure plasma jets are categorised in chapter 4 according to their electrode structures and their implications on how easily individual plasma jets may be parallelised in an atmospheric plasma jet array. The resulting understanding of these common single APGD jets leads to the design of a hybrid capillary-ring electrode configuration as the base architecture of the elemental plasma jet for use in a plasma jet array.

The capillary-ring plasma jet is characterised in detail through direct comparison with two single-electrode plasma jets using a capillary electrode or a ring electrode respectively. The capillary-ring plasma jet should have its capillary electrode powered and its ring electrode grounded in order to take the full advantage of the electrode design. It is found that the capillary-ring plasma jet is advantageous over the two single-electrode jets due to the elevated electric field between its capillary and ring electrodes in the upstream region.

In the free-burning mode, the capillary-ring plasma jet is shown to have the lowest ignition voltage but the longest jet plume length among the three plasma jets at a given applied voltage. Its plume length is longer than 22 mm when the peak applied voltage is above 3.5 kV. The dynamics of the capillary-ring plasma jet reveal the presence of two distinct modes, namely the bullet mode and the continuous mode. The transition occurs around the peak applied voltage of 3.0 kV and accounts for a significant increase of the plume length in the continuous mode.

When treating a downstream metal sample, the plasma plume intensity from the nozzle to the sample surface, the charge transfer to the downstream metal surface and the optical emission measured from the plasma contact point on the downstream sample all suggest that the capillary-ring plasma jet is superior to the other two plasma jets. When treating a downstream dielectric surface, the end-view images and the radial range of the reactive plasma species on the sample surface also confirm the capillary-ring plasma jet as the best choice among the three plasma jets.

Absolute atomic oxygen and ozone densities are measured with a specially designed mass spectrometer system as a function of the nozzle-to-orifice distance for a capillary-ring jet supplied with 4 slm helium and 40 sccm oxygen. The peak atomic oxygen density is 4.5×10^{14} cm^{-3} at 10 ~ 14 mm away from jet nozzle while the peak ozone density is 1.2×10^{15} cm^{-3} at 18 mm. These measurements are indicative of the level of reactive oxygen species produced by the plasma jet.

8.1.3 1D array of atmospheric pressure plasma jets

Chapter 5 reports a one-dimensional array of atmospheric pressure plasma jets. This jet array covers a length of 3.2 cm and each jet is connected with a ballast resistor to provide negative feedback to the applied voltage. The

latter enables an effective self-adjustment mechanism when all jets work together in an array. The jet array is able to fire its all individual jets when treating vastly three-dimensional objects. The synchronised operation of the jets in the jet array is demonstrated by the discharge current traces and fast imaging when the array is used to treat both flat and sloped substrate surfaces. Spatial jet-to-jet uniformity is further confirmed by optical emission intensities measured from the plasma contact points on the downstream metal surface. It is found that the jet array has much smaller intensity variation among individual jets from 6% for a downstream flat surface to 12% for a downstream sloped surface at 15°, while the intensity variation for a comparable scanning single jet is 48% in the sloped surface case. The jet array maintains robust temporal stability and spatial jet-to-jet uniformity.

The architecture of the 1D jet array allows its up-scaling, and this is demonstrated with a 1D array of 30 plasma jets.

8.1.4 2D arrays of atmospheric pressure plasma jets

Chapter 6 reports a detailed study of 2D arrays of atmospheric pressure plasma jets. The 2D jet array comprises hexagonally arranged capillary-ring plasma jets. The jet density, a measure of how tightly individual jets are packed in an array, is the highest among all the published jet arrays. A 2D 7-jet array is shown to have a broad operation range even when no ballast resistors are added to the circuits. It is capable of firing all its individual jets simultaneously against both flat metallic and dielectric samples placed downstream, as well as vastly three-dimensional objects. It is believed that the capacitive jet-housing structure acts as a distributed built-in ballast system and this helps achieve simultaneous firing of all individual jets. There is an optimal frequency range around 10 kHz for jet-jet uniformity.

The dynamic of the 2D 7-jet array is found to have intriguing features. In

the negative half cycle of the applied voltage, only the central jet can produce plasma plume but the plume cannot reach the glass substrate which is placed downstream at 13 mm from array nozzles. In the positive half cycle, all plasma channels produce plasma plumes and they all can reach the substrate. The ignition of the central jet occurs slightly later than those of the surrounding jets. This suggests different jet-to-jet interactions between 1D and 2D jet arrays. When different amounts of oxygen are mixed into helium, the best spatial uniformity is achieved when O_2/He = 0.5%.

End-view images with an exposure time of 10 ns and with one cycle time of the applied voltage are used to demonstrate that good jet-to-jet uniformity is achieved. The intensity of the central jet tends to be weaker and better spatial uniformity is expected to be achieved by using individualised ballast. Through *E. coli* inactivation experiments, the impact of reaction chemistry induced by individual jets is shown to overlap to allow for uniform treatment. For the bacterial inactivation experiment detailed in this chapter, the spatial reach of reactive plasma species is found to have an impact diameter of 27 mm and 35 mm respectively after plasma treatment of *E. coli* cells for three and five minutes. This is significantly larger than the physical size of the 2D 7-jet array.

The scalability of the 2D jet array is demonstrated by the successful development of a larger 2D 19-jet array and a 37-jet array. The 37-jet array is estimated to have a reaction chemistry impact diameter of 48 mm. This suggests that 2D jet arrays offer a viable and previously unavailable option as a practical and reliable plasma source for biomedical applications.

8.1.5 Dual-frequency plasma jet

Chapter 7 presents a spatially separated dual-frequency jet, for which a megahertz RF electric field is applied to the upstream region of a jet structure

containing three electrodes while a kilohertz AC electric field is applied to its downstream region. This arrangement makes it possible to separately control three fundamental plasma parameters, namely plasma plume length, plasma density and gas temperature.

It is found that the use of two very different frequencies can achieve a plume length up to 36 mm, significantly longer than the longest plume length achieved by single frequency plasma jets. The plasma density is inferred with emission intensity at the downstream plasma contact point and it is shown that the plasma density achieved by the dual-frequency plasma jet can be at least 3 times and 4 times of the maximum density achieved by the corresponding RF jet and AC jet respectively. Moreover, the attainment of high plasma density by the dual-frequency plasma jet is reached at lower gas temperature than the singe frequency jets.

The advantages of the dual-frequency plasma jet are a result of the interaction between the influences of the spatially separated plasma excitations at two very different frequencies. The upstream RF discharge provides a rich source of seed electrons which can be drawn to the downstream to the AC discharge for the latter to acquire higher plasma density and longer plume length without undue increase in gas temperature. Because of the spatially separated control, plasma plume length, plasma density and gas temperature of the dual-frequency plasma jet can be tailored to suit specific applications. They can also be used as the elemental plasma jet to form 1D and 2D plasma jet arrays of improved process control.

8.2 Future work and improvement

The work presented in this thesis is a systematic development of large-scale plasma sources aiming primarily at biomedical applications. Parallelisation of spatially extended atmospheric plasma jets in 1D and 2D

arrangements is proposed and demonstrated to possess many significant benefits important to many applications. The 1D and 2D jet arrays represent a platform technique for up-scalable atmospheric pressure plasma sources. Some of the future work is summarised below.

Given that the dual-frequency excitations offer an effective route towards separate control of key plasma parameters, it is logical to implement the dual-frequency excitations concept in the 2D jet array. This new 2D array is likely to attain higher plasma density and longer plasma plumes, and in turn these could improve the processing efficiency. With dual-frequency excitations, the capacity of the AC power supply is envisaged as a limiting factor to the maximum plasma density that can be achieved in the downstream region as more and more plasma jets are added to the array. Better or alternative design of AC power supplies will need to be studied in detail. For treating a very large object, several jet arrays can work in a modular fashion, each with its own power supply.

Plasma chemistry needs to be further investigated. The plasma sources presented in this thesis mostly use helium as the carrier gas. It is known that helium is relatively expensive. This may restrict the scope of the application of the plasma jets and jet arrays. Argon can also be used as the plasma forming gas[8.1,8.2], although streamers are easy to form in an argon plasma plume. Investigation should be directed to achieve uniform argon plasmas in 1D and 2D jet arrays. Ideally air should be considered since this would greatly reduce operation costs[8.3]. Atomic oxygen is commonly regarded as a major species accounting for bactericidal effect and this is why oxygen is often added in the work presented here. Nevertheless UV and nitric oxide are also important in biomedical applications[8.4,8.5]. Future research should look into mixing nitrogen or both nitrogen and oxygen into a carrier gas for accessing different plasma chemistries.

Another line of research can be directed to the use of alternative power

sources. Pulse power is known to be able to produce higher electron density than kilohertz AC[8.2,8.6] and it can be used to drive a plasma jet array. The increased electron density is expected to contribute to an increased yield of reactive species and hence an improved processing efficiency. Pulsed-modulated RF technology is also expected to benefit the future development of the jet array as it can lower power consumption and gas temperature[8.7]. It should be noted from the dual-frequency jet study of Chapter 7 that while the dual-frequency jet brings a high plasma density, the gas temperature is also increased. Pulsed-modulated RF excitation applied to the upstream region may considerably reduce gas temperature.

Last but not the least, more detailed plasma diagnostics are worth further investigation as direct measurements for key plasma parameters such as electron density and electron temperature are at present insufficiently developed. These parameters are very important in terms of understanding and optimising the physics of plasma sources. At low-pressure, ion flux and ion energy can be separately controlled to benefit the applications of the plasma technology for microelectronics fabrication. At atmospheric pressure, whether electron density and electron temperature can be separately controlled by the proposed spatially separated dual-frequency excitation is a fundamental question waiting for an answer. As the dual-frequency jet can achieve much higher electron density than its single frequency counterparts, electron density measurement using Stark broadening with a detection limit of $\sim 10^{13}$ cm^{-3} may become possible.

References

[8.1] H. S. Uhm, J. P. Lim and S. Z. Li, Appl. Phys. Lett. 90, 261501 (2007).

[8.2] J. L. Walsh and M. G. Kong, Appl. Phys. Lett. 91, 221502 (2007).

[8.3] J. F. Kolb, A. -A H. Mohamed, R. O. Price, R. J. Swanson, A. Bowman, R. L. Chiavarini, M. Stacey and K. H. Schoenbach, Appl. Phys. Lett. 92, 241501 (2008).

[8.4] M. G. Kong, G. Kroesen, G. Morfill, T. Nosenko, T. Shimizu, J. van Dijk and J. L. Zimmermann, New J. Phys. 11, 115012 (2009).

[8.5] G. Fridman, G. Friedman, A. Gutsol, A. B. Shekhter, V. N. Vasilets and A. Fridman, Plasma Process. Polym. 5, 503 (2008).

[8.6] J. L. Walsh, J. J. Shi and M. G. Kong, Appl. Phys. Lett. 88, 171501 (2006).

[8.7] J. J. Shi, J. Zhang, G. Qiu, J. L. Walsh and M. G. Kong, Appl. Phys. Lett. 93, 041502 (2008).